MEASUREMENT OF THE UPSILON(NS) CROSS SECTIONS IN PP COLLISIONS AT SQRT(S) = 7 TEV

A Dissertation

Submitted to the Faculty

of

Purdue University

by

Yu Zheng

In Partial Fulfillment of the

Requirements for the Degree

of

Doctor of Philosophy

December 2012

Purdue University

West Lafayette, Indiana

To my dearest parents Ling Wang and Jianghong Zheng

ACKNOWLEDGMENTS

I would like to express my deep gratitude to those who are important to the realization of this thesis and in my daily life.

First of all, I would like to thank my advisor Prof. Ian Shipsey. He is such a nice person to work and talk with. Without his guidance and endless support, I would not be able to go this far on the path to becoming an experimental physicist. His warmest care to his students eases my graduate life.

I would also like to thank Dr. Marco De Mattia for being such a wonderful colleague to work with. His well-known patience and prudence greatly enhanced the work environment. I would also like to thank Dr. Nuno Leonardo and Dr. Zoltan Gecse who have shared their profound knowledge with me.

I am also grateful to my friends during my three-years stay at Fermilab. My great thanks go to Zhen Hu, Fan Yang, Ping Tan, Si Liu and Jie Chen for their long-time support and all the happiness they generated. I want to also express my thanks to my friends back to Purdue, Xiaoting Zhou, Jianfang Zhu, Ran An, Shunyuan Zhang and Hao Sun. I treasure the days we spent together in the first two years in West Lafayette.

In the end, I want to say thanks to everyone that made my life what it is and helped me develop along the way.

TABLE OF CONTENTS

Page

LIST OF TABLES vi

LIST OF FIGURES xxii

ABSTRACT xxviii

1 HEAVY FLAVOR PHYSICS 1
- 1.1 The Standard Model of Particle Physics 1
- 1.2 Quantum Chromodynamics 2
- 1.3 Quarkonium Production 3
  - 1.3.1 Quarkonium Production Models 4
  - 1.3.2 Non-Relativistic QCD Factorization Method 5
  - 1.3.3 Bottomonium Production 7
- 1.4 Bottomonium Measurements at Tevatron 8
  - 1.4.1 Bottomonium Cross Sections 9
  - 1.4.2 Bottomonium Polarizations 10

2 THE COMPACT MUON SOLENOID EXPERIMENT AT THE CERN LARGE HADRON COLLIDER 16
- 2.1 The Large Hadron Collider 16
  - 2.1.1 The Accelerator Chain 17
  - 2.1.2 The Luminosity 18
- 2.2 The CMS Experiment 19
  - 2.2.1 Magnet 22
  - 2.2.2 Tracker 23
  - 2.2.3 Calorimetry 23
  - 2.2.4 Muon System 26
  - 2.2.5 Trigger and Data Acquisition 28

3 UPSILON(NS) PRODUCTION CROSS SECTION MEASUREMENT . 30
- 3.1 Υ(nS) Measurements with Early Data 30
- 3.2 Introduction 36
- 3.3 Analysis strategy 38
- 3.4 Data samples and online selection 40
  - 3.4.1 Trigger 40
  - 3.4.2 Datasets and skimming 41
  - 3.4.3 Luminosity 42
- 3.5 Monte Carlo event samples 43

Page
3.6 Event reconstruction 45
3.6.1 Muon reconstruction 45
3.6.2 Offline selection 45
3.7 Fit to the dimuon invariant mass spectrum 49
3.8 Acceptance 55
3.9 Efficiency 61
3.9.1 Track Embedding 61
3.9.2 Tag and probe method 63
3.9.3 Muon identification efficiency 65
3.9.4 Trigger efficiency 65
3.9.5 Track quality efficiency 71
3.9.6 Efficiency of additional selection 71
3.9.7 Computation of the total correction factor 73
3.10 Measurement of the inclusive differential cross section 74
3.11 Systematic uncertainties 76
3.11.1 Statistical contributions 78
3.11.2 Acceptance 78
3.11.3 Efficiency 81
3.11.4 Luminosity 84
3.11.5 Results of estimations 84
3.12 Measurement of the differential fiducial cross section 84
3.13 Results and Comparisons to Theory and Other Experiments 86
3.14 Results utilizing the polarization measurement from CMS 88
3.15 Summary 89

4 SUMMARY 94

LIST OF REFERENCES 152

A Track embedding 156

B Monte Carlo Closure Test 161

C Like Sign Background 170

VITA 171

LIST OF TABLES

Table Page

1.1 Stages in the hadroproduction of Υ(nS) resonances. 9

3.1 MC samples 44

3.2 Upsilon signal yields observed in the specified p_{T} ranges. 53

3.3 $\Upsilon(1S)$ unpolarized acceptance in bins of p_T^{Υ} for $|y^{\Upsilon}| < 2.4$. 58

3.4 $\Upsilon(2S)$ unpolarized acceptance in bins of p_T^{Υ} for $|y^{\Upsilon}| < 2.4$. 59

3.5 $\Upsilon(3S)$ unpolarized acceptance in bins of p_T^{Υ} for $|y^{\Upsilon}| < 2.4$. 59

3.6 Track reconstruction efficiencies as a function of p_T (GeV/c) and η for muons embedded into 7 TeV data. 62

3.7 Single muon identification efficiencies from J/ψ T&P; the uncertainties are statistical only. 67

3.8 Single-leg HLT_DoubleMu0 muon trigger efficiencies from J/ψ T&P; the uncertainties are statistical only. 68

3.9 Single-leg HLT_DoubleMu0_Quarkonium_v1 muon trigger efficiencies from J/ψ T&P; the uncertainties are statistical only. 69

3.10 The fractional change in percent to the central value of the cross section integrated over the rapidity range $|y^{\Upsilon}| < 2.4$, relative to the unpolarized value for four polarization scenarios in two frames: the helicity frame (HX) and Collins-Soper (CS) frame, each for L= 100% longitudinal, $\frac{1}{2}$L = 50% longitudinal, $\frac{1}{4}$L = 25% longitudinal, T= 100% transverse, $\frac{1}{2}$T= 50% transverse and $\frac{1}{4}$T= 25% transverse. 77

3.11 Energy dependence of the cross section 91

4.1 The product of the Υ(1S) integrated and differential fiducial cross sections and the dimuon branching fraction, in nb, integrated over the rapidity range $|y^{\Upsilon}| < 2.4$. The statistical uncertainty (stat.), the sum of the systematic uncertainties in quadrature ($\Sigma_{\mathrm{syst.}}$), and the total uncertainty ($\Delta\sigma$; including stat., $\sum_{\mathrm{syst.}}$, luminosity terms) are in percent. The numbers in parentheses are negative variations. 99

Table Page

4.2 The product of the $\Upsilon(2S)$ integrated and differential fiducial cross sections and the dimuon branching fraction, in nb, integrated over the rapidity range $|y^{\Upsilon}| < 2.4$. The statistical uncertainty (stat.), the sum of the systematic uncertainties in quadrature ($\Sigma_{\text{syst.}}$), and the total uncertainty ($\Delta\sigma$; including stat., $\sum_{\text{syst.}}$, luminosity terms) are in percent. The numbers in parentheses are negative variations. 100

4.3 The product of the $\Upsilon(3S)$ integrated and differential fiducial cross sections and the dimuon branching fraction, in nb, integrated over the rapidity range $|y^{\Upsilon}| < 2.4$. The statistical uncertainty (stat.), the sum of the systematic uncertainties in quadrature ($\Sigma_{\text{syst.}}$), and the total uncertainty ($\Delta\sigma$; including stat., $\sum_{\text{syst.}}$, luminosity terms) are in percent. The numbers in parentheses are negative variations. 101

4.4 The product of the $\Upsilon(nS)$ integrated and differential fiducial cross sections and the dimuon branching fraction, in nb, integrated over the rapidity range $|y^{\Upsilon}| < 0.4$. The statistical uncertainty (stat.), the sum of the systematic uncertainties in quadrature ($\Sigma_{\text{syst.}}$), and the total uncertainty ($\Delta\sigma$; including stat., $\sum_{\text{syst.}}$, luminosity terms) are in percent. The numbers in parentheses are negative variations. 102

4.5 The product of the $\Upsilon(1S)$ integrated and differential fiducial cross sections and the dimuon branching fraction, in nb, integrated over the rapidity range $0.4 < |y^{\Upsilon}| < 0.8$. The statistical uncertainty (stat.), the sum of the systematic uncertainties in quadrature ($\Sigma_{\text{syst.}}$), and the total uncertainty ($\Delta\sigma$; including stat., $\sum_{\text{syst.}}$, luminosity terms) are in percent. The numbers in parentheses are negative variations. 103

4.6 The product of the $\Upsilon(1S)$ integrated and differential fiducial cross sections and the dimuon branching fraction, in nb, integrated over the rapidity range $0.8 < |y^{\Upsilon}| < 1.2$. The statistical uncertainty (stat.), the sum of the systematic uncertainties in quadrature ($\Sigma_{\text{syst.}}$), and the total uncertainty ($\Delta\sigma$; including stat., $\sum_{\text{syst.}}$, luminosity terms) are in percent. The numbers in parentheses are negative variations. 104

4.7 The product of the $\Upsilon(1S)$ integrated and differential fiducial cross sections and the dimuon branching fraction, in nb, integrated over the rapidity range $1.2 < |y^{\Upsilon}| < 1.6$. The statistical uncertainty (stat.), the sum of the systematic uncertainties in quadrature ($\Sigma_{\text{syst.}}$), and the total uncertainty ($\Delta\sigma$; including stat., $\sum_{\text{syst.}}$, luminosity terms) are in percent. The numbers in parentheses are negative variations. 105

Table Page

4.8 The product of the $\Upsilon(1S)$ integrated and differential fiducial cross sections and the dimuon branching fraction, in nb, integrated over the rapidity range $1.6 < |y^{\Upsilon}| < 2.0$. The statistical uncertainty (stat.), the sum of the systematic uncertainties in quadrature ($\Sigma_{\text{syst.}}$), and the total uncertainty ($\Delta\sigma$; including stat., $\sum_{\text{syst.}}$, luminosity terms) are in percent. The numbers in parentheses are negative variations. 106

4.9 The product of the $\Upsilon(1S)$ integrated and differential fiducial cross sections and the dimuon branching fraction, in nb, integrated over the rapidity range $2.0 < |y^{\Upsilon}| < 2.4$. The statistical uncertainty (stat.), the sum of the systematic uncertainties in quadrature ($\Sigma_{\text{syst.}}$), and the total uncertainty ($\Delta\sigma$; including stat., $\sum_{\text{syst.}}$, luminosity terms) are in percent. The numbers in parentheses are negative variations. 107

4.10 The product of the $\Upsilon(nS)$ integrated and rapidity differential fiducial cross sections and the dimuon branching fraction, in nb, integrated over the p_{T} range $p_{\text{T}}^{\Upsilon} < 50\,\text{GeV}/c$. The statistical uncertainty (stat.), the sum of the systematic uncertainties in quadrature ($\Sigma_{\text{syst.}}$), and the total uncertainty ($\Delta\sigma$; including stat., $\sum_{\text{syst.}}$, luminosity terms) are in percent. The numbers in parentheses are negative variations. 108

4.11 The ratio of $\Upsilon(nS)$ fiducial cross sections, and its p_{T} dependence, with statistical and systematic uncertainties combined in The numbers in parentheses are negative variations. 109

4.12 The ratio of $\Upsilon(nS)$ fiducial cross sections, and its rapidity dependence, with statistical and systematic uncertainties combined in quadrature. The numbers in parentheses are negative variations. 109

4.13 Relative values of the systematic uncertainties on the $\Upsilon(1S)$ integrated and differential fiducial cross section times the dimuon branching fraction, for $|y| < 2.4$, in units of percent. The p_{T} intervals are in units of GeV/c. The following abbreviations are used: ϵ_{muid}, ϵ_{trig}, ϵ_{ρ}, ϵ_{func}, ϵ_{trk}, PDF_{CB}, PDF_{bkgd} and M_{scale}, for the systematic uncertainties arising from the statistical uncertainties from tag and probe efficiencies, fixing the tail parameters in fitting, the background PDF, the mismeasurement of the track momentum shifts that broadens the reconstructed dimuon resonances, fixing the tail parameters in fitting, the statistical uncertainties in tracking efficiencies, the choice of bin size for the efficiencies and from ρ factors. The luminosity uncertainty of 4% is not shown in the table. The numbers in parentheses are negative variations. 110

Table Page

4.14 Relative values of the systematic uncertainties on the $\Upsilon(2S)$ integrated and differential fiducial cross section times the dimuon branching fraction, for $|y| < 2.4$, in units of percent. The p_T intervals are in units of GeV/c. The following abbreviations are used: ϵ_{muid}, ϵ_{trig}, ϵ_{ρ}, ϵ_{func}, ϵ_{trk}, PDF_{CB}, PDF_{bkgd} and M_{scale}, for the systematic uncertainties arising from the statistical uncertainties from tag and probe efficiencies, fixinging the tail parameters in fitting, the background PDF, the mismeasurement of the track momentum shifts that broadens the reconstructed dimuon resonances, fixing the tail parameters in fitting, the statistical uncertainties in tracking efficiencies, the choice of bin size for the efficiencies and from ρ factors. The luminosity uncertainty of 4% is not shown in the table. The numbers in parentheses are negative variations. 111

4.15 Relative values of the systematic uncertainties on the $\Upsilon(3S)$ integrated and differential fiducial cross section times the dimuon branching fraction, for $|y| < 2.4$, in units of percent. The p_T intervals are in units of GeV/c. The following abbreviations are used: ϵ_{muid}, ϵ_{trig}, ϵ_{ρ}, ϵ_{func}, ϵ_{trk}, PDF_{CB}, PDF_{bkgd} and M_{scale}, for the systematic uncertainties arising from the statistical uncertainties from tag and probe identification efficiencies, trigger efficiencies, the ρ factors, the choice of bin size of the efficiencies, the statistical uncertainties in tracking efficiencies, fixinging the tail parameters in fitting, the background PDF and the mismeasurement of the track momentum shifts that broadens the reconstructed dimuon resonances. The luminosity uncertainty of 4% is not shown in the table. The numbers in parentheses are negative variations. 112

4.16 Relative values of the systematic uncertainties on the $\Upsilon(nS)$ integrated and differential fiducial cross section times the dimuon branching fraction, for $|y| < 0.4$, in units of percent. The p_T intervals are in units of GeV/c. The following abbreviations are used: ϵ_{muid}, ϵ_{trig}, ϵ_{ρ}, ϵ_{func}, ϵ_{trk}, PDF_{CB}, PDF_{bkgd} and M_{scale}, for the systematic uncertainties arising from the statistical uncertainties from tag and probe identification efficiencies, trigger efficiencies, the ρ factors, the choice of bin size of the efficiencies, the statistical uncertainties in tracking efficiencies, fixinging the tail parameters in fitting, the background PDF and the mismeasurement of the track momentum shifts that broadens the reconstructed dimuon resonances. The luminosity uncertainty of 4% is not shown in the table. The numbers in parentheses are negative variations. 113

Table Page

4.17 Relative values of the systematic uncertainties on the Υ(nS) integrated and differential fiducial cross section times the dimuon branching fraction, for $0.4 < |y| < 0.8$, in units of percent. The p_{T} intervals are in units of GeV/c. The following abbreviations are used: ϵ_{muid}, ϵ_{trig}, ϵ_{ρ}, ϵ_{func}, ϵ_{trk}, PDF_{CB}, PDF_{bkgd} and M_{scale}, for the systematic uncertainties arising from the statistical uncertainties from tag and probe identification efficiencies, trigger efficiencies, the ρ factors, the choice of bin size of the efficiencies, the statistical uncertainties in tracking efficiencies, fixinging the tail parameters in fitting, the background PDF and the mismeasurement of the track momentum shifts that broadens the reconstructed dimuon resonances. The luminosity uncertainty of 4% is not shown in the table. The numbers in parentheses are negative variations. 114

4.18 Relative values of the systematic uncertainties on the Υ(nS) integrated and differential fiducial cross section times the dimuon branching fraction, for $0.8 < |y| < 1.2$, in units of percent. The p_{T} intervals are in units of GeV/c. The following abbreviations are used: ϵ_{muid}, ϵ_{trig}, ϵ_{ρ}, ϵ_{func}, ϵ_{trk}, PDF_{CB}, PDF_{bkgd} and M_{scale}, for the systematic uncertainties arising from the statistical uncertainties from tag and probe identification efficiencies, trigger efficiencies, the ρ factors, the choice of bin size of the efficiencies, the statistical uncertainties in tracking efficiencies, fixinging the tail parameters in fitting, the background PDF and the mismeasurement of the track momentum shifts that broadens the reconstructed dimuon resonances. The luminosity uncertainty of 4% is not shown in the table. The numbers in parentheses are negative variations. 115

4.19 Relative values of the systematic uncertainties on the Υ(nS) integrated and differential fiducial cross section times the dimuon branching fraction, for $1.2 < |y| < 1.6$, in units of percent. The p_{T} intervals are in units of GeV/c. The following abbreviations are used: ϵ_{muid}, ϵ_{trig}, ϵ_{ρ}, ϵ_{func}, ϵ_{trk}, PDF_{CB}, PDF_{bkgd} and M_{scale}, for the systematic uncertainties arising from the statistical uncertainties from tag and probe identification efficiencies, trigger efficiencies, the ρ factors, the choice of bin size of the efficiencies, the statistical uncertainties in tracking efficiencies, fixinging the tail parameters in fitting, the background PDF and the mismeasurement of the track momentum shifts that broadens the reconstructed dimuon resonances. The luminosity uncertainty of 4% is not shown in the table. The numbers in parentheses are negative variations. 116

Table Page

4.20 Relative values of the systematic uncertainties on the Υ(nS) integrated and differential fiducial cross section times the dimuon branching fraction, for $1.6 < |y| < 2.0$, in units of percent. The p_{T} intervals are in units of GeV/c. The following abbreviations are used: ϵ_{muid}, ϵ_{trig}, ϵ_{ρ}, ϵ_{func}, ϵ_{trk}, PDF_{CB}, PDF_{bkgd} and M_{scale}, for the systematic uncertainties arising from the statistical uncertainties from tag and probe identification efficiencies, trigger efficiencies, the ρ factors, the choice of bin size of the efficiencies, the statistical uncertainties in tracking efficiencies, fixinging the tail parameters in fitting, the background PDF and the mismeasurement of the track momentum shifts that broadens the reconstructed dimuon resonances. The luminosity uncertainty of 4% is not shown in the table. The numbers in parentheses are negative variations. 117

4.21 Relative values of the systematic uncertainties on the Υ(nS) integrated and differential fiducial cross section times the dimuon branching fraction, for $2.0 < |y| < 2.4$, in units of percent. The p_{T} intervals are in units of GeV/c. The following abbreviations are used: ϵ_{muid}, ϵ_{trig}, ϵ_{ρ}, ϵ_{func}, ϵ_{trk}, PDF_{CB}, PDF_{bkgd} and M_{scale}, for the systematic uncertainties arising from the statistical uncertainties from tag and probe identification efficiencies, trigger efficiencies, the ρ factors, the choice of bin size of the efficiencies, the statistical uncertainties in tracking efficiencies, fixinging the tail parameters in fitting, the background PDF and the mismeasurement of the track momentum shifts that broadens the reconstructed dimuon resonances. The luminosity uncertainty of 4% is not shown in the table. The numbers in parentheses are negative variations. 118

4.22 Relative values of the systematic uncertainties on the Υ(nS) integrated and rapidity differential fiducial cross section times the dimuon branching fraction, for $p_{\mathrm{T}} < 50$ GeV/c, in units of percent. The following abbreviations are used: ϵ_{muid}, ϵ_{trig}, ϵ_{ρ}, ϵ_{func}, ϵ_{trk}, PDF_{CB}, PDF_{bkgd} and M_{scale}, for the systematic uncertainties arising from the statistical uncertainties from tag and probe identification efficiencies, trigger efficiencies, the ρ factors, the choice of bin size of the efficiencies, the statistical uncertainties in tracking efficiencies, fixinging the tail parameters in fitting, the background PDF and the mismeasurement of the track momentum shifts that broadens the reconstructed dimuon resonances. The luminosity uncertainty of 4% is not shown in the table. The numbers in parentheses are negative variations. 119

Table Page

4.23 The product of the Υ(nS) production cross sections and the dimuon branching fraction, in nb, integrated over the rapidity range $|y^{\Upsilon}| < 1.2$ and the p_{T} range from 10 to 50 GeV/c. The cross sections assume the Υ(nS) are unpolarized. The statistical uncertainty (stat.), the sum in quadrature of the systematic uncertainties apart from the ones from the polarization ($\sum_{\mathrm{syst.}}$), the systematic uncertainties from the polarization (syst.(pol)), and the total uncertainty ($\Delta\sigma$; including stat., $\sum_{\mathrm{syst.}}$, syst.(pol), luminosity terms) are in percent. The numbers in parentheses are negative variations. 120

4.24 The product of the Υ(1S) integrated and differential production cross sections and the dimuon branching fraction, in nb, measured for four polarization scenarios, in helicity frame (HX) and Collins-Soper (CS) frame, each for L= 100% longitudinal, and T= 100% transverse, integrated over the rapidity range $|y^{\Upsilon}| < 2.4$. The statistical uncertainty (stat.), the sum of the systematic uncertainties in quadrature ($\Sigma_{\mathrm{syst.}}$), and the total uncertainty ($\Delta\sigma$; including stat., $\sum_{\mathrm{syst.}}$, luminosity terms) are in percent. For the four polarization scenarios the fractional change in percent to the central value of the cross section relative to the unpolarized value is given. The numbers in parentheses are negative variations. 126

4.25 The product of the Υ(2S) integrated and differential production cross sections and the dimuon branching fraction, in nb, measured for four polarization scenarios, in helicity frame (HX) and Collins-Soper (CS) frame, each for L= 100% longitudinal, and T= 100% transverse, integrated over the rapidity range $|y^{\Upsilon}| < 2.4$. The statistical uncertainty (stat.), the sum of the systematic uncertainties in quadrature ($\Sigma_{\mathrm{syst.}}$), and the total uncertainty ($\Delta\sigma$; including stat., $\sum_{\mathrm{syst.}}$, luminosity terms) are in percent. For the four polarization scenarios the fractional change in percent to the central value of the cross section relative to the unpolarized value is given. The numbers in parentheses are negative variations. 127

4.26 The product of the Υ(3S) integrated and differential production cross sections and the dimuon branching fraction, in nb, measured for four polarization scenarios, in helicity frame (HX) and Collins-Soper (CS) frame, each for L= 100% longitudinal, and T= 100% transverse, integrated over the rapidity range $|y^{\Upsilon}| < 2.4$. The statistical uncertainty (stat.), the sum of the systematic uncertainties in quadrature ($\Sigma_{\mathrm{syst.}}$), and the total uncertainty ($\Delta\sigma$; including stat., $\sum_{\mathrm{syst.}}$, luminosity terms) are in percent. For the four polarization scenarios the fractional change in percent to the central value of the cross section relative to the unpolarized value is given. The numbers in parentheses are negative variations. 128

Table Page

4.27 The product of the Υ(nS) integrated and differential production cross sections and the dimuon branching fraction, in nb, measured for four polarization scenarios, in helicity frame (HX) and Collins-Soper (CS) frame, each for L= 100% longitudinal, and T= 100% transverse, integrated over the rapidity range $|y^{\Upsilon}| < 0.4$. The statistical uncertainty (stat.), the sum of the systematic uncertainties in quadrature ($\Sigma_{\text{syst.}}$), and the total uncertainty ($\Delta\sigma$; including stat., $\sum_{\text{syst.}}$, luminosity terms) are in percent. For the four polarization scenarios the fractional change in percent to the central value of the cross section relative to the unpolarized value is given. The numbers in parentheses are negative variations. 129

4.28 The product of the Υ(nS) integrated and differential production cross sections and the dimuon branching fraction, in nb, measured for four polarization scenarios, in helicity frame (HX) and Collins-Soper (CS) frame, each for L= 100% longitudinal, and T= 100% transverse, integrated over the rapidity range $0.4 < |y^{\Upsilon}| < 0.8$. The statistical uncertainty (stat.), the sum of the systematic uncertainties in quadrature ($\Sigma_{\text{syst.}}$), and the total uncertainty ($\Delta\sigma$; including stat., $\sum_{\text{syst.}}$, luminosity terms) are in percent. For the four polarization scenarios the fractional change in percent to the central value of the cross section relative to the unpolarized value is given. The numbers in parentheses are negative variations. 130

4.29 The product of the Υ(nS) integrated and differential production cross sections and the dimuon branching fraction, in nb, measured for four polarization scenarios, in helicity frame (HX) and Collins-Soper (CS) frame, each for L= 100% longitudinal, and T= 100% transverse, integrated over the rapidity range $0.8 < |y^{\Upsilon}| < 1.2$ The statistical uncertainty (stat.), the sum of the systematic uncertainties in quadrature ($\Sigma_{\text{syst.}}$), and the total uncertainty ($\Delta\sigma$; including stat., $\sum_{\text{syst.}}$, luminosity terms) are in percent. For the four polarization scenarios the fractional change in percent to the central value of the cross section relative to the unpolarized value is given. The numbers in parentheses are negative variations. 131

4.30 The product of the Υ(nS) integrated and differential production cross sections and the dimuon branching fraction, in nb, measured for four polarization scenarios, in helicity frame (HX) and Collins-Soper (CS) frame, each for L= 100% longitudinal, and T= 100% transverse, integrated over the rapidity range $1.2 < |y^{\Upsilon}| < 1.6$ The statistical uncertainty (stat.), the sum of the systematic uncertainties in quadrature ($\Sigma_{\text{syst.}}$), and the total uncertainty ($\Delta\sigma$; including stat., $\sum_{\text{syst.}}$, luminosity terms) are in percent. For the four polarization scenarios the fractional change in percent to the central value of the cross section relative to the unpolarized value is given. The numbers in parentheses are negative variations. 132

Table Page

4.31 The product of the Υ(nS) integrated and differential production cross sections and the dimuon branching fraction, in nb, measured for four polarization scenarios, in helicity frame (HX) and Collins-Soper (CS) frame, each for L= 100% longitudinal, and T= 100% transverse, integrated over the rapidity range $1.6 < |y^{\Upsilon}| < 2.0$. The statistical uncertainty (stat.), the sum of the systematic uncertainties in quadrature ($\Sigma_{\text{syst.}}$), and the total uncertainty ($\Delta\sigma$; including stat., $\sum_{\text{syst.}}$, luminosity terms) are in percent. For the four polarization scenarios the fractional change in percent to the central value of the cross section relative to the unpolarized value is given. The numbers in parentheses are negative variations. 133

4.32 The product of the Υ(nS) integrated and differential production cross sections and the dimuon branching fraction, in nb, measured for four polarization scenarios, in helicity frame (HX) and Collins-Soper (CS) frame, each for L= 100% longitudinal, and T= 100% transverse, integrated over the rapidity range $2.0 < |y^{\Upsilon}| < 2.4$. The statistical uncertainty (stat.), the sum of the systematic uncertainties in quadrature ($\Sigma_{\text{syst.}}$), and the total uncertainty ($\Delta\sigma$; including stat., $\sum_{\text{syst.}}$, luminosity terms) are in percent. For the four polarization scenarios the fractional change in percent to the central value of the cross section relative to the unpolarized value is given. 134

4.33 The product of the Υ(1S) integrated and rapidity differential production cross sections and the dimuon branching fraction, in nb, measured for four polarization scenarios, in helicity frame (HX) and Collins-Soper (CS) frame, each for L= 100% longitudinal, and T= 100% transverse, integrated over the p_{T} range $p_{\text{T}}^{\Upsilon} < 50\,\text{GeV}/c$. The statistical uncertainty (stat.), the sum of the systematic uncertainties in quadrature ($\Sigma_{\text{syst.}}$), and the total uncertainty ($\Delta\sigma$; including stat., $\sum_{\text{syst.}}$, luminosity terms) are in percent. For the four polarization scenarios the fractional change in percent to the central value of the cross section relative to the unpolarized value is given. The numbers in parentheses are negative variations. 135

4.34 The ratio of Υ(nS) cross sections, and its p_{T} dependence, for the unpolarized scenario, with statistical and systematic uncertainties combined in quadrature. The numbers in parentheses are negative variations. 136

4.35 The ratio of Υ(nS) cross sections, and its rapidity dependence, with statistical and systematic uncertainties combined in quadrature. The numbers in parentheses are negative variations. 136

Table Page

4.36 Relative values of the systematic uncertainties on the $\Upsilon(1S)$ integrated and differential production cross section times the dimuon branching fraction, for $|y| < 2.4$, assuming null production polarization, in units of percent. The p_{T} intervals are in units of GeV/c. The following abbreviations are used: A, S_p, $A_{p_{\mathrm{T}}}$, A_{fsr}, ϵ_{muid}, ϵ_{trig}, ϵ_{ρ}, ϵ_{func}, ϵ_{trk}, PDF_{CB}, PDF_{bkgd} and M_{scale} for the systematic uncertainties arising from the statistical uncertainties in acceptance, imperfect knowledge of the production p_{T} spectrum, imperfect knowledge of the momentum scale, the modeling of FSR, the statistical uncertainties in tag and probe muon identification, trigger efficiencies and the ρ factor, the choice of bin size for the efficiencies, the statistical uncertainties in tracking efficiencies, fixing the tail parameters in fitting, the background PDF and imperfect knowledge of the momentum scale. The luminosity uncertainty of 4% is not shown in the table. The numbers in parentheses are negative variations. 137

4.37 Relative values of the systematic uncertainties on the $\Upsilon(2S)$ integrated and differential production cross section times the dimuon branching fraction, for $|y| < 2.4$, assuming null production polarization, in units of percent. The p_{T} intervals are in units of GeV/c. The following abbreviations are used: A, S_p, $A_{p_{\mathrm{T}}}$, A_{fsr}, ϵ_{muid}, ϵ_{trig}, ϵ_{ρ}, ϵ_{func}, ϵ_{trk}, PDF_{CB}, PDF_{bkgd} and M_{scale} for the systematic uncertainties arising from the statistical uncertainties in acceptance, imperfect knowledge of the production p_{T} spectrum, imperfect knowledge of the momentum scale, the modeling of FSR, the statistical uncertainties in tag and probe muon identification, trigger efficiencies and the ρ factor, the choice of bin size for the efficiencies, the statistical uncertainties in tracking efficiencies, fixinging the tail parameters in fitting, the background PDF and imperfect knowledge of the momentum scale. The luminosity uncertainty of 4% is not shown in the table. The numbers in parentheses are negative variations. 138

Table Page

4.38 Relative values of the systematic uncertainties on the Υ(3S) integrated and differential production cross section times the dimuon branching fraction, for $|y| < 2.4$, assuming null production polarization, in units of percent. The p_{T} intervals are in units of GeV/c. The following abbreviations are used: A, S_p, $A_{p_{\mathrm{T}}}$, A_{fsr}, ϵ_{muid}, ϵ_{trig}, ϵ_{ρ}, ϵ_{func}, ϵ_{trk}, PDF_{CB}, PDF_{bkgd} and M_{scale} for the systematic uncertainties arising from the statistical uncertainties in acceptance, imperfect knowledge of the production p_{T} spectrum, imperfect knowledge of the momentum scale, the modeling of FSR, the statistical uncertainties in tag and probe muon identification, trigger efficiencies and the ρ factor, the choice of bin size for the efficiencies, the statistical uncertainties in tracking efficiencies, fixinging the tail parameters in fitting, the background PDF and imperfect knowledge of the momentum scale. The luminosity uncertainty of 4% is not shown in the table. The numbers in parentheses are negative variations. 139

4.39 Relative values of the systematic uncertainties on the Υ(nS) integrated and differential production cross section times the dimuon branching fraction, for $|y| < 0.4$, assuming null production polarization, in units of percent. The p_{T} intervals are in units of GeV/c. The following abbreviations are used: A, S_p, $A_{p_{\mathrm{T}}}$, A_{fsr}, ϵ_{muid}, ϵ_{trig}, ϵ_{ρ}, ϵ_{func}, ϵ_{trk}, PDF_{CB}, PDF_{bkgd} and M_{scale} for the systematic uncertainties arising from the statistical uncertainties in acceptance, imperfect knowledge of the production p_{T} spectrum, imperfect knowledge of the momentum scale, the modeling of FSR, the statistical uncertainties in tag and probe muon identification, trigger efficiencies and the ρ factor, the choice of bin size for the efficiencies, the statistical uncertainties in tracking efficiencies, fixinging the tail parameters in fitting, the background PDF and imperfect knowledge of the momentum scale. The luminosity uncertainty of 4% is not shown in the table. The numbers in parentheses are negative variations. 140

Table Page

4.40 Relative values of the systematic uncertainties on the Υ(nS) integrated and differential production cross section times the dimuon branching fraction, for $0.4 < |y| < 0.8$, assuming null production polarization, in units of percent. The p_{T} intervals are in units of GeV/c. The following abbreviations are used: A, S_p, $A_{p_{\mathrm{T}}}$, A_{fsr}, ϵ_{muid}, ϵ_{trig}, ϵ_{ρ}, ϵ_{func}, ϵ_{trk}, PDF_{CB}, PDF_{bkgd} and M_{scale} for the systematic uncertainties arising from the statistical uncertainties in acceptance, imperfect knowledge of the production p_{T} spectrum, imperfect knowledge of the momentum scale, the modeling of FSR, the statistical uncertainties in tag and probe muon identification, trigger efficiencies and the ρ factor, the choice of bin size for the efficiencies, the statistical uncertainties in tracking efficiencies, fixinging the tail parameters in fitting, the background PDF and imperfect knowledge of the momentum scale. The luminosity uncertainty of 4% is not shown in the table. The numbers in parentheses are negative variations. 141

4.41 Relative values of the systematic uncertainties on the Υ(nS) integrated and differential production cross section times the dimuon branching fraction, for $0.8 < |y| < 1.2$, assuming null production polarization, in units of percent. The p_{T} intervals are in units of GeV/c. The following abbreviations are used: A, S_p, $A_{p_{\mathrm{T}}}$, A_{fsr}, ϵ_{muid}, ϵ_{trig}, ϵ_{ρ}, ϵ_{func}, ϵ_{trk}, PDF_{CB}, PDF_{bkgd} and M_{scale} for the systematic uncertainties arising from the statistical uncertainties in acceptance, imperfect knowledge of the production p_{T} spectrum, imperfect knowledge of the momentum scale, the modeling of FSR, the statistical uncertainties in tag and probe muon identification, trigger efficiencies and the ρ factor, the choice of bin size for the efficiencies, the statistical uncertainties in tracking efficiencies, fixinging the tail parameters in fitting, the background PDF and imperfect knowledge of the momentum scale. The luminosity uncertainty of 4% is not shown in the table. The numbers in parentheses are negative variations. 142

Table Page

4.42 Relative values of the systematic uncertainties on the Υ(nS) integrated and differential production cross section times the dimuon branching fraction, for $1.2 < |y| < 1.6$, assuming null production polarization, in units of percent. The p_{T} intervals are in units of GeV/c. The following abbreviations are used: A, S_p, $A_{p_{\mathrm{T}}}$, A_{fsr}, ϵ_{muid}, ϵ_{trig}, ϵ_{ρ}, ϵ_{func}, ϵ_{trk}, PDF_{CB}, PDF_{bkgd} and M_{scale} for the systematic uncertainties arising from the statistical uncertainties in acceptance, imperfect knowledge of the production p_{T} spectrum, imperfect knowledge of the momentum scale, the modeling of FSR, the statistical uncertainties in tag and probe muon identification, trigger efficiencies and the ρ factor, the choice of bin size for the efficiencies, the statistical uncertainties in tracking efficiencies, fixinging the tail parameters in fitting, the background PDF and imperfect knowledge of the momentum scale. The luminosity uncertainty of 4% is not shown in the table. The numbers in parentheses are negative variations. 143

4.43 Relative values of the systematic uncertainties on the Υ(nS) integrated and differential production cross section times the dimuon branching fraction, for $1.6 < |y| < 2.4$, assuming null production polarization, in units of percent. The p_{T} intervals are in units of GeV/c. The following abbreviations are used: A, S_p, $A_{p_{\mathrm{T}}}$, A_{fsr}, ϵ_{muid}, ϵ_{trig}, ϵ_{ρ}, ϵ_{func}, ϵ_{trk}, PDF_{CB}, PDF_{bkgd} and M_{scale} for the systematic uncertainties arising from the statistical uncertainties in acceptance, imperfect knowledge of the production p_{T} spectrum, imperfect knowledge of the momentum scale, the modeling of FSR, the statistical uncertainties in tag and probe muon identification, trigger efficiencies and the ρ factor, the choice of bin size for the efficiencies, the statistical uncertainties in tracking efficiencies, fixinging the tail parameters in fitting, the background PDF and imperfect knowledge of the momentum scale. The luminosity uncertainty of 4% is not shown in the table. The numbers in parentheses are negative variations. 144

Table Page

4.44 Relative values of the systematic uncertainties on the Υ(nS) integrated and differential production cross section times the dimuon branching fraction, for $2.0 < |y| < 2.4$, assuming null production polarization, in units of percent. The p_{T} intervals are in units of GeV/c. The following abbreviations are used: A, S_p, $A_{p_{\mathrm{T}}}$, A_{fsr}, ϵ_{muid}, ϵ_{trig}, ϵ_{ρ}, ϵ_{func}, ϵ_{trk}, PDF_{CB}, PDF_{bkgd} and M_{scale} for the systematic uncertainties arising from the statistical uncertainties in acceptance, imperfect knowledge of the production p_{T} spectrum, imperfect knowledge of the momentum scale, the modeling of FSR, the statistical uncertainties in tag and probe muon identification, trigger efficiencies and the ρ factor, the choice of bin size for the efficiencies, the statistical uncertainties in tracking efficiencies, fixinging the tail parameters in fitting, the background PDF and imperfect knowledge of the momentum scale. The luminosity uncertainty of 4% is not shown in the table. The numbers in parentheses are negative variations. 145

4.45 Relative values of the systematic uncertainties on the Υ(1S) integrated and rapidity differential production cross section times the dimuon branching fraction, for $p_{\mathrm{T}} < 50$ GeV/c, assuming null production polarization, in units of percent. The following abbreviations are used: A, S_p, $A_{p_{\mathrm{T}}}$, A_{fsr}, ϵ_{muid}, ϵ_{trig}, ϵ_{ρ}, ϵ_{func}, ϵ_{trk}, PDF_{CB}, PDF_{bkgd} and M_{scale} for the systematic uncertainties arising from the statistical uncertainties in acceptance, imperfect knowledge of the production p_{T} spectrum, imperfect knowledge of the momentum scale, the modeling of FSR, the statistical uncertainties in tag and probe muon identification, trigger efficiencies and the ρ factor, the choice of bin size for the efficiencies, the statistical uncertainties in tracking efficiencies, fixinging the tail parameters in fitting, the background PDF and imperfect knowledge of the momentum scale. The luminosity uncertainty of 4% is not shown in the table. The numbers in parentheses are negative variations. 146

4.46 The product of the Υ(nS) production cross sections and the dimuon branching fraction, in nb, integrated over the rapidity range $|y^{\Upsilon}| < 1.2$ and the p_{T} range from 10 to 50 GeV/c. The cross sections assume the Υ(nS) are unpolarized. The statistical uncertainty (stat.), the sum in quadrature of the systematic uncertainties apart from the ones from the polarization ($\sum_{\mathrm{syst.}}$), the systematic uncertainties from the polarization (syst.(pol)), and the total uncertainty ($\Delta\sigma$; including stat., $\sum_{\mathrm{syst.}}$, syst.(pol), luminosity terms) are in percent. The numbers in parentheses are negative variations. 147

Table Page

4.47 The product of the Υ(nS) integrated and differential production cross sections and the dimuon branching fraction, in nb, integrated over the rapidity range $|y^{\Upsilon}| < 1.2$ and the $p_{\mathrm{T}}^{\Upsilon}$ range from 10 to 50 GeV/c. The cross sections assume the Υ(nS) are unpolarized. The statistical uncertainty (stat.), the sum in quadrature of the systematic uncertainties excluding the contribution from the polarization uncertainty ($\sum_{\mathrm{syst.}}$), the systematic uncertainties from the polarization (syst.(pol)), and the total uncertainty ($\Delta\sigma$; including stat., $\sum_{\mathrm{syst.}}$, syst.(pol), and the uncertainty in the integrated luminosity) are in percent. The numbers in parentheses are negative variations. 149

4.48 The product of the Υ(nS) integrated and differential production cross sections and the dimuon branching fraction, in nb, measured for four polarization scenarios, in helicity frame (HX) and Collins-Soper (CS) frame, each for L= 100% longitudinal, and T= 100% transverse, integrated over the rapidity range $|y^{\Upsilon}| < 0.6$. The statistical uncertainty (stat.), the sum of the systematic uncertainties in quadrature ($\Sigma_{\mathrm{syst.}}$), and the total uncertainty ($\Delta\sigma$; including stat., $\sum_{\mathrm{syst.}}$, luminosity terms) are in percent. For the four polarization scenarios the fractional change in percent to the central value of the cross section relative to the unpolarized value is given. The numbers in parentheses are negative variations. 150

4.49 The product of the Υ(nS) integrated and differential production cross sections and the dimuon branching fraction, in nb, measured for four polarization scenarios, in helicity frame (HX) and Collins-Soper (CS) frame, each for L= 100% longitudinal, and T= 100% transverse, integrated over the rapidity range $0.6 < |y^{\Upsilon}| < 1.2$. The statistical uncertainty (stat.), the sum of the systematic uncertainties in quadrature ($\Sigma_{\mathrm{syst.}}$), and the total uncertainty ($\Delta\sigma$; including stat., $\sum_{\mathrm{syst.}}$, luminosity terms) are in percent. For the four polarization scenarios the fractional change in percent to the central value of the cross section relative to the unpolarized value is given. The numbers in parentheses are negative variations. 151

A.1 Muon track acceptance as a function of p_T (GeV/c) and η for muons embedded into 7 TeV data. 156

A.2 Muon track acceptance as a function of p_T (GeV/c) and η for muons embedded into 7 TeV data. 157

A.3 Muon track reconstruction efficiencies as a function of p_T (GeV/c) and η for muons embedded into 7 TeV data. 157

A.4 Muon track reconstruction efficiencies as a function of p_T (GeV/c) and η for muons embedded into 7 TeV data. 158

Table Page

A.5 Muon track acceptance as a function of p_T (GeV/c) and η for muons embedded into 7 TeV data. 159

A.6 Muon track acceptance as a function of p_T (GeV/c) and η for muons embedded into 7 TeV data. 159

A.7 Muon track reconstruction efficiencies as a function of p_T (GeV/c) and η for muons embedded into 7 TeV data. 160

A.8 Muon track reconstruction efficiencies as a function of p_T (GeV/c) and η for muons embedded into 7 TeV data. 160

LIST OF FIGURES

Figure Page

1.1 Polarization variable α vs p_{T} at $\sqrt{s} = 2.0$ TeV for inclusive $\Upsilon(1\mathrm{S})$ (shaded band). The curves are the central values for direct $\Upsilon(1\mathrm{S})$, $\Upsilon(1\mathrm{S})$ from $\Upsilon(1\mathrm{S}) + \pi\pi$, and $\Upsilon(1\mathrm{S})$ from $\chi_b(1\mathrm{P}) + \gamma$ or $\chi_b(2\mathrm{P}) + \gamma$. From Ref. [4]. 8

1.2 Bottomonium states. 9

1.3 Inclusive $\Upsilon(1\mathrm{S})$ cross-section at the Tevatron as a function of p_{T}. The data points are the CDF measurements [5]. The solid curve is the NRQCD factorization fit, and the other curves are individual contributions to the NRQCD factorization fit. From Ref. [3]. 11

1.4 Differential cross-sections for $\Upsilon(1\mathrm{S})$ (top left), $\Upsilon(2\mathrm{S})$ (top right), and $\Upsilon(3\mathrm{S})$ (bottom) at the Tevatron as a function of p_{T}. The data points are the CDF measurements [5]. The solid curves are the CEM predictions at NLO with $\langle k_T^2 \rangle = 3.0\ GeV^2$. The dashed curves are multiplied by a K-factor of 1.4. From Ref. [3]. 12

1.5 Results for $\Upsilon(1\mathrm{S}) + X$ at LO (α_S^3), for associated production (α_S^4), for full NLO ($\alpha_S^3 + \alpha_S^4$), and for NNLO* (up to α_S^5) compared with the direct yield at $\sqrt{s}$ =1.8 TeV measured by the CDF collaboration [5]. From Ref. [6]. 13

1.6 Normalized differential cross sections for $\Upsilon(1\mathrm{S})$ production at $\sqrt{s} = 1.96$ TeV by D0 experiment [7] compared with CDF results at $\sqrt{s} = 1.8$ TeV [5]. The errors shown are statistical only. 14

1.7 The polarization parameter $\Upsilon(1\mathrm{S})$ measured by CDF (a, the band is the NRQCD prediction) and D0 (b, D0 results are shown as black points; CDF RunI results are shown as green points; the band is the NRQCD prediction; curves are two limiting cases (see text) of the k_{T}-factorization model). A comparison between CDF Run I, Run II results and D0 results is also shown (c). From Ref. [8] and Ref. [9]. 15

2.1 CERN accelerator complex [16] 18

2.2 LHC performance in 2010 [17], 2011 [18] and 2012 [19] 20

2.3 Three-dimensional view of the CMS detector [20]. 22

2.4 Transverse slice through CMS showing particles incident on the different sub-detectors [13]. 22

Figure Page

2.5 Layout of the CMS silicon tracker [13] 24

2.6 Structure of the electromagnetic calorimeter of the CMS. [13] 25

2.7 Structure of the hadronic calorimeter of the CMS. [13] 26

2.8 Layout of one quarter of the CMS muon system for initial low luminosity running [22]. 28

3.1 The dimuon invariant mass distribution in the vicinity of the Υ(nS) resonances for $|y| < 2$. The invariant mass distribution is fit to the sum of a signal component and a background component (dark line). Each Υ resonance is described by a Crystal Ball function. The combinatorial background is described by a first order polynomial (light gray line). 31

3.2 Differential cross section of the p_{T} as a function of in the rapidity range $|y| < 2$ compared to various theoretical predictions. 31

3.3 Side-band-subtracted distribution of Υ(1S) transverse momentum compared to PYTHIA MC simulation. The data are not corrected for acceptance and efficiencies. The MC is normalized to the yield in data. . 32

3.4 Side-band-subtracted distribution of Υ(1S) rapidity compared to PYTHIA MC simulation. The data are not corrected for acceptance and efficiencies. The MC is normalized to the yield in data. 32

3.5 Side-band-subtracted distribution of muon transverse momentum from Υ candidates compared to PYTHIA MC simulation. The data are not corrected for acceptance and efficiencies. The MC is normalized to the yield in data. 33

3.6 Side-band-subtracted distribution of muon pseudorapidity from Υ candidates compared to PYTHIA MC simulation. The data are not corrected for acceptance and efficiencies. The MC is normalized to the yield in data. 33

3.7 Υ(nS) differential cross sections in the rapidity interval $|y| < 2$ (top left), and in the rapidity intervals $|y| < 1$ and $1 < |y| < 2$ for the Υ(1S) (top right), Υ(2S) (bottom left) and Υ(3S) (bottom right). The uncertainties on the points represent the sum of the statistical and systematic uncertainties added in quadrature, excluding the uncertainty on the integrated luminosity (11%). 34

3.8 Cross-section ratios for Υ(nS) states as a function of p_{T} in the rapidity range $|y| < 2$. 35

3.9 Detectability of the muons from Υ(1S) 46

3.10 Detectability of the muons from Υ(1S) 47

Figure Page

3.11 The dimuon invariant mass distribution in the vicinity of the Υ(nS) resonances for $|y| < 2.4$ (left) and for $\eta^{\mu} < 1.0$ (right). The invariant mass distribution is fit to the sum of a signal component and a background component (dark line). 50

3.12 The dimuon invariant mass distribution in the specified p_{T} regions. . . 51

3.12 The dimuon invariant mass distribution in the specified p_{T} regions. . . 52

3.13 The Υ(1S) mass resolution as a function of rapidity for Data and MC. 54

3.14 (a) Unpolarized $\Upsilon(1S)$ acceptance as a function of p_{T} and y; (b) The unpolarized Upsilon acceptance integrated over rapidity as a function of p_{T}. 57

3.15 Acceptance of Υ(1S) for the four polarized scenarios. 60

3.16 Acceptance of Υ(1S) for the unpolarized and four polarized scenarios as a function of p_{T}. 60

3.17 Single muon identification efficiencies as a function of p_{T}^{μ} for eight $|\eta^{\mu}|$ regions 66

3.18 Single-leg muon trigger efficiencies as a function of p_{T}^{μ} for nine $|\eta^{\mu}|$ regions, from J/ψ Data T&P, for HLT_DoubleMu0 (red), HLT_DoubleMu0_Quarkonium_v1 (blue) and Monte Carlo (black). 70

3.19 L3/L2 single muon trigger efficiencies as a function of p_{T}^{μ} for six $|\eta^{\mu}|$ regions requiring tag muons pass MuXTrackY trigger(closed cirlcles) or the Mu5L2Mu0 trigger (triangles). 72

3.20 Difference between the L3/L2 single muon trigger efficiencies requiring tag muons pass MuXTrackY trigger and the Mu5L2Mu0 trigger. 73

3.21 ρ factor as a function of p_{T} and rapidity for Υ 74

3.22 Fit of the Upsilon yield in the full p_{T} range. 75

3.23 Acceptance of Υ(1S) for the unpolarized and four polarized scenarios as a function of p_{T} by varying the three anisotropy parameters in Eqn. 3.4 coherently by $\pm 1\sigma$ in the center-of-mass helicity(HX) and Collins-Soper(CS) frames. 77

3.24 Effects of FSR on acceptance for $\Upsilon(1S)$. 79

3.25 Change in acceptance as a result of track p_T bias. 80

3.26 Change in acceptance as a result of change in p_T resolution. 81

3.27 Change in acceptance as a result of change in p_T spectrum. 81

Figure Page

3.28 Single muon identification efficiencies as a function of p_{T}^{μ} for eight $|\eta^{\mu}|$ regions and the fitting results with fitted values. 83

3.29 Single-leg muon trigger efficiencies as a function of p_{T}^{μ} for nine $|\eta^{\mu}|$ regions, from J/ψ Data T&P, for HLT_DoubleMu0 , and the fitting results with fitted values. 92

3.30 Single-leg muon trigger efficiencies as a function ofp_{T}^{μ} for nine $|\eta^{\mu}|$ regions, from J/ψ Data T&P, for HLT_DoubleMu0_Quarkonium_v1 , and the fitting results with fitted values. 93

4.1 Differential fiducial cross section of the Υ(nS) as a function of p_{T} in the rapidity range $|y| < 2.4$. 95

4.2 Ratio of differential fiducial cross section of the Υ(nS) as a function of p_{T} in the rapidity range $|y| < 2.4$. 95

4.3 Ratio of differential fiducial cross section of the Υ(nS) as a function of rapidity in the p_{T} range $p_T < 50GeV/c$. 96

4.4 Differential fiducial cross section of the Υ(nS) as a function of rapidity. 96

4.5 Differential fiducial cross section results of the Υ(nS) as a function of p_{T} in two rapidity regions. 97

4.6 Differential fiducial cross section of the (a) Υ(1S), (b) Υ(2S) and (c) Υ(3S) as a function of $p_{\mathrm{T}}^{\Upsilon}$ in the rapidity range $|y^{\Upsilon}| < 2.4$, and comparison to CASCADE and PYTHIA. (d) Differential fiducial cross section of the Υ(nS) as a function of rapidity and comparison to CASCADE and PYTHIA. The width of a band indicates an estimate of the uncertainty in the prediction by the author of the prediction. 98

4.7 Differential cross section of the Υ(nS) as a function of p_{T} in the rapidity range $|y| < 2.4$. 120

4.8 Ratio of differential cross section of the Υ(nS) as a function of rapidity in the p_{T} range $p_T < 50\,\mathrm{GeV}/c$. 121

4.9 Differential production cross section of the Υ(nS) as a function of rapidity. 121

4.10 Differential production cross section results of the Υ(nS) as a function of p_{T} in six rapidity regions. 122

4.11 Ratios of differential cross sections for Υ(nS) as a function of $p_{\mathrm{T}}^{\Upsilon}$ in the rapidity range $|y|^{\Upsilon} < 2.4$ and comparison to CASCADE and PYTHIA. The width of a band indicates an estimate of the uncertainty in the prediction by the author of the prediction. 123

Figure Page

4.12 Differential cross section of the (a) $\Upsilon(1S)$, (b) $\Upsilon(2S)$ and (c) $\Upsilon(3S)$ as a function of p_T^{Υ} in the rapidity range $|y|^{\Upsilon} < 2$, and comparison to various theoretical predictions. (d) Differential cross section of the $\Upsilon(nS)$ as a function of rapidity and comparison to CASCADE and PYTHIA. The width of a band indicates an estimate of the uncertainty in the prediction by the author of the prediction. 124

4.13 Differential cross section of the $\Upsilon(1S)$ as a function of rapidity and comparison to LHCb results. 125

4.14 Differential cross section of the $\Upsilon(1S)$ as a function of p_{T} in the rapidity range $|y| < 2.0$, and comparison to the previous results using 3 pb^{-1} of data. 125

4.15 Differential cross sections of the $\Upsilon(nS)$ as a function of $p_{\mathrm{T}}^{\Upsilon}$ for $10 < p_{\mathrm{T}}^{\Upsilon} < 50\,\mathrm{GeV}/c$, $|y^{\Upsilon}| < 1.2$. The total uncertainties include the systematic uncertainty from the polarization measurement in Ref. [49]. 147

4.16 Differential production cross section results of the $\Upsilon(nS)$ as a function of p_{T} in two rapidity regions for $10 < p_{\mathrm{T}}^{\Upsilon} < 50\,\mathrm{GeV}/c$. The total uncertainties include the systematic uncertainty from the polarization measurement in Ref. [49]. 148

B.1 The distribution of the longitudinal separation between the two muons along the beam axis 162

B.2 The mass fits before and after adding the Ddz cuts 162

B.3 1D acceptance used in closure test comparing with the default acceptance 163

B.4 The pull distribution for checking acceptance 164

B.5 The pull distribution for checking track quality efficiency 164

B.6 The pull distribution for checking MC truth dimuon(Υ) identification efficiency 165

B.7 The pull distribution for checking MC truth single muon identification efficiency product 165

B.8 The pull distribution for checking MC truth single muon identification efficiency product corrected with ρ' factor 166

B.9 The pull distribution for checking MC truth Υ trigger efficiency 166

B.10 The pull distribution for checking MC truth single muon trigger efficiency measured with Υ sample 167

Figure Page

B.11 The pull distribution for checking MC truth single muon trigger efficiency measured with Υ sample and corrected with ρ' 167

B.12 The pull distribution for checking MC truth single muon ID efficiencies measured with J/ψ sample and trigger efficiencies measured with Υ sample, corrected with ρ' factor 168

B.13 The pull distribution for checking MC truth single muon efficiencies product measured with J/ψ sample and corrected with ρ' factor 168

B.14 The pull distribution for checking MC tag and probe muon efficiencies product measured with J/ψ sample and corrected with ρ' factor 168

B.15 The pull distribution for checking MC tag and probe muon efficiencies product measured with J/ψ sample and corrected with the combined ρ factor 169

B.16 The pull distribution for checking the tag and probe efficiencies corrected with ρ factor and the measured yield is extracted via an unbinned maximum likelihood fit. 169

C.1 The nominal fit to the dimuon invariant mass using total statistics and is layed together with the likesign background(red line). 170

ABSTRACT

Zheng, Yu. Ph.D., Purdue University, December 2012. Measurement of the Upsilon(nS) Cross Sections in pp Collisions at sqrt(s) = 7 TeV . Major Professor: Ian P. Shipsey.

The Υ(nS) production cross sections are measured using a data sample corresponding to an integrated luminosity of 35.8 ± 1.4 pb^{-1} of proton-proton collisions at $\sqrt{s} = 7$ TeV, collected with the CMS detector at the CERN LHC. Integrated over the transverse momentum range $p_{\mathrm{T}} < 50$ GeV/c and rapidity range $|y| < 2.4$, and assuming unpolarized Υ(nS) production, the products of the Υ(nS) production cross sections and branching fractions are

$$\sigma(pp \to \Upsilon(1\mathrm{S})X) \cdot \mathcal{B}(\Upsilon(1\mathrm{S}) \to \mu^+\mu^-) = (8.55 \pm 0.05^{+0.74}_{-0.71} \pm 0.34)\ \mathrm{nb}\,,$$

$$\sigma(pp \to \Upsilon(2\mathrm{S})X) \cdot \mathcal{B}(\Upsilon(2\mathrm{S}) \to \mu^+\mu^-) = (2.21 \pm 0.03^{+0.21}_{-0.20} \pm 0.09)\ \mathrm{nb}\,,$$

$$\sigma(pp \to \Upsilon(3\mathrm{S})X) \cdot \mathcal{B}(\Upsilon(3\mathrm{S}) \to \mu^+\mu^-) = (1.11 \pm 0.02^{+0.12}_{-0.11} \pm 0.04)\ \mathrm{nb}\,,$$

where the first uncertainty is statistical, the second is systematic, and the third is associated with the estimation of the integrated luminosity of the data sample. The Υ(1S), Υ(2S), and Υ(3S) differential cross sections in transverse momentum and rapidity and the cross section ratios Υ(nS)/Υ(mS) are presented. Cross section measurements performed within a restricted muon kinematic range and not corrected for the acceptance are also provided. These measurements are independent of Υ(nS) polarization assumptions.

1. HEAVY FLAVOR PHYSICS

1.1 The Standard Model of Particle Physics

The Standard Model (SM) of particle physics is a theory of particle properties and particle interactions [1]. It describes the strong, weak, and electromagnetic forces between the fundamental particles of matter. Special relativity and quantum mechanics form the basis for quantum field theory and the SM.

The SM includes 12 elementary particles of spin $\frac{1}{2}$ known as fermions. The fermions of the SM are classified according to how they interact (or equivalently, by what charges they carry). There are six quarks (up, down, charm, strange, top, bottom), and six leptons (electron, electron neutrino, muon, muon neutrino, tau, tau neutrino). Quarks are characterized by a fractional electric charge (+2/3,-1/3) and for each quark there exists a charge-conjugated anti-quark. Quarks bind to each other via the strong interaction, forming color-neutral composite particles (hadrons) containing either a quark and an antiquark (mesons) or three quarks (baryons). There are three different flavors of leptons, or electron-like particles: the electron, muon, and tau, each with a flavor-specific neutrino (electron neutrino, muon neutrino, and tau neutrino). Neutrinos have no electrical charge while electrons, muons, and tau particles have one unit of electrical charge. All leptons have corresponding anti-particles.

The SM includes gauge bosons which are defined as force carriers that mediate the strong, weak, and electromagnetic fundamental interactions. Photons mediate the electromagnetic force between electrically charged particles. The W^+, W^-, and Z gauge bosons mediate the weak interactions between particles of different flavors (all quarks and leptons). The eight gluons mediate the strong interactions between color charged particles (the quarks). The Higgs boson plays a unique role in the SM, by explaining why the other elementary particles, except the photon and gluon,

are massive. In particular, the Higgs boson would explain why the photon has no mass, while the W and Z bosons are very heavy. Elementary particle masses, and the differences between electromagnetism (mediated by the photon) and the weak force (mediated by the W and Z bosons), are critical to many aspects of the structure of microscopic (and hence macroscopic) matter. In electroweak theory, the Higgs boson generates the masses of the leptons (electron, muon, and tau) and quarks. As the Higgs boson is massive, it must interact with itself.

1.2 Quantum Chromodynamics

Quantum chromodynamics (QCD) is a theory of the strong interaction (color force), a fundamental force describing the interactions between quarks and gluons, and is the SU(3) component of the SU(3)×SU(2)×SU(1) Standard Model of Particle Physics. Color charge has analogies with the notion of electric charge of particles. A quark's color can take one of three values, called red, green, and blue. An antiquark can take one of three anticolors. Gluons are mixtures of two colors, such as red and antigreen, which constitutes their color charge. The color charge is conserved like electric charge is conserved. Strong interaction bind quarks into hadrons, such as proton or pion. Also, force between nucleons is strong force, and strong interaction is responsible for binding protons and neutrons into a nucleus. Since the gluons carry color charge, they can interact with other gluons.

Unlike the components in weakly bound systems, which may be separated if sufficient energy is added, quarks and gluons are not seen in high-energy collisions due to color confinement. The color confinement is the physics phenomenon that color charged particles (such as quarks) cannot be isolated singularly, and therefore cannot be directly observed. When quarks become separated, as happens in particle accelerator collisions, new $q\bar{q}$ pairs are spontaneously generated and recombine to form more hadrons. This process is called hadronization, which is one of the least understood processes in particle physics.

In QCD, the coupling constant α_s describing the interaction between quarks is analogous to the electromagnetic coupling constant α. Due to the self-coupling of the gluons, the value of α_s has a strong dependence on the energy-scale k^2 of the interaction. This dependence is known as "running coupling constant". In perturbative QCD (pQCD), The coupling decreases logarithmically approximately as,

$$\alpha_s(k^2) = \frac{1}{\beta_0 \ln(\frac{k^2}{\Lambda^2})}, \tag{1.1}$$

where β_0 is a constant computed by Wilczek, Gross and Politzer, and Λ represents the characteristic scale of confinement. When $k^2 \to \infty$, the strong coupling vanishes so that quarks can be considered as "free" particles, a phenomenon known as asymptotic freedom. At low energies, the coupling is so strong that perturbation theory breaks down so that it is not possible to detach individual quarks from hadrons, which explains the confinement.

1.3 Quarkonium Production

Quarkonium designates a flavorless meson made of a quark and its own antiquark. Examples of quarkonia are the J/Ψ meson (an example of charmonium, $c\bar{c}$) and the Υ meson (bottomonium, $b\bar{b}$). Heavy quarkonium production in hadronic collisions provides a standard candle for the understanding of QCD. The calculations of hadronic cross sections can be factorized into perturbative and non-perturbative parts. The production of the heavy quark pair occurs at short distances and can be calculated perturbatively due to the large scale of the quark masses, whereas the nonperturbative QCD effects that bind the heavy quark-antiquark pair into quarkonium can only be factorized into a wave function. Three types of models have been used to describe quarkonium formation: the color-singlet model (CSM)[7], the color-evaporation model (CEM)[8], and the color-octet model (COM)[10]. In the CSM, the quarkonium meson retains the quantum numbers of the produced $c\bar{c}$ ($b\bar{b}$) pair, and thus each J^{PC} state can only be directly produced via the corresponding hard scattering color-singlet sub-

processes. In the CEM, the directly produced quarkonium meson is not constrained to the same J^{PC} state as the $c\bar{c}$ ($b\bar{b}$) pair produced in the hard scatter because of the emission of soft gluons during the meson's formation. The color-octet mechanism extends the color-singlet approach by taking into account the production of $c\bar{c}$ ($b\bar{b}$) pairs in a color-octet configuration. The color-octet state evolves into a color-singlet state via emission of soft gluons.

1.3.1 Quarkonium Production Models

The first quarkonium production description in hadron-hadron and electron-proton collisions was based on calculations in the CSM. In this model, the production of a quarkonium state is assumed to proceed through parton processes that produce a $q\bar{q}$ pair in a color-singlet state with the appropriate quantum numbers. The cross section for producing a quarkonium state in any high energy process can be predicted in terms of a single non-perturbative parameter for each orbital-angular-momentum multiplet. Despite its great predictive power, the model is incomplete. The predictions of the CSM at the lowest order in α_s disagree dramatically with the Tevatron data. This discrepancy leads to two theoretical developments in heavy quarkonium physics. The first was the realization that heavy quarkonium at large transverse momentum is produced primarily by fragmentation, the hadronization of individual high p_{T} partons. The second development was the idea that the color-octet mechanism in which the $q\bar{q}$ pair is produced at short distances in a color-octet state sometimes dominates the production. This is often referred to as COM. Contrary to the basic assumption of the CSM, a $q\bar{q}$ that is produced in a color-octet state can also bind to form quarkonium. These mechanisms can be analyzed systematically using the factorization formalism based on an effective field theory called Non-Relativistic QCD (NRQCD).

CEM [2] is an alternative model for quarkonium production, which was developed at the same time as the CSM. It assumes the color exchange in the soft interactions

randomize the color charges such that no information remains of the color configuration given by the proceeding hard interactions. Probabilities for color charge states can be obtained from color SU(3) algebra, with the relation $3 \bigotimes 3 = 1 \bigoplus 8$ being applicable to a $q\bar{q}$ pair composed of a triplet and an anti-triplet. With all color charge states having equal weight, this implies that the $q\bar{q}$ pair has a probability 1/9 to be in a color singlet state and 8/9 to be in a color octet state. All color singlet $q\bar{q}$ pairs with invariant mass below the threshold for open charm or bottom will form a quarkonium state. Color singlet states above this threshold, as well as the $q\bar{q}$ pairs in a color-octet state will produce open charm or bottom through the hadronization mechanism. The cross section for bottomonium can then be written as:

$$\sigma_{b\bar{b}} = \frac{1}{9} \int_{2m_b}^{2m_B} dm_{b\bar{b}} \frac{d\sigma_{b\bar{b}}}{dm_{b\bar{b}}}, \tag{1.2}$$

where $m_{b\bar{b}}$ is the invariant mass of the $b\bar{b}$, m_b is the bottom quark mass and $2m_B$ is the $B\bar{B}$ threshold. The differential parton level cross $\frac{d\sigma_{b\bar{b}}}{dm_{b\bar{b}}}$ is the usual convolution of the perturbative QCD cross section with the parton density functions for the initial hadrons.

The total quarkonium cross section is then split in the different quarkonim states:

$$\sigma_i = \rho_i \sigma_{b\bar{b}}, \tag{1.3}$$

where relative rates ρ_i are assumed to be independent of process and energy. These non-perturbative parameters must be determined from comparison with data.

The CEM is one of the simplest approaches to color neutralization, where the effect of soft interactions is implicit in the non-perturbative factors.

1.3.2 Non-Relativistic QCD Factorization Method

Non-Relativistic QCD (NRQCD) [3] is an effective field theory for two heavy quarks that follows from QCD by integrating out the hard scale m. In this model,

bottomonium production is described as a two-step process: $b\bar{b}$ pair production at the perturbative level, followed by the evolution to a colorless quarkonium state through soft-gluon emission in the non-perturbative region.

The Non-Relativistic QCD factorization method is a general factorization formalism. This formalism can be used to factor quarkonium production cross sections into the short-distance parts that can be calculated using perturbative QCD and the long distance effects that are factored into parameters called NRQCD matrix elements. These non-perturbative parameters are universal, so values extracted from one high energy physics experiment can be used to predict the production rate in others.

The inclusive cross-section for the direct production of the quarkonium H at large transverse momentum (p_{T} of order m or larger) in hadron colliders can be written as a sum of products of NRQCD matrix elements and short-distance coefficients:

$$\sigma[H] = \sum_n \sigma_n(\Lambda)\langle O_n^H(\Lambda)\rangle, \tag{1.4}$$

where Λ is the ultraviolet cutoff of the effective theory, the σ_n are short-distance coefficients, and the $\langle O_n^H\rangle$ are vacuum-expectation values of four-fermion operators in NRQCD.

The inclusive $\Upsilon(\mathrm{nS})$ production, including direct production and feed down from higher states can be written as:

$$\begin{aligned}
\sigma[\Upsilon(\mathrm{nS})\,] = {} & \sigma[b\bar{b}_1(^3S_1)]\langle O_1^{\Upsilon}(\mathrm{nS})\,(^3S_1)\rangle_{inc} \\
& +\sigma[b\bar{b}_8(^3S_1)]\langle O_8^{\Upsilon}(\mathrm{nS})\,(^3S_1)\rangle_{inc} \\
& +\sigma[b\bar{b}_8(^3S_0)]\langle O_8^{\Upsilon}(\mathrm{nS})\,(^3S_0)\rangle_{inc} \\
& +\sigma[b\bar{b}_1(^3P_J)]\langle O_1^{\Upsilon}(\mathrm{nS})\,(^3P_J)\rangle_{inc} \\
& +\sum_J (2J+1)\sigma[b\bar{b}_8(^3P_J)]\langle O_8^{\Upsilon}(\mathrm{nS})\,(^3P_0)\rangle_{inc},
\end{aligned} \tag{1.5}$$

where the inclusive NRQCD matrix elements are:

$$\langle O^{\Upsilon(\mathrm{nS})}[n]\rangle_{inc} = \sum_H B_{H\to\Upsilon(\mathrm{nS})}\langle O^H[n]\rangle, \tag{1.6}$$

$\langle O_1^{\Upsilon}(\mathrm{nS})\,(^3S_1)\rangle_{inc}$ is the color-singlet matrix element, $\langle O_8^{\Upsilon}(\mathrm{nS})\,(^3S_1)\rangle_{inc}$, $\langle O_8^{\Upsilon}(\mathrm{nS})\,(^3S_0)\rangle_{inc}$, and $\langle O_8^{\Upsilon}(\mathrm{nS})\,(^3P_0)\rangle_{incx}$ are the three color-octet matrix elements.

The NRQCD matrix elements can be used to predict the cross sections and polarizations of the bottomonium states. At high p_{T}, the matrix element $\langle O_8^{\Upsilon}(\mathrm{nS})\,(^3S_1)\rangle_{inc}$ represents the gluon fragmentation contributions. The NRQCD predicts [4] the $\Upsilon(1\mathrm{S})$ is transversely polarized at high p_{T} as shown in Fig. 1.1. The parameter $\alpha = 1(-1)$ corresponds to 100% transverse (longitudinal) $\Upsilon(\mathrm{nS})$ polarization. The model also predicts a much larger polarization for the more massive bottomonium states $\Upsilon(2\mathrm{S})$ and $\Upsilon(3\mathrm{S})$, which are produced more directly than $\Upsilon(1\mathrm{S})$.

1.3.3 Bottomonium Production

Bottomonium is a general term that applies to any meson that has one bottom quark and one anti-bottom quark. States with different quantum numbers have different names. For example, a bottomonium with quantum numbers $J^{PC} = 1^{--}$ is called an Υ, where J is the total angular momentum, P is the parity quantum number, and C is the charge conjugation quantum number. A χ_{bJ} is a bottomonium with quantum number $J^{PC} = 0,\ 1,\ 2^{++}$. J can be 0, 1,or 2, which corresponds to three states for each of the $\chi_{bJ}(\mathrm{mP})$.

The Υ states can be produced in two ways in high-energy hadron collisions, summarized in Table 1.1. One is called direct production, in which a $b\bar{b}$ pair is produced in the particle collision, and the two quarks combine, producing a colorless $\Upsilon(\mathrm{nS})$ meson. The other is called indirect production, in which the $\Upsilon(\mathrm{nS})$ mesons are produced indirectly as a result of a decay of a higher mass state, e.g. the production of the $\Upsilon(1\mathrm{S})$ in the decay of χ_b or $\Upsilon(2\mathrm{S})$. The possible decay sequences are shown in Fig. 1.2. The lifetime of Υ is short comparing to the detector resolution. Therefore, in all cases

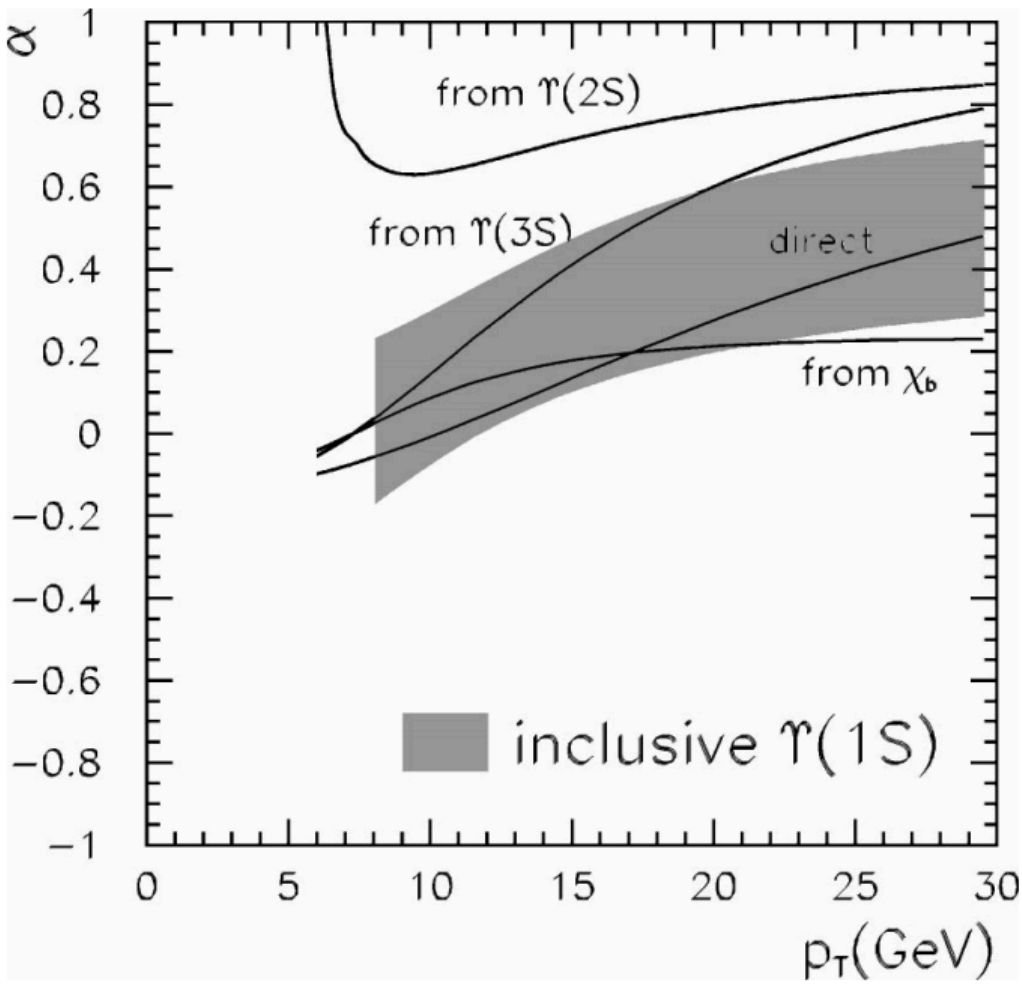

Figure 1.1.: Polarization variable α vs p_{T} at $\sqrt{s} = 2.0$ TeV for inclusive $\Upsilon(1\mathrm{S})$ (shaded band). The curves are the central values for direct $\Upsilon(1\mathrm{S})$, $\Upsilon(1\mathrm{S})$ from $\Upsilon(1\mathrm{S}) + \pi\pi$, and $\Upsilon(1\mathrm{S})$ from $\chi_b(1\mathrm{P}) + \gamma$ or $\chi_b(2\mathrm{P}) + \gamma$. From Ref. [4].

bottomonium production occurs at the interaction point so is prompt. It is due to the short lifetime of the particles

1.4 Bottomonium Measurements at Tevatron

Bottomonium were produced copiously in the Tevatron, a $p\bar{p}$ collider operating at Fermilab with centre-of-mass energy of 1.8 TeV in Run I and 1.96 TeV in Run II.

Table 1.1: Stages in the hadroproduction of Υ(nS) resonances.

1st step	2nd step	3rd step	production type
	$bb \to \Upsilon(\mathrm{nS})$	–	prompt, direct
$p\bar{p} \to b\bar{b} + X$	$b\bar{b} \to \chi_b$	$\chi_b \to \Upsilon(\mathrm{nS}) + \gamma$	prompt, indirect
	$b\bar{b} \to \Upsilon(\mathrm{n'S})$	$\Upsilon(\mathrm{n'S}) \to \Upsilon(\mathrm{nS}) + X$	prompt, indirect

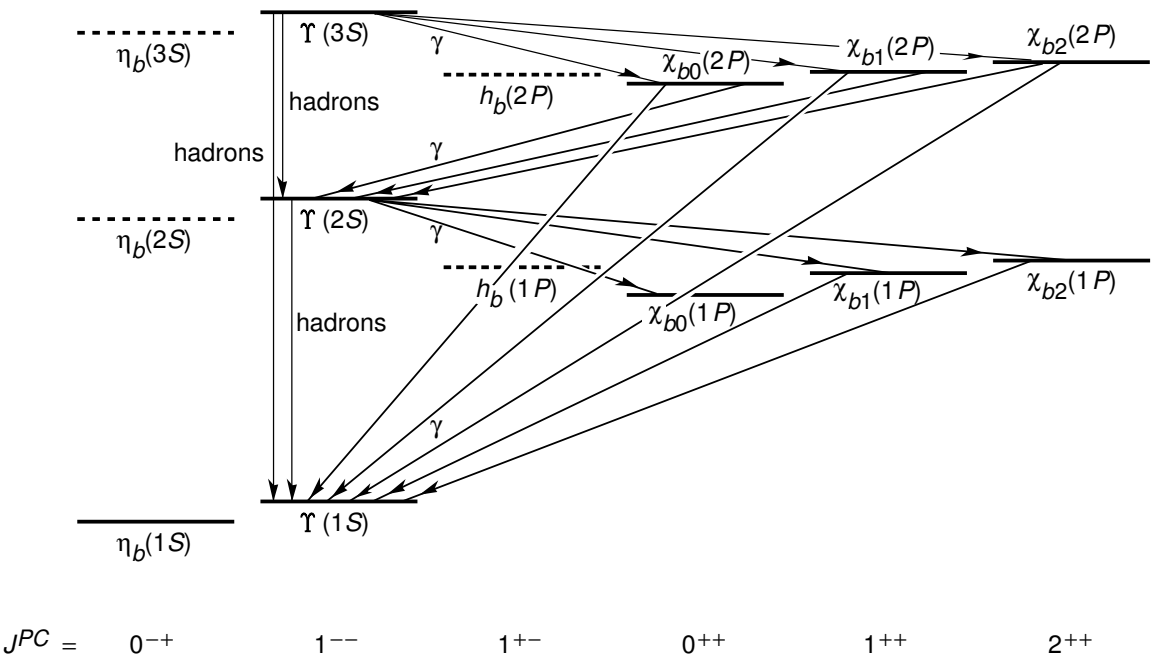

Figure 1.2.: Bottomonium states.

1.4.1 Bottomonium Cross Sections

Using Run I data, the CDF Collaboration has reported inclusive production cross-sections for the Υ(nS) states in the region $0 < p_{\mathrm{T}} < 20\,\mathrm{GeV}/c$ [5]. In Fig. 1.3, a comparison between $\Upsilon(1\mathrm{S})$ p_{T}-differential cross section and CSM and COM predictions is shown for $|\eta^{\Upsilon(1\mathrm{S})}| < 0.4$. The rates of inclusive production of the Υ(nS) states for $p_{\mathrm{T}} > 4\,\mathrm{GeV}/c$ were found to be higher than the rates predicted by CSM calculations by a factor of about five. The COM predictions within the NRQCD framework can well describe the observed cross-sections for $p_{\mathrm{T}} > 8\,\mathrm{GeV}/c$ but not the low p_{T} region,

where requires NLO corrections and a resumption of multiple gluon radiation. The CEM predictions are compared with the CDF data for Υ(nS) in Fig. 1.4. Both of he normalization and the shape of the bottomonium cross-sections at the Tevatron are described reasonably well by CEM. The predicted cross-sections for Υ(1S) and Υ(3S) production are a little below the data; the normalizations can be improved by multiplying the cross-sections by a K-factor of 1.4. The comparison of the color-singlet predictions for direct production of Υ(1S) at $\sqrt{s}$ =1.8 TeV with the CDF results are shown in Fig. 1.5. In order to compare the calculation for direct Υ(1S) production with the CDF data, the prompt Υ(1S) cross section measurement of [5] has been multiplied by the direct fraction 0.5 ± 0.12 [6]. The LO and NLO results are very similar at low p_{T}. The relative importance of the NLO corrections dramatically increases at larger p_{T}, which significantly reduces the discrepancy with the experimental data that is found at LO. However, the NLO prediction still drops too fast in comparison with the data. The NNLO* corresponds to the sum of the NLO yield and the $\Upsilon + jjj$ contributions. The contribution of production with three light partons fills the gap between the data and the NLO calculation.

For Run II at $\sqrt{s}$ =1.8 TeV, so far only D0 have analyzed data for the Υ(1S) cross section measurement. The normalized differential cross sections for Υ(1S) production measured by the D0 experiment at $\sqrt{s}$ = 1.96 TeV [7] and the CDF experiment at $\sqrt{s}$ = 1.8 TeV are shown in Fig. 1.6, and are in agreement with each other.

1.4.2 Bottomonium Polarizations

Although the cross-section measurements performed by CDF and D0 experiments are in good agreement, the polarization measurements differ substantially. Fig. 1.7 shows the comparison between the theoretical prediction of Υ(1S) (colored band) and the most recent CDF [8] and D0 [9] experimental results. In the low p_{T} region, CDF shows nearly unpolarized results, which is consistent with the CDF Run I result as shown in Fig. 1.7(c); D0 shows partially longitudinally polarized results. At higher p_{T},

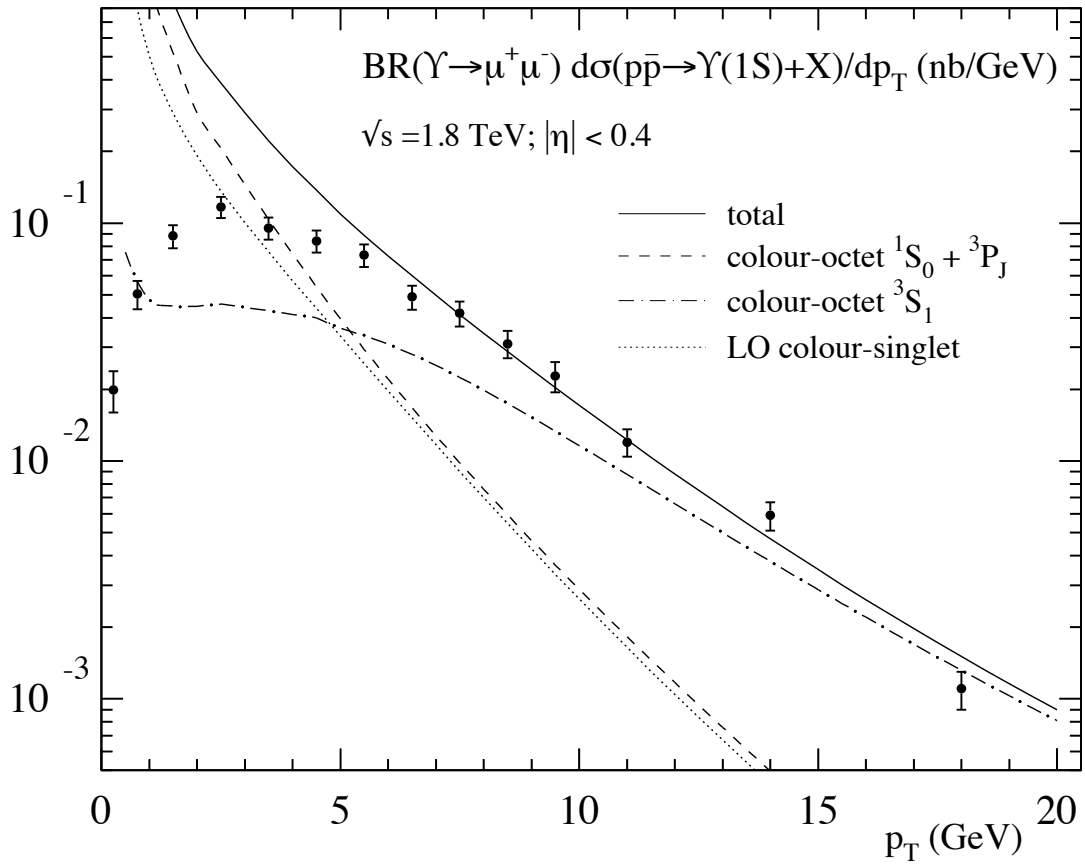

Figure 1.3.: Inclusive $\Upsilon(1S)$ cross-section at the Tevatron as a function of p_{T}. The data points are the CDF measurements [5]. The solid curve is the NRQCD factorization fit, and the other curves are individual contributions to the NRQCD factorization fit. From Ref. [3].

the CDF results tend toward longitudinal polarization while the D0 result indicates transverse polarization. Both CDF and D0 results at high p_{T} deviate from theoretical predictions.

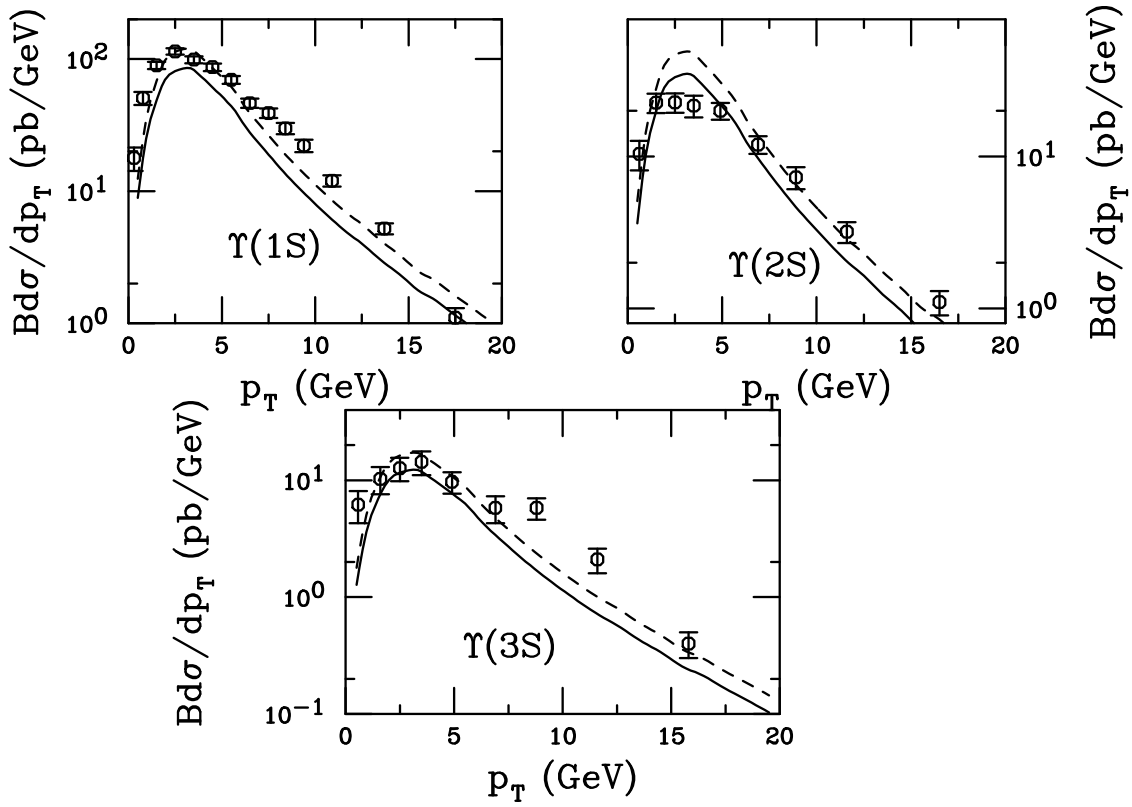

Figure 1.4.: Differential cross-sections for $\Upsilon(1S)$ (top left), $\Upsilon(2S)$ (top right), and $\Upsilon(3S)$ (bottom) at the Tevatron as a function of p_{T}. The data points are the CDF measurements [5]. The solid curves are the CEM predictions at NLO with $\langle k_T^2 \rangle = 3.0$ GeV^2. The dashed curves are multiplied by a K-factor of 1.4. From Ref. [3].

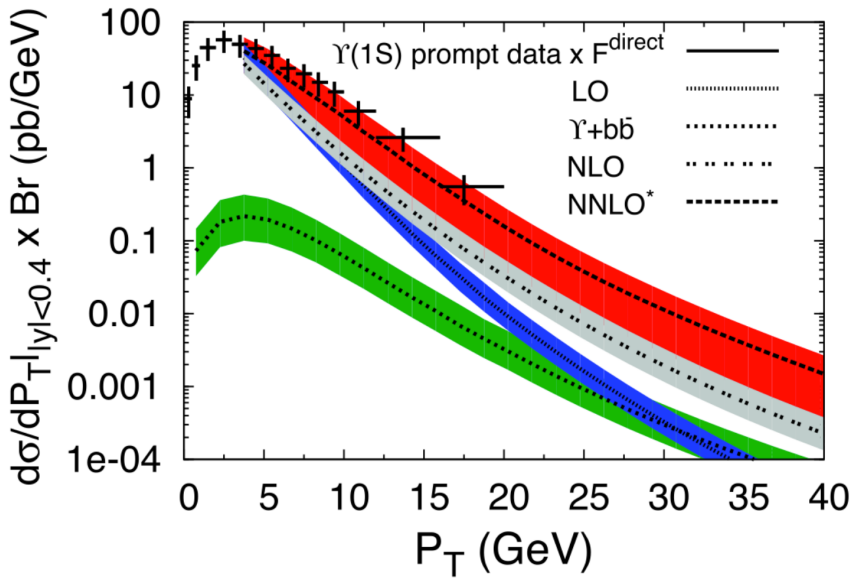

Figure 1.5.: Results for $\Upsilon(1S) + X$ at LO (α_S^3), for associated production (α_S^4), for full NLO ($\alpha_S^3 + \alpha_S^4$), and for NNLO* (up to α_S^5) compared with the direct yield at $\sqrt{s}$ =1.8 TeV measured by the CDF collaboration [5]. From Ref. [6].

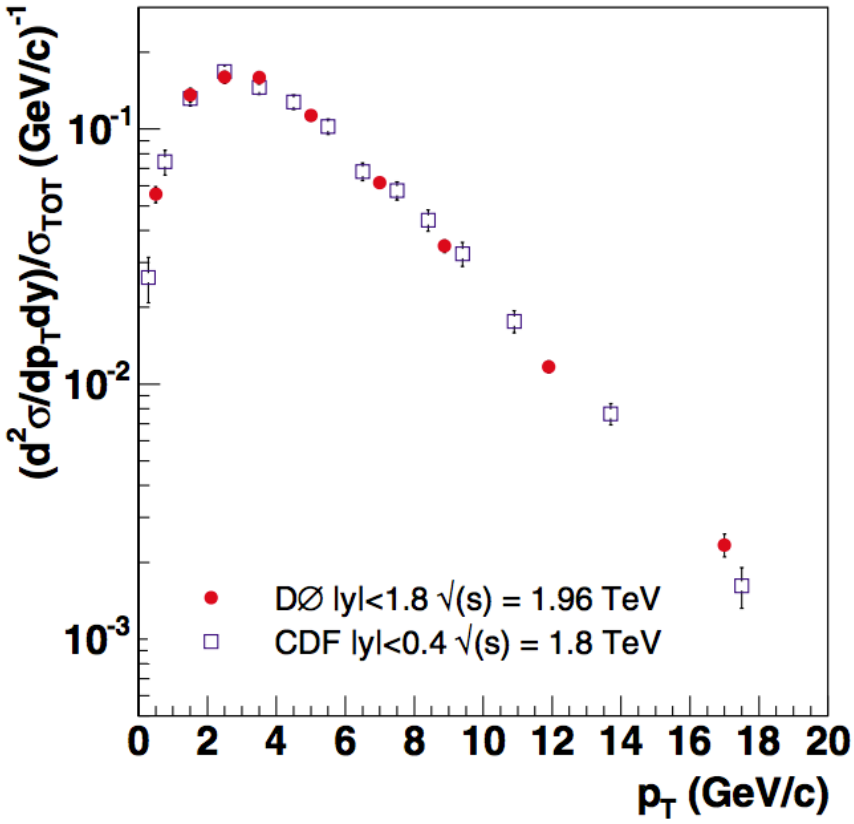

Figure 1.6.: Normalized differential cross sections for $\Upsilon(1S)$ production at $\sqrt{s} = 1.96$ TeV by D0 experiment [7] compared with CDF results at $\sqrt{s} = 1.8$ TeV [5]. The errors shown are statistical only.

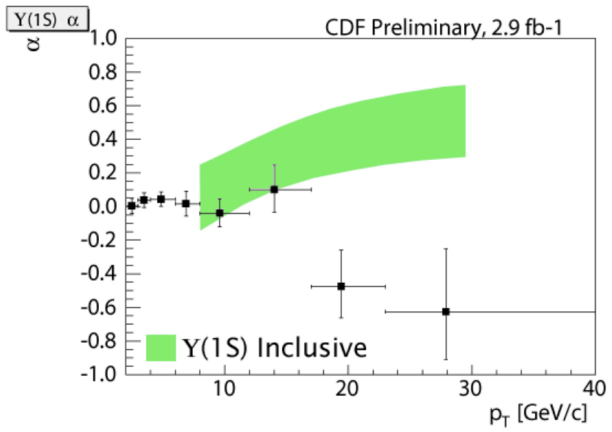

(a)

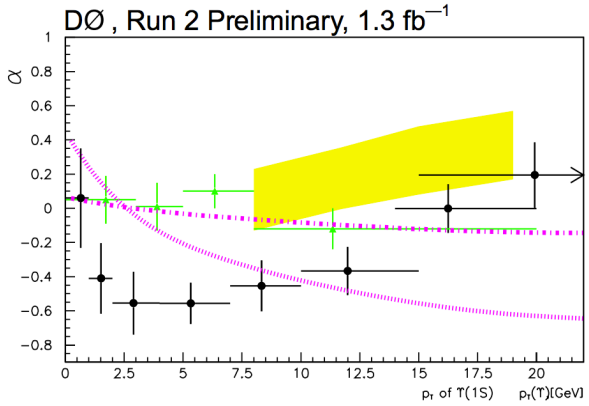

(b)

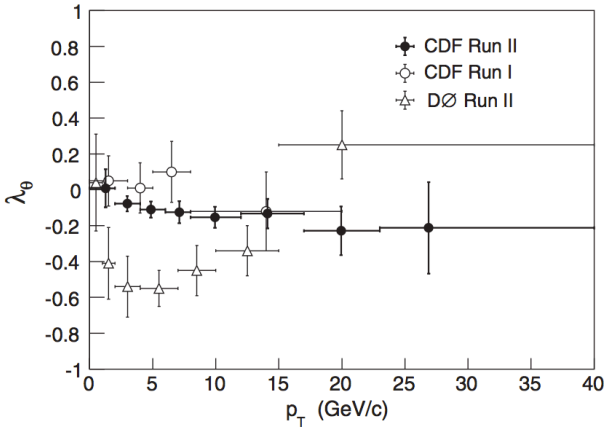

(c)

Figure 1.7.: The polarization parameter $\Upsilon(1S)$ measured by CDF (a, the band is the NRQCD prediction) and D0 (b, D0 results are shown as black points; CDF RunI results are shown as green points; the band is the NRQCD prediction; curves are two limiting cases (see text) of the k_T-factorization model). A comparison between CDF Run I, Run II results and D0 results is also shown (c). From Ref. [8] and Ref. [9].

2. THE COMPACT MUON SOLENOID EXPERIMENT AT THE CERN LARGE HADRON COLLIDER

The Large Hadron Collider (LHC) is a particle accelerator built by the European Organization for Nuclear Research (CERN). Its main purpose is to help answer some of the fundamental open questions in physics, for example, searching for the missing Higgs particle at higher energy scales of physics which had not yet been reached. Data is also needed from high energy particle experiments to discriminate among various theoretical models. It is expected that studying quarkonia hadroproduction at higher center-of-mass energies and over a wider rapidity and momentum range will facilitate significant improvements in our understanding of the process involved.

The LHC machine is described in more detail in Sec. 2.1 while the description of one of the general-purpose detectors of the LHC, namely the CMS experiment, is given in Sec. 2.2. All elements of the description of the LHC found here, unless otherwise noted, are taken from Ref. [10].

2.1 The Large Hadron Collider

The LHC is a proton-proton accelerator located in a tunnel 27 kilometers in circumference and about 100 meters under the French-Swiss border outside Geneva. The tunnel was originally built for the Large Electron-Positron collider [11] (LEP). For the LHC operation, they have been upgraded to provide beams of protons for collisions at unprecedented energies.

Technical limitations in the production and storage of antiprotons led to the decision to build a proton-proton collider. Accelerated electrons and positrons suffer large energy loss due to the synchrotron radiation, which is proportional to $E^4/(Rm^4)$, where E is the electron energy, m is the particle's mass and R the accelerator radius.

Therefore, only massive charged particles could have been used, e.g. protons and heavy nuclei, in order to obtain energies of the order of TeV at the fixed accelerator radius.

2.1.1 The Accelerator Chain

The LHC is constituted by 1232 super-conducting dipole magnets each 15 m long, delivering a 8.3 T magnetic field to let the beams circulate inside their trajectories along the 27 km circumference. Two vacuum pipes are utilized to let beams circulate in opposite directions. More than 8000 other magnets are utilized for the beam injection, their collimation, trajectory correction, crossing. All the magnets are kept cool by superfluid helium at 1.9 K temperature. The beams are accelerated from 450 GeV (the injection energy from the SPS) to 7 TeV with 16 Radio Frequency cavities (8 per beam) which raise the beam energy by 16 MeV each round with an electric field of 5 MV/m oscillating at 400 MHz frequency. Before the injection into the LHC, the beams are produced and accelerated by different 26 components of the CERN accelerator complex. Being produced from ionized hydrogen atoms, protons are accelerated by the linear accelerator LINAC, Booster and the Proton Synchrotron (PS) up to 26 GeV energy, the bunches being separated by 25 ns each. The beams are then injected into the Super Proton Synchrotron (SPS) where they are accelerated up to 450 GeV. They are then finally transferred to the LHC and accelerated up to 7 TeV energy per beam.

There are four experiments installed in the caverns along the ring: two general purpose particle detectors ATLAS (A Toroidal LHC ApparatuS) [12] and CMS (Compact Muon Solenoid) [13], the LHCb (Large Hadron Collider beauty) [14], dedicated to B physics, and ALICE (A Large Ion Collider Experiment) [15], devoted to study heavy ion collisions. An schematic view of the accelerator complex with the injection chain is shown in Fig. 2.1.

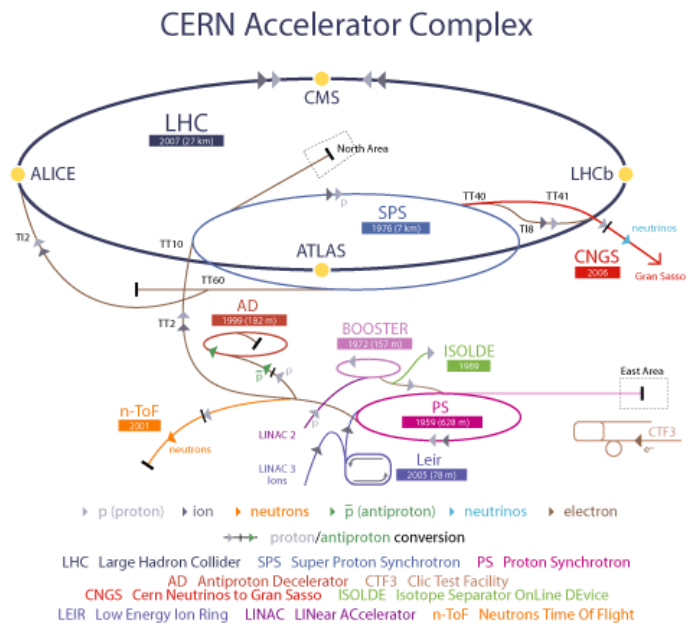

Figure 2.1.: CERN accelerator complex [16]

2.1.2 The Luminosity

The number of events per second generated in the LHC collisions is given by:

$$\mathcal{N}_{event} = \mathcal{L}\sigma_{event} \tag{2.1}$$

where σ_{event} is the cross section for the physics process under study and $\mathcal{L}$ is the machine luminosity, which depends only on the beam parameters. It can be written for a Gaussian transverse beam profile distribution as:

$$\mathcal{L} = \frac{N_b^2 n_b f_{rev} \gamma_r}{4\pi\epsilon_n \beta*} F \tag{2.2}$$

where N_b is the number of particles per bunch, n_b the number of bunches per beam, f_{rev} the revolution frequency, γ_r the relativistic gamma factor, ϵ_n the normalized transverse beam emittance, $\beta*$ the beta function at the collision point, and F the

geometric luminosity reduction factor due to the crossing angle at the interaction point (IP):

$$F = (1 + (\frac{\theta_c \sigma_z}{2\sigma *})^2)^{-1/2} \tag{2.3}$$

θ_c is the full crossing angle at the IP, σ_z the RMS bunch length, and $\sigma *$ the transverse RMS beam size at the IP. The luminosity of the machine is important since it represents how many physics events occur in an specific time period T. For rare processes, a higher luminosity would increase the probability of being observed in the experiment.

The LHC has two high luminosity experiments, ATLAS and CMS, both aiming at a peak luminosity of $L = 10^{34} cm^2 s^1$ for proton operation. LHCb is a low luminosity experiment, aiming at a peak luminosity of $L = 10^{32} cm^2 s^1$. The LHC has one dedicated ion experiment, ALICE, the experiment dedicated to heavy ion studies, is aiming at a peak luminosity of $L = 10^{27} cm^2 s^1$ for nominal lead-lead ion operation.

The LHC started its operations in December 2009 with center of mass energy $\sqrt{s}$ at 0.9 TeV. The center of mass energy was set to 7 TeV in 2010, and the performance during 2010 and 2011 raised dramatically. In 2010 the peak luminosity reached $L = 2 \times 10^{32} cm^{-2} s^{-1}$ ($200 \mu b{-}1 s^{-1}$, with 368 bunches) and during 2011 increased by a factor 10 in up to $L = 3.5 \times 10^{33} cm{-}2s{-}1$ ($3.5 nb^{-1} s^{-1}$, with 1380 bunches). The integrated luminosity in 2010 has been $L = 40 pb^{-1}$, while in 2011 it increased by a factor 100 up to $5 fb^{-1}$. In April 2012, the LHC has started producing collisions at the record high 8 TeV centre-of-mass energy. By April 11, the LHC had already delivered a total integrated luminosity of 0.2 fb^{-1} to the experiments. It took six weeks to achieve the same number in 2010. The LHC performance is summarized in Fig. 2.2.

2.2 The CMS Experiment

The CMS experiment is a general purpose proton-proton detector designed to run at the highest luminosity of LHC. Fig. 2.3 gives a 3D structure view of the CMS

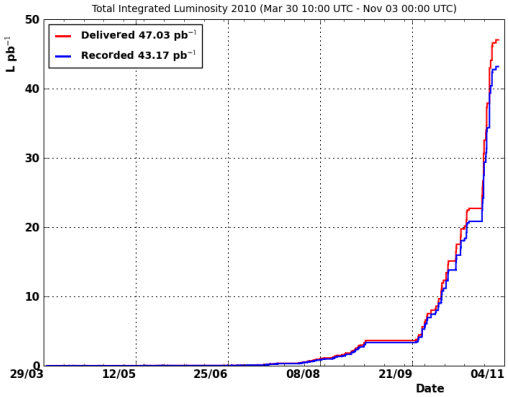

(a) 2010

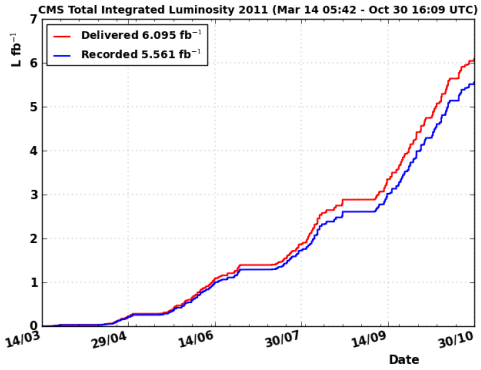

(b) 2011

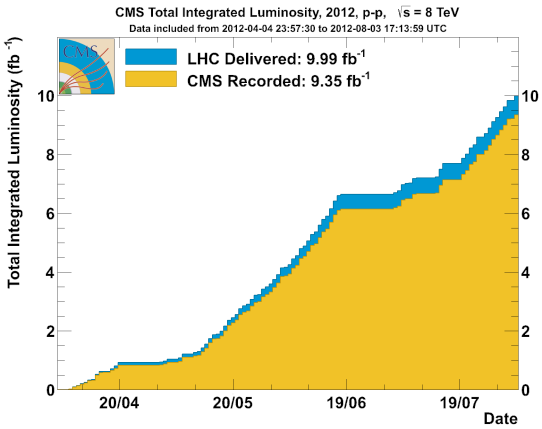

(c) 2012

Figure 2.2.: LHC performance in 2010 [17], 2011 [18] and 2012 [19]

detector. The design of the CMS detector is based on a compact superconducting solenoid coupled with a muon detector system for optimized muon detection. The CMS solenoid magnet produces a solenoidal field along the beam of 3.8 T for charged particle tracking whereas the yoke is responsible for the return of the magnetic flux with a corresponding magnetic field of 2 T. From inside out, CMS is arranged as follows. At the center is the tracking system: Pixel detector and Silicon Strip Tracker. Outside the trackers are the calorimeters: Electromagnetic (ECAL) and Hadronic (HCAL), which are inside the superconducting solenoid coil. The outermost layers make up the muon system: Cathode Strip Chambers (CSC), Resistive Plate Chambers (RPC), and Drift Tubes (DT). A slice of the transverse view of the CMS detector is shown in Fig. 2.4. The principle of detection of charged and neutral particles in the various sub-detectors is shown. All charged particles leave signals in the inner tracking system. Electrons and photons deposit their energy in the electromagnetic calorimeter. Charged Hadrons ($K^{\pm}$, $\pi^{\pm}$...) and neutrons deposit their energy in the hadronic calorimeter. Muon is a particle which passes through calorimeters without interacting much, but which leaves a track of its passage in the muon chambers. Neutrinos, barely interacting, will escape from all direct detections. While adding the transverse momenta of all the particles detected by the detector, one can determine the imbalance of energy in the transverse plane, so called the missing transverse energy.

The coordinates system in CMS are as follows: The origin of the coordinate system is situated at the nominal interaction point. The z-axis along the beam direction, the x-axis points radially inward to the centre of the LHC ring, and the y-axis directed upward, orthogonally to the z and x axes. The azimuthal angle ϕ is measured in the x-y-plane from the x-axis. The pseudo-rapidity η is defined as $\eta = -\ln(\tan(\theta/2))$ where θ s the polar angle with respect to the beam axis in the y-z-plane. The use of pseudo-rapidity instead of the polar angle is motivated by the fact that the difference in pseudo-rapidity between two particles is invariant under Lorentz boosts along the beam axis.

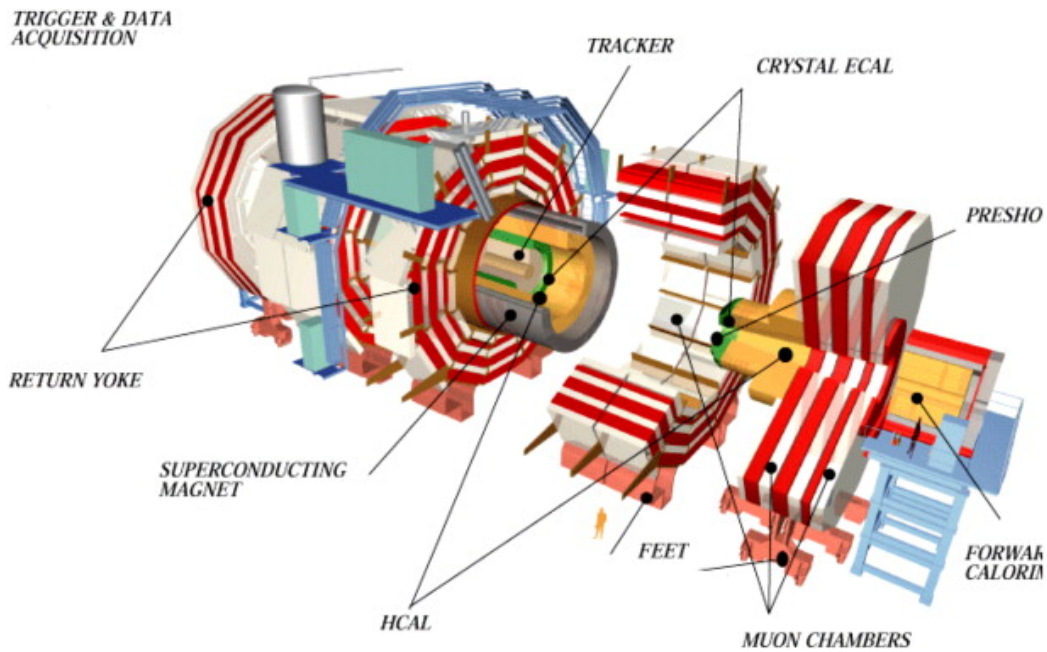

Figure 2.3.: Three-dimensional view of the CMS detector [20].

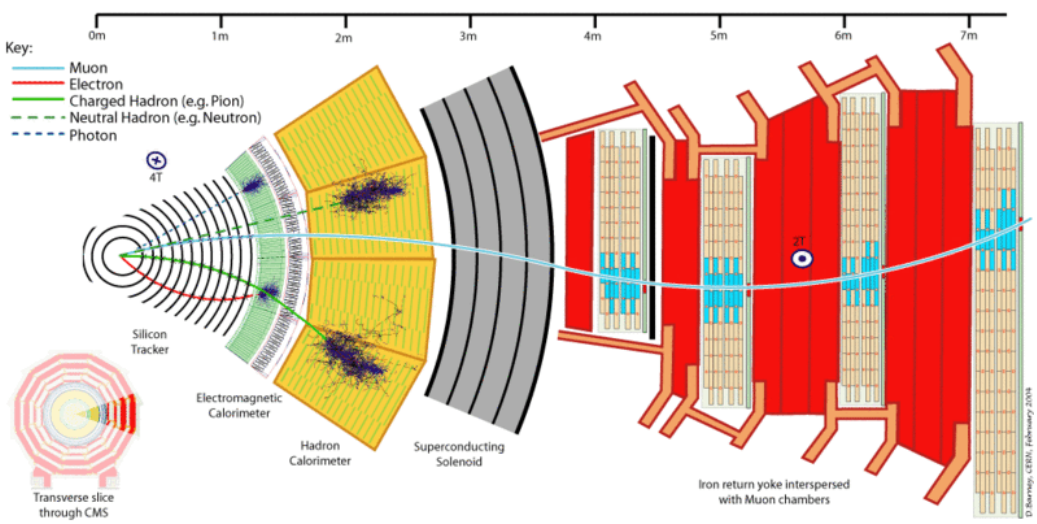

Figure 2.4.: Transverse slice through CMS showing particles incident on the different sub-detectors [13].

2.2.1 Magnet

The superconducting solenoid magnet reaches a maximum magnetic field of 3.8 T in the positive z direction in the inner detectors. A high magnetic field provides

a large bending power in the transverse plane for charged particles, which makes possible to reach precise measurement of muon momenta. The magnet is 12.5 m long and with an inner radius of 6 m and is made of four-layers of NbTi. It is the largest superconducting magnet ever built, with the capacity to store an energy of 2.6 GJ at full current. The magnetic flux is returned via a 1.5 m thick iron yoke instrumented with four stations of muon chambers. In this part of the detector the magnetic field is saturated at 2 T. More detailed information can be found in reference [21].

2.2.2 Tracker

The Tracker is the subdetector system which is closest to the interaction point, a general layout is presented in Fig. 2.5. It is designed to provide an efficient measurement of the trajectories of charged particles emerging from the LHC collisions, as well as a precise reconstruction of secondary vertices. The CMS Tracking System is composed of q silicon pixel detector close to the interaction region and a strip detector covering radii from 0.2 m to 1.1 m. The Pixel Detector consists of 1440 pixel modules arranged in three barrel layers and two disks in each end-cap. The barrel layers are located at radii of 4.4, 7.3 and 10.2 cm around the interaction point with a length of 53 cm. On each side of the barrel, two discs are placed at $|z| = 32.5$ cm and 46.5 cm.

2.2.3 Calorimetry

ECAL

The electromagnetic calorimeter (ECAL) is used to measure the energy of photons and electrons. The ECAL is a high precision scintillating crystal calorimeter. The structure of the ECAL can be seen in Fig. 2.6. It is composed of 61,200 lead tungstate (PbWO4) crystals in the barrel region and 7,324 crystals in the endcaps. The choice of that material is motivated by its fast response and high radiation resistance and its very good resolution. In front of each ECAL Endcap is a preshower detector (ES),

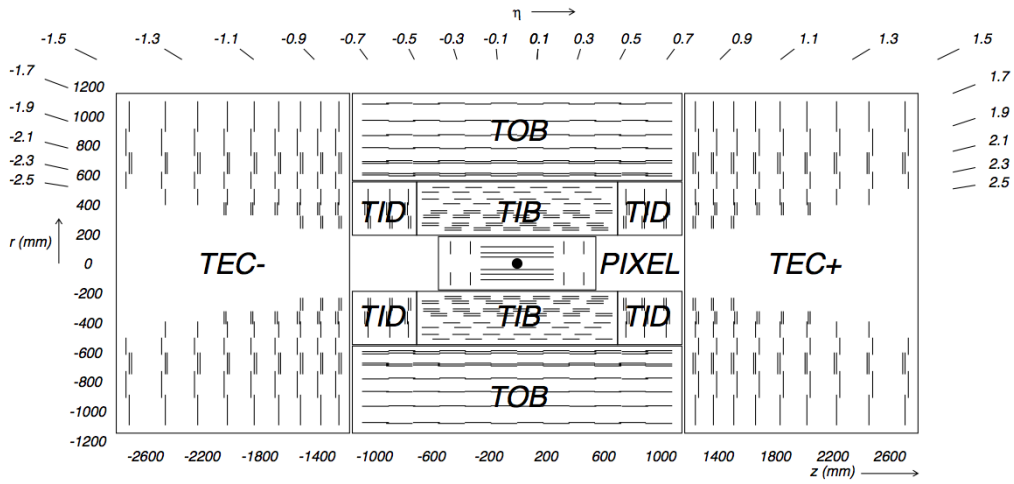

Figure 2.5.: Layout of the CMS silicon tracker [13]

from $1.65 < |\eta| < 2.6$ made from silicon strip detectors in order to identify neutral pions (π^0). The nominal energy resolution, measured with electron beams having momenta between 20 and 250 GeV, is:

$$(\frac{\sigma_E}{E})^2 = (\frac{S}{\sqrt{E}})^2 + (\frac{N}{E})^2 + C^2 \tag{2.4}$$

where S is the stochastic term, which includes fluctuations in the shower containment as well as a contribution from photostatistics, N is the noise term, which accounts for the electronic, digitization, and pileup noise, and C is the constant term, which comes from the light collection non-uniformity, errors on the inter-calibration among the modules, and the energy leakage from the back of the crystal.

HCAL

The hadronic calorimeter (HCAL) is designed to measure the energy of hadrons. The HCAL is comprised of four subsystems: the HCAL Barrel (HB), the outer calorimeter (HO), the HCAL Endcap (HE), and the forward calorimeter (HF). Figure 2.7 gives a schematic overview on the HCAL sub-detector. The HB is a sampling

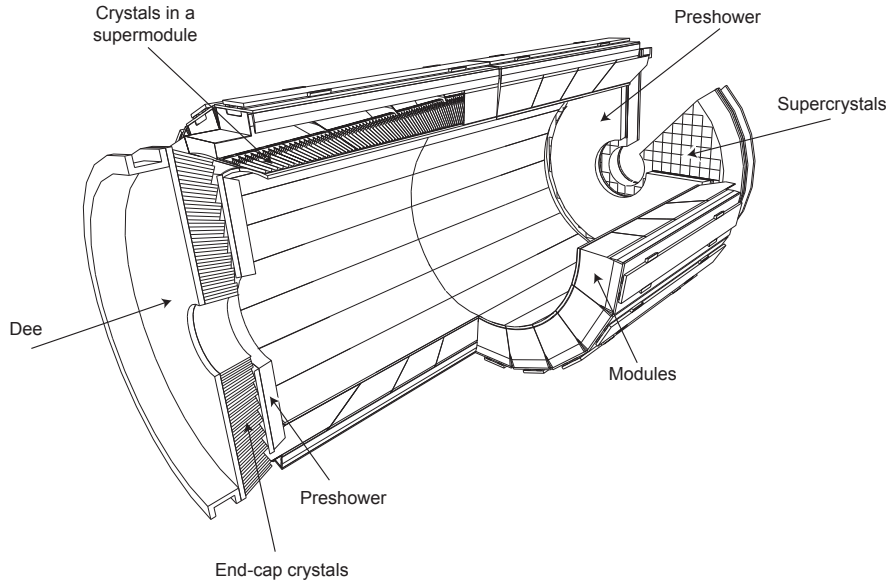

Figure 2.6.: Structure of the electromagnetic calorimeter of the CMS. [13]

calorimeter that covers the range $|\eta| < 1.3$. It consists of 36 identical azimuthal wedges aligned parallel to the beamline. It is located between the ECAL and the solenoid coil and is supplemented by the HO located between the solenoid and the muon chambers. The HO is designed to absorb the remnant of the hadronic shower which has not been fully absorbed in the HB. The HE covers a large portion of the solid angle, $1.3 < |\eta| < 3$. Beyond that region, the HF placed at 11.2 m from the interaction point extends the pseudorapidity coverage up to $|\eta| < 5.2$. The HE must have high radiation tolerance, with 10 Mrad expected after 10 years of operation. The reason for the absorber material to be non-magnetic is that it must not affect the magnetic field. The HF experiences the harshest radiation environment and therefore requires an extremely radiation tolerant material. The active material chosen is quartz fibers that generate Cherenkov light. The fibers are mounted in grooves in the steel absorber plates. The inner part of the HF will be exposed to close to 100

Mrad/year. As the absorber will become radioactive the entire HF can be moved into a garage to limit exposure of personnel during maintenance periods.

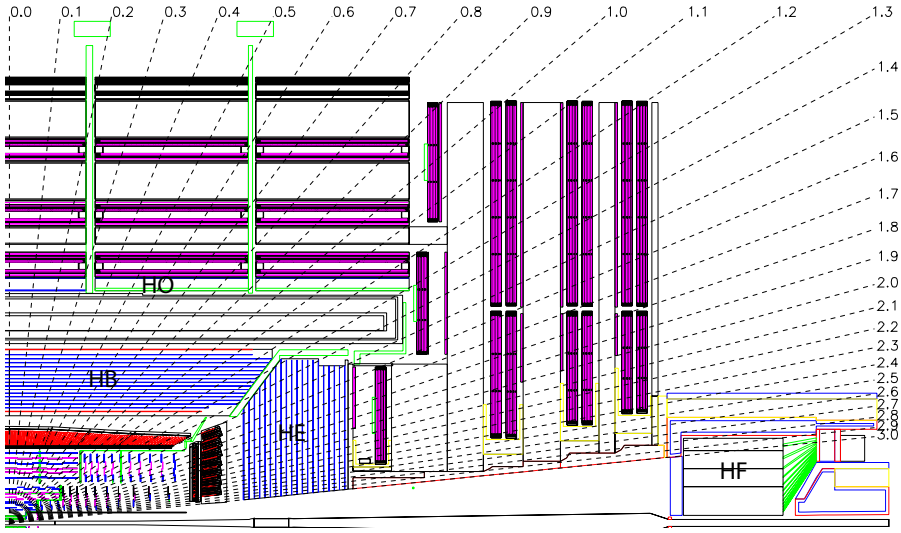

Figure 2.7.: Structure of the hadronic calorimeter of the CMS. [13]

2.2.4 Muon System

One of the main design objectives of the CMS detector was to obtain a high precision muon momentum measurement, for its key role both in new physics searches and in Standard Model measurements. The CMS muon system [13] uses three different types of gaseous detectors to detect muons. In the barrel region, Drift Tubes (DTs) and Resistive Plate Chambers (RPCs) are used, while in the endcap there are Cathode Strip Chambers (CSCs) and also RPCs. The layout of the CMS muon system is shown in Fig. 2.8.

Drift Tubes

In the central region of CMS, $|\eta| < 1.2$, the muon system consists of four concentric cylinders containing 250 gas drift chambers. Each Drift Tube is filled will a mix of 85% Argon and 15% CO^2 with active wires for charge collection. As muons pass through the gas they leave an ionization trail. The charge drifts to the wires, which detect the charge. The size of the drift cell was chosen so the maximum drift time is 380 ns. There are ∼172000 active wires in the entire system. The use of DTs is only possible in this region due its low magnetic field.

Cathode Strip Chambers

In the endcap, the muon system is comprised of Cathode Strip Chambers (CSC). The CSC's cover the $0.9< |\eta| <2.4$ pseudorapidity range. Each CSC is trapezoidal in shape and consists of 6 gas gaps, each gap having a plane of radial cathode strips and a plane of anode wires running almost perpendicularly to the strips. The CSC is a fast detector (response time of ∼4.5 ns), but with rather coarse position resolution; a precise position measurement is made by determining the centre-of-gravity of the charge distribution induced on the cathode strips (spatial resolution ∼200 μm, angular resolution ∼10 mrad).

Resistive Plate Chambers

In order to improve muon trigger system and for a good measurement of the bunch crossing time, resistive plate chambers (RPC) are mounted in the barrel and endcap region ($|\eta| <1.6$). The RPCs are able to provide independent and fast trigger with high segmentation and sharp pT threshold over a large portion of the pseudorapidity range. However, the RPCs have coarser position resolution making them more useful for the trigger.

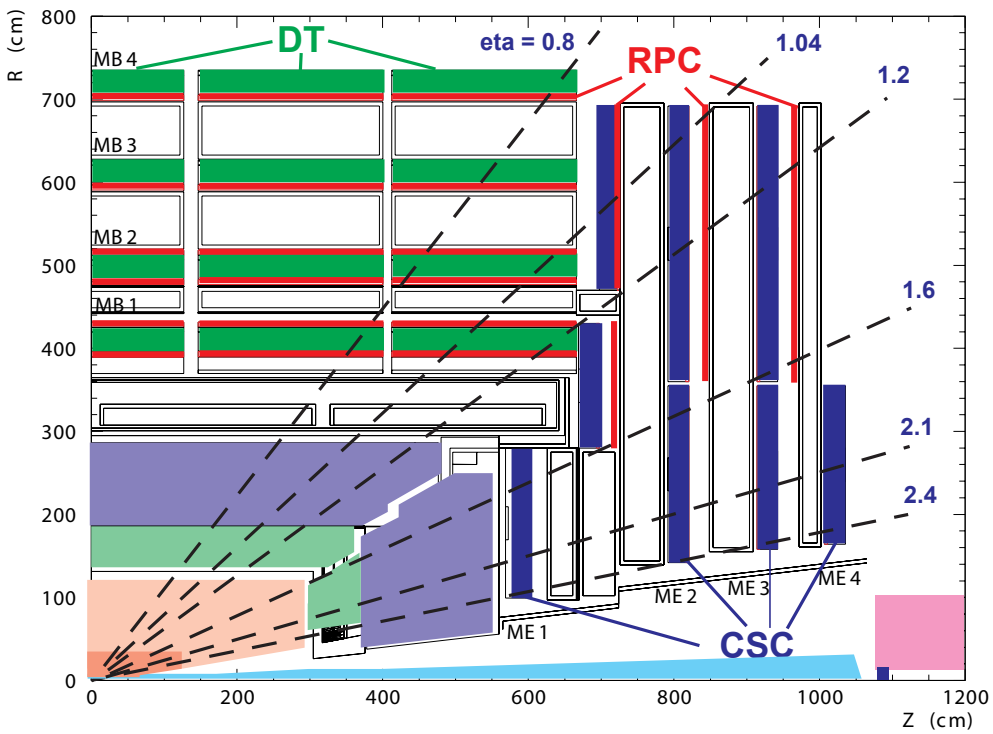

Figure 2.8.: Layout of one quarter of the CMS muon system for initial low luminosity running [22].

2.2.5 Trigger and Data Acquisition

The CMS trigger system is designed to cope with an unprecedented high luminosity and interactions rates. The LHC will collide proton bunches at a rate of 40 MHz which leads to $\sim 10^9$ interactions per second at design luminosity. Since it is not possible to record events at this rate, a two-part trigger system, consisting of a hardware-based trigger (Level 1) and a software-based trigger (High Level Trigger) is used [23, 24]. The rate is then reduced by a factor of 10^6.

Level 1 Trigger

The Level 1 (L1) trigger is designed to achieve a maximum output rate of 100 kHz and consists of custom-designed, programmable electronics. The front-end (FE)

electronics can store information from up to 128 consecutive events, which equates to $\sim$3 μs. To cope with the time limitation, the L1 trigger system uses only coarsely segmented data from the muon system and the calorimeters while the full granularity data are stored in the FE electronics waiting for the L1 decision. The L1 muon trigger is organized into subsystems representing the three different muon detectors: the DT trigger in the barrel, the CSC trigger in the endcap and the RPC trigger covering both barrel and endcap. The Level-1 muon trigger also has the Global Muon Trigger (GMT) that combines the trigger information from the DT, CSC, and RPC muon subsystems, as well as from the calorimeter subsystem, and sends it to the Level-1 Global Trigger.

High Level Trigger

The High Level Trigger (HLT) exploits the full amount of collected data for each bunch crossing accepted by Level 1 Trigger and is capable of complex calculations such as the offline ones. It is structured in two levels, Level 2 (L2) and Level 3 (L3) implemented in software. The L2 uses information from the muon spectrometer (parameters from the L1 muon candidates converted into seeds) to perform a standalone reconstruction, providing a muon p_T measurement with a precision of about 15%. The L2 reconstruction follows closely the offline standalone reconstruction using Kalman-filter techniques. The L3 takes L2 candidates as seeds and adds information from the inner tracker by performing track reconstruction in the silicon tracker. This reconstruction is regional, it performs pattern recognition and track fitting only in a small $\eta - \phi$ slice of the tracker, to keep execution time low. Trajectories are then reconstructed using Kalman-filter techniques. Level 3 provides a much more precise p_T measurement (1% - 2% in the barrel region) than Level 2, as well as the ability to select on the basis of the track impact parameter with respect to the beam spot. After the HLT decisions, the event rate decreases down to 100Hz for mass storage which corresponds to a data rate of 150 Mbyte/s.

3. UPSILON(NS) PRODUCTION CROSS SECTION MEASUREMENT

3.1 Υ(nS) Measurements with Early Data

We performed the first measurement of the $\Upsilon(1S)$ production cross section in proton-proton collisions at $\sqrt{s} = 7$ TeV using data recorded by the CMS between April and July 2010. The data sample corresponds to a total integrated luminosity of 280± 31 nb^{-1} [25]. The dimuon invariant mass spectrum after offline selection in the region is shown in Fig. 3.1. The observed yield of the $\Upsilon(1S)$ reconstructed in the dimuon decay channel is 678 ± 38. With this amount of signal events, we were able to measure the p_{T} differential $\Upsilon(1S)$ cross section as show in Fig. 3.2. The results were presented in the ICHEP conference in Paris in July 2010. At the end of 2010, we published the Υ(nS) p_{T} and rapidity differential cross section results with a dataset corresponding to an integrated luminosity of 3.1±0.3 pb^{-1} [25]. We compared the kinematic distributions of Υ and muons from Υ in data and MC, and found them to be consistent, as shown in Fig. 3.3, Fig. 3.4, Fig: 3.5, and Fig. 3.6. The Υ(nS) integrated production cross sections for the range $|y| < 2$ were measured to be:

$$\sigma(pp \to \Upsilon(1S)X) \cdot \mathcal{B}(\Upsilon(1S) \to \mu^+\mu^-) = (8.55 \pm 0.05^{+0.74}_{-0.71} \pm 0.34)\ \mathrm{nb}\,,$$

$$\sigma(pp \to \Upsilon(2S)X) \cdot \mathcal{B}(\Upsilon(2S) \to \mu^+\mu^-) = (2.21 \pm 0.03^{+0.21}_{-0.20} \pm 0.09)\ \mathrm{nb}\,,$$

$$\sigma(pp \to \Upsilon(3S)X) \cdot \mathcal{B}(\Upsilon(3S) \to \mu^+\mu^-) = (1.11 \pm 0.02^{+0.12}_{-0.11} \pm 0.04)\ \mathrm{nb}\,,$$

The differential Υ(nS) cross sections as a function of p_{T} for the rapidity intervals $|y| < 1$, $1 < |y| < 2$, and $|y| < 2$ are shown in Fig. 3.7. The cross section ratios as a function of p_{T} were also measured as shown in the right plot of Fig. 3.8.

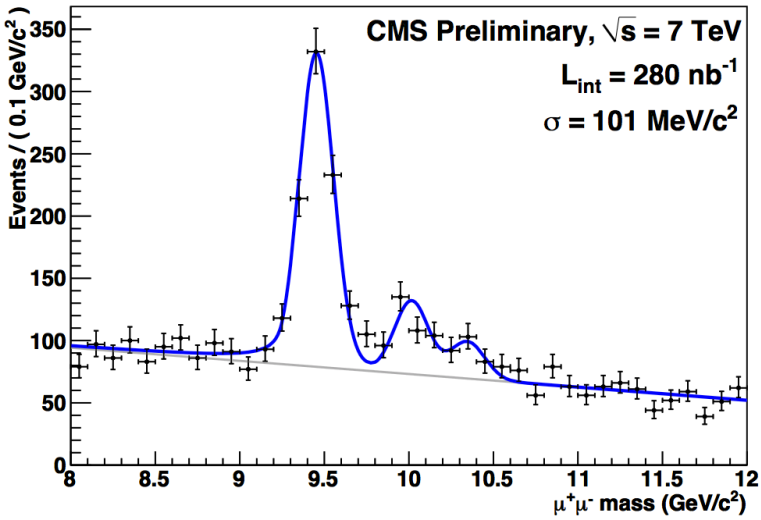

Figure 3.1.: The dimuon invariant mass distribution in the vicinity of the Υ(nS) resonances for $|y| < 2$. The invariant mass distribution is fit to the sum of a signal component and a background component (dark line). Each Υ resonance is described by a Crystal Ball function. The combinatorial background is described by a first order polynomial (light gray line).

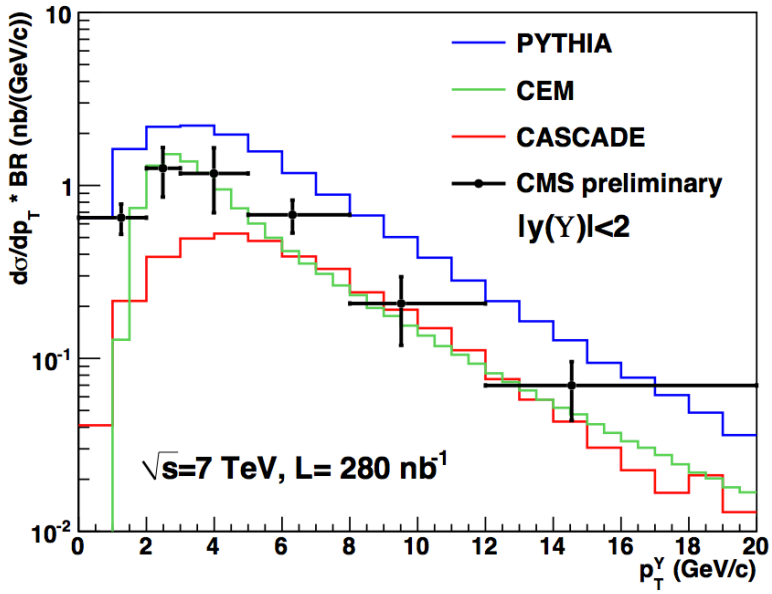

Figure 3.2.: Differential cross section of the p_{T} as a function of in the rapidity range $|y| < 2$ compared to various theoretical predictions.

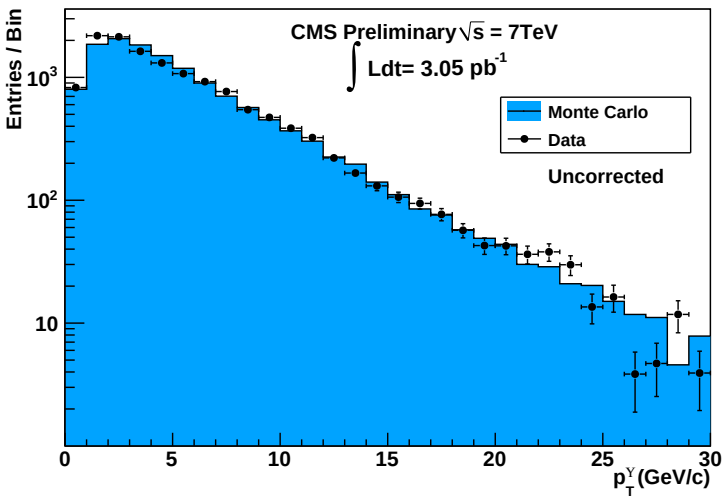

Figure 3.3.: Side-band-subtracted distribution of $\Upsilon(1S)$ transverse momentum compared to PYTHIA MC simulation. The data are not corrected for acceptance and efficiencies. The MC is normalized to the yield in data.

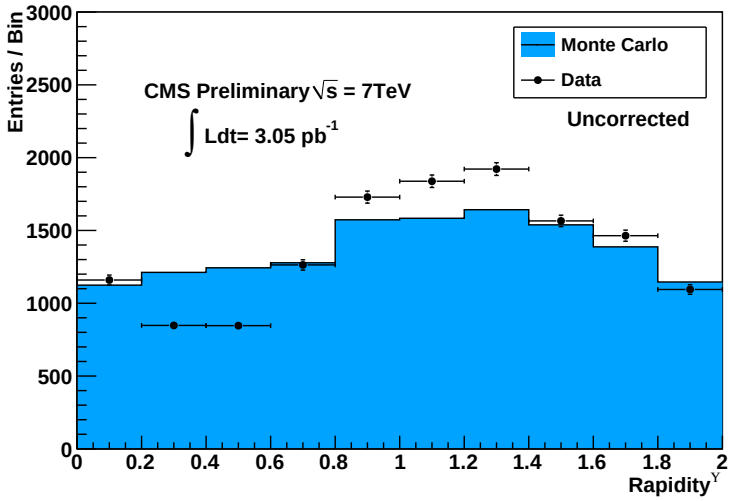

Figure 3.4.: Side-band-subtracted distribution of $\Upsilon(1S)$ rapidity compared to PYTHIA MC simulation. The data are not corrected for acceptance and efficiencies. The MC is normalized to the yield in data.

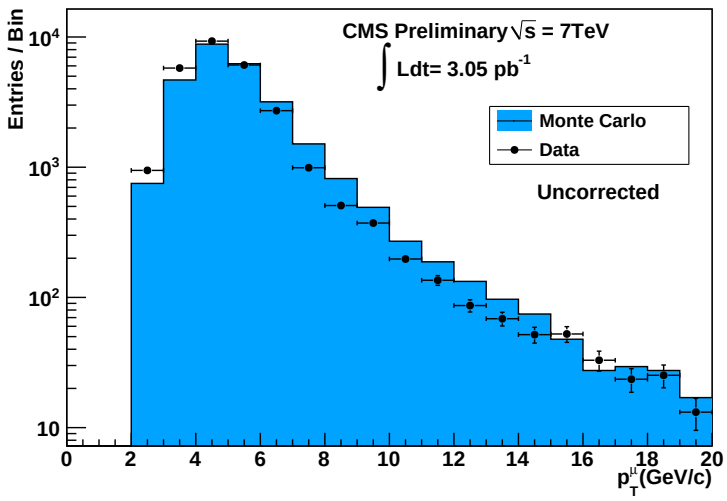

Figure 3.5.: Side-band-subtracted distribution of muon transverse momentum from Υ candidates compared to PYTHIA MC simulation. The data are not corrected for acceptance and efficiencies. The MC is normalized to the yield in data.

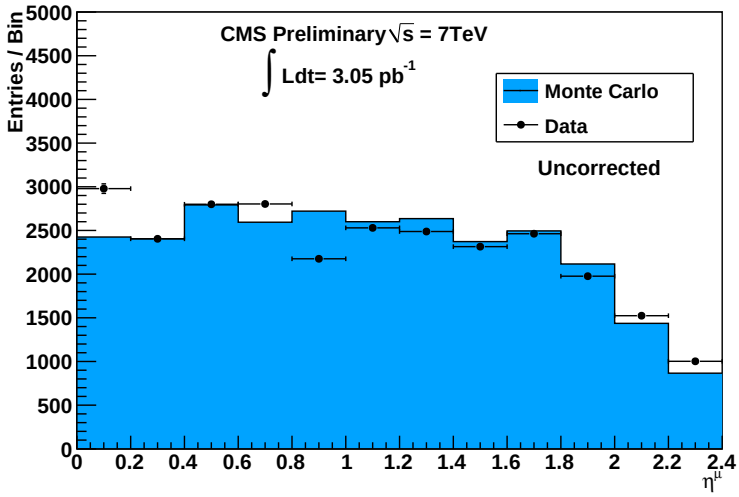

Figure 3.6.: Side-band-subtracted distribution of muon pseudorapidity from Υ candidates compared to PYTHIA MC simulation. The data are not corrected for acceptance and efficiencies. The MC is normalized to the yield in data.

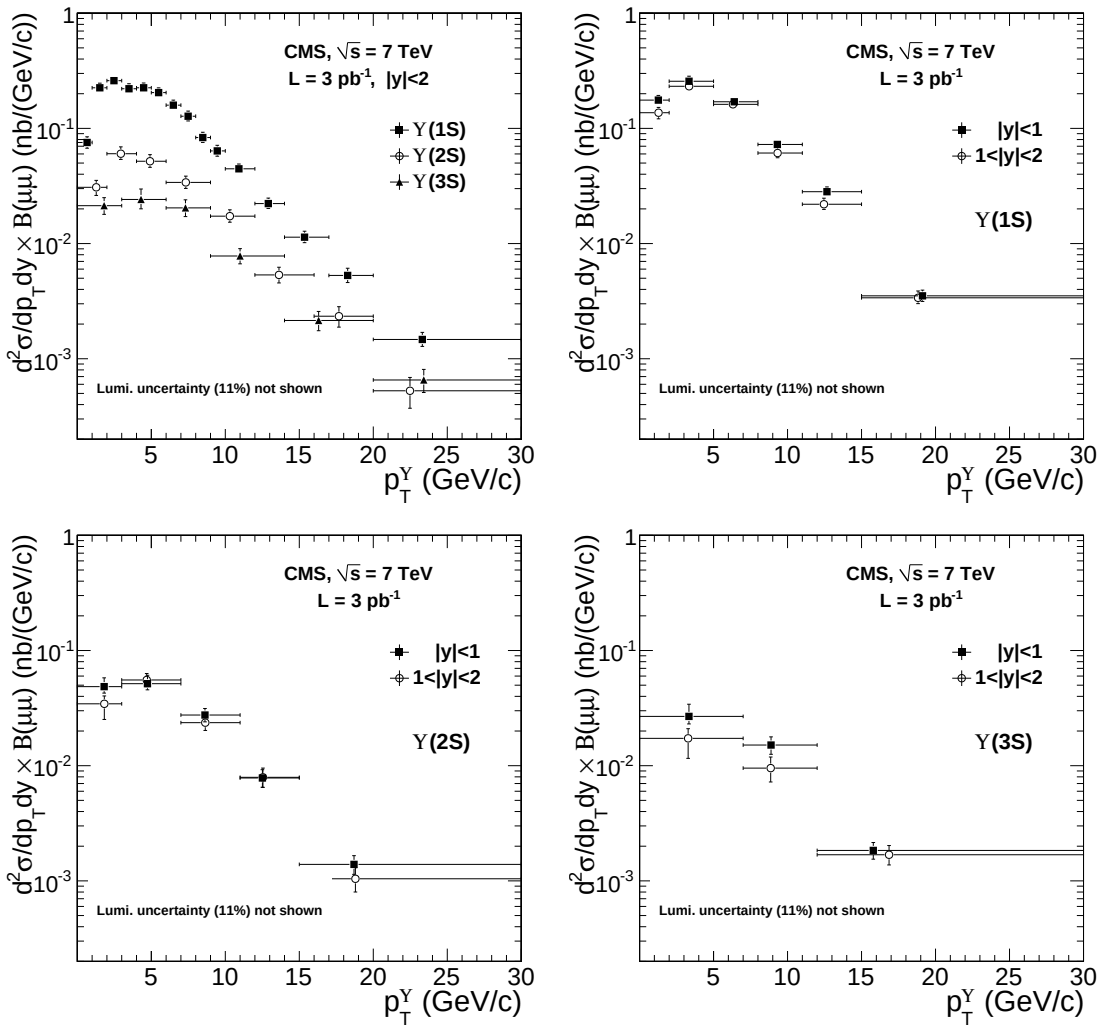

Figure 3.7.: Υ(nS) differential cross sections in the rapidity interval $|y| < 2$ (top left), and in the rapidity intervals $|y| < 1$ and $1 < |y| < 2$ for the Υ(1S) (top right), Υ(2S) (bottom left) and Υ(3S) (bottom right). The uncertainties on the points represent the sum of the statistical and systematic uncertainties added in quadrature, excluding the uncertainty on the integrated luminosity (11%).

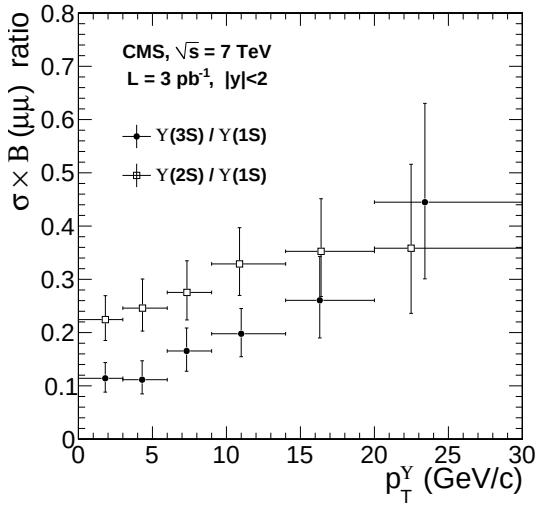

Figure 3.8.: Cross-section ratios for Υ(nS) states as a function of p_{T} in the rapidity range $|y| < 2$.

3.2 Introduction

This analysis constitutes an extension of the first cross-section measurement, based on the rest of 2010 dataset, which corresponds to $35.8\,\mathrm{pb}^{-1}$. The first $3\,\mathrm{pb}^{-1}$ of data is not included in this analysis.

The measurements are based on the analysis of dimuons produced by the decay of the Υ resonances. The data were collected using a trigger that required the presence of two muons, without explicit momentum thresholds applied. The Υ candidates are formed from pairs of muon candidates having opposite charge. The efficiency with which the muons satisfy the trigger, identification, and quality requirements is determined with the tag and probe data-driven technique.

The Υ cross section has also been measured at the Tevatron at 1.8 and 1.96 TeV center-of-mass energies by the CDF [26], and D0 [27] experiments. The production mechanism of the Υ in hadronic collisions is not yet understood [28]. The current theoretical approach is based on non-relativistic QCD (NRQCD) factorization, a recent paper is Ref. [6]. In the first step a $b\bar{b}$ quark pair is produced in a bound state with specific quantum numbers. This amplitude is calculated with perturbative QCD. In the second step, the $b\bar{b}$ state may evolve directly to an Υ(nS) state or to a higher mass bottomonium state which subsequently decays to an Υ(nS). In all cases Υ(nS) production is prompt.

The leading order (LO) NRQCD calculation [29–31] is unable to predict the yield or p_T dependence of the measured cross section. With the inclusion of higher order corrections the yield and the p_T dependence can be reproduced, but at the price of introducing unknown long-distance-matrix NRQCD matrix elements that are determined from fits to the data [32]. However, the polarization predicted disagrees with both the published CDF [26] and D0 measurements [27]. Ref. [6] contains a recent update to the NRQCD calculations which succeed in reproducing the data, and contain predictions for Υ(nS) production at the LHC.

This analysis will be presented as follows. The analysis strategy is described in Sec. 3.3. The Data and Monte Carlo event samples are described in Sec. 3.4 and 3.5, the event reconstruction and selection in Sec. 3.6, the model employed to fit the dimuon invariant mass spectrum is presented in Sec. 3.7, the acceptance in Sec. 3.8, the estimation of the efficiency by the data-driven tag and probe technique in Sec. 3.9, the cross section measurement in Sec. 3.10 along with the estimation of systematic uncertainties in Sec. 3.11 and a discussion of the results obtained is provided in Sec. 3.13. The results of fiducial cross section are in Sec. 3.12 with a discussion of the results obtained is provided, together with a summary in Sec. 3.15.

3.3 Analysis strategy

The measurement of the Υ(1S), Υ(2S) and Υ(3S) differential production cross sections, $d\sigma\left(\Upsilon(\mathrm{nS})\right)/dp_T$, is performed in this analysis in the di-muon decay channel which has a branching fraction of approximately 2%. At hadron colliders one expects the Υ(nS) production cross section to be uniform in rapidity, y, therefore we measure the differential production cross section integrated in the rapidity range $|y| < 2.4$. The strategy can be summarized in the following expression:

$$\left.\frac{d\sigma\left(pp \to \Upsilon(\mathrm{nS})X\right)}{dp_T}\right|_{|y|<2.4} \mathcal{B}\left(\Upsilon(\mathrm{nS}) \to \mu^+\mu^-\right) = \frac{N^{\mathrm{fit}}_{\Upsilon(\mathrm{nS})}(p_T; \mathcal{A}, \varepsilon_{\mathrm{track}}, \varepsilon_{\mathrm{id}}, \varepsilon_{\mathrm{trig}})}{\int \mathcal{L}dt \cdot \Delta p_T \cdot \Delta y},$$

where

- $N^{\mathrm{fit}}_{\Upsilon(\mathrm{nS})}$ – is the yield of Υ(nS) obtained from a fit to the dimuon invariant mass in a given p_T bin.
- $\mathcal{A}(p_T^{\Upsilon}, y^{\Upsilon})$ – is the geometric and kinematic acceptance of Upsilon candidates as obtained from MC simulations.
- $\varepsilon_{\mathrm{track}}$ – is the tracking reconstruction efficiency.
- $\varepsilon_{\mathrm{id}}(p_T^{\mu}, \eta^{\mu})$, $\varepsilon_{\mathrm{trig}}(p_T^{\mu}, \eta^{\mu})$ – are the muon identification and trigger efficiencies, respectively, both obtained with the "Tag and Probe" data driven technique.
- $\int ldt$ – are the integrated luminosity.
- Δp_T, Δy – is the Υ transverse momentum and rapidity bin sizes.

The acceptance and efficiency terms are parameterized in terms of the Υ candidate (transverse momentum, rapidity) and its daughter muons (transverse momentum, pseudo-rapidity) kinematic properties. Event weights are assigned based on this information, thus allowing for the corrected yield and its uncertainty to be determined directly from an unbinned maximum likelihood fit performed in the invariant mass space of the dimuon Upsilon candidates.

The p_{T} differential and integrated cross sections are separately extracted for each of the three Upsilon states, for the following rapidity ranges: $|y| < 0.4$, $0.4 < |y| < 0.8$, $0.8 < |y| < 1.2$, $1.2 < |y| < 1.6$, $1.6 < |y| < 2.4$ and $|y| < 2.4$. The ratio of cross sections is determined as a function of p_{T}. The p_{T} integrated, rapidity differential cross section for the $\Upsilon(1\mathrm{S})$ state is extracted.

In order to reduce theoretical uncertainties on the acceptance that depend on the poorly known polarization, we also show the results of the fiducial cross section. The fiducial cross section is defined within the kinematic cuts on both muons:

$$\left.\frac{d\sigma\left(pp \to \Upsilon(\mathrm{nS})X\right)}{dp_T}\right|_{|y|<2.4} \mathcal{B}\left(\Upsilon(\mathrm{nS}) \to \mu^+\mu^-\right) = \frac{N^{\mathrm{fit}}_{\Upsilon(\mathrm{nS})}(p_T; \varepsilon_{\mathrm{track}}, \varepsilon_{\mathrm{id}}, \varepsilon_{\mathrm{trig}})}{\int \mathcal{L}dt \ \cdot \Delta p_T \cdot \Delta y},$$

3.4 Data samples and online selection

The data sample in this analysis was recorded by the CMS detector in pp collisions at a centre-of-mass energy of 7 TeV. The sample corresponds to a total integrated luminosity of 35.8 pb^{-1}.

Data are included in the analysis for all periods where the silicon tracker, the muon system, and the trigger were performing well and a luminosity measurement is available.

3.4.1 Trigger

The CMS trigger system performs the online event selection in two steps called Level-1 (L1) Trigger and High-Level Trigger (HLT) [13]. The L1 Trigger consists of custom-designed, largely programmable electronics, whereas the HLT is a software system implemented in a filter farm of about one thousand commercial processors.

The Muon trigger at L1 uses all the three muon systems, the DT, the CSC and the RPC and has local, regional and global components. The barrel DT chambers provide local trigger information in the form of track segments in the φ-projection and hit patterns in the η-projection. The endcap CSCs deliver 3-dimensional track segments. All chamber types also identify the bunch crossing from which an event originated. The Regional Muon Trigger consists of the DT and CSC Track Finders that join segments to complete tracks and assign physical parameters to them. In addition, the RPC trigger chambers deliver their own track candidates based on regional hit patterns. The Global Muon Trigger then combines the information from the three sub-detectors, achieving an improved momentum resolution and efficiency compared to the stand-alone systems. The trigger objects are ranked according to their momentum and quality and based on the best four candidates a decision is made whether to send the event to the HLT for further processing.

In the HLT the event selection is performed in two stages, the so called Level-2 (L2) and Level-3 (L3). At L2, the L1 candidates are used to seed track reconstruction

in the muon system only. To improve the transverse momentum measurement the beam-spot constraint is used. At the end of L2, muon candidates are preselected based on their pseudo-rapidity and transverse momentum. At L3 the track reconstruction continues in the silicon tracker. To keep the execution time short this reconstruction is performed only in the regions of the L2 muon candidates. The final selection of the event is based on the refined transverse momentum of the muon candidates at L3.

The data used in the current analysis were collected with two trigger paths. The HLT_DoubleMu0 requires the detection of two muons at the L3 level without an explicit p_{T} requirement. The two-dimensional Δxy between each L3 muon and the beam spot must be less than 2 cm. The HLT_DoubleMu0 got prescaled during the data taking thus the HLT_DoubleMu0_Quarkonium_v1 was used afterwards, which requires the two muons with opposite signs and with mass in the quarkonium mass window (1.5,14.5) in addition to the requirements that imposed on the HLT_DoubleMu0 . All three muon systems, DT, CSC and RPC, take part in the trigger decision.

Anomalous events arising from beam-gas interactions or beam scraping in the beam transport system near the interaction point, which produce a large number of hits in the pixel detector, are removed with offline software filters [33]. A good primary vertex is also required, as defined in Ref. [33]. The detector systems are aligned and calibrated using LHC collision data and cosmic muon events [34].

3.4.2 Datasets and skimming

The raw data collected with the HLT_DoubleMu0 from run 146240 to 147116 and HLT_DoubleMu0_Quarkonium_v1 from run 147196 to 149711 were stored in the following dataset published in the DBS:

`/MuOnia/Run2010B-v1/RAW, Runs: 146240-149711`

The raw dataset was reconstructed offline with `CMSSW` version 3.8.6 and stored in the dataset:

`/MuOnia/Run2010B-Nov4ReReco_v1/RECO`

As a final step of reconstruction, muons with silicon tracks of opposite electric charge have been paired and the probability of common vertex was calculated. In addition the trigger objects of the trigger paths were matched to the offline muons and the events were saved in the format of Physics Analysis Tools (PAT). The list of software packages used in addition to CMSSW 3.8.7 is

```
HeavyFlavorAnalysis/Onia2MuMu V00-12-01
MuonAnalysis/MuonAssociators V01-11-00
```

The PAT sample is the input for the final selection of events for analysis.

3.4.3 Luminosity

An integrated luminosity $\mathcal{L} = 35.8 \pm 1.4$ pb^{-1} was measured for the three trigger paths in the datasets listed in Sec. 3.4.2 using signals from the Forward Hadronic Calorimeter (HF). Two methods for extracting a real-time relative instantaneous luminosity are used. The "zero counting," method in which the average fraction of empty towers is used to infer the mean number of interactions per bunch crossing. The second method exploits the linear relationship between the average transverse energy per tower and the luminosity. The luminosity is calibrated using separation scans first pioneered by Van Der Meer at the ISR [35]. A detailed description of the procedure employed can be found in [36].

3.5 Monte Carlo event samples

Simulated events are used to tune the selection criteria and to compare with data. Upsilon events are produced using Pythia [37], which generates events based on the leading-order color singlet and octet mechanisms. Color octet states undergo a shower evolution. The NRQCD matrix element tuning obtained by comparing NRQCD calculations with CDF data [38] is employed. Background events are generated from generic QCD events with Pythia. The response of the CMS detector is simulated with a GEANT4-based [39] Monte Carlo (MC). The simulated events are processed with the same reconstruction algorithms used for data. Final state radiation is implemented using PHOTOS [40, 41].

The Monte Carlo samples used in this study have been produced by the CMS collaboration as part of the "Fall10"("Summer10") production sequence with CMSSW version 3.8.X (3.6.2). Events were generated with PYTHIA and the Upsilons were decayed with PHOTOS within EvtGen to introduce final state radiation. GEANT was used for the detector simulation followed by the L1 Trigger emulation, the HLT processing and offline reconstruction.

Events with an Upsilon resonance were generated at $\sqrt{s} = 7$ TeV within the NRQCD framework via the leading order singlet and octet mechanism. The long distance matrix elements, that are postulated to be universal, are obtained from fits to the CDF data. To obviate time-consuming simulation and storage of events in which one or both muons are generated outside of the geometric and kinematic acceptance, an event filter immediately post-generation is implemented. The filter requires two muons (not necessarily from the Υ) with

$$|\eta^{\mu}| < 2.5\,.$$

Table 3.1 summarizes the statistics, integrated luminosity and effective cross section (i.e. including branching fraction to muons and filter efficiency) of the MC signal samples. To determine the generated cross section in the $|y^{\Upsilon(\mathrm{nS})}| < 2.4$ rapidity

range, we have generated (but not simulated) Υ samples without the generator level two muon filter.

Table 3.1: MC samples

Sample	Events	σ_{eff} (nb)	$\int \mathcal{L}dt$ (pb^{-1})
/Upsilon1SToMuMu_2MuEtaFilter_7TeV-pythia6-evtgen/Fall10-START38_V12-v1	2.4M	14.3	166
/Upsilon2SToMuMu_2MuEtaFilter_7TeV-pythia6-evtgen/Fall10-START36_V12-v1	1.2M	6.0	193
/Upsilon3SToMuMu_2MuEtaFilter_7TeV-pythia6/Fall10-START36_V12-v1	0.6M	1.6	372
/QCD_2MuPEtaFilter_7TeV-pythia6/Summer10-START36_V9_S09-v2	43M	40700	1.1

The main source of background to $\Upsilon(\text{nS}) \to \mu^+\mu^-$ arises from the QCD production of heavy quarks that decay by the weak interaction to muons, and the muons combine to an invariant mass near the $\Upsilon(\text{nS})$ mass. Additional contributions come from in-flight decays of charged pions and kaons to muons. The corresponding sample is listed in the Table 3.1. It contains a generator level filter that requires two muons to satisfy the cuts:

$$p^\mu > 2.5 \text{ GeV} \quad \text{and} \quad |\eta^\mu| < 2.5\,.$$

Other sources of background that are not simulated arise from Drell-Yan and fake muons from hadronic punch-through. The Drell-Yan contribution is estimated to be 1% of the QCD one. All known backgrounds produce a smooth dimuon invariant mass distribution that does not peak in the signal region.

3.6 Event reconstruction

3.6.1 Muon reconstruction

There are three reconstruction algorithms for muons in CMS [42]: Stand-alone Muon, Global Muon and Tracker Muon:

- `Stand-alone Muons` are tracks that have been reconstructed based on hits in the Muon System (MU) only. Hits in the CSC and DT layers are aggregated to segments. The tracking algorithm requires at least two segments in CSC/DT or one segment in CSC/DT and one RPC hit. The final track fit uses the beam spot constraint.

- `Global Muon` reconstruction starts from a Stand-alone Muon and finds matching tracks in the Silicon Tracker. A global fit is performed using the hits of both tracks. The global track with the best normalized χ^2 is identified as a Global Muon.

- `Tracker Muons` are tracks in the Silicon Tracker (SiTRK) that are identified as a muon track if extrapolation to the Muon System matches a muon segment.

These various muon reconstruction categories are used in studies reported in this document. They are employed for example in the measurement of muon efficiencies in Section 3.9. In the Υ signal selection for the cross section measurement muons of the latter class, i.e. tracker muons, are used. The pseudorapidity coverage for muon reconstruction is $|\eta| < 2.4$. Tracks are reconstructed using a Kalman filter technique which starts from hits in the pixel system and extrapolates outward to the silicon strip tracker.

3.6.2 Offline selection

Upsilon candidates are reconstructed from Tracker Muon pairs, which pass the selection type `TMOneStationTight`. Tracker Muons are tracks in the silicon tracker

that are identified as muons through matching to a muon segment once extrapolated to the muon system. The selection type `TMOneStationTight` requires that the tracker muon with one well matched segment.

The soft spectrum of muons from the decay of the Υ(nS) motivates the choice of Tracker Muons as they have the highest efficiency.

The tracks found in SiTRK are required to be matched to at least one muon segment in one muon chamber. If two (or more) tracks are spatially close, it is possible that the same muon segment or set of segments is associated with more than one track. In this case the extrapolated track with the closest match is selected. Further details may be found in Ref. [42].

The detectability criterion for the muons coming from the Υ decay is that each muon should lie within the geometric acceptance of the muon detectors. The detectability contours in the two planes $p_T - \eta$ and $p - \eta$ are shown in Fig. 3.9 and Fig. 3.10

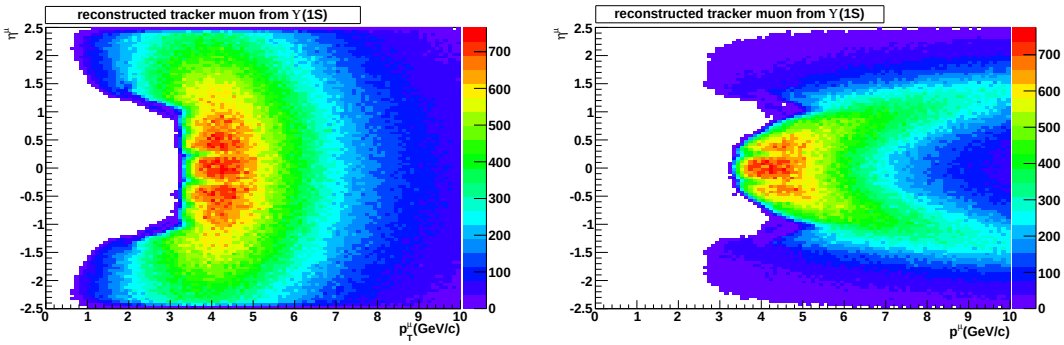

(a) Distribution of the detectable muons from Υ(1S) as a function of p_T versus η

(b) Distribution of the detectable muons from Υ(1S) as a function of p versus η

Figure 3.9.: Detectability of the muons from Υ(1S)

Additional selection criteria are applied to the tracks, to reject fake muons and muons from kaon and pion decays. The tracks are required to have at least twelve hits in the silicon tracker, at least one of which must be in the pixel detector, a track fit χ^2 per degree of freedom smaller than five, and to emanate from a cylinder of

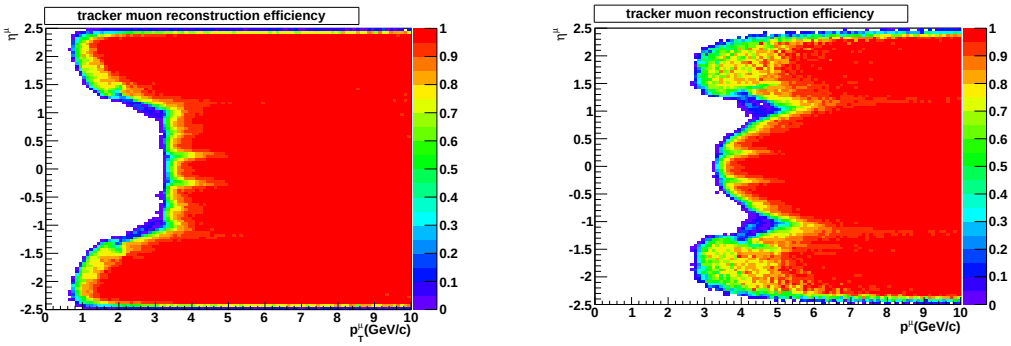

(a) Detectability of the detectable muons from Υ(1S) as a function of p_T versus η

(b) Detectability of the detectable muons from Υ(1S) as a function of p versus η

Figure 3.10.: Detectability of the muons from Υ(1S)

radius 2 mm and length 25 cm centered on the vertex of the primary interaction and parallel to the beam line.

Muons are required to satisfy:

$$\begin{aligned} p_{\mathrm{T}}^{\mu} &> 3.75 \ \ \mathrm{GeV}/c \quad \text{if} \quad |\eta^{\mu}| < 0.8\,, \\ p_{\mathrm{T}}^{\mu} &> 3.5 \ \ \mathrm{GeV}/c \quad \text{if} \quad 0.8 < |\eta^{\mu}| < 1.6\,, \\ p_{\mathrm{T}}^{\mu} &> 3.0 \ \ \mathrm{GeV}/c \quad \text{if} \quad 1.6 < |\eta^{\mu}| < 2.4\,. \end{aligned} \tag{3.1}$$

These kinematic acceptance criteria are chosen to ensure that the trigger and muon reconstruction efficiencies are high and not rapidly changing.

The momentum measurement of charged tracks in the CMS detector is affected by systematic uncertainties caused by imperfect knowledge of the magnetic field, the material budget model, and sub-detector misalignments, as well as by biases in the algorithms which fit the track trajectory. The mismeasurement of the track momentum shifts and broadens the reconstructed peaks of dimuon resonances. The momentum measurement is corrected with data collected with cosmic-ray muons and with LHC collisions [34, 43, 44], and the residual effects are determined by studying the dependence of the reconstructed J/ψ dimuon invariant mass distribution on the

muon kinematics. The residual relative correction in muon transverse momenta is parameterized by

$$p_{\mathrm{T}}^{\mathrm{corr.}} = (a_1 + a_2|\eta|) \cdot p_{\mathrm{T}} \ , \tag{3.2}$$

where: $a_1 = (3.8 \pm 1.9) \cdot 10^{-4}$, and $a_2 = (3.0 \pm 0.7) \cdot 10^{-4}$ [45].

To identify events containing an Υ decay, muons with opposite charge were paired and their invariant mass computed. The invariant mass of the muon pair is required to be between 7 and 14 GeV/c^2. The two muon helices are fit with a common vertex constraint, and events are retained if the fit χ^2 probability is larger than 0.1%. The longitudinal separation between the two muons along the beam axis is required to be less than 2 cm. The dimuon candidate is required to satisfy the trigger requirements offline. If multiple candidates are found in the same event, the candidate with the best vertex quality is retained. Based on a study of high statistics MC Υ(1S) samples, on average there are 1.003 upsilon candidates per selected event.

3.7 Fit to the dimuon invariant mass spectrum

The signal yield in the sample is extracted via an extended unbinned maximum likelihood fit performed in the dimuon mass space. The natural widths of the Υ(nS) states are much smaller than the reconstructed dimuon mass resolution.

Each Upsilon signal state is parameterized via a "Crystall Ball" (CB) ansatz. This is formed of a core Gaussian resolution and an exponential radiative tail to the left of the peak describing internal bremmstrahlung (FSR). While the resolution parameters are floating parameters in the fit, the FSR tail is fixed to its MC prediction. As the resonances overlap, we fit for the presence of all three Upsilon states simultaneously. Therefore the signal PDF consists of three CB. The fit is performed over a range of Upsilon p_{T} and rapidity. In this range the resolution of the mass peak varies and a single resolution term in the gaussian component of the CB can be not enough to reach a good fit to the data. For this reason, in bins with sufficiently high statistics the sum of two CBs per Υ state is used. The FSR tail parameters are still fixed to the MC prediction, but each resolution is left free and the fit determines also the relative fraction of the two CBs.

In the nominal configuration, a product of an error function with an exponential model [46] is adopted for describing the background in the mass range 7-14 GeV/c^2. When the background shape tends to be flat, especially when Υ p_{T} is relatively high, the exponential model is adopted without an error function.

The mass of the Υ(1S) is a parameter left free in the fit, to allow for uncertainties in the momentum scale calibration. The number of free parameters is reduced by fixing the relative mass differences $m(\Upsilon(1\mathrm{S})) - m(\Upsilon(2\mathrm{S}))$ and $m((\Upsilon(2\mathrm{S})) - m(\Upsilon(3\mathrm{S}))$ to the world average values.

Validation of the fitting procedure is verified using toy Monte Carlo experiments. A cross check of the analysis techniques is also performed employing high statistics realistic Monte Carlo samples [25].

The dimuon invariant mass spectrum in the Υ(nS) region in the interval $p_{\mathrm{T}} < 50$ GeV/c is shown in Fig. 3.11 and Fig. 3.22(a), and in the twenty four p_{T} intervals used for the Υ(1S) differential cross section measurement in Fig. 3.12. The observed signal yields are reported in Table 3.2.

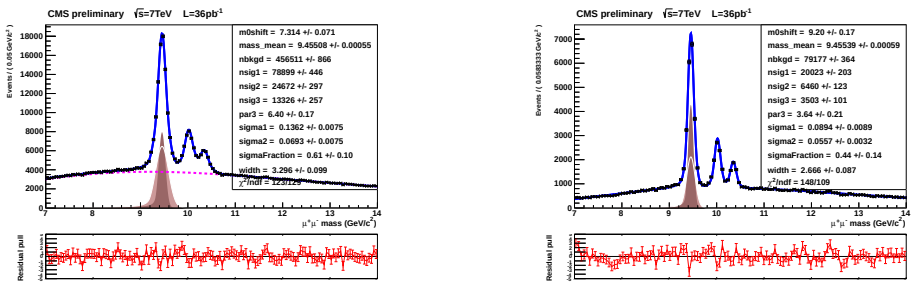

Figure 3.11.: The dimuon invariant mass distribution in the vicinity of the Υ(nS) resonances for $|y| < 2.4$ (left) and for $\eta^{\mu} < 1.0$ (right). The invariant mass distribution is fit to the sum of a signal component and a background component (dark line).

The momentum resolution of muons varies with η. The resulting dimuon mass resolution, given by the Gaussian width fit parameter, is shown in Fig. 3.13 as a function of the Υ rapidity.

From the fit to the data we obtain a common Υ(nS) mass resolution of 88 ± 2 MeV/c^2 with muons from the whole pseudorapidity range and 50 ± 2 MeV/c^2 when $|\eta^{\mu}| < 1.0$. After the application of the momentum scale correction Eq. (3.2), the Υ(1S) mass which is a free parameter in the fit, is found to be consistent with the world average value.

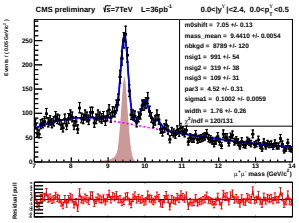

(a) $0.0 < p_{\mathrm{T}} < 0.5$

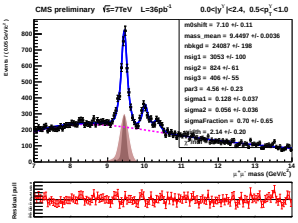

(b) $0.5 < p_{\mathrm{T}} < 1.0$

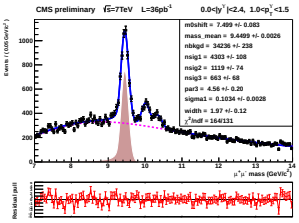

(c) $1.0 < p_{\mathrm{T}} < 1.5$

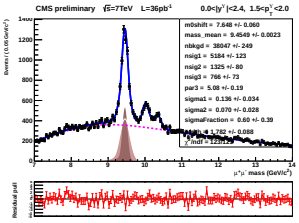

(d) $1.5 < p_{\mathrm{T}} < 2.0$

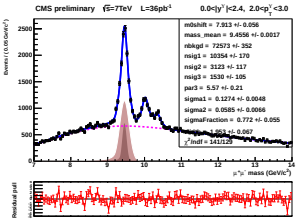

(e) $2.0 < p_{\mathrm{T}} < 3.0$

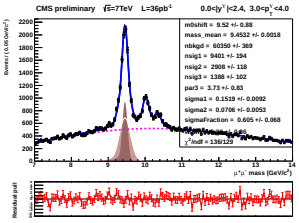

(f) $3.0 < p_{\mathrm{T}} < 4.0$

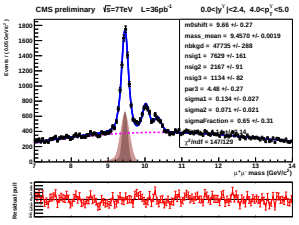

(g) $4.0 < p_{\mathrm{T}} < 5.0$

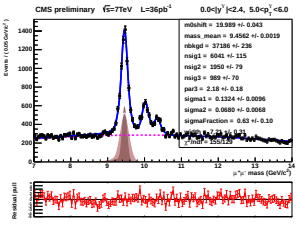

(h) $5.0 < p_{\mathrm{T}} < 6.0$

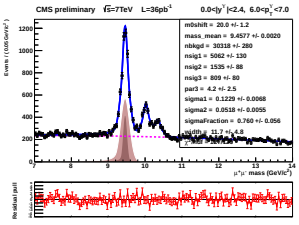

(i) $6.0 < p_{\mathrm{T}} < 7.0$

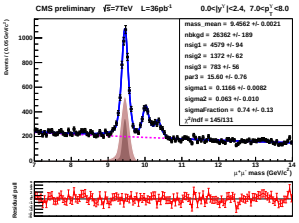

(j) $7.0 < p_{\mathrm{T}} < 8.0$

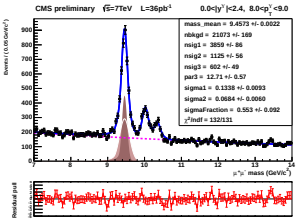

(k) $8.0 < p_{\mathrm{T}} < 9.0$

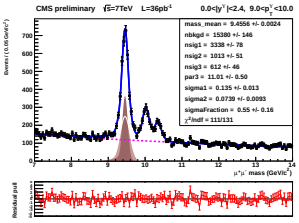

(l) $9.0 < p_{\mathrm{T}} < 10.0$

Figure 3.12.: The dimuon invariant mass distribution in the specified p_{T} regions.

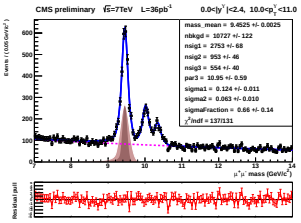

(a) $10.0 < p_{\mathrm{T}} < 11.0$

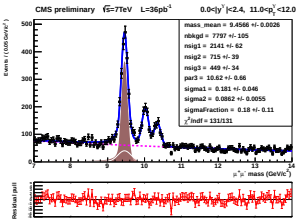

(b) $11.0 < p_{\mathrm{T}} < 12.0$

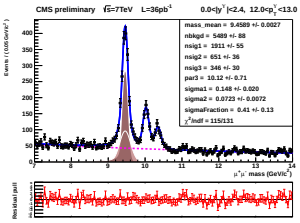

(c) $12.0 < p_{\mathrm{T}} < 13.0$

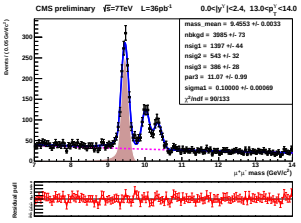

(d) $13.0 < p_{\mathrm{T}} < 14.0$

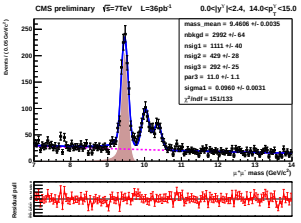

(e) $14.0 < p_{\mathrm{T}} < 15.0$

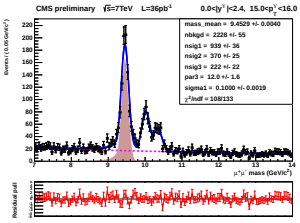

(f) $15.0 < p_{\mathrm{T}} < 16.0$

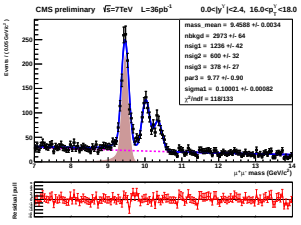

(g) $16.0 < p_{\mathrm{T}} < 18.0$

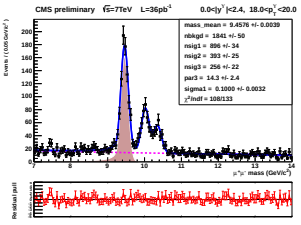

(h) $18.0 < p_{\mathrm{T}} < 20.0$

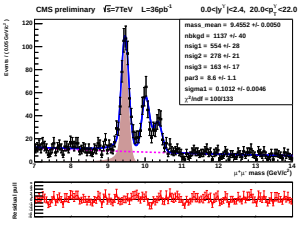

(i) $20.0 < p_{\mathrm{T}} < 22.0$

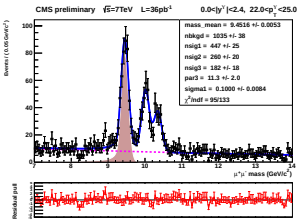

(j) $22.0 < p_{\mathrm{T}} < 25.0$

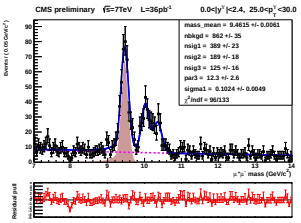

(k) $25.0 < p_{\mathrm{T}} < 30.0$

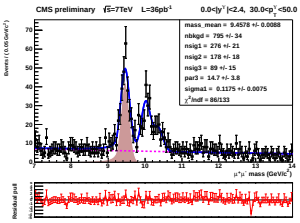

(l) $30.0 < p_{\mathrm{T}} < 50.0$

Figure 3.12.: The dimuon invariant mass distribution in the specified p_{T} regions.

Table 3.2: Upsilon signal yields observed in the specified p_{T} ranges.

p_{T} (GeV/c) range	p_{T} (GeV/c) mean	signal yield	p_{T} (GeV/c) range	p_{T} (GeV/c) mean	signal yield
			Υ(2S)		
Υ(1S)			0 - 1	0.66	1151±73
0 - 0.5	0.33	991±54	1 - 2.5	1.86	4103±140
0.5 - 1	0.77	3053±95	2.5 - 4.0	3.14	4370±136
1 - 1.5	1.26	4305±108	4.0 - 5.5	4.80	3232±108
1.5 - 2	1.75	5183±125	5.5 - 7.0	6.13	2445±88
2 - 3	2.49	10354±170	7.0 - 8.5	7.80	1965±77
3 - 4	3.48	9401±194	8.5 - 10	9.13	1613±67
4 - 5	4.48	7629±161	10 - 11.5	10.78	1361±56
5 - 6	5.49	6041±115	11.5 - 13	12.14	1012±46
6 - 7	6.49	5062±130	13 - 14.5	13.79	766±40
7 - 8	7.49	4579±94	14.5 - 16	15.21	582±33
8 - 9	8.48	3859±86	16 - 18	16.92	592±32
9 - 10	9.48	3338±78	18 - 19.5	18.86	305±23
10 - 11	10.48	2753±68	19.5 - 22	20.60	360±25
11 - 12	11.49	2141±62	22 - 26	23.70	304±23
12 - 13	12.49	1911±55	26 - 42	31.30	278±22
13 - 14	13.47	1397±44	sum		23847±290
14 - 15	14.49	1111±40	combined fit		24671±291
15 - 16	15.48	939±36	Υ(3S)		
16 - 18	16.91	1236±42	0 - 2.5	1.56	2687±143
18 - 20	18.98	896±34	2.5 - 5	3.58	3327±145
20 - 22	20.94	554±28	5 - 7.5	6.20	2171±101
22 - 25	23.30	447±25	7.5 - 10	8.57	1691±81
25 - 30	27.03	389±23	10 - 13	11.32	1394±63
30 - 50	35.97	276±21	13 - 16	14.31	893±45
			16 - 18	16.95	370±28
sum		77845±431	18 - 22	19.72	413±28
combined fit		78899±459	22 - 38	26.52	362±27
			sum		12308±258
			combined fit		13328±258

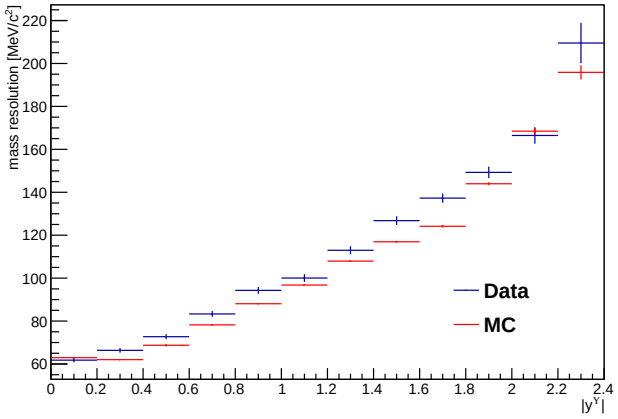

(a)

Figure 3.13.: The $\Upsilon(1S)$ mass resolution as a function of rapidity for Data and MC.

3.8 Acceptance

The Muon System covers the pseudorapidity range $|\eta| < 2.5$ with Drift Tube (DT) and Cathode Strip Chamber (CSC) detectors. In addition Resistive Plate Capacitor (RPC) detectors, that enhance triggering capability, are installed in the range $|\eta| < 2.1$. Because of ionization energy losses muons with transverse momentum $p_T \lesssim 3$ GeV in the central pseudorapidity region do not reach the Muon System.

The calculation of the acceptance of the CMS detector for $\Upsilon \to \mu^+\mu^-$ is a product of the theoretical acceptance which accounts for how much of the total cross section falls within the kinematic phase space which the detector is sensitive to, and the track acceptance for each track, accounting for the probability that each muon leaves a track which is detectable by the tracker system. Both components are measured in simulation, and parametrized as a function of the p_T and y of the Υ.

We define the acceptance by the following ratio:

$$\mathcal{A}\left(p_T^{\Upsilon}, y^{\Upsilon}\right) = \frac{N^{\text{reco}}\left(p_T^{\Upsilon}, y^{\Upsilon} \middle| \text{SiTRK track pair satisfies Eq. (3.1)}\right)}{N^{\text{gen}}\left(p'^{\Upsilon}_T, y'^{\Upsilon}\right)}, \tag{3.3}$$

where p'^{Υ}_T, y'^{Υ} and p_T^{Υ}, y^{Υ} are the generated and reconstructed values respectively. N^{gen} is the total number of generated Upsilons in a $(p'^{\Upsilon}_T, y'^{\Upsilon})$ bin, while N^{reco} is the number of Upsilons reconstructed with SiTRK tracks satisfying Eq. (3.1) in the corresponding $(p_T^{\Upsilon}, y^{\Upsilon})$ bin. In addition the numerator requires the two tracks to be reconstructed with opposite charge and within the Υ mass fit window of $7 - 14$ GeV/c^2.

The acceptance is measured using a simple Υ production Monte Carlo, forcing the decay to two muons with specific polarization using the EvtGen [47] package, including the effects of final state radiation (FSR). There are no particles in the event besides the Υ, its daughter muons and final state radiation. This sample is then fully simulated and reconstructed with the most recent version of the CMS detector simulation software to assess the effects of multiple scattering and finite resolution of

the detector. The acceptance is binned in reconstructed p_T and y of the Υ used in event-by-event yield corrections.

The two dimensional map of Υ(1S) acceptance for the unpolarized scenario is found in Fig. 3.14(a). There are no accepted events beyond $|y| = 2.4$. Near $p_T = 5$ GeV/c the acceptance is minimized chiefly as a result of the trailing μ failing the p_T cut. Average values of the acceptance are given in Table 3.3,Table 3.4 and Table 3.5.

The unknown polarization of the Υ strongly influences the muon angular distributions and is predicted to change as a function of p_T^{Υ}. In order to account for this, the acceptance is taken from simulation with five separate assumptions for the polarization: unpolarized, and polarized longitudinally and transversely with respect to two different reference frames. The first is the helicity frame, defined by the direction of the Upsilon boost direction in the Upsilon rest frame. The second, the Collins-Soper frame [48] is an approximation to the frame connecting the incoming partons in the collision, defined by the bisection of the incoming hadron directions in the Upsilon rest frame. The average polarization of any $J^{PC} = 1^{--}$ quarkonium can be determined by measuring its dilepton decay distribution, which has the general observable form [49]

$$w(\cos\vartheta, \varphi \mid \vec{\lambda}) = \frac{3/(4\pi)}{(3+\lambda_\vartheta)} \left(1 + \lambda_\vartheta \cos^2\vartheta + \lambda_\varphi \sin^2\vartheta \cos 2\varphi + \lambda_{\vartheta\varphi} \sin 2\vartheta \cos\varphi\right), \quad (3.4)$$

where ϑ and φ are the polar and azimuthal angles of the positive lepton in the quarkonium rest frame with respect to, respectively, a suitably defined polarization axis z and the plane containing the momenta of the colliding beams and of the quarkonium. For fully longitudinally(transversely) polarization scenarios, we set λ_ϑ to be -1(+1) and λ_φ and $\lambda_{\vartheta\varphi}$ to be 0. The Υ(1S) acceptance maps for these polarization scenarios are shown in Fig. 3.15. Comparisons as a function of p_T^{Υ} are shown in Fig. 3.16. They are obtained from a sample of 40 million generated unpolarized $\Upsilon(1S)$. To produce the polarized maps, each event is assigned a weight based on its muon decay

angle. The validity of this procedure was verified using smaller samples decayed in EvtGen with polarization included.

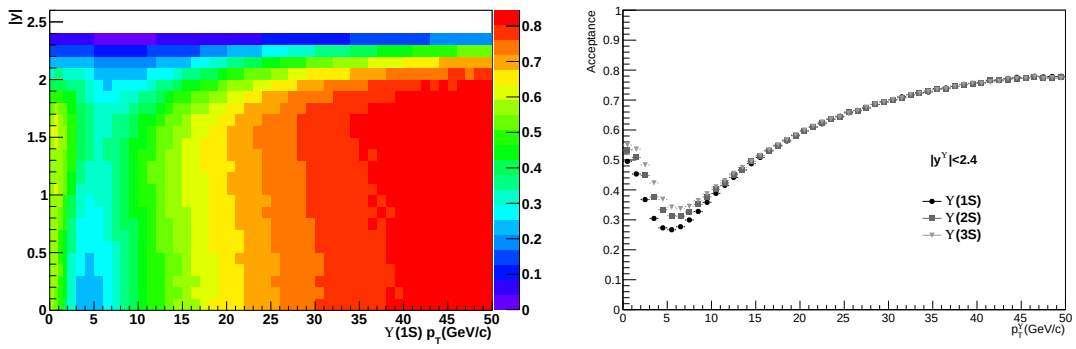

(a) (b)

Figure 3.14.: (a) Unpolarized $\Upsilon(1S)$ acceptance as a function of p_{T} and y; (b) The unpolarized Upsilon acceptance integrated over rapidity as a function of p_{T}.

Migration from bin to bin from differences in generated and reconstructed quantities affects the value of acceptance obtained. Differences in bias and resolution between the simulation used to calculate acceptance and data are treated as a systematic uncertainty.

Table 3.3: $\Upsilon(1S)$ unpolarized acceptance in bins of p_T^{Υ} for $|y^{\Upsilon}| < 2.4$.

p_T (GeV/c)	A^{Υ}				
	UNPOL	HX T	HX L	CS T	CS L
$\Upsilon(1S)$					
0 - 0.5	0.493 ± 0.001	0.414 ± 0.001	0.651 ± 0.001	0.412 ± 0.001	0.656 ± 0.001
0.5 - 1.0	0.500 ± 0.001	0.421 ± 0.001	0.658 ± 0.001	0.416 ± 0.001	0.669 ± 0.001
1.0 - 1.5	0.471 ± 0.001	0.397 ± 0.001	0.619 ± 0.001	0.389 ± 0.001	0.635 ± 0.001
1.5 - 2.0	0.436 ± 0.001	0.367 ± 0.001	0.574 ± 0.001	0.358 ± 0.001	0.592 ± 0.001
2.0 - 3.0	0.367 ± 0.001	0.306 ± 0.000	0.491 ± 0.001	0.301 ± 0.000	0.500 ± 0.001
3.0 - 4.0	0.303 ± 0.000	0.252 ± 0.000	0.406 ± 0.001	0.250 ± 0.000	0.408 ± 0.001
4.0 - 5.0	0.274 ± 0.000	0.229 ± 0.000	0.365 ± 0.001	0.230 ± 0.000	0.363 ± 0.001
5.0 - 6.0	0.266 ± 0.000	0.223 ± 0.000	0.352 ± 0.001	0.228 ± 0.000	0.341 ± 0.001
6.0 - 7.0	0.276 ± 0.000	0.233 ± 0.000	0.363 ± 0.001	0.244 ± 0.000	0.340 ± 0.001
7.0 - 8.0	0.302 ± 0.000	0.257 ± 0.000	0.392 ± 0.001	0.277 ± 0.000	0.352 ± 0.001
8.0 - 9.0	0.329 ± 0.000	0.282 ± 0.000	0.424 ± 0.001	0.312 ± 0.000	0.363 ± 0.001
9.0 - 10.0	0.359 ± 0.001	0.308 ± 0.000	0.460 ± 0.001	0.349 ± 0.001	0.379 ± 0.001
10.0 - 11.0	0.388 ± 0.001	0.335 ± 0.000	0.494 ± 0.001	0.384 ± 0.001	0.396 ± 0.001
11.0 - 12.0	0.414 ± 0.001	0.359 ± 0.000	0.526 ± 0.001	0.415 ± 0.001	0.412 ± 0.001
12.0 - 13.0	0.440 ± 0.001	0.382 ± 0.001	0.556 ± 0.001	0.446 ± 0.001	0.429 ± 0.001
13.0 - 14.0	0.466 ± 0.001	0.407 ± 0.001	0.586 ± 0.001	0.476 ± 0.001	0.448 ± 0.001
14.0 - 15.0	0.487 ± 0.001	0.425 ± 0.001	0.610 ± 0.001	0.499 ± 0.001	0.462 ± 0.001
15.0 - 16.0	0.508 ± 0.001	0.446 ± 0.001	0.633 ± 0.001	0.523 ± 0.001	0.478 ± 0.001
16.0 - 18.0	0.538 ± 0.000	0.474 ± 0.000	0.666 ± 0.000	0.556 ± 0.000	0.502 ± 0.000
18.0 - 20.0	0.572 ± 0.000	0.508 ± 0.000	0.702 ± 0.000	0.594 ± 0.000	0.531 ± 0.000
20.0 - 22.0	0.602 ± 0.000	0.537 ± 0.000	0.733 ± 0.000	0.625 ± 0.000	0.557 ± 0.000
22.0 - 25.0	0.634 ± 0.000	0.569 ± 0.000	0.764 ± 0.000	0.659 ± 0.000	0.586 ± 0.000
25.0 - 30.0	0.676 ± 0.000	0.613 ± 0.000	0.802 ± 0.000	0.703 ± 0.000	0.625 ± 0.000
30.0 - 50.0	0.695 ± 0.000	0.644 ± 0.000	0.796 ± 0.000	0.716 ± 0.000	0.652 ± 0.000

Table 3.4: $\Upsilon(2S)$ unpolarized acceptance in bins of p_T^{Υ} for $|y^{\Upsilon}| < 2.4$.

p_T (GeV/c)	A^{Υ}				
	UNPOL	HX T	HX L	CS T	CS L
$\Upsilon(2S)$					
0 - 1.0	0.534 ± 0.001	0.456 ± 0.001	0.689 ± 0.001	0.452 ± 0.001	0.696 ± 0.001
1.0 - 2.5	0.495 ± 0.001	0.424 ± 0.001	0.638 ± 0.001	0.413 ± 0.001	0.659 ± 0.001
2.5 - 4.0	0.394 ± 0.001	0.334 ± 0.001	0.514 ± 0.001	0.327 ± 0.001	0.528 ± 0.001
4.0 - 5.5	0.328 ± 0.001	0.277 ± 0.001	0.428 ± 0.001	0.277 ± 0.001	0.430 ± 0.001
5.5 - 7.0	0.312 ± 0.001	0.266 ± 0.001	0.404 ± 0.001	0.274 ± 0.001	0.389 ± 0.001
7.0 - 8.5	0.332 ± 0.001	0.285 ± 0.001	0.426 ± 0.001	0.306 ± 0.001	0.385 ± 0.001
8.5 - 10.0	0.370 ± 0.001	0.320 ± 0.001	0.469 ± 0.001	0.355 ± 0.001	0.400 ± 0.001
10.0 - 11.5	0.407 ± 0.001	0.354 ± 0.001	0.513 ± 0.001	0.401 ± 0.001	0.418 ± 0.001
11.5 - 13.0	0.444 ± 0.001	0.388 ± 0.001	0.555 ± 0.001	0.445 ± 0.001	0.440 ± 0.001
13.0 - 14.5	0.476 ± 0.001	0.417 ± 0.001	0.593 ± 0.001	0.483 ± 0.001	0.460 ± 0.001
14.5 - 16.0	0.509 ± 0.001	0.448 ± 0.001	0.630 ± 0.001	0.521 ± 0.001	0.486 ± 0.001
16.0 - 18.0	0.540 ± 0.001	0.478 ± 0.001	0.664 ± 0.001	0.555 ± 0.001	0.509 ± 0.001
18.0 - 19.5	0.569 ± 0.001	0.506 ± 0.001	0.695 ± 0.001	0.587 ± 0.001	0.532 ± 0.001
19.5 - 22.0	0.599 ± 0.001	0.536 ± 0.001	0.726 ± 0.001	0.620 ± 0.001	0.558 ± 0.001
22.0 - 26.0	0.641 ± 0.001	0.578 ± 0.001	0.768 ± 0.001	0.664 ± 0.001	0.596 ± 0.001
26.0 - 42.0	0.722 ± 0.000	0.664 ± 0.000	0.838 ± 0.000	0.746 ± 0.000	0.675 ± 0.000

Table 3.5: $\Upsilon(3S)$ unpolarized acceptance in bins of p_T^{Υ} for $|y^{\Upsilon}| < 2.4$.

p_T (GeV/c)	A^{Υ}				
	UNPOL	HX T	HX L	CS T	CS L
$\Upsilon(3S)$					
0 - 2.5	0.534 ± 0.001	0.460 ± 0.001	0.681 ± 0.001	0.452 ± 0.001	0.697 ± 0.001
2.5 - 5.0	0.411 ± 0.001	0.353 ± 0.001	0.527 ± 0.001	0.344 ± 0.001	0.544 ± 0.001
5.0 - 7.5	0.340 ± 0.001	0.292 ± 0.001	0.436 ± 0.001	0.298 ± 0.001	0.424 ± 0.001
7.5 - 10.0	0.370 ± 0.001	0.321 ± 0.001	0.467 ± 0.001	0.348 ± 0.001	0.413 ± 0.001
10.0 - 13.0	0.432 ± 0.001	0.378 ± 0.001	0.540 ± 0.001	0.428 ± 0.001	0.440 ± 0.001
13.0 - 16.0	0.495 ± 0.001	0.437 ± 0.001	0.611 ± 0.001	0.503 ± 0.001	0.480 ± 0.001
16.0 - 18.0	0.542 ± 0.001	0.481 ± 0.001	0.663 ± 0.001	0.556 ± 0.001	0.513 ± 0.001
18.0 - 22.0	0.591 ± 0.001	0.529 ± 0.001	0.715 ± 0.001	0.609 ± 0.001	0.554 ± 0.001
22.0 - 38.0	0.692 ± 0.000	0.633 ± 0.000	0.811 ± 0.000	0.716 ± 0.000	0.646 ± 0.000

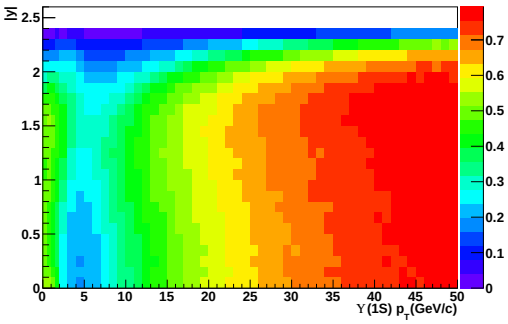

(a) $\Upsilon(1S)$ acceptance for transverse polarization in the helicity frame as a function of p_T^{Υ} and y^{Υ}

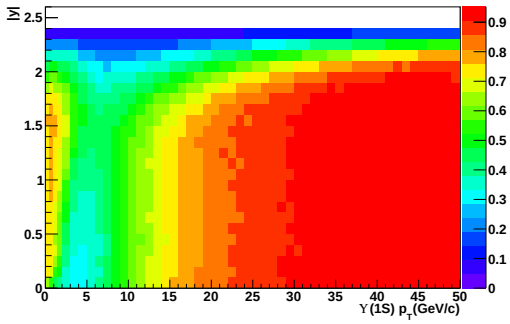

(b) $\Upsilon(1S)$ acceptance for longitudinal polarization in the helicity frame as a function of p_T^{Υ} and y^{Υ}

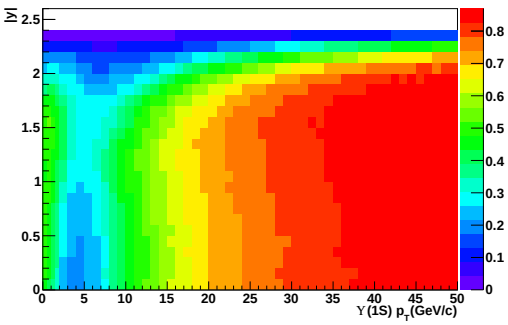

(c) $\Upsilon(1S)$ acceptance for transverse polarization in the Collins-Soper frame as a function of p_T^{Υ} and y^{Υ}

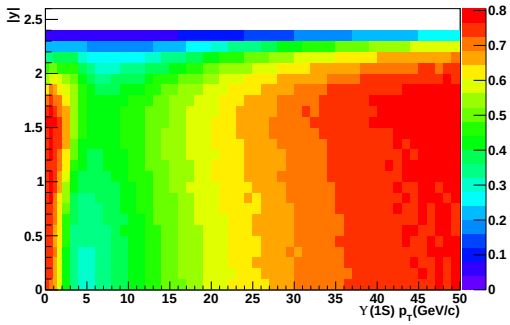

(d) $\Upsilon(1S)$ acceptance for longitudinal polarization in the Collins-Soper frame as a function of p_T^{Υ} and y^{Υ}

Figure 3.15.: Acceptance of Υ(1S) for the four polarized scenarios.

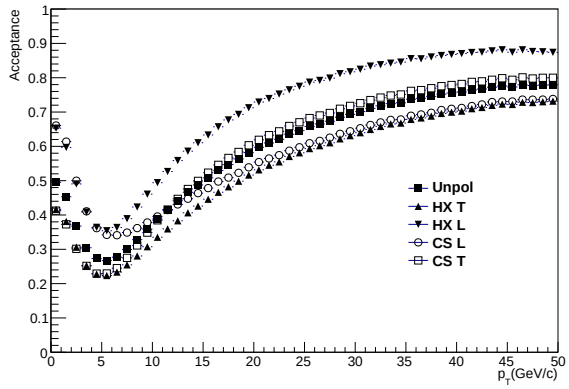

Figure 3.16.: Acceptance of Υ(1S) for the unpolarized and four polarized scenarios as a function of p_{T}.

3.9 Efficiency

We factor the total muon efficiency into the following three conditional terms

$$\varepsilon(\text{total}) = \varepsilon(\text{trig}|\text{id}) \times \varepsilon(\text{id}|\text{track}) \times \varepsilon(\text{track}|\text{accepted}) \equiv \varepsilon_{\text{trig}} \times \varepsilon_{\text{id}} \times \varepsilon_{\text{track}} \,. \quad (3.5)$$

- $\varepsilon_{\text{track}}$ - is the tracking efficiency, i.e. the efficiency that the accepted tracker track of a muon from a Υ(nS) decay is found in a pp collision event at 7 TeV. It is determined with the track embedding technique, described in Sec. 3.9.1 .
- ε_{id} - is the muon identification efficiency, i.e. the efficiency that the reconstructed tracker track of the muon is identified as a muon with the offline selection quality cuts and measured with the Tag and Probe method, Sec. 3.9.3 .
- $\varepsilon_{\text{trig}}$ - is the trigger efficiency, i.e. the efficiency that an identified muon is matched to a trigger object, also measured with the Tag and Probe method, Sec. 3.9.4 .

The methods used to obtain each efficiency term are now described.

3.9.1 Track Embedding

The absolute track reconstruction efficiency in *pp* collisions is difficult to precisely quantify using data because of the lack of a pure, high-statistics sample of tracks with known kinematic properties that is free from selection or trigger biases. Nevertheless, by factoring out the single track acceptance, which is a geometric quantity calculable using the material model for the detector in Monte Carlo, the factors that contribute to tracking inefficiency are expected to be pattern recognition failures in the tracking algorithms. Such failures can result when hits associated with a track are either lost, or when hits not associated with track are incorrectly included in its trajectory fit. Both effects are expected to be driven by the tracker occupancy in the vicinity of the track in question, for which the accuracy of a simulation can be difficult to

quantify or defend. We provide an estimate of the absolute track reconstruction efficiency, with respect to which relative track quality and muon ID efficiencies are defined, by measuring the fraction of simulated tracks that fail to be reconstructed after superimposing hits from pp collisions recorded at $\sqrt{s} = 7$ TeV.

The track embedding procedure used here is described in Ref. [50], and follows closely the approach used by the CDF experiment. A sample of pp collision events is analyzed and the position of the primary vertex in each event is determined. Simulated muons with p_T ranging from 0.5 to 500 GeV/c and with pseudo-rapidity in the range $|\eta| < 3$ were generated with initial positions corresponding to the primary vertices reconstructed in the data. These simulated muons were processed using the Monte Carlo detector simulation and event reconstruction procedure and were classified as being within the detector acceptance if a reconstructed track was found that had at least 75% of its hits originating from the generated muon. The pixel and strip detector hits from the pp collision were then merged with the simulated muon hits and the event reconstruction was repeated. The tracking inefficiency is calculated by dividing the fraction of embedded tracks that fail to be reconstructed after superimposing hits from pp collision events. The efficiency map obtained in this way is shown in Table 3.6.

Table 3.6: Track reconstruction efficiencies as a function of p_T (GeV/c) and η for muons embedded into 7 TeV data.

p_T	η						
	(-2.4, -2.1)	(-2.1, -1.2)	(-1.2, -0.8)	(-0.8, 0.8)	(0.8, 1.2)	(1.2, 2.1)	(2.1, 2.4)
50	.9990±.0010	.9994±.0005	1.0±.0009	.9989±.0005	1.0±.0010	.9993±.0005	1.0±.0012
20	.9989±.0011	.9987±.0007	.9993±.0007	.9977±.0007	.9985±.0011	.9984±.0007	.9990±.0010
10	.9990±.0010	.9980±.0008	.9978±.0013	.9971±.0007	.9992±.0008	.9993±.0005	1.0±.0012
5	.9981±.0013	.9987±.0007	1.0±.0009	.9981±.0006	.9992±.0008	.9970±.0010	1.0±.0012
2	1.000 ±.0016	.9982±.0009	.9970±.0017	.9967±.0009	.9960±.0020	.9978±.0010	1.0±.0015

By applying this procedure, we find that the pixel detector and silicon tracker occupancies observed in the data recorded so far result in a loss of track reconstruc-

tion efficiency that is less than 0.5% for muons with $p_T > 1$ GeV/c and $|\eta| < 2.4$. However, this result is not free from various assumptions. Due to the fact that the detector alignment used to reconstruct pp collision events differs from the nominal alignment used in the simulation, hits from charged particles in the pp event may fail to be associated with reconstructed tracks and remain, in principle, to be misassociated with the embedded track. Likewise, hits on the embedded track are less likely to be misassociated with other tracks when these are not efficiently identified in the misaligned geometry. These effects have been evaluated by studying track embedding in Monte Carlo events and are expected to account for an additional loss of tracking efficiency of at most 0.4%. What remains to be demonstrated is that the detector material model, on which the accurate calculation of track acceptance relies, is consistent with information from pp collisions. We have verified that the distribution of hit residuals and cluster widths is similar in data and Monte Carlo and will compare the distributions of conversion radius, to search for inconsistencies in the number of radiation lengths of material in the detector model. The number of nuclear interaction lengths can be compared by examining the distribution of the radius of the last hit on a track, and the distribution of secondary vertices found outside the beam pipe, as these are indicators of nuclear interactions of hadrons with detector material. Finally, the efficiency with which track segments reconstructed in the pixel detector are associated with tracks found in the silicon tracker will be compared between data and Monte Carlo. Although the purity of these track samples is questionable, particularly at high p_T, the shapes of the normalized distributions as a function of η will provide an important consistency check.

3.9.2 Tag and probe method

"Tag and Probe" (T&P) is a data driven method used in this analysis to determine the track quality, muon trigger and muon identification efficiencies. It utilizes well known dimuon decays, for example $J/\psi \to \mu\mu$, to provide a sample of probe

objects. A well-identified muon called a Tag is combined with a second object in the event called a Probe and the invariant mass is computed. The Tag-Probe pairs are divided into two samples based on whether the Probe satisfies the criteria for the efficiency being measured. The two Tag-Probe mass distributions of each sample contain a J/ψ peak, the area of which corresponds to the number of probes from the decay, that satisfy and fail to satisfy the criteria imposed, respectively. The efficiency parameter is extracted from a simultaneous unbinned maximum-likelihood fit to both mass distributions.

To obtain a precise determination of the efficiencies via the T&P method, the J/ψ resonance is utilized, as it provides a larger yield and, furthermore, a statistically independent sample [51]. The upsilon resonance could not be used directly for a reliable T&P determination of the efficiencies, given the absence of a suitable trigger dataset: the dedicated `muon+track` trigger paths collect events on a mass window around the J/ψ, while single muon paths such as `HLT_Mu3` have been prescaled for most part of the data taking period.

For avoiding trigger biases imposed on the probe sample, the tag is required to satisfy the trigger requirements used to collect the data sample. In particular the tag muon must have fired the MuXTrackY trigger path which is an OR of the trigger paths HLT_Mu0_Track0_JPsi, HLT_Mu3_Track0_JPsi, HLT_Mu5_Track0_JPsi, HLT_Mu3_Track3_JPsi and HLT_Mu3_Track5_JPsi . In the first three trigger paths no p_{T} thresholds are imposed on the track, while in the last two the track is asked to have a transverse momentum higher than 3 GeV/c. All of these paths are set to collect events within the J/ψ mass window $[2.7, 3.5]$ GeV/c^2.

The following additional requirements have been used for the Tag muon:

- `Global` muon
- $|\Delta z| < 35$ cm and $|dxy| < 4$ cm, both parameters for the inner track

The data sample used for the determination of the muon identification and trigger efficiencies via the T&P method is that specified in Sec. 3.4, and corresponds to an

integrated luminosity of 35.8 ± 1.4 pb^{-1}. Those efficiencies measured with data go into the cross section measurement.

3.9.3 Muon identification efficiency

The *probes* for the muon indentifition efficiency measurement are tracks reconstructed in the silicon tracker, and the *passing probes* are matched muon candidates required to satisfy the muon identification and selection requirements defined in Sec. 3.6.

The single muon identification efficiencies as a function of p_{T}^{μ} for eight $|\eta^{\mu}|$ regions are shown in Fig. 3.17 and Table 3.7.

3.9.4 Trigger efficiency

The probes that satisfy the muon identification criteria are in turn the probes for the study of the trigger efficiency. The resulting trigger efficiencies for one leg (probe) of the path HLT_DoubleMu0 as a function of p_{T}^{μ} for nine $|\eta^{\mu}|$ regions are shown in Table 3.8. The resulting trigger efficiencies for one leg (probe) of the path HLT_DoubleMu0_Quarkonium_v1 as a function of p_{T}^{μ} for nine $|\eta^{\mu}|$ regions are shown in Table 3.9. The comparisons between the efficiencies of the two triggers measured with data and Monte Carlo J/Ψ samples are shown in Fig. 3.18

Differences between MC truth single and dimuon efficiencies and those measured with the T&P technique can arise from the kinematic distributions of the probes and from bin averaging. This is evaluated by comparing J/ψ MC T&P single muon and dimuon efficiencies to MC truth. In addition, effects arising from differences in the kinematic distributions between the Υ and the J/ψ decay muons are investigated by comparing the efficiencies for Υ MC truth to J/ψ MC truth. They are all considered in ρ factors, explained in Sec. 3.9.7. The data determined efficiencies are used to obtain the final results.

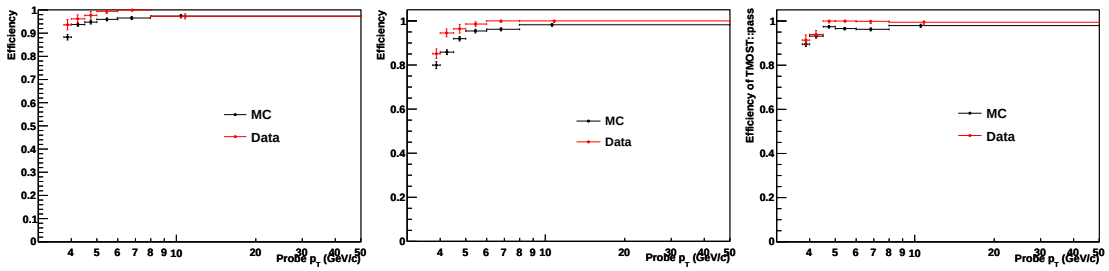

(a) $|\eta^{\mu}| < 0.2$

(b) $0.2 < |\eta^{\mu}| < 0.4$

(c) $0.4 < |\eta^{\mu}| < 0.6$

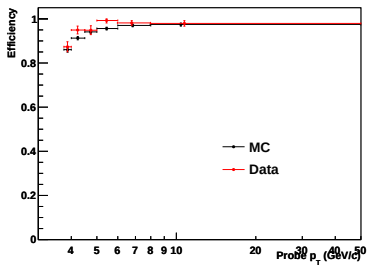

(d) $0.6 < |\eta^{\mu}| < 0.8$

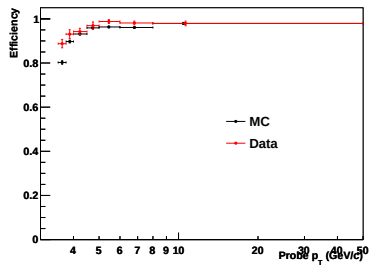

(e) $0.8 < |\eta^{\mu}| < 1.2$

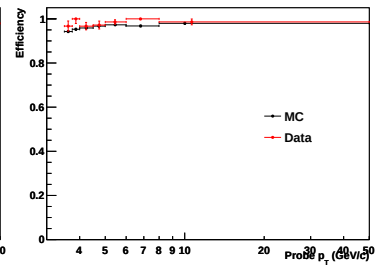

(f) $1.2 < |\eta^{\mu}| < 1.6$

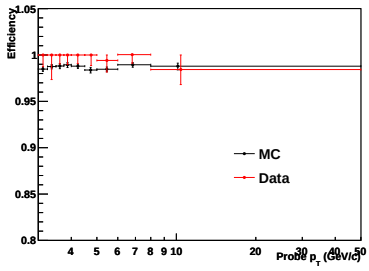

(g) $1.6 < |\eta^{\mu}| < 2.0$

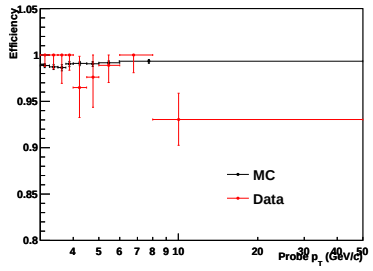

(h) $2.0 < |\eta^{\mu}| < 2.4$

Figure 3.17.: Single muon identification efficiencies as a function of p_{T}^{μ} for eight $|\eta^{\mu}|$ regions

.

Table 3.7: Single muon identification efficiencies from J/ψ T&P; the uncertainties are statistical only.

p_T^{μ}(GeV) $\backslash \eta^{\mu}$	(0.0, 0.2)	(0.2, 0.4)	(0.4, 0.6)	(0.6, 0.8)	(0.8, 1.2)	(1.2, 1.6)	(1.6, 2.0)	(2.0, 2.4)
(3.00- 3.25)							$1.000^{+0.000}_{-0.013}$	$1.000^{+0.000}_{-0.012}$
(3.25- 3.50)							$1.000^{+0.000}_{-0.026}$	$1.000^{+0.000}_{-0.015}$
(3.50- 3.75)					$0.888^{+0.019}_{-0.019}$	$0.967^{+0.023}_{-0.022}$	$1.000^{+0.000}_{-0.010}$	$1.000^{+0.000}_{-0.031}$
(3.75- 4.00)	$0.936^{+0.022}_{-0.022}$	$0.851^{+0.022}_{-0.021}$	$0.913^{+0.024}_{-0.023}$	$0.873^{+0.023}_{-0.022}$	$0.931^{+0.020}_{-0.019}$	$1.000^{+0.000}_{-0.021}$	$1.000^{+0.000}_{-0.010}$	$1.000^{+0.000}_{-0.016}$
(4.00- 4.50)	$0.962^{+0.017}_{-0.017}$	$0.945^{+0.018}_{-0.017}$	$0.939^{+0.018}_{-0.017}$	$0.949^{+0.018}_{-0.018}$	$0.942^{+0.015}_{-0.015}$	$0.967^{+0.017}_{-0.017}$	$1.000^{+0.000}_{-0.009}$	$0.964^{+0.034}_{-0.032}$
(4.50- 5.00)	$0.977^{+0.017}_{-0.017}$	$0.964^{+0.019}_{-0.019}$	$1.000^{+0.000}_{-0.008}$	$0.948^{+0.020}_{-0.020}$	$0.969^{+0.017}_{-0.016}$	$0.972^{+0.018}_{-0.018}$	$1.000^{+0.000}_{-0.011}$	$0.976^{+0.024}_{-0.033}$
(5.00- 6.00)	$0.994^{+0.006}_{-0.009}$	$0.986^{+0.010}_{-0.010}$	$1.000^{+0.000}_{-0.004}$	$0.992^{+0.008}_{-0.011}$	$0.988^{+0.009}_{-0.009}$	$0.986^{+0.010}_{-0.010}$	$0.994^{+0.006}_{-0.012}$	$0.989^{+0.011}_{-0.019}$
(6.00- 8.00)	$1.000^{+0.000}_{-0.004}$	$1.000^{+0.000}_{-0.006}$	$0.999^{+0.001}_{-0.010}$	$0.981^{+0.011}_{-0.010}$	$0.981^{+0.008}_{-0.008}$	$1.000^{+0.000}_{-0.004}$	$1.000^{+0.000}_{-0.009}$	$1.000^{+0.000}_{-0.019}$
(8.00-50.00)	$0.973^{+0.011}_{-0.011}$	$1.000^{+0.000}_{-0.007}$	$0.995^{+0.005}_{-0.012}$	$0.979^{+0.012}_{-0.012}$	$0.979^{+0.010}_{-0.010}$	$0.984^{+0.013}_{-0.013}$	$0.984^{+0.016}_{-0.016}$	$0.930^{+0.028}_{-0.028}$

Table 3.8: Single-leg HLT_DoubleMu0 muon trigger efficiencies from J/ψ T&P; the uncertainties are statistical only.

p_T^μ(GeV) \η^μ	(0.00, 0.20)	(0.20, 0.40)	(0.40, 0.60)	(0.60, 0.80)	(0.80, 1.20)	(1.20, 1.60)	(1.60, 2.00)	(2.00, 2.40)
(3.00- 3.25)							$0.876^{+0.010}_{-0.010}$	$0.881^{+0.011}_{-0.012}$
(3.25- 3.50)							$0.875^{+0.010}_{-0.010}$	$0.885^{+0.012}_{-0.012}$
(3.50- 3.75)					$0.326^{+0.012}_{-0.012}$	$0.901^{+0.008}_{-0.008}$	$0.906^{+0.009}_{-0.010}$	$0.884^{+0.013}_{-0.014}$
(3.75- 4.00)	$0.450^{+0.019}_{-0.019}$	$0.403^{+0.019}_{-0.019}$	$0.481^{+0.019}_{-0.019}$	$0.524^{+0.017}_{-0.018}$	$0.530^{+0.013}_{-0.013}$	$0.933^{+0.007}_{-0.008}$	$0.901^{+0.010}_{-0.011}$	$0.885^{+0.014}_{-0.014}$
(4.00- 4.50)	$0.687^{+0.013}_{-0.013}$	$0.584^{+0.015}_{-0.015}$	$0.680^{+0.014}_{-0.014}$	$0.708^{+0.012}_{-0.013}$	$0.743^{+0.009}_{-0.009}$	$0.949^{+0.005}_{-0.005}$	$0.907^{+0.008}_{-0.008}$	$0.906^{+0.010}_{-0.011}$
(4.50- 5.00)	$0.783^{+0.014}_{-0.014}$	$0.644^{+0.016}_{-0.017}$	$0.850^{+0.012}_{-0.013}$	$0.754^{+0.014}_{-0.015}$	$0.854^{+0.009}_{-0.009}$	$0.948^{+0.006}_{-0.006}$	$0.926^{+0.009}_{-0.009}$	$0.911^{+0.012}_{-0.013}$
(5.00- 6.00)	$0.905^{+0.009}_{-0.009}$	$0.760^{+0.013}_{-0.013}$	$0.945^{+0.007}_{-0.007}$	$0.827^{+0.011}_{-0.012}$	$0.910^{+0.006}_{-0.006}$	$0.967^{+0.005}_{-0.005}$	$0.925^{+0.007}_{-0.008}$	$0.928^{+0.010}_{-0.011}$
(6.00- 8.00)	$0.966^{+0.006}_{-0.006}$	$0.853^{+0.011}_{-0.012}$	$0.973^{+0.005}_{-0.006}$	$0.908^{+0.009}_{-0.009}$	$0.934^{+0.006}_{-0.006}$	$0.956^{+0.005}_{-0.006}$	$0.926^{+0.008}_{-0.008}$	$0.923^{+0.011}_{-0.012}$
(8.00-50.00)	$0.978^{+0.006}_{-0.007}$	$0.894^{+0.012}_{-0.013}$	$0.974^{+0.006}_{-0.007}$	$0.959^{+0.008}_{-0.009}$	$0.929^{+0.008}_{-0.008}$	$0.970^{+0.006}_{-0.007}$	$0.931^{+0.010}_{-0.011}$	$0.912^{+0.018}_{-0.020}$

Table 3.9: Single-leg HLT_DoubleMu0_Quarkonium_v1 muon trigger efficiencies from J/ψ T&P; the uncertainties are statistical only.

p_T^μ(GeV) \ η^μ	(0.00, 0.20)	(0.20, 0.40)	(0.40, 0.60)	(0.60, 0.80)	(0.80, 1.20)	(1.20, 1.60)	(1.60, 2.00)	(2.00, 2.40)
(3.00- 3.25)							$0.849^{+0.020}_{-0.021}$	$0.862^{+0.028}_{-0.030}$
(3.25- 3.50)							$0.877^{+0.022}_{-0.024}$	$0.842^{+0.028}_{-0.031}$
(3.50- 3.75)					$0.318^{+0.026}_{-0.025}$	$0.921^{+0.015}_{-0.017}$	$0.908^{+0.018}_{-0.020}$	$0.928^{+0.026}_{-0.029}$
(3.75- 4.00)	$0.420^{+0.035}_{-0.035}$	$0.481^{+0.036}_{-0.036}$	$0.470^{+0.037}_{-0.037}$	$0.538^{+0.036}_{-0.036}$	$0.570^{+0.027}_{-0.027}$	$0.939^{+0.014}_{-0.016}$	$0.932^{+0.017}_{-0.020}$	$0.923^{+0.026}_{-0.031}$
(4.00- 4.50)	$0.626^{+0.029}_{-0.030}$	$0.558^{+0.029}_{-0.030}$	$0.695^{+0.025}_{-0.026}$	$0.734^{+0.025}_{-0.026}$	$0.737^{+0.019}_{-0.020}$	$0.943^{+0.011}_{-0.012}$	$0.921^{+0.015}_{-0.017}$	$0.963^{+0.015}_{-0.018}$
(4.50- 5.00)	$0.818^{+0.022}_{-0.023}$	$0.655^{+0.029}_{-0.030}$	$0.865^{+0.020}_{-0.022}$	$0.766^{+0.024}_{-0.025}$	$0.883^{+0.014}_{-0.015}$	$0.948^{+0.010}_{-0.011}$	$0.905^{+0.013}_{-0.014}$	$0.931^{+0.016}_{-0.018}$
(5.00- 6.00)	$0.913^{+0.005}_{-0.005}$	$0.764^{+0.007}_{-0.008}$	$0.946^{+0.004}_{-0.004}$	$0.832^{+0.007}_{-0.007}$	$0.912^{+0.004}_{-0.004}$	$0.959^{+0.003}_{-0.003}$	$0.929^{+0.004}_{-0.005}$	$0.917^{+0.006}_{-0.007}$
(6.00- 8.00)	$0.969^{+0.003}_{-0.003}$	$0.865^{+0.006}_{-0.006}$	$0.976^{+0.003}_{-0.003}$	$0.914^{+0.005}_{-0.005}$	$0.936^{+0.003}_{-0.003}$	$0.965^{+0.003}_{-0.003}$	$0.932^{+0.004}_{-0.005}$	$0.932^{+0.006}_{-0.007}$
(8.00-50.00)	$0.972^{+0.004}_{-0.004}$	$0.892^{+0.007}_{-0.007}$	$0.981^{+0.003}_{-0.003}$	$0.963^{+0.004}_{-0.005}$	$0.943^{+0.004}_{-0.004}$	$0.963^{+0.004}_{-0.004}$	$0.922^{+0.006}_{-0.007}$	$0.941^{+0.010}_{-0.011}$

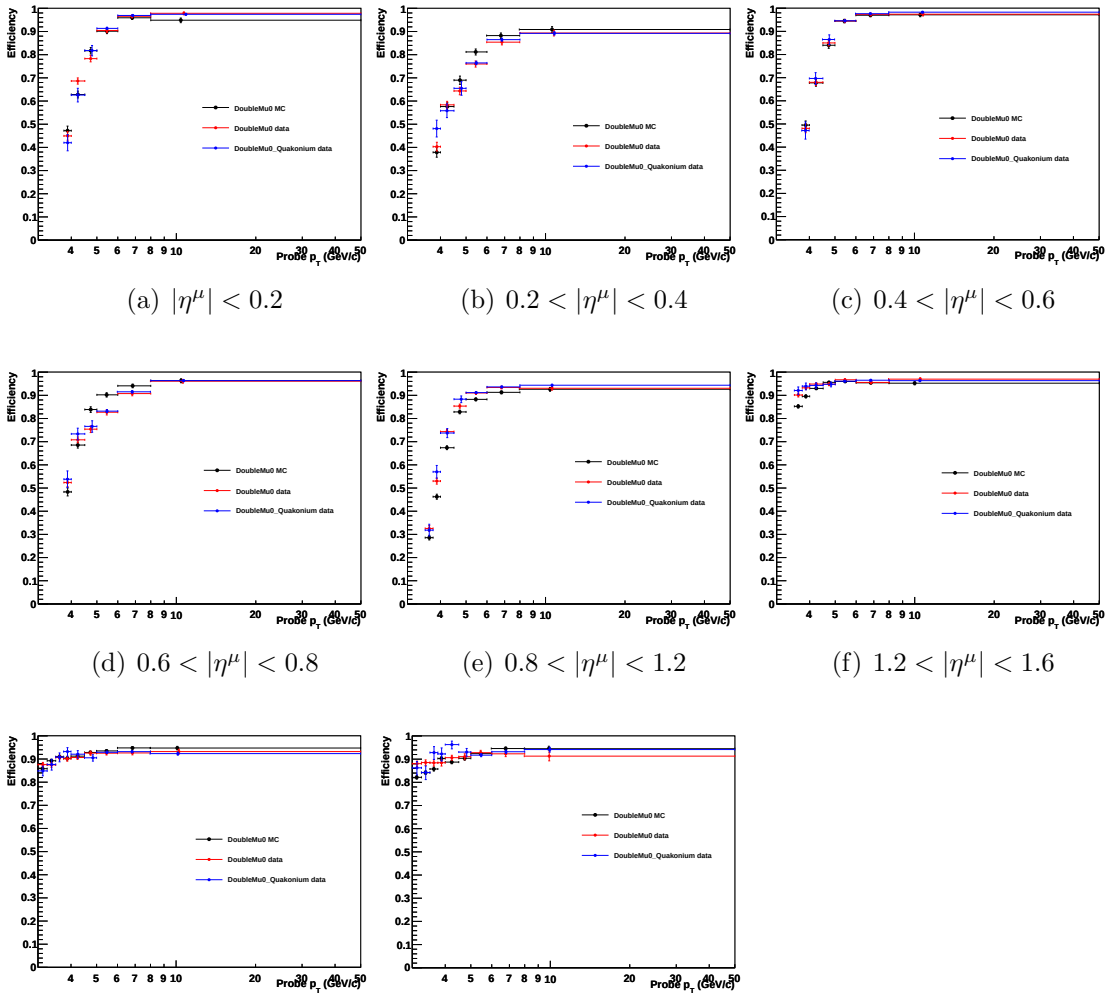

(a) $|\eta^{\mu}| < 0.2$ (b) $0.2 < |\eta^{\mu}| < 0.4$ (c) $0.4 < |\eta^{\mu}| < 0.6$

(d) $0.6 < |\eta^{\mu}| < 0.8$ (e) $0.8 < |\eta^{\mu}| < 1.2$ (f) $1.2 < |\eta^{\mu}| < 1.6$

(g) $1.6 < |\eta^{\mu}| < 2.0$ (h) $2.0 < |\eta^{\mu}| < 2.4$

Figure 3.18.: Single-leg muon trigger efficiencies as a function of p_{T}^{μ} for nine $|\eta^{\mu}|$ regions, from J/ψ Data T&P, for HLT_DoubleMu0 (red), HLT_DoubleMu0_Quarkonium_v1 (blue) and Monte Carlo (black).

Trigger efficiency bias

For avoiding trigger biases imposed on the probe sample, the tag is required to satisfy the muon leg of the MuXTrackY trigger. However, the way it is set up may still induce small biases in the L3 muon efficiency due to the requirements on the second leg of the MuXTrackY trigger which is allowed to belong to the probe sample. To estimate the bias, we made comparisons of the L3/L2 efficiency that were obtained

by requiring that the tag muon passes (i) the MuXTrackY trigger (in which case the second trigger leg may bias the probe sample), or (ii) the Mu5L2Mu0 trigger (which requires the detection of a muon at the L3 level, seeded by a L2 muon with p_{T} higher than 5 GeV/c, and which therefore does not bias the probe sample for the measurement of the L3 efficiency). The probes are required to pass the L2DoubleMu0 trigger, which requires the detection of at least two muons at the L2 level and each of them are seeded by a L2 muon without any p_{T} cut. The resulting L3/L2 efficiencies are shown in Fig. 3.19 and the differences are shown in Fig. 3.20. The differences in most bins are not significant within the available precision.

3.9.5 Track quality efficiency

The efficiency of the track quality criteria, see Sec. 3.6.2,

- number of valid silicon hits > 11, with at least one hit in the Pixel Tracker
- normalized χ^2 of the global track fit < 5

is determined via the T&P method. The track quality efficiency is nearly uniform and has an average value of 0.9866 ± 0.0005.

3.9.6 Efficiency of additional selection

The efficiency of the vertex χ^2 probability cut is determined using the J/ψ resonance. A high purity sample of J/ψ dimuons is identified by requiring that each muon satisfies the selection criteria in Sec. 3.6.2. A fit to the dimuon invariant mass distribution is performed with and without the vertex probability criterion imposed. The efficiency is found to be $(99.2 \pm 0.2)\%$. A possible difference between the efficiency of the vertex χ^2 probability cut for the J/ψ and Υ is evaluated by applying the same technique to large MC signal samples of each resonance. No significant difference in the efficiencies is found.

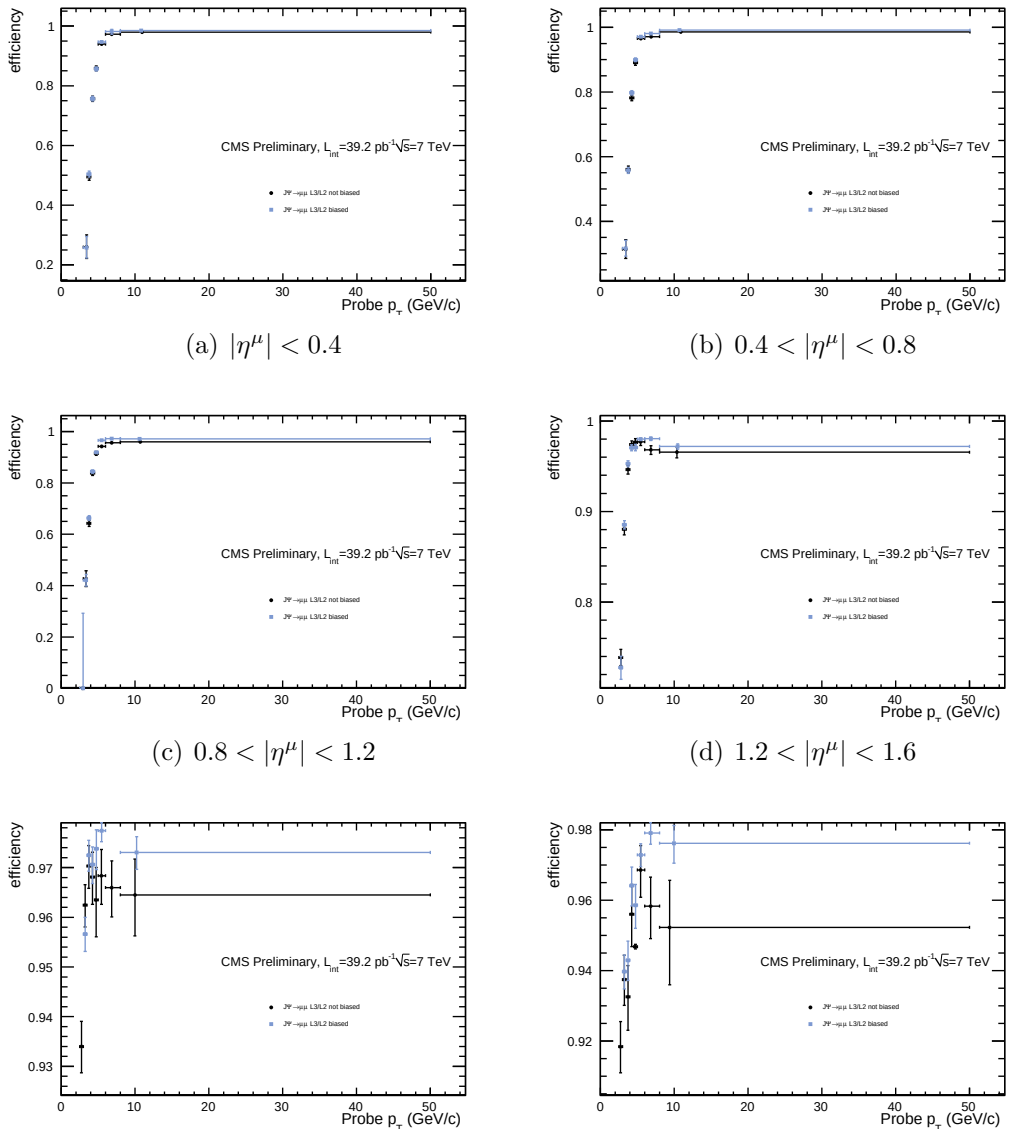

(a) $|\eta^{\mu}| < 0.4$ (b) $0.4 < |\eta^{\mu}| < 0.8$

(c) $0.8 < |\eta^{\mu}| < 1.2$ (d) $1.2 < |\eta^{\mu}| < 1.6$

(e) $1.6 < |\eta^{\mu}| < 2.0$ (f) $2.0 < |\eta^{\mu}| < 2.4$

Figure 3.19.: L3/L2 single muon trigger efficiencies as a function of p_{T}^{μ} for six $|\eta^{\mu}|$ regions requiring tag muons pass MuXTrackY trigger(closed cirlcles) or the Mu5L2Mu0 trigger (triangles).

The sanity-type selection criteria requiring the muons to be consistent with emanating from the same primary vertex are set intentionally loose so as not to introduce any signal inefficiency. This has been confirmed in data and simulation.

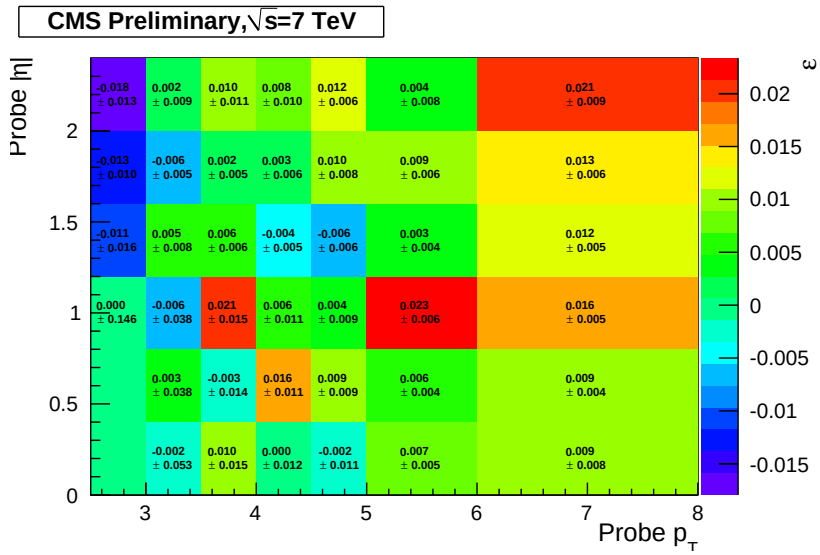

Figure 3.20.: Difference between the L3/L2 single muon trigger efficiencies requiring tag muons pass MuXTrackY trigger and the Mu5L2Mu0 trigger.

3.9.7 Computation of the total correction factor

A ρ factor is needed as a correction to the factorization hypothesis and accounts for possible bias introduced by the Tag and Probe efficiency measurement with J/Ψ resonance. The details can be found in Sec. B.

We define the ρ factor as

$$\epsilon(\Upsilon) = \epsilon(\mu^{+}_{J/\Psi}) \cdot \epsilon(\mu^{-}_{J/\Psi}) \cdot \rho, \tag{3.6}$$

The ρ factor is measured entirely from Monte Carlo. It is defined as the efficiency for a Υ to pass trigger and muon id selection divided by the product of the same efficiencies for single muons, where the Υ efficiency is taken from Monte Carlo truth matching and the single muons efficiencies are from Tag and Probe utilizing the Monte Carlo J/Ψ samples. Fig. 3.21 shows the ρ factor as a function of p_{T} and rapidity for Υ.

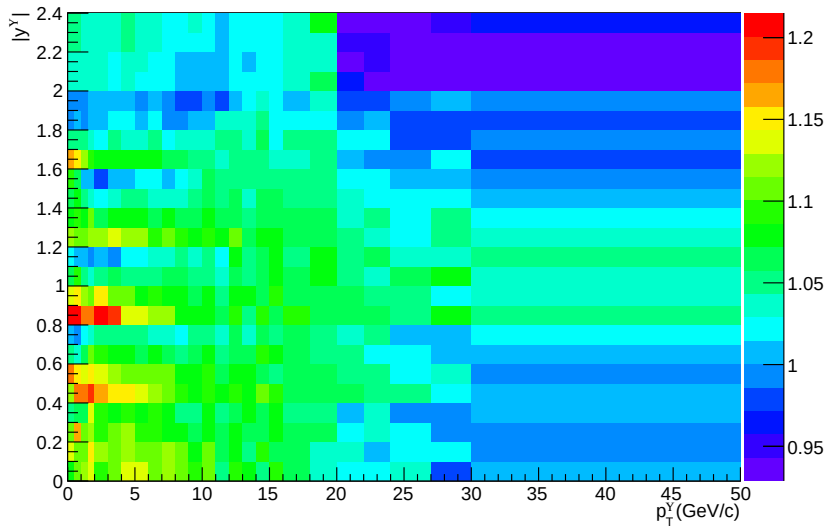

Figure 3.21.: ρ factor as a function of p_{T} and rapidity for Υ

3.10 Measurement of the inclusive differential cross section

The differential cross section is determined from the acceptance and efficiency corrected signal yield N^{fit}, obtained directly from the weighted fit,

$$\left.\frac{d\sigma\left(pp \to \Upsilon(\mathrm{nS})\right)}{dp_T}\right|_{|y|<2.4} \mathcal{B}\left(\Upsilon(\mathrm{nS}) \to \mu^+\mu^-\right) = \frac{N^{\mathrm{fit}}_{\Upsilon(\mathrm{nS})}(p_T; \mathcal{A}, \varepsilon_{\mathrm{track}}, \varepsilon_{\mathrm{id}}, \varepsilon_{\mathrm{trig}})}{\mathcal{L} \cdot \Delta p_T}, \quad (3.7)$$

upon normalization by the integrated luminosity of the dataset, $\mathcal{L}$, and by the bin width Δp_T of the Υ transverse momentum.

Given the strong η and p_T dependence of the efficiency and acceptance of the muons from the Υ(nS) decays, we correct for the inefficiency on a candidate-by-candidate basis before performing the mass fit. An Υ candidate with p_T^{Υ} and rapidity y^{Υ} reconstructed from muons with $p_T^{\mu_{1,2}}$ and $\eta^{\mu_{1,2}}$ is corrected with a weight

$$w \equiv w_{\mathrm{acc}} \cdot w_{\mathrm{track}} \cdot w_{\mathrm{id}} \cdot w_{\mathrm{trigger}} \cdot w_{\rho} \quad (3.8)$$

given by the following factors:

- Acceptance: $w_{\text{acc}} = 1/\mathcal{A}(p_T^{\Upsilon}, y^{\Upsilon})$
- Tracking: $w_{\text{track}} = 1/\left[\varepsilon_{\text{track}}(p_T^{\mu_1}, \eta^{\mu_1}) \cdot \varepsilon_{\text{track}}(p_T^{\mu_2}, \eta^{\mu_2})\right]$
- Identification: $w_{\text{id}} = 1/\left[\varepsilon_{\text{id}}(p_T^{\mu_1}, \eta^{\mu_1}) \cdot \varepsilon_{\text{id}}(p_T^{\mu_2}, \eta^{\mu_2})\right]$
- Trigger: $w_{\text{trigger}} = 1/\left[\varepsilon_{\text{trig}}(p_T^{\mu_1}, \eta^{\mu_1}) \cdot \varepsilon_{\text{trig}}(p_T^{\mu_2}, \eta^{\mu_2})\right]$
- ρ factor: $w_{\rho} = 1/\rho(p_T^{\Upsilon}, y^{\Upsilon})$

The results obtained by fitting the Υ(nS) mass distribution sampled before and after applying candidate-by-candidate weighting are displayed in Fig. 3.22(a) and Fig. 3.22(b). The acceptance and efficiency corrected signal yields extracted from the fit in Fig. 3.22(b) constitute the input for the cross section determination, namely the numerator in Eqn. 3.7.

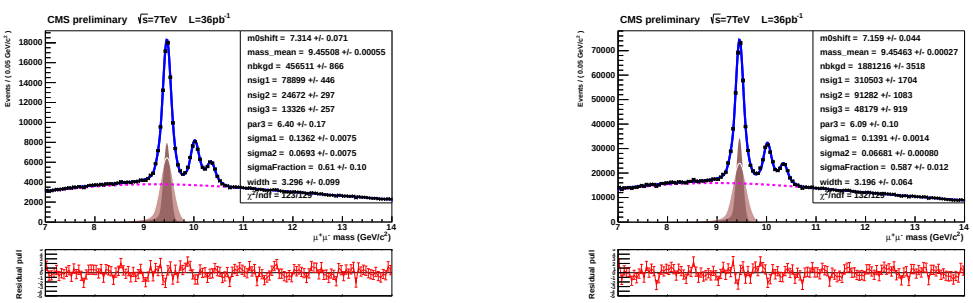

(a) Unweighted mass distribution.

(b) Mass spectrum after per event weighting.

Figure 3.22.: Fit of the Upsilon yield in the full p_{T} range.

The acceptance is a function of the dimuon mass, and has an average value that is about 10% larger for the Υ(3S) than for the Υ(1S). To account for this the fit is performed three times. The corrected yield for the Υ(1S)[Υ(2S), Υ(3S)] is obtained from a fit using the Υ(1S) [Υ(2S), Υ(3S)] acceptance.

To determine the Υ(nS) integrated cross section for $p_{\text{T}} < 50$ GeV/c $|y| < 2.4$ we employ the above procedure separately for each Upsilon resonance for each polarization scenario. We divide the data into several intervals of transverse momentum and

repeat the fits to obtain the Υ(nS) cross sections. The twenty-four p_{T} intervals used for the Υ(1S) differential cross section measurement are shown in Fig. 3.12. For the Υ(2S) and Υ(3S) the signal yields are lower and sixteen and nine p_{T} intervals are used, respectively. The results are summarized in Table 4.24, Table 4.25 and Table 4.26. We also divide the data into six ranges of rapidity $|y^{\Upsilon}|$: (0,0.4), (0.4,0.8), (0.8,1.2), (1.2,1.6), (1.6,2.0), (2.0,2.4) and repeat the fits to obtain the Υ(nS) differential cross section. These are reported in Table 4.27, Table 4.28, Table 4.29, Table 4.30, Table 4.31 and Table 4.31. The Υ(1S) p_{T}-integrated, rapidity differential cross section results are shown in Table 4.33. The ratios of Υ(nS) p_{T}-differential cross sections are reported in Table 4.34.

3.11 Systematic uncertainties

There are several sources of systematic uncertainty that contribute to the measured value of the Υ(nS) cross section. We now summarize sources of systematic uncertainty and the method of their determination.

The unknown polarization of the Υ strongly influences the muon angular distributions and is predicted to change as a function of $p_{\mathrm{T}}^{\Upsilon}$. In order to show the sensitivity of the result to the polarization and to allow for interpolation, we provide cross-section measurements for unpolarized (default), and for 25%, 50% and 100% longitudinal and transverse polarization with respect to two different reference frames. The measurement uses acceptance maps corresponding to different polarization scenarios. The values of cross sections obtained vary linearly by about 5%, 10%, and 20% assuming 25%, 50%, and 100% longitudinal and transverse polarization, as shown in Table 3.10. The cross-section measurement is also performed for $10 < p_{\mathrm{T}}^{\Upsilon} < 50\,\mathrm{GeV}/c$, $|y^{\Upsilon}| < 1.2$ corresponding to the $p_{\mathrm{T}}^{\Upsilon}$ and y^{Υ} range of Ref. [49] using the polarization measurements from Ref. [49] to compute the acceptance corrections.The three anisotropy parameters in Eqn. 3.4 in the center-of-mass helicity and Collins-Soper frames are varied coherently by $\pm 1\sigma$ and the largest positive and negative variations with re-

spect to the nominal (no polarization) case are taken as systematic uncertainties.The $\Upsilon(1S)$ acceptance as a function of p_T for these variations are shown in Fig. 3.23. The systematic uncertainties are listed in Table 4.46. They are found to be comparable to, or smaller than, the 25% variation for the $\Upsilon(1S)$ case, while they are between the 25% and 50% variations for $\Upsilon(2S)$ and $\Upsilon(3S)$. The acceptance is not used to determine the fiducial cross section therefore the systematic uncertainties arising from the acceptance do not apply to the fiducial results.

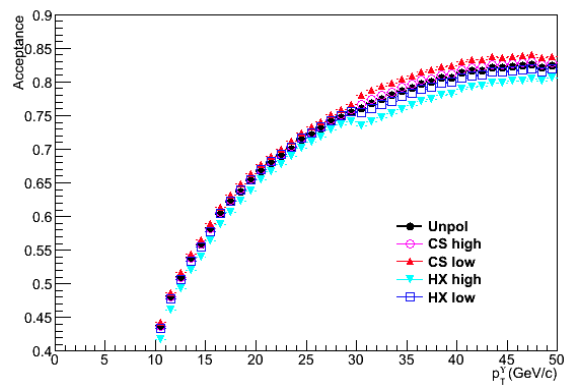

Figure 3.23.: Acceptance of $\Upsilon(1S)$ for the unpolarized and four polarized scenarios as a function of p_T by varying the three anisotropy parameters in Eqn. 3.4 coherently by $\pm 1\sigma$ in the center-of-mass helicity(HX) and Collins-Soper(CS) frames.

Table 3.10: The fractional change in percent to the central value of the cross section integrated over the rapidity range $|y^{\Upsilon}| < 2.4$, relative to the unpolarized value for four polarization scenarios in two frames: the helicity frame (HX) and Collins-Soper (CS) frame, each for L= 100% longitudinal, $\frac{1}{2}$L = 50% longitudinal, $\frac{1}{4}$L = 25% longitudinal, T= 100% transverse, $\frac{1}{2}$T= 50% transverse and $\frac{1}{4}$T= 25% transverse.

$|\mathbf{y^{\Upsilon}}| < \mathbf{2.4}$

	p_T	HXT	HXL	CST	CSL	HX$\frac{1}{2}$T	HX$\frac{1}{2}$L	CS$\frac{1}{2}$T	CS$\frac{1}{2}$L	HX$\frac{1}{4}$T	HX$\frac{1}{4}$L	CS$\frac{1}{4}$T	CS$\frac{1}{4}$L
$\Upsilon(1S)$	$0.0 - 50.0$	$+19$	-24	$+16$	-19	$+10$	-11	$+8$	-9	$+5$	-5	$+4$	-5
$\Upsilon(2S)$	$0.0 - 42.0$	$+14$	-24	$+13$	-20	$+5$	-12	$+6$	-10	$+3$	-7	$+2$	-6
$\Upsilon(3S)$	$0.0 - 38.0$	$+16$	-21	$+14$	-17	$+9$	-9	$+8$	-7	$+5$	-4	$+5$	-3

3.11.1 Statistical contributions

The statistical uncertainty on the acceptance and all of the efficiencies, and hence weights (Eqn. 3.8), involved in the determination of the cross section, Eqn. 3.7 , gives rise to a systematic uncertainty in the cross section measurement. To assess this uncertainty we vary the weights used in the mass fit coherently by $\pm 1\sigma$(stat.), the resultant magnitude of the variation in the cross section measurement is taken as a measure of the systematic uncertainty from this source.

3.11.2 Acceptance

Final state radiation is incorporated into the simulation using the PHOTOS algorithm. To estimate the systematic uncertainty associated with this procedure the acceptance is calculated using a subsample without FSR and the difference from the full sample is taken as the systematic uncertainty associated with FSR simulation. This subsample is obtained by removing all events produced by PHOTOS including a generated photon. This is necessarily an overestimate of the systematic uncertainty. Figure 3.24 shows the effect of removing FSR on the unpolarized acceptance and the generated photon spectrum. At low Upsilon p_T and mid-rapidity, the acceptance for Upsilons without FSR is as much as 5% higher.

The definition of acceptance used in this analysis requires that the muon daughters produce reconstructable tracks. The final kinematic cuts and the binning in Υp_T and y depend on the reconstructed values of these tracks. Uncertainties on the measurement of track parameters enter into the acceptance as a systematic uncertainty. The dominant parameter uncertainty is the measurement of the track transverse momentum. There are a number of effects that influence the track momentum scale that we treat together:

- Material budget
- Magnetic Field

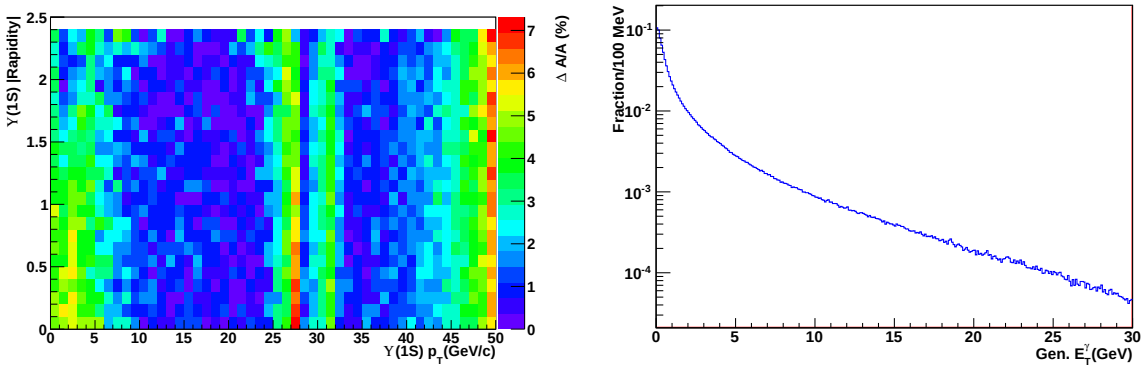

(a) $\Delta(A)/A$ between unpolarized $\Upsilon(1S)$ without FSR and with FSR model in PHOTOS.

(b) Generated E_T spectrum for FSR photons in the sample used to calculate acceptance.

Figure 3.24.: Effects of FSR on acceptance for $\Upsilon(1S)$.

- Alignment
- Reconstruction biases

The acceptance is sensitive to both biases in track momentum and differences in resolution between simulation and data. The magnitude of these effects is quantified by comparing measurements of resonance mass and width between the simulation and data [45]. To determine the effect on the Upsilon acceptance, we introduce a track p_T bias of 0.2%, chosen based on the momentum scale biases seen in simulation and data. This bias covers the range of differences seen between uncorrected momentum in simulation used for the acceptance calculation and corrected momentum used in data. Contributions come from material modeling, magnetic field, and other effects on tracking. We also vary the transverse momentum resolution by $\pm 10\%$ corresponding to the uncertainty in the resolution measurement using J/ψ in early data and as such this reflects a conservative estimation of resolution effects. The map is then reproduced, and the difference from the nominal acceptance map defines the systematic uncertainty. Figure 3.25 and figure 3.26 demonstrate these effects. This bias in track p_T results in changes of almost 1% for low Upsilon p_T and mid-rapidity. This change in the resolution does not significantly effect the acceptance.

Imperfect knowledge of the production p_{T} spectrum of the Υ resonances at $\sqrt{s} =$ 7 TeV contributes a systematic uncertainty. The Υ MC sample used for the acceptance calculations was generated flat in p_{T}, whereas the p_{T} spectrum in the data peaks at a few GeV/c, and behaves as a power law above 5 GeV/c. To study the effect of this difference we have re-weighted the sample in p_{T} to more closely describe the expected distribution in data based on a fit to the spectrum obtained from PYTHIA. The acceptance map was recalculated and the difference from the nominal acceptance map is used as a systematic uncertainty, shown in Fig. 3.27.

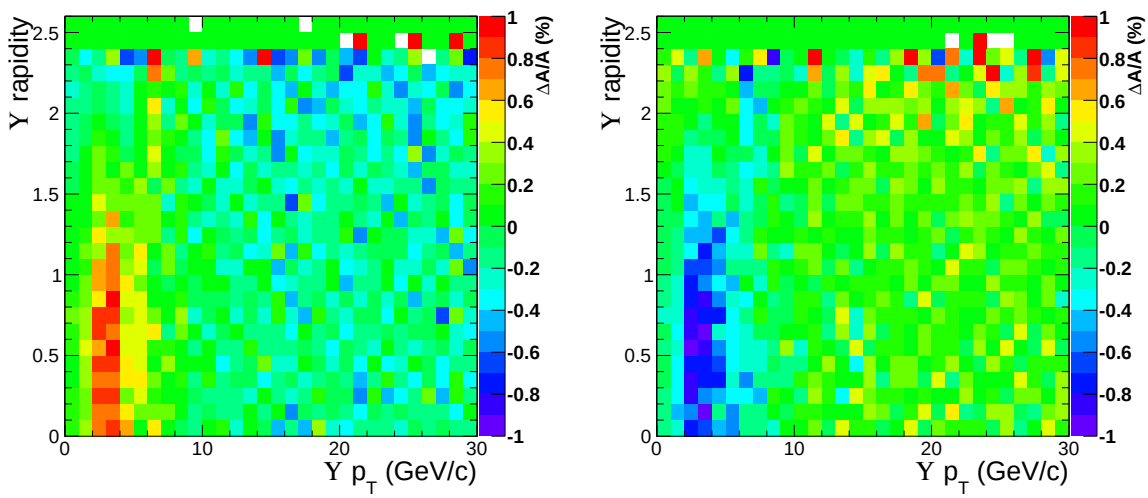

(a) $\Delta(A)/A$ for p_T bias high of 0.2%.

(b) $\Delta(A)/A$ for p_T bias low of 0.2%.

Figure 3.25.: Change in acceptance as a result of track p_T bias.

The distribution of the z-position of the pp interaction point influences the acceptance. We have generated several samples of Υ(nS), at different positions along the beam line (between -10 and +10 cm with respect to the center of the nominal collision region) and found a negligible variation of the acceptance.

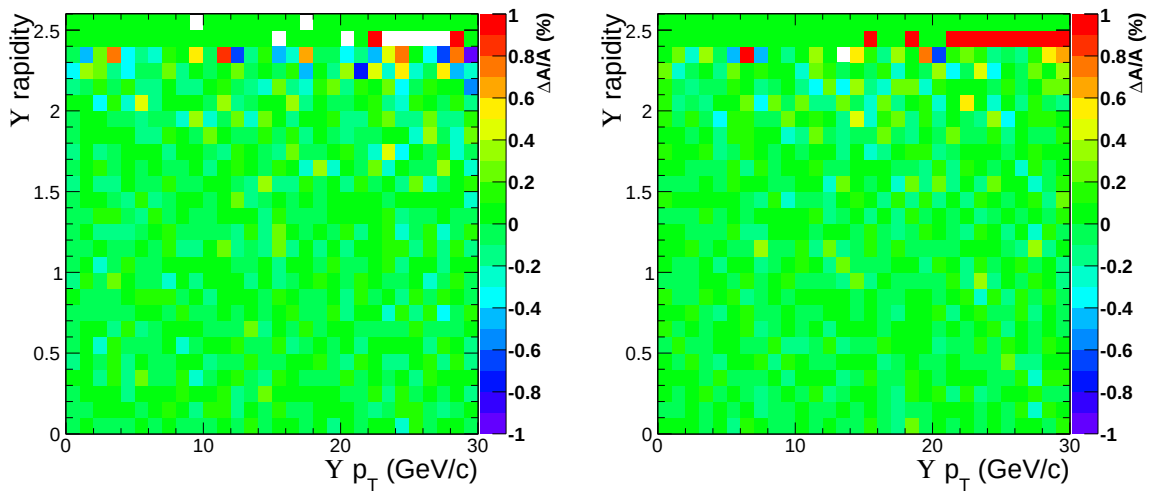

(a) $\Delta(A)/A$ for 10% worse p_T resolution.

(b) $\Delta(A)/A$ for 10% better p_T resolution.

Figure 3.26.: Change in acceptance as a result of change in p_T resolution.

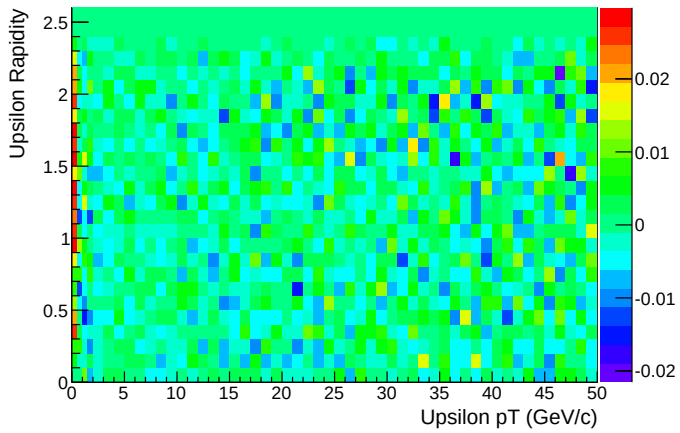

Figure 3.27.: Change in acceptance as a result of change in p_T spectrum.

3.11.3 Efficiency

High statistics Monte Carlo simulations are performed comparing T&P single muon and dimuon efficiencies to Monte Carlo truth.

Deviations associated to the estimation of the double muon efficiencies from T&P measured single muon terms are estimated from MC.

The differences are now covered by the ρ factor described in Sec. 3.9.7. Repeating the measurements with unit ρ factor, the difference in the signal yield is taken as systematic uncertainties.

The systematic uncertainty arising from the choice of bin size for the efficiencies is determined by fitting the efficiencies turn-on curves as a function of muon p_T in different $|\eta|$ region using a hyperbolic tangent function

$$f(x; a, b, c, d) = a + b \cdot tanh(c \cdot (x - d)), \tag{3.9}$$

and taking the muon efficiencies from the function instead of the binned value to recompute the cross section. The fits with fitted value for muon identification and trigger efficiencies are shown in Fig. 3.28, Fig. 3.29 and Fig. 3.30

The sanity-type selection criteria requiring the muons to be consistent with emanating from the same primary vertex do not introduce any significant signal inefficiency. They therefore do not contribute a systematic uncertainty. The muon charge misassignment is estimated to be less than 0.01% [52] and contributes a negligible systematic uncertainty.

There may be systematic effects due to differences between the shape PDF's chosen to parameterize the signal and background and the shapes present in the data. In particular the two parameters which model the FSR tail of the Crystal Ball function are fixed to values extracted from MC. These two parameters are also highly correlated. We estimate the uncertainty due to the fixing of these parameters by fitting the full statistics data with free tail parameters and use the parameters obtained to fix the tail parameters and redo the fits.

The shape of the background is an exponential with or without an error function. The yields are also extracted using a second order polynomial as an alternative model for the background, while restricting the fit to the mass range (8,12) GeV/c^2. The difference in the signal yields is used as the systematic uncertainty associated with

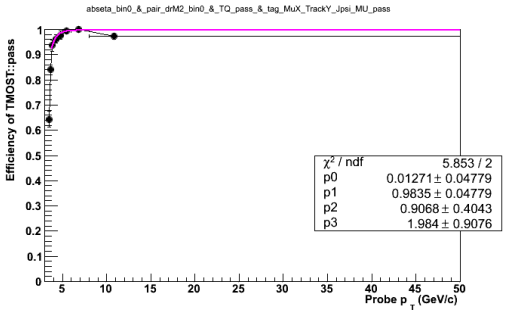

(a) $|\eta^{\mu}| < 0.2$

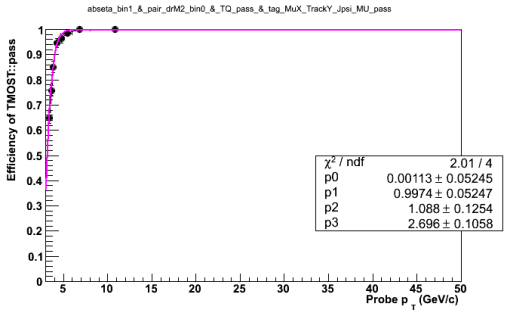

(b) $0.2 < |\eta^{\mu}| < 0.4$

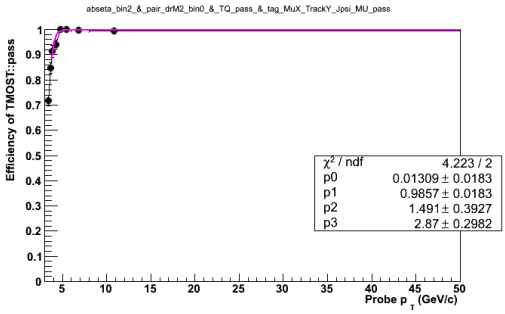

(c) $0.4 < |\eta^{\mu}| < 0.6$

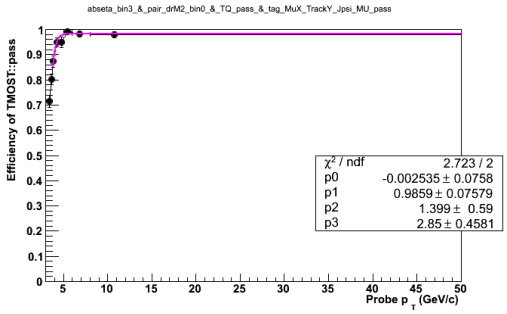

(d) $0.6 < |\eta^{\mu}| < 0.8$

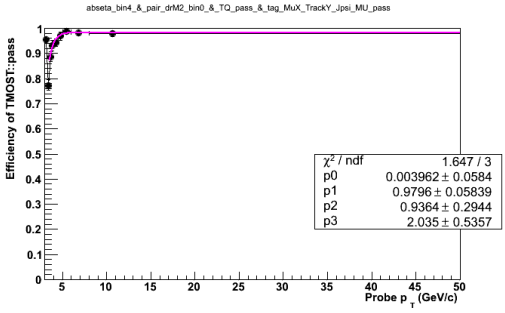

(e) $0.8 < |\eta^{\mu}| < 1.2$

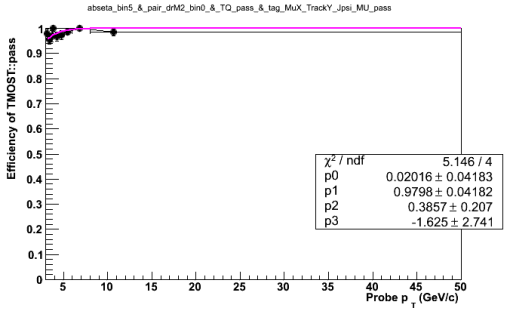

(f) $1.2 < |\eta^{\mu}| < 1.6$

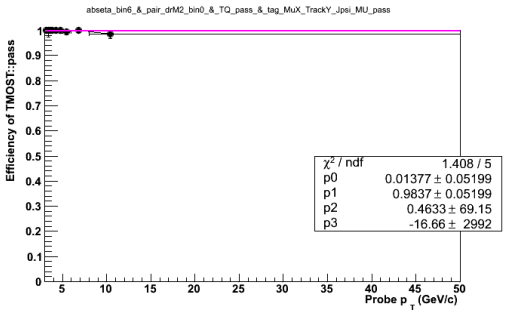

(g) $1.6 < |\eta^{\mu}| < 2.0$

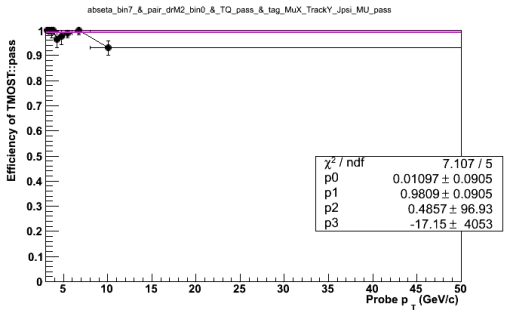

(h) $2.0 < |\eta^{\mu}| < 2.4$

Figure 3.28.: Single muon identification efficiencies as a function of p_{T}^{μ} for eight $|\eta^{\mu}|$ regions and the fitting results with fitted values.

the choice of background PDF. A shape derived from fake muons or same-sign muons in data is also studied in Section C.

3.11.4 Luminosity

The systematic uncertainty corresponding to the luminosity normalization is estimated to be about 4%.

3.11.5 Results of estimations

The relative systematic uncertainties from each source on the p_{T}-differential cross section are summarized in Table 4.36,Table 4.37 and Table 4.38 for the full rapidity range, and in Tables 4.39, 4.40, 4.41, 4.42, 4.43, 4.44; and in Table 4.45 for the rapidity differential measurements. The dominant sources of systematic uncertainty on the cross-section measurement arise from the T&P determination of the muon trigger and identification efficiencies (dominant) and from the luminosity normalization.

3.12 Measurement of the differential fiducial cross section

In Sec. (3.8), we showed that the acceptance has a strong dependence on polarization assumptions. Corrections of the data with acceptance introduces uncertainties due to the unknown polarization. In this section, the differential fiducial cross section is determined from the efficiency corrected signal yield but defined within a restricted range of muon kinematics where both muons satisfy Eq. (3.1).

The results of the $\Upsilon(\mathrm{nS})$ integrated fiducial cross section for $p_{\mathrm{T}} < 50$ GeV/c $|y| < 2.4$ within muon acceptance region are summarized in Table 4.1, Table 4.2 and Table 4.3. To determine the differential fiducial cross sections we divide the data into twenty-four intervals of transverse momentum for $\Upsilon(1\mathrm{S})$, sixteen intervals for $\Upsilon(2\mathrm{S})$ and nine intervals for $\Upsilon(3\mathrm{S})$, and repeat the fits to obtain the $\Upsilon(\mathrm{nS})$ fiducial cross sections reported in Table 4.4, Table 4.5, Table 4.6, Table 4.7, Table 4.8, Ta-

ble 4.9. The $\Upsilon(1S)$ p_T-integrated, rapidity differential fiducial cross section results are shown in Table 4.10.

The $\Upsilon(nS)$ integrated fiducial cross sections at $\sqrt{s} = 7$ TeV for $|y| < 2.4$ within muon acceptance region:

$$\sigma(pp \to \Upsilon(1S)X) \cdot \mathcal{B}(\Upsilon(1S) \to \mu^+\mu^-) = (3.06 \pm 0.02^{+0.27}_{-0.25} \pm 0.12)\ \text{nb}\,,$$

$$\sigma(pp \to \Upsilon(2S)X) \cdot \mathcal{B}(\Upsilon(2S) \to \mu^+\mu^-) = (0.91 \pm 0.01^{+0.08}_{-0.07} \pm 0.04)\ \text{nb}\,,$$

$$\sigma(pp \to \Upsilon(3S)X) \cdot \mathcal{B}(\Upsilon(3S) \to \mu^+\mu^-) = (0.49 \pm 0.01^{+0.04}_{-0.04} \pm 0.02)\ \text{nb}\,,$$

The $\Upsilon(nS)$ p_T differential fiducial cross section results for the rapidity region $|y^\Upsilon| < 2.4$ is shown in Fig. 4.1, and for six rapidity bins in Fig. 4.5. The dependence on p_T is consistent within the uncertainties for the six rapidity regions.

The $\Upsilon(nS)$ p_T-integrated, rapidity differential fiducial cross section results are shown in Fig. 4.4.

The ratios of $\Upsilon(nS)$ p_T-differential fiducial cross sections are shown in Fig. 4.2 and reported in Table 4.11.

The ratios of $\Upsilon(nS)$ rapidity differential fiducial cross sections are shown in Fig. 4.3 and reported in Table 4.12.

The sources of systematic uncertainty that contribute to the measured value of the $\Upsilon(nS)$ fiducial cross section are very similar to the ones explained in Sec. (3.11) except those related to acceptance are removed.

The relative systematic uncertainties from each source on the p_T-differential cross section are summarized in Table 4.13,Table 4.14 and Table 4.15 for the full rapidity range, and in Tables 4.16, Tables 4.17, Tables 4.18, Tables 4.19,Tables 4.20 and Tables 4.21 for six different rapidity ranges; and in Table 4.22 for the rapidity differential measurements.

A comparison between the fiducial cross-section measurement and theory is shown in Fig. 4.6. Each of the predictions is for unpolarized $\Upsilon(nS)$ production. The com-

parison is made to the CASCADE [53] MC generator in the fixed-order-plus-next-to-leading-log (FONLL) framework, including feed-down from $\chi_b(1P)$, $\chi_b(2P)$, $\chi_b(3P)$ [54], and higher order Υ states, and to PYTHIA [37] including feed-down for the $\Upsilon(1S)$ and $\Upsilon(2S)$ from P wave states with the same principal quantum number as the state under study. The p_T dependence of the cross section predicted by CASCADE agrees well with data for the $\Upsilon(1S)$, but not for the $\Upsilon(2S)$ and $\Upsilon(3S)$ where it predicts a softer p_T spectrum. CASCADE also describes the rapidity dependence well throughout the range of the measurement for $\Upsilon(1S)$ and $\Upsilon(3S)$, but not for $\Upsilon(2S)$ as shown in Fig. 4.6(d). The total cross section predicted by PYTHIA is higher than the measured cross section. In Fig. 4.6, the PYTHIA prediction is normalized to the measured cross section. The PYTHIA prediction agrees well with data for the $\Upsilon(1S)$ and $\Upsilon(3S)$ but not for the $\Upsilon(2S)$. For the $\Upsilon(1S)$ the p_T spectrum of a direct-only prediction is harder than the data, as expected. For the $\Upsilon(2S)$ the direct-only prediction is found to be in good agreement with the data, while including feed-down leads to a softer spectrum. PYTHIA provides a good description of the rapidity dependence for the three states.

3.13 Results and Comparisons to Theory and Other Experiments

The analysis of the initial LHC collision data acquired by the CMS experiment, corresponding to an integrated luminosity of 35.8 ± 1.4 pb^{-1}, yields a measurement of the $\Upsilon(nS)$ integrated production cross sections at $\sqrt{s} = 7$ TeV for $|y| < 2.4$:

$$\sigma(pp \to \Upsilon(1S)X) \cdot \mathcal{B}(\Upsilon(1S) \to \mu^+\mu^-) = (8.55 \pm 0.05^{+0.74}_{-0.71} \pm 0.34)\ \text{nb}\,,$$

$$\sigma(pp \to \Upsilon(2S)X) \cdot \mathcal{B}(\Upsilon(2S) \to \mu^+\mu^-) = (2.21 \pm 0.03^{+0.21}_{-0.20} \pm 0.09)\ \text{nb}\,,$$

$$\sigma(pp \to \Upsilon(3S)X) \cdot \mathcal{B}(\Upsilon(3S) \to \mu^+\mu^-) = (1.11 \pm 0.02^{+0.12}_{-0.11} \pm 0.04)\ \text{nb}\,,$$

The $\Upsilon(nS)$ p_T differential cross section results for the rapidity region $|y^\Upsilon| < 2.4$ is shown in Fig. 4.7, and for five rapidity bins in Fig. 4.10. The dependence on p_T is consistent within the uncertainties for the five regions. The $\Upsilon(nS)$ p_T-integrated,

rapidity differential cross section results are shown in Fig. 4.9. A decrease in the cross section at larger rapidities is observed, and consistent with Pythia expectation.

The $\Upsilon(1S)$ cross section results for the central rapidity region are compared to the previous results from CDF [26] and D0 [27]. The energy dependence of the $\Upsilon(1S)$ cross section is summarized in Table 3.11. Due to the processes $\Upsilon(3S) \rightarrow \Upsilon(2S)\,X$, $\Upsilon(3S) \rightarrow \Upsilon(1S)\,\pi\pi$, and $\Upsilon(2S) \rightarrow \Upsilon(1S)\,X$, under the assumption that the dependence of the direct differential production cross section on p_{T} for each Upsilon resonance is the same, it is expected that the ratios $\Upsilon(3S)/\Upsilon(1S)$, $\Upsilon(3S)/\Upsilon(2S)$ and $\Upsilon(2S)\,/\Upsilon(1S)$ will increase with p_{T}. The data support this. The ratios of $\Upsilon(\mathrm{nS})\,p_{\mathrm{T}}$-differential cross sections and the CASCADE predictions are shown in Fig. 4.11 and reported in Table 4.34. The ratios increase with $p_{\mathrm{T}}^{\Upsilon}$, as they did for the fiducial cross section. A possible explanation was described earlier in this work. The CASCADE prediction is consistent with the $\Upsilon(2S)/\Upsilon(1S)$ ratio while it does not describe the variation of the $\Upsilon(3S)/\Upsilon(1S)$ and $\Upsilon(3S)/\Upsilon(2S)$ ratios at higher p_{T}. The ratios of $\Upsilon(\mathrm{nS})$ rapidity differential cross sections are shown in Fig. 4.8 and reported in Table 4.35.

A comparison between the cross-section measurement and theory is shown in Fig. 4.12. In Fig. 4.12(a), Fig. 4.12(b) and Fig. 4.12(c), each of the predictions is for unpolarized $\Upsilon(\mathrm{nS})$ production, and both the measurement and the prediction are for $|y|^{\Upsilon} < 2.0$. The comparison is made to the CASCADE MC generator and PYTHIA (as explained in section 3.12), the Color Evaporation Model (CEM) [2] (feed-down is not included), nonrelativistic QCD (NRQCD) to next-to-leading order (NLO) including feed-down as described in Ref. [55], the Color Singlet Model (CSM) to NLO and to next-to-next-to-leading order (NNLO*) [56] where the feed-down is accounted for by scaling the $\Upsilon(1S)$ direct production cross section by a factor 2 and the direct $\Upsilon(2S)$ cross section by a factor 1.43. No feed-down is included for the $\Upsilon(3S)$. The width of a band indicates an estimate of the uncertainty in the prediction by the author of the prediction. The theory predictions are private communications [2, 53, 55, 56] as no predictions for unpolarized $\Upsilon(\mathrm{nS})$ production are available in the

literature at $\sqrt{s} = 7$ TeV. Our measured Υ(1S) cross section is lower than the CEM prediction at low $p_{\mathrm{T}}^{\Upsilon}$. The data agree well with NRQCD above p_{T} =10 GeV/c for the Υ(1S) and agree well with CASCADE for the Υ(1S), but not for the Υ(2S) and Υ(3S). The NLO CSM cannot describe the data while the NNLO* CSM shows better agreement with data within the large uncertainties. The total cross section predicted by PYTHIA is higher than the measured cross section. In Fig. 4.12, the PYTHIA prediction is normalized to the measured cross section. The p_{T} dependence of the cross section predicted by PYTHIA agrees well with data for the Υ(1S) and Υ(3S) but not for the Υ(2S). For the Υ(1S) the p_{T} spectrum of a direct-only prediction is harder than the data, as expected. For the Υ(2S) the direct-only prediction is found to be in good agreement with the data, while including feed-down leads to a softer spectrum. PYTHIA also describes the rapidity dependence well throughout the range of the measurement as shown in Fig. 4.12(d).

3.14 Results utilizing the polarization measurement from CMS

Recently, CMS has measured the polarizations of the Υ(nS) in pp collisions at $\sqrt{s} = 7$ TeV for $10 < p_{\mathrm{T}}^{\Upsilon} < 50\,\mathrm{GeV}/c$, $|y|^{\Upsilon} < 1.2$ and found them to be small [49]. Cross section measurements are provided also in the $p_{\mathrm{T}}^{\Upsilon}$ and y^{Υ} range matching that of the polarization measurement, and these polarization results are used to estimate the associated systematic uncertainty. Nevertheless, they suggest the polarization is likely small at the $p_{\mathrm{T}}^{\Upsilon}$ and y^{Υ} explored here, therefore no net polarization is assumed for the main results. However, to show the sensitivity of the results to the polarization and to allow for interpolation, we provide cross-section measurements for other polarization assumptions. We also provide cross-section measurements in the $p_{\mathrm{T}}^{\Upsilon}$ and y^{Υ} range of Ref. [49] and use the polarization results of Ref. [49] to assign a systematic uncertainty.

The three anisotropy parameters in the center-of-mass helicity and Colins-Soper frames are varied coherently by $\pm 1\sigma$ and the largest positive and negative variations with respect to the nominal (no polarization) case are taken as systematic uncertain-

ties. The systematic uncertainties are listed in Table 4.46. They are found to be comparable to, or smaller than, the 25% variation for the Υ(1S) case, while they are between the 25% and 50% variations for Υ(2S) and Υ(3S).

The Υ(nS) production cross sections at $\sqrt{s} = 7$ TeV for the same $p_{\mathrm{T}}^{\Upsilon}$ and y^{Υ} range as in Ref. [49] are:

$$\sigma(pp \to \Upsilon(1\mathrm{S})X) \cdot \mathcal{B}(\Upsilon(1\mathrm{S}) \to \mu^+\mu^-) = (0.558 \pm 0.007^{+0.048}_{-0.042}{}^{+0.020}_{-0.008} \pm 0.022)\ \mathrm{nb}\,,$$

$$\sigma(pp \to \Upsilon(2\mathrm{S})X) \cdot \mathcal{B}(\Upsilon(2\mathrm{S}) \to \mu^+\mu^-) = (0.213 \pm 0.005^{+0.016}_{-0.016}{}^{+0.016}_{-0.007} \pm 0.009)\ \mathrm{nb}\,,$$

$$\sigma(pp \to \Upsilon(3\mathrm{S})X) \cdot \mathcal{B}(\Upsilon(3\mathrm{S}) \to \mu^+\mu^-) = (0.127 \pm 0.004^{+0.011}_{-0.010}{}^{+0.008}_{-0.004} \pm 0.005)\ \mathrm{nb}\,,$$

where the first uncertainty is statistical, the second is systematic, the third is associated with the polarization measurement, and the fourth is associated with the estimation of the integrated luminosity of the data sample. The Υ(1S) and Υ(2S) measurements include feed-down contributions from higher-mass bottomonium states, such as the χ_b family and the Υ(3S).

The Υ(nS) p_{T} differential cross section results for the rapidity region $|y^{\Upsilon}| < 1.2$ is shown in Fig. 4.15 and summarized in Table 4.47, and for two rapidity bins in Fig. 4.16 and Table 4.48 and Table 4.49.

3.15 Summary

We have presented the measurement of the Υ(nS) differential production cross section in the dimuon channel in proton-proton collisions at $\sqrt{s} = 7$ TeV, with CMS. Integrated over the range $p_{\mathrm{T}} < 50$ GeV/c and $|y| < 2.4$, we find the product of the Υ(nS) production cross section and branching fraction to be

$$\sigma(pp \to \Upsilon(1\mathrm{S})X) \cdot \mathcal{B}(\Upsilon(1\mathrm{S}) \to \mu^+\mu^-) = (8.55 \pm 0.05^{+0.74}_{-0.71} \pm 0.34)\ \mathrm{nb}\,,$$

$$\sigma(pp \to \Upsilon(2\mathrm{S})X) \cdot \mathcal{B}(\Upsilon(2\mathrm{S}) \to \mu^+\mu^-) = (2.21 \pm 0.03^{+0.21}_{-0.20} \pm 0.09)\ \mathrm{nb}\,,$$

$$\sigma(pp \to \Upsilon(3\mathrm{S})X) \cdot \mathcal{B}(\Upsilon(3\mathrm{S}) \to \mu^+\mu^-) = (1.11 \pm 0.02^{+0.12}_{-0.11} \pm 0.04)\ \mathrm{nb}\,,$$

And integrated over the rapidity range $\mid y \mid < 2.4$, requiring both muons with transverse momentum $p_T^\mu > 3.75\,\mathrm{GeV}/c$ when pseudorapidity $|\eta^\mu| < 0.8$, $p_T^\mu > 3.5\,\mathrm{GeV}/c$ when $0.8 < |\eta^\mu| < 1.6$ and $p_T^\mu > 3.0\,\mathrm{GeV}/c$ when $1.6 < |\eta^\mu| < 2.4$, we find the product of $\Upsilon(\mathrm{nS})$ fiducial cross section and dimuon branching fraction to be

$$\sigma(pp \to \Upsilon(1\mathrm{S})X) \cdot \mathcal{B}(\Upsilon(1\mathrm{S}) \to \mu^+\mu^-) = (3.06 \pm 0.02^{+0.27}_{-0.25} \pm 0.12)\ \mathrm{nb}\,,$$

$$\sigma(pp \to \Upsilon(2\mathrm{S})X) \cdot \mathcal{B}(\Upsilon(2\mathrm{S}) \to \mu^+\mu^-) = (0.91 \pm 0.01^{+0.08}_{-0.07} \pm 0.04)\ \mathrm{nb}\,,$$

$$\sigma(pp \to \Upsilon(3\mathrm{S})X) \cdot \mathcal{B}(\Upsilon(3\mathrm{S}) \to \mu^+\mu^-) = (0.49 \pm 0.01^{+0.04}_{-0.04} \pm 0.02)\ \mathrm{nb}\,,$$

where the first uncertainty is statistical, the second is systematic, and the third is associated with the estimation of the integrated luminosity of the data sample. The differential cross sections for each $\Upsilon(\mathrm{nS})$ state has been measured also as a function of p_T and rapidity. The differential measurements have been compared to theory within $|y| < 2.0$. Finally, the cross section ratios of the three $\Upsilon(\mathrm{nS})$ have been measured.

The dominant sources of systematic uncertainty on the cross section measurements arise from the T&P determination of the muon identification and trigger efficiency, which dominates, and from the luminosity normalization. The nominal production cross section values obtained in this work assume unpolarized $\Upsilon(\mathrm{nS})$ production. Scenarios of extreme polarization variations have been equally studied, yielding variations on the measured cross section values of up to 20%.

The measurements obtained in this work are fully compatible with the first LHC Υ cross section results, that CMS has recently reported based on the first $3\mathrm{pb}^{-1}$ dataset, and further extend them in terms of the precision attained and the covered kinematic reach ($50\,\mathrm{GeV}/c$ and 2.4, compared to earlier $30\,\mathrm{GeV}/c$ and 2.0, respectively, in p_T and rapidity) .

The Υ provides important information on the process of hadro-production of heavy quarks. The results presented in this work allow a more precise determination of the parameters of the various bottomonium production models.

Table 3.11: Energy dependence of the cross section

Expt.	$\sqrt{s}(TeV)$	$\sigma \times B \times 1/\Delta y$	measurement range	CEM
CDF	1.8	$680 \pm 15 \pm 18 \pm 26$ pb	$\|y\| < 0.6$	600 pb
D0	1.96	$732 \pm 19 \pm 73 \pm 48$ pb	$\|y\| < 0.6$	630 pb
CMS	7.0	$1.51 \pm 0.02^{+0.13}_{-0.12} \pm 0.06$ nb	$\|y\| < 0.4$	3.1 nb

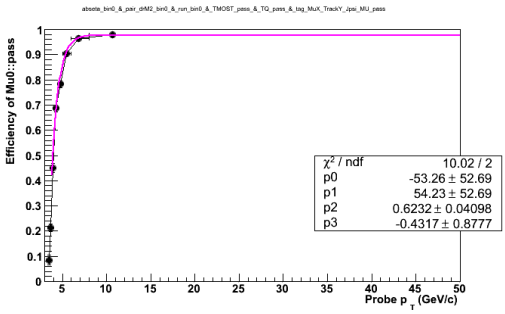

(a) $|\eta^{\mu}| < 0.2$

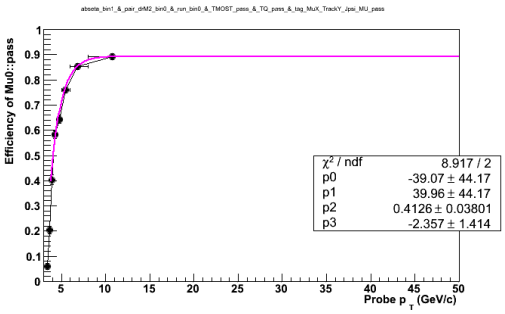

(b) $0.2 < |\eta^{\mu}| < 0.4$

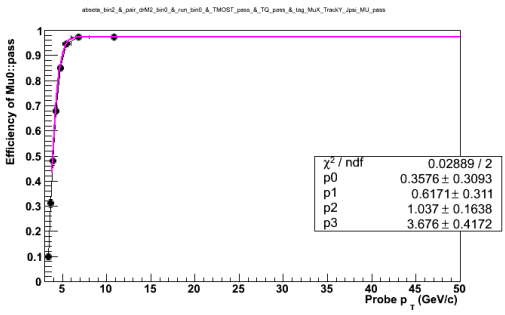

(c) $0.4 < |\eta^{\mu}| < 0.6$

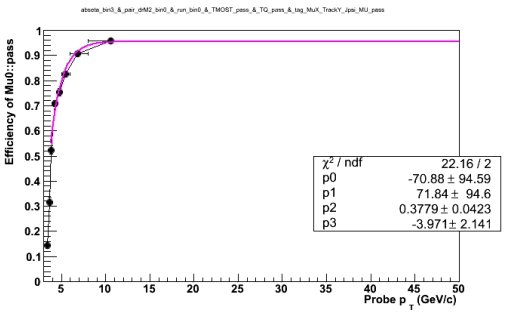

(d) $0.6 < |\eta^{\mu}| < 0.8$

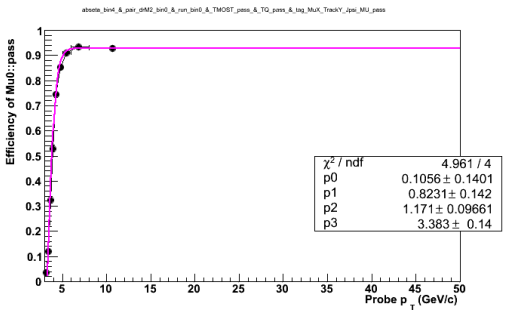

(e) $0.8 < |\eta^{\mu}| < 1.2$

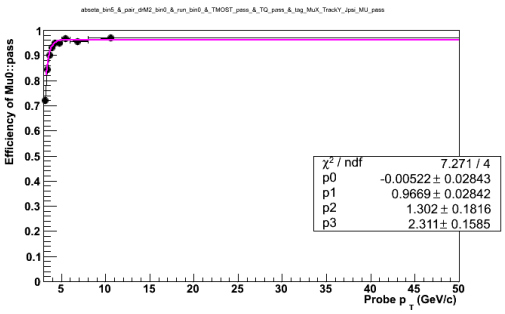

(f) $1.2 < |\eta^{\mu}| < 1.6$

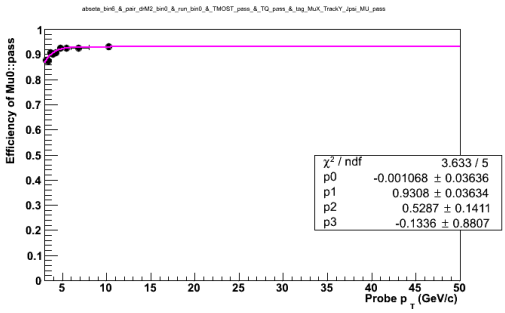

(g) $1.6 < |\eta^{\mu}| < 2.0$

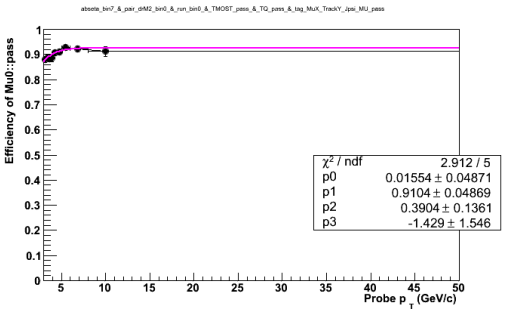

(h) $2.0 < |\eta^{\mu}| < 2.4$

Figure 3.29.: Single-leg muon trigger efficiencies as a function of p_{T}^{μ} for nine $|\eta^{\mu}|$ regions, from J/ψ Data T&P, for HLT_DoubleMu0 , and the fitting results with fitted values.

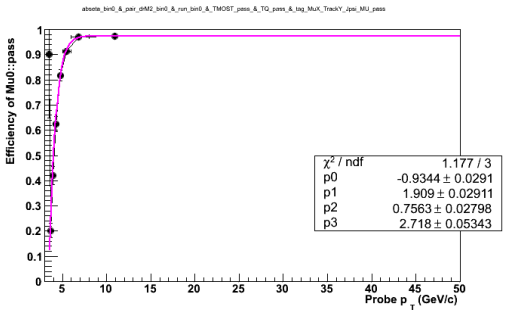

(a) $|\eta^{\mu}| < 0.2$

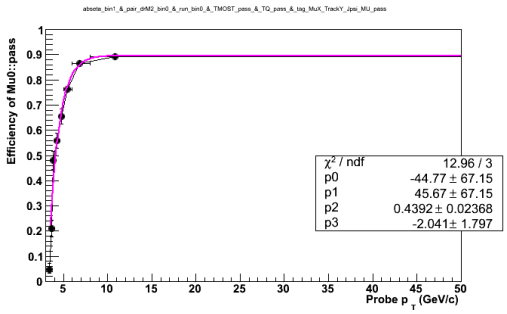

(b) $0.2 < |\eta^{\mu}| < 0.4$

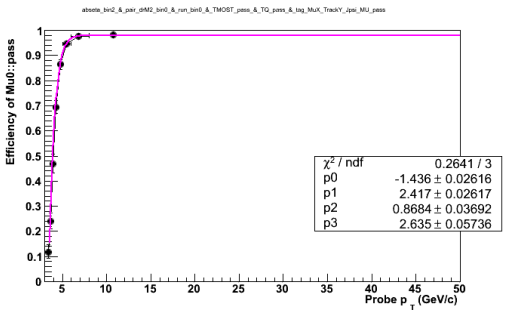

(c) $0.4 < |\eta^{\mu}| < 0.6$

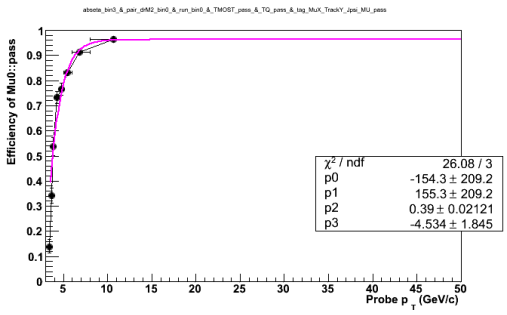

(d) $0.6 < |\eta^{\mu}| < 0.8$

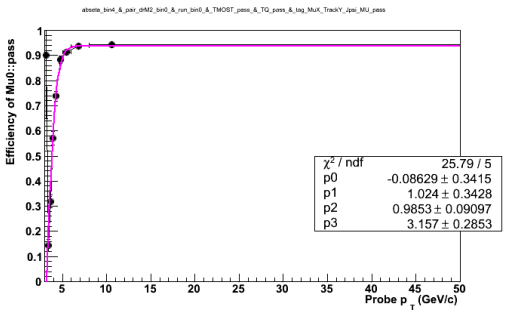

(e) $0.8 < |\eta^{\mu}| < 1.2$

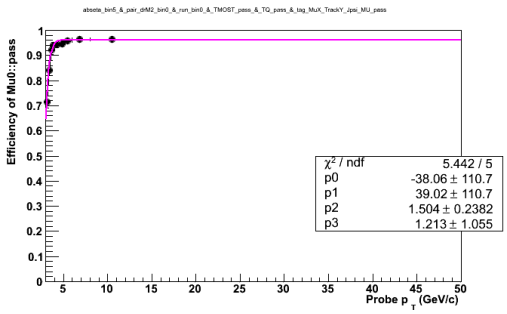

(f) $1.2 < |\eta^{\mu}| < 1.6$

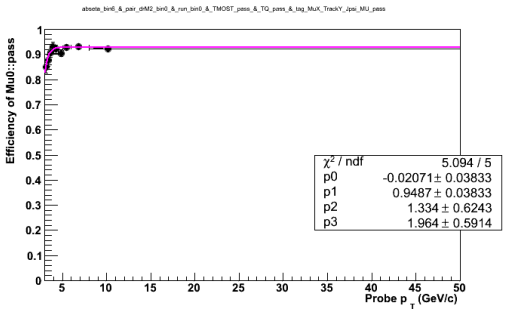

(g) $1.6 < |\eta^{\mu}| < 2.0$

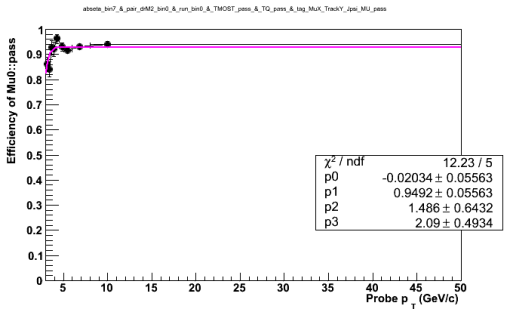

(h) $2.0 < |\eta^{\mu}| < 2.4$

Figure 3.30.: Single-leg muon trigger efficiencies as a function ofp_{T}^{μ} for nine $|\eta^{\mu}|$ regions, from J/ψ Data T&P, for HLT_DoubleMu0_Quarkonium_v1 , and the fitting results with fitted values.

4. SUMMARY

The main result of this thesis is a measurement of the inclusive Υ(nS) cross section based on the decay of Υ(nS) into muons. It is based on an integrated luminosity of 35.8 ± 1.4 pb^{-1} collected by the CMS detector at the CERN LHC collider during the first months of high-energy collision data- taking in the second half of year 2010.

The large b-quark production cross section gives high statistics data samples for the Υ cross section measurement. Though the CMS detector is primarily designed for high transverse momentum physics, it is also an excellent facility for the study of heavy flavor physics thanks to the muon system capable to identify low transverse momentum muons and the excellent tracking detectors. The study of the inclusive differential production cross section of the Υ(nS) family of resonances at CMS provides important information on the process of hadro-production of heavy quarks and calibration of the CMS detector for low p_T muons.

The measurements obtained in this thesis are consistent with the first LHC Υ cross section results, reported by the CMS Collaboration based on the early 2010 dataset [25], corresponding to less than 10% of the integrated luminosity analyzed here, and further extend them in terms of the precision attained and the kinematic reach. In addition, this work expands upon the previous work by the inclusion of fiducial cross section measurements and the polarization systematics utilizing the recent Υ polarization results from CMS. The results presented here will allow for a more precise determination of the parameters of the various bottomonium production models.

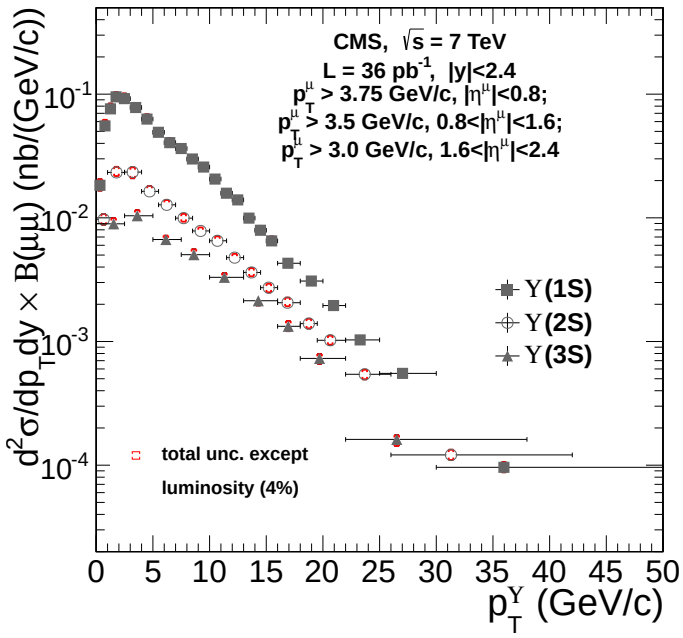

Figure 4.1.: Differential fiducial cross section of the Υ(nS) as a function of p_{T} in the rapidity range $|y| < 2.4$.

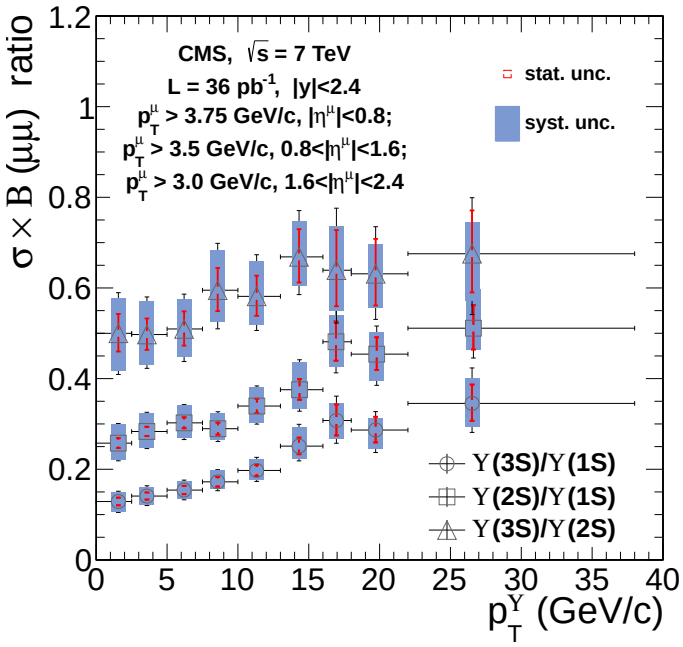

Figure 4.2.: Ratio of differential fiducial cross section of the Υ(nS) as a function of p_{T} in the rapidity range $|y| < 2.4$.

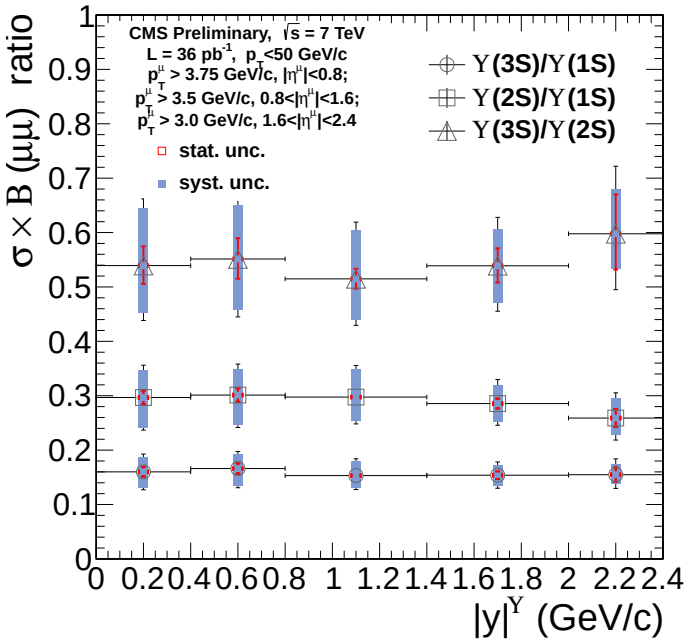

Figure 4.3.: Ratio of differential fiducial cross section of the Υ(nS) as a function of rapidity in the p_{T} range $p_T < 50 GeV/c$.

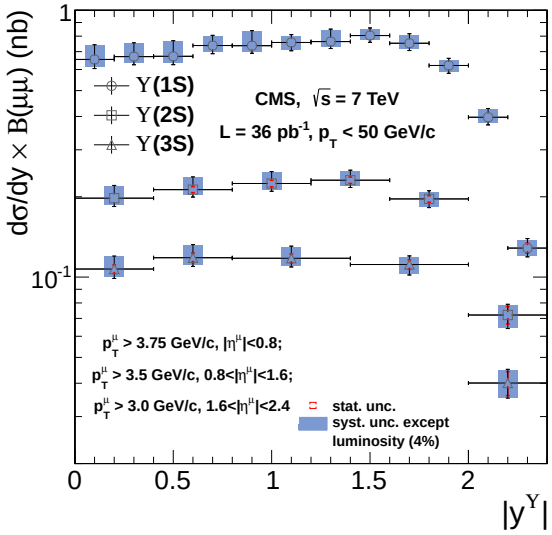

Figure 4.4.: Differential fiducial cross section of the Υ(nS) as a function of rapidity.

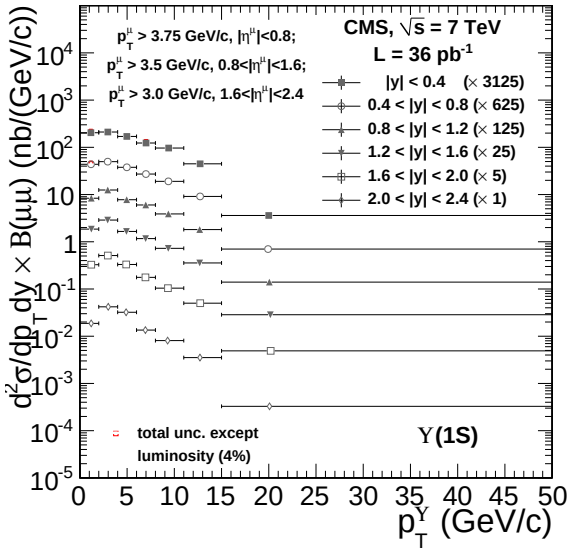

(a) Υ(1S)

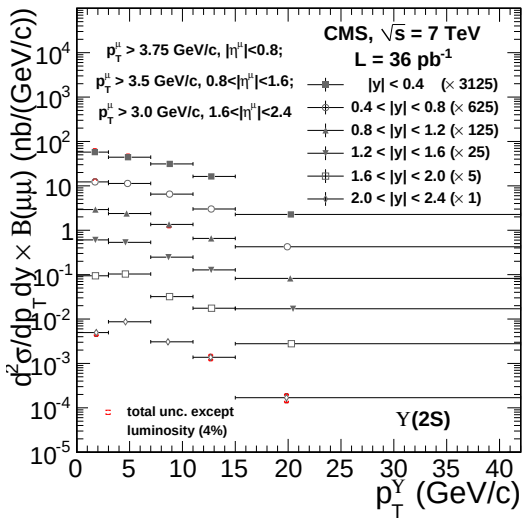

(b) Υ(2S)

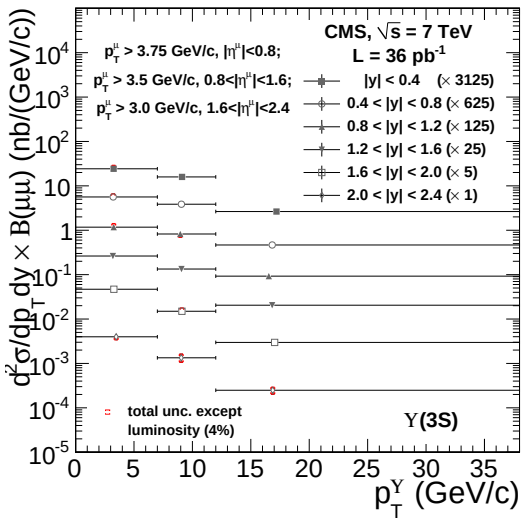

(c) Υ(3S)

Figure 4.5.: Differential fiducial cross section results of the Υ(nS) as a function of p_{T} in two rapidity regions.

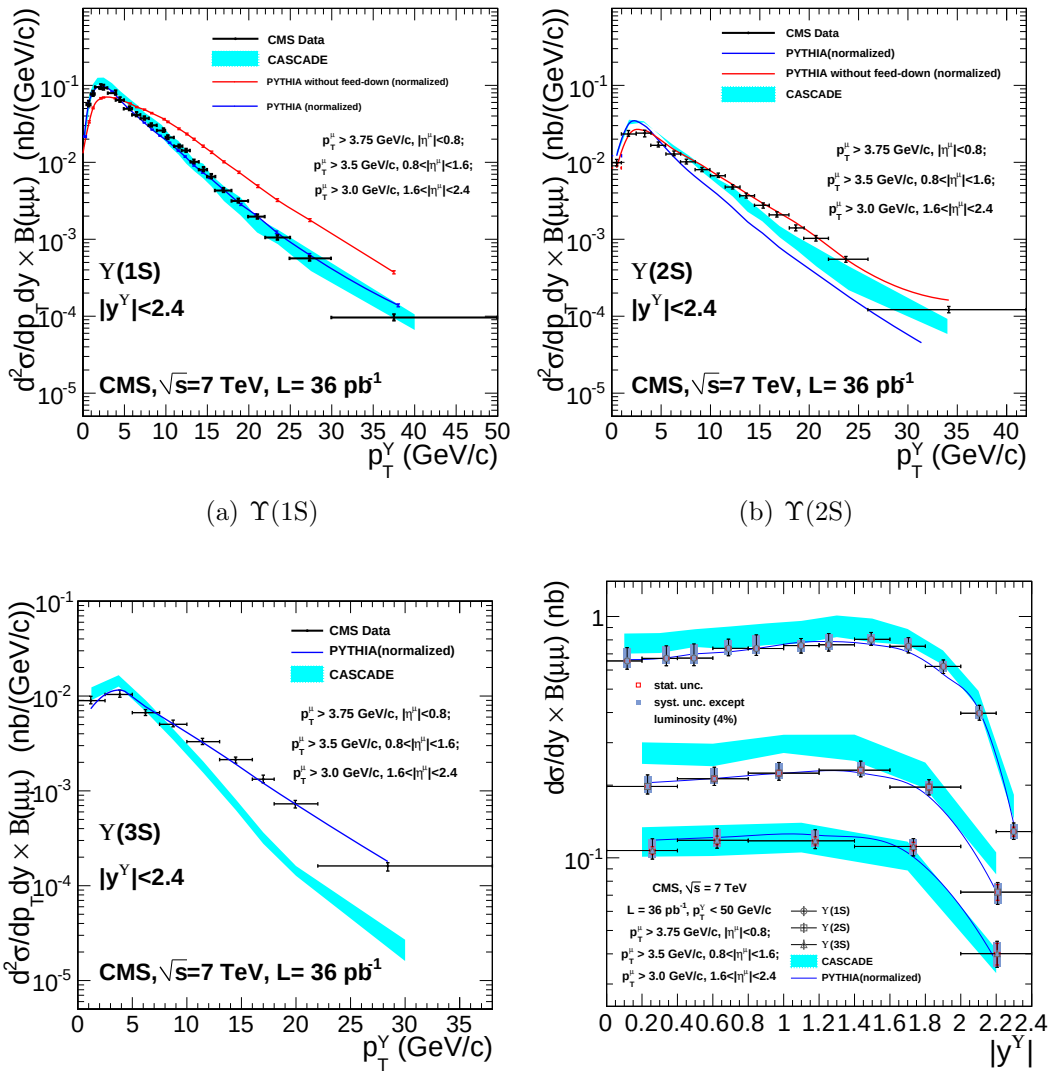

(a) Υ(1S) (b) Υ(2S)

(c) Υ(3S) (d)

Figure 4.6.: Differential fiducial cross section of the (a) Υ(1S), (b) Υ(2S) and (c) Υ(3S) as a function of p_T^Υ in the rapidity range $|y^\Upsilon| < 2.4$, and comparison to CASCADE and PYTHIA. (d) Differential fiducial cross section of the Υ(nS) as a function of rapidity and comparison to CASCADE and PYTHIA. The width of a band indicates an estimate of the uncertainty in the prediction by the author of the prediction.

Table 4.1: The product of the $\Upsilon(1S)$ integrated and differential fiducial cross sections and the dimuon branching fraction, in nb, integrated over the rapidity range $|y^{\Upsilon}| < 2.4$. The statistical uncertainty (stat.), the sum of the systematic uncertainties in quadrature ($\Sigma_{\text{syst.}}$), and the total uncertainty ($\Delta\sigma$; including stat., $\sum_{\text{syst.}}$, luminosity terms) are in percent. The numbers in parentheses are negative variations.

$|y^{\Upsilon}| < 2.4$

$\Upsilon(1S)$

p_{T} (GeV/c)	σ	stat./σ	$\sum_{\text{syst.}}/\sigma$	$\Delta\sigma/\sigma$
0.0 – 50.0	3.06	0.6	9 (8)	10 (9)
0.0 – 0.5	0.04	5.4	11 (11)	13 (13)
0.5 – 1.0	0.13	3.1	11 (11)	12 (12)
1.0 – 1.5	0.18	2.5	10 (10)	11 (11)
1.5 – 2.0	0.23	2.4	9 (8)	10 (10)
2.0 – 3.0	0.44	1.6	10 (9)	11 (10)
3.0 – 4.0	0.37	1.8	9 (8)	10 (10)
4.0 – 5.0	0.30	1.8	9 (9)	10 (10)
5.0 – 6.0	0.24	2.0	7 (7)	9 (8)
6.0 – 7.0	0.19	2.0	8 (8)	9 (9)
7.0 – 8.0	0.17	2.1	6 (6)	8 (7)
8.0 – 9.0	0.14	2.3	6 (6)	8 (7)
9.0 – 10.0	0.12	2.4	7 (6)	8 (8)
10.0 – 11.0	0.10	2.5	8 (7)	9 (9)
11.0 – 12.0	0.08	2.8	5 (4)	7 (7)
12.0 – 13.0	0.07	2.9	5 (5)	7 (7)
13.0 – 14.0	0.05	3.3	6 (6)	8 (8)
14.0 – 15.0	0.04	3.6	8 (7)	9 (9)
15.0 – 16.0	0.03	4.0	7 (7)	9 (9)
16.0 – 18.0	0.04	3.5	8 (7)	9 (9)
18.0 – 20.0	0.03	4.0	7 (6)	9 (8)
20.0 – 22.0	0.02	5.1	5 (5)	8 (8)
22.0 – 25.0	0.01	5.8	5 (5)	9 (9)
25.0 – 30.0	0.01	6.1	4 (4)	9 (8)
30.0 – 50.0	0.01	7.8	7 (7)	11 (11)

Table 4.2: The product of the $\Upsilon(2S)$ integrated and differential fiducial cross sections and the dimuon branching fraction, in nb, integrated over the rapidity range $|y^{\Upsilon}| < 2.4$. The statistical uncertainty (stat.), the sum of the systematic uncertainties in quadrature ($\Sigma_{\text{syst.}}$), and the total uncertainty ($\Delta\sigma$; including stat., $\sum_{\text{syst.}}$, luminosity terms) are in percent. The numbers in parentheses are negative variations.

$|y^{\Upsilon}| < 2.4$

$\Upsilon(2S)$

p_{T} (GeV/c)	σ	stat./σ	$\sum_{\text{syst.}}/\sigma$	$\Delta\sigma/\sigma$
0.0 – 42.0	0.91	1.2	8 (8)	9 (9)
0.0 – 1.0	0.05	6.3	9 (10)	12 (13)
1.0 – 2.5	0.17	3.4	11 (11)	12 (12)
2.5 – 4.0	0.17	3.1	10 (13)	11 (14)
4.0 – 5.5	0.12	3.3	10 (10)	12 (11)
5.5 – 7.0	0.09	3.6	9 (8)	10 (10)
7.0 – 8.5	0.07	3.4	9 (9)	10 (10)
8.5 – 10.0	0.06	4.0	6 (7)	9 (9)
10.0 – 11.5	0.05	4.1	7 (7)	9 (9)
11.5 – 13.0	0.03	4.6	6 (6)	8 (9)
13.0 – 14.5	0.03	5.2	7 (7)	9 (10)
14.5 – 16.0	0.02	5.7	6 (8)	9 (10)
16.0 – 18.0	0.02	5.5	8 (8)	11 (11)
18.0 – 19.5	0.01	7.5	6 (6)	10 (11)
19.5 – 22.0	0.01	6.8	6 (6)	10 (10)
22.0 – 26.0	0.01	7.4	5 (6)	10 (10)
26.0 – 42.0	0.01	8.0	7 (7)	11 (11)

Table 4.3: The product of the $\Upsilon(3S)$ integrated and differential fiducial cross sections and the dimuon branching fraction, in nb, integrated over the rapidity range $|y^{\Upsilon}| < 2.4$. The statistical uncertainty (stat.), the sum of the systematic uncertainties in quadrature ($\Sigma_{\text{syst.}}$), and the total uncertainty ($\Delta\sigma$; including stat., $\sum_{\text{syst.}}$, luminosity terms) are in percent. The numbers in parentheses are negative variations.

$|y^{\Upsilon}| < 2.4$

$\Upsilon(3S)$

p_{T} (GeV/c)	σ	stat./σ	$\sum_{\text{syst.}}/\sigma$	$\Delta\sigma/\sigma$
$0.0 - 38.0$	0.49	2.0	9 (8)	10 (9)
$0.0 - 2.5$	0.11	5.3	10 (10)	12 (12)
$2.5 - 5.0$	0.12	4.5	10 (10)	12 (12)
$5.0 - 7.5$	0.08	4.7	7 (6)	9 (9)
$7.5 - 10.0$	0.06	4.8	10 (9)	11 (11)
$10.0 - 13.0$	0.05	4.5	7 (8)	9 (10)
$13.0 - 16.0$	0.03	5.1	5 (7)	8 (9)
$16.0 - 18.0$	0.01	7.5	8 (7)	12 (11)
$18.0 - 22.0$	0.01	6.9	8 (8)	11 (11)
$22.0 - 38.0$	0.01	7.4	9 (9)	12 (12)

Table 4.4: The product of the Υ(nS) integrated and differential fiducial cross sections and the dimuon branching fraction, in nb, integrated over the rapidity range $|y^{\Upsilon}| < 0.4$. The statistical uncertainty (stat.), the sum of the systematic uncertainties in quadrature ($\Sigma_{\text{syst.}}$), and the total uncertainty ($\Delta\sigma$; including stat., $\sum_{\text{syst.}}$, luminosity terms) are in percent. The numbers in parentheses are negative variations.

$|y^{\Upsilon}| < 0.4$

Υ(1S)

p_{T} (GeV/c)	σ	stat./σ	$\sum_{\text{syst.}}/\sigma$	$\Delta\sigma/\sigma$
0.0 – 50.0	0.51	0.2	9 (8)	10 (9)
0.0 – 2.0	0.10	3.5	17 (16)	18 (17)
2.0 – 4.0	0.11	3.1	14 (13)	15 (14)
4.0 – 6.0	0.09	2.9	14 (13)	15 (14)
6.0 – 8.0	0.06	3.3	17 (17)	18 (18)
8.0 – 11.0	0.07	2.9	10 (10)	11 (11)
11.0 – 15.0	0.05	3.3	8 (8)	9 (9)
15.0 – 50.0	0.03	3.7	5 (6)	8 (8)

Υ(2S)

p_{T} (GeV/c)	σ	stat./σ	$\sum_{\text{syst.}}/\sigma$	$\Delta\sigma/\sigma$
0.0 – 42.0	0.15	0.5	9 (9)	10 (9)
0.0 – 3.0	0.04	7.0	17 (16)	19 (18)
3.0 – 7.0	0.05	4.9	16 (16)	17 (17)
7.0 – 11.0	0.03	5.3	12 (11)	13 (13)
11.0 – 15.0	0.02	6.1	9 (8)	11 (11)
15.0 – 42.0	0.02	5.7	6 (6)	9 (9)

Υ(3S)

p_{T} (GeV/c)	σ	stat./σ	$\sum_{\text{syst.}}/\sigma$	$\Delta\sigma/\sigma$
0.0 – 38.0	0.08	0.7	10 (9)	10 (10)
0.0 – 7.0	0.04	6.5	18 (17)	20 (19)
7.0 – 12.0	0.02	7.5	12 (12)	15 (15)
12.0 – 38.0	0.02	5.9	8 (7)	10 (10)

Table 4.5: The product of the $\Upsilon(1S)$ integrated and differential fiducial cross sections and the dimuon branching fraction, in nb, integrated over the rapidity range $0.4 < |y^{\Upsilon}| < 0.8$. The statistical uncertainty (stat.), the sum of the systematic uncertainties in quadrature ($\Sigma_{\text{syst.}}$), and the total uncertainty ($\Delta\sigma$; including stat., $\sum_{\text{syst.}}$, luminosity terms) are in percent. The numbers in parentheses are negative variations.

$0.4 < |y^{\Upsilon}| < 0.8$

$\Upsilon(1S)$				
p_{T} (GeV/c)	σ	stat./σ	$\sum_{\text{syst.}}/\sigma$	$\Delta\sigma/\sigma$
0.0 – 50.0	0.56	0.2	9 (8)	10 (9)
0.0 – 2.0	0.11	3.3	15 (14)	16 (15)
2.0 – 4.0	0.13	3.0	13 (13)	14 (14)
4.0 – 6.0	0.10	2.8	11 (11)	12 (12)
6.0 – 8.0	0.07	3.3	14 (14)	15 (15)
8.0 – 11.0	0.07	2.9	8 (8)	10 (9)
11.0 – 15.0	0.05	3.3	8 (8)	10 (10)
15.0 – 50.0	0.03	0.8	6 (6)	7 (7)
$\Upsilon(2S)$				
p_{T} (GeV/c)	σ	stat./σ	$\sum_{\text{syst.}}/\sigma$	$\Delta\sigma/\sigma$
0.0 – 42.0	0.17	0.5	8 (8)	9 (9)
0.0 – 3.0	0.05	7.2	15 (14)	17 (16)
3.0 – 7.0	0.06	4.5	10 (10)	12 (12)
7.0 – 11.0	0.03	5.2	10 (8)	12 (10)
11.0 – 15.0	0.02	6.6	7 (8)	11 (11)
15.0 – 42.0	0.01	5.9	6 (6)	9 (10)
$\Upsilon(3S)$				
p_{T} (GeV/c)	σ	stat./σ	$\sum_{\text{syst.}}/\sigma$	$\Delta\sigma/\sigma$
0.0 – 38.0	0.09	0.8	10 (9)	10 (10)
0.0 – 7.0	0.05	6.8	17 (16)	18 (18)
7.0 – 12.0	0.02	6.8	10 (9)	12 (12)
12.0 – 38.0	0.02	6.5	8 (8)	11 (11)

Table 4.6: The product of the $\Upsilon(1S)$ integrated and differential fiducial cross sections and the dimuon branching fraction, in nb, integrated over the rapidity range $0.8 < |y^{\Upsilon}| < 1.2$. The statistical uncertainty (stat.), the sum of the systematic uncertainties in quadrature ($\Sigma_{\text{syst.}}$), and the total uncertainty ($\Delta\sigma$; including stat., $\sum_{\text{syst.}}$, luminosity terms) are in percent. The numbers in parentheses are negative variations.

$0.8 < |y^{\Upsilon}| < 1.2$

$\Upsilon(1S)$				
p_{T} (GeV/c)	σ	stat./σ	$\sum_{\text{syst.}}/\sigma$	$\Delta\sigma/\sigma$
0.0 – 50.0	0.60	0.2	9 (8)	10 (9)
0.0 – 2.0	0.11	3.7	12 (12)	13 (13)
2.0 – 4.0	0.16	2.7	12 (12)	13 (13)
4.0 – 6.0	0.10	2.9	9 (9)	11 (10)
6.0 – 8.0	0.08	3.1	13 (13)	14 (14)
8.0 – 11.0	0.07	2.9	7 (9)	9 (11)
11.0 – 15.0	0.05	3.4	8 (8)	9 (9)
15.0 – 50.0	0.03	3.8	7 (8)	9 (10)
$\Upsilon(2S)$				
p_{T} (GeV/c)	σ	stat./σ	$\sum_{\text{syst.}}/\sigma$	$\Delta\sigma/\sigma$
0.0 – 42.0	0.18	0.6	8 (8)	9 (9)
0.0 – 3.0	0.06	6.1	13 (13)	15 (15)
3.0 – 7.0	0.06	5.0	11 (10)	13 (12)
7.0 – 11.0	0.03	5.3	15 (15)	16 (16)
11.0 – 15.0	0.02	6.2	8 (8)	11 (11)
15.0 – 42.0	0.01	6.2	8 (9)	11 (11)
$\Upsilon(3S)$				
p_{T} (GeV/c)	σ	stat./σ	$\sum_{\text{syst.}}/\sigma$	$\Delta\sigma/\sigma$
0.0 – 38.0	0.09	0.9	9 (8)	10 (9)
0.0 – 7.0	0.05	7.7	18 (18)	20 (20)
7.0 – 12.0	0.03	6.9	13 (15)	15 (17)
12.0 – 38.0	0.02	6.8	11 (11)	14 (14)

Table 4.7: The product of the $\Upsilon(1S)$ integrated and differential fiducial cross sections and the dimuon branching fraction, in nb, integrated over the rapidity range $1.2 < |y^{\Upsilon}| < 1.6$. The statistical uncertainty (stat.), the sum of the systematic uncertainties in quadrature ($\Sigma_{\text{syst.}}$), and the total uncertainty ($\Delta\sigma$; including stat., $\sum_{\text{syst.}}$, luminosity terms) are in percent. The numbers in parentheses are negative variations.

$1.2 < |y^{\Upsilon}| < 1.6$

$\Upsilon(1S)$				
p_{T} (GeV/c)	σ	stat./σ	$\sum_{\text{syst.}}/\sigma$	$\Delta\sigma/\sigma$
0.0 – 50.0	0.63	0.2	9 (8)	10 (9)
0.0 – 2.0	0.12	3.5	7 (12)	9 (13)
2.0 – 4.0	0.18	2.4	8 (7)	9 (9)
4.0 – 6.0	0.11	2.8	8 (8)	9 (9)
6.0 – 8.0	0.07	3.0	7 (7)	9 (9)
8.0 – 11.0	0.07	3.0	7 (7)	9 (9)
11.0 – 15.0	0.05	3.3	7 (7)	9 (9)
15.0 – 50.0	0.03	3.8	8 (9)	10 (11)
$\Upsilon(2S)$				
p_{T} (GeV/c)	σ	stat./σ	$\sum_{\text{syst.}}/\sigma$	$\Delta\sigma/\sigma$
0.0 – 42.0	0.19	0.6	8 (8)	9 (9)
0.0 – 3.0	0.06	6.2	8 (8)	11 (11)
3.0 – 7.0	0.07	4.5	8 (8)	10 (10)
7.0 – 11.0	0.03	5.5	7 (8)	10 (10)
11.0 – 15.0	0.02	6.5	7 (7)	10 (10)
15.0 – 42.0	0.01	6.4	9 (10)	12 (13)
$\Upsilon(3S)$				
p_{T} (GeV/c)	σ	stat./σ	$\sum_{\text{syst.}}/\sigma$	$\Delta\sigma/\sigma$
0.0 – 38.0	0.10	0.9	9 (8)	10 (9)
0.0 – 7.0	0.06	6.9	8 (8)	11 (11)
7.0 – 12.0	0.02	7.7	11 (10)	14 (13)
12.0 – 38.0	0.02	6.7	9 (9)	12 (12)

Table 4.8: The product of the $\Upsilon(1S)$ integrated and differential fiducial cross sections and the dimuon branching fraction, in nb, integrated over the rapidity range $1.6 < |y^{\Upsilon}| < 2.0$. The statistical uncertainty (stat.), the sum of the systematic uncertainties in quadrature ($\Sigma_{\text{syst.}}$), and the total uncertainty ($\Delta\sigma$; including stat., $\sum_{\text{syst.}}$, luminosity terms) are in percent. The numbers in parentheses are negative variations.

$1.6 < |y^{\Upsilon}| < 2.0$

$\Upsilon(1S)$				
p_{T} (GeV/c)	σ	stat./σ	$\sum_{\text{syst.}}/\sigma$	$\Delta\sigma/\sigma$
0.0 – 50.0	0.54	0.2	9 (8)	10 (9)
0.0 – 2.0	0.10	3.1	9 (9)	11 (10)
2.0 – 4.0	0.16	2.5	7 (6)	8 (7)
4.0 – 6.0	0.11	2.7	6 (5)	8 (7)
6.0 – 8.0	0.06	3.2	5 (5)	7 (7)
8.0 – 11.0	0.05	3.4	6 (6)	8 (8)
11.0 – 15.0	0.03	4.1	6 (5)	8 (8)
15.0 – 50.0	0.03	4.4	6 (6)	8 (8)
$\Upsilon(2S)$				
p_{T} (GeV/c)	σ	stat./σ	$\sum_{\text{syst.}}/\sigma$	$\Delta\sigma/\sigma$
0.0 – 42.0	0.16	0.5	8 (8)	9 (9)
0.0 – 3.0	0.05	6.2	9 (9)	12 (11)
3.0 – 7.0	0.07	4.3	7 (6)	9 (9)
7.0 – 11.0	0.02	7.0	10 (10)	13 (13)
11.0 – 15.0	0.01	8.3	6 (6)	11 (11)
15.0 – 42.0	0.01	8.1	6 (6)	11 (11)
$\Upsilon(3S)$				
p_{T} (GeV/c)	σ	stat./σ	$\sum_{\text{syst.}}/\sigma$	$\Delta\sigma/\sigma$
0.0 – 38.0	0.08	0.8	9 (8)	10 (9)
0.0 – 7.0	0.05	7.2	10 (9)	13 (12)
7.0 – 12.0	0.01	10.6	15 (15)	19 (19)
12.0 – 38.0	0.01	8.8	7 (7)	12 (12)

Table 4.9: The product of the $\Upsilon(1S)$ integrated and differential fiducial cross sections and the dimuon branching fraction, in nb, integrated over the rapidity range $2.0 < |y^{\Upsilon}| < 2.4$. The statistical uncertainty (stat.), the sum of the systematic uncertainties in quadrature ($\Sigma_{\text{syst.}}$), and the total uncertainty ($\Delta\sigma$; including stat., $\sum_{\text{syst.}}$, luminosity terms) are in percent. The numbers in parentheses are negative variations.

$2.0 < |y^{\Upsilon}| < 2.4$

$\Upsilon(1S)$				
p_{T} (GeV/c)	σ	stat./σ	$\sum_{\text{syst.}}/\sigma$	$\Delta\sigma/\sigma$
0.0 – 50.0	0.21	0.1	9 (8)	10 (9)
0.0 – 2.0	0.03	5.3	10 (10)	12 (12)
2.0 – 4.0	0.07	2.8	7 (4)	8 (7)
4.0 – 6.0	0.05	3.7	12 (12)	13 (13)
6.0 – 8.0	0.02	5.6	6 (8)	9 (10)
8.0 – 11.0	0.02	5.8	6 (6)	9 (9)
11.0 – 15.0	0.01	7.2	9 (8)	12 (12)
15.0 – 50.0	0.01	9.1	13 (12)	16 (16)
$\Upsilon(2S)$				
p_{T} (GeV/c)	σ	stat./σ	$\sum_{\text{syst.}}/\sigma$	$\Delta\sigma/\sigma$
0.0 – 42.0	0.06	0.3	8 (8)	9 (9)
0.0 – 3.0	0.01	13.2	11 (11)	18 (18)
3.0 – 7.0	0.03	7.6	9 (8)	12 (12)
7.0 – 11.0	0.01	10.9	9 (8)	15 (14)
11.0 – 15.0	0.00	14.7	8 (7)	17 (17)
15.0 – 42.0	0.00	20.4	10 (9)	23 (23)
$\Upsilon(3S)$				
p_{T} (GeV/c)	σ	stat./σ	$\sum_{\text{syst.}}/\sigma$	$\Delta\sigma/\sigma$
0.0 – 38.0	0.03	0.6	9 (8)	10 (9)
0.0 – 7.0	0.02	11.2	10 (10)	16 (15)
7.0 – 12.0	0.01	19.3	8 (7)	21 (21)
12.0 – 38.0	0.01	15.8	8 (8)	18 (18)

Table 4.10: The product of the Υ(nS) integrated and rapidity differential fiducial cross sections and the dimuon branching fraction, in nb, integrated over the p_{T} range $p_{\mathrm{T}}^{\Upsilon} < 50\,\mathrm{GeV}/c$. The statistical uncertainty (stat.), the sum of the systematic uncertainties in quadrature ($\Sigma_{\mathrm{syst.}}$), and the total uncertainty ($\Delta\sigma$; including stat., $\sum_{\mathrm{syst.}}$, luminosity terms) are in percent. The numbers in parentheses are negative variations.

$\mathbf{p_{T}^{\Upsilon} < 50\,GeV/c}$

Υ(1S)				
$\lvert y\rvert$	σ	stat./σ	$\sum_{\mathrm{syst.}}/\sigma$	$\Delta\sigma/\sigma$
0.0 – 2.4	3.08	0.5	9 (8)	10 (9)
0.0 – 0.2	0.26	1.7	13 (13)	14 (13)
0.2 – 0.4	0.27	1.7	12 (12)	12 (12)
0.4 – 0.6	0.27	1.7	14 (14)	15 (14)
0.6 – 0.8	0.30	1.7	9 (8)	10 (9)
0.8 – 1.0	0.29	1.7	13 (13)	14 (14)
1.0 – 1.2	0.30	1.8	7 (6)	8 (8)
1.2 – 1.4	0.31	1.7	11 (10)	11 (11)
1.4 – 1.6	0.32	1.7	6 (5)	7 (6)
1.6 – 1.8	0.30	1.7	8 (7)	9 (9)
1.8 – 2.0	0.25	1.9	6 (5)	7 (7)
2.0 – 2.2	0.16	2.3	7 (5)	9 (7)
2.2 – 2.4	0.05	4.3	7 (5)	9 (8)
Υ(2S)				
$\lvert y\rvert$	σ	stat./σ	$\sum_{\mathrm{syst.}}/\sigma$	$\Delta\sigma/\sigma$
0.0 – 2.4	0.91	1.2	8 (8)	9 (9)
0.0 – 0.4	0.16	2.4	11 (11)	12 (12)
0.4 – 0.8	0.17	2.6	11 (10)	12 (11)
0.8 – 1.2	0.18	2.8	10 (10)	11 (11)
1.2 – 1.6	0.18	2.7	8 (8)	9 (9)
1.6 – 2.0	0.16	2.9	7 (6)	9 (8)
2.0 – 2.4	0.06	7.6	7 (7)	11 (11)
Υ(3S)				
$\lvert y\rvert$	σ	stat./σ	$\sum_{\mathrm{syst.}}/\sigma$	$\Delta\sigma/\sigma$
0.0 – 2.4	0.49	2.0	9 (8)	10 (9)
0.0 – 0.4	0.09	3.7	11 (11)	13 (12)
0.4 – 0.8	0.09	4.0	11 (10)	12 (12)
0.8 – 1.4	0.14	3.8	10 (10)	11 (11)
1.4 – 2.0	0.13	4.0	8 (7)	10 (9)
2.0 – 2.4	0.03	10.3	7 (6)	13 (12)

Table 4.11: The ratio of Υ(nS) fiducial cross sections, and its p_{T} dependence, with statistical and systematic uncertainties combined in The numbers in parentheses are negative variations.

p_{T} (GeV/c)	Υ(3S) /Υ(1S)	Υ(2S) /Υ(1S)	Υ(3S) /Υ(2S)
$0-50$	$0.16 \pm 0.02\,(0.02)$	$0.30 \pm 0.04\,(0.04)$	$0.53 \pm 0.07\,(0.06)$
$0-2$	$0.13 \pm 0.02\,(0.02)$	$0.26 \pm 0.04\,(0.04)$	$0.50 \pm 0.09\,(0.09)$
$2-5$	$0.14 \pm 0.02\,(0.02)$	$0.28 \pm 0.04\,(0.04)$	$0.50 \pm 0.08\,(0.07)$
$5-8$	$0.15 \pm 0.02\,(0.02)$	$0.30 \pm 0.04\,(0.04)$	$0.51 \pm 0.08\,(0.07)$
$8-10$	$0.17 \pm 0.03\,(0.02)$	$0.29 \pm 0.04\,(0.03)$	$0.60 \pm 0.10\,(0.09)$
$10-13$	$0.20 \pm 0.03\,(0.02)$	$0.34 \pm 0.04\,(0.04)$	$0.58 \pm 0.09\,(0.08)$
$13-16$	$0.25 \pm 0.05\,(0.03)$	$0.38 \pm 0.07\,(0.05)$	$0.67 \pm 0.10\,(0.08)$
$16-19$	$0.31 \pm 0.05\,(0.05)$	$0.48 \pm 0.07\,(0.07)$	$0.64 \pm 0.14\,(0.12)$
$19-22$	$0.29 \pm 0.04\,(0.05)$	$0.45 \pm 0.06\,(0.07)$	$0.63 \pm 0.10\,(0.10)$
$22-50$	$0.35 \pm 0.08\,(0.06)$	$0.51 \pm 0.11\,(0.07)$	$0.68 \pm 0.12\,(0.13)$

Table 4.12: The ratio of Υ(nS) fiducial cross sections, and its rapidity dependence, with statistical and systematic uncertainties combined in quadrature. The numbers in parentheses are negative variations.

$\lvert y\rvert$	Υ(3S) /Υ(1S)	Υ(2S) /Υ(1S)	Υ(3S) /Υ(2S)
$0.0-2.4$	$0.16 \pm 0.03\,(0.02)$	$0.30 \pm 0.05\,(0.04)$	$0.53 \pm 0.09\,(0.08)$
$0.0-0.4$	$0.16 \pm 0.03\,(0.03)$	$0.30 \pm 0.06\,(0.05)$	$0.54 \pm 0.11\,(0.09)$
$0.4-0.8$	$0.17 \pm 0.03\,(0.03)$	$0.30 \pm 0.05\,(0.05)$	$0.55 \pm 0.10\,(0.10)$
$0.8-1.4$	$0.15 \pm 0.03\,(0.02)$	$0.30 \pm 0.05\,(0.04)$	$0.51 \pm 0.10\,(0.08)$
$1.4-2.0$	$0.15 \pm 0.02\,(0.02)$	$0.29 \pm 0.04\,(0.04)$	$0.54 \pm 0.08\,(0.08)$
$2.0-2.4$	$0.15 \pm 0.03\,(0.03)$	$0.26 \pm 0.04\,(0.04)$	$0.60 \pm 0.12\,(0.11)$

Table 4.13: Relative values of the systematic uncertainties on the $\Upsilon(1S)$ integrated and differential fiducial cross section times the dimuon branching fraction, for $|y| < 2.4$, in units of percent. The p_T intervals are in units of GeV/c. The following abbreviations are used: ϵ_{muid}, ϵ_{trig}, ϵ_{ρ}, ϵ_{func}, ϵ_{trk}, PDF_{CB}, PDF_{bkgd} and M_{scale}, for the systematic uncertainties arising from the statistical uncertainties from tag and probe efficiencies, fixing the tail parameters in fitting, the background PDF, the mismeasurement of the track momentum shifts that broadens the reconstructed dimuon resonances, fixing the tail parameters in fitting, the statistical uncertainties in tracking efficiencies, the choice of bin size for the efficiencies and from ρ factors. The luminosity uncertainty of 4% is not shown in the table. The numbers in parentheses are negative variations.

$|\mathbf{y}^{\Upsilon}| < \mathbf{2.4}$

$\Upsilon(1S)$

p_T	$\varepsilon_{\text{muid}}$	$\varepsilon_{\text{trig}}$	ε_{ρ}	$\varepsilon_{\text{func}}$	ε_{trk}	PDF_{CB}	PDF_{bkgd}	M_{scale}
0.0 – 50.0	3.0 (2.1)	3.8 (3.3)	6.9	1.8	0.4 (0.3)	1.7	0.2	0.0 (0.0)
0.0 – 0.5	3.9 (3.1)	5.9 (5.1)	8.0	0.2	0.4 (0.3)	1.9	0.7	0.1 (4.1)
0.5 – 1.0	4.0 (4.0)	4.1 (4.4)	9.1	1.2	2.2 (2.2)	1.7	1.5	0.9 (0.1)
1.0 – 1.5	3.4 (2.7)	4.8 (4.2)	7.2	3.8	0.3 (0.3)	2.1	1.0	0.1 (0.1)
1.5 – 2.0	3.4 (2.5)	5.1 (4.4)	3.3	3.6	0.3 (0.3)	1.6	4.0	0.0 (0.0)
2.0 – 3.0	3.3 (2.3)	4.8 (4.2)	7.0	2.4	0.3 (0.3)	1.7	2.8	0.0 (0.0)
3.0 – 4.0	3.1 (1.9)	3.2 (3.2)	7.0	1.9	0.4 (0.3)	1.9	1.2	0.0 (0.1)
4.0 – 5.0	2.9 (1.8)	3.9 (2.4)	7.2	1.9	2.8 (2.8)	1.5	0.1	0.0 (3.0)
5.0 – 6.0	2.8 (1.8)	3.9 (3.0)	3.5	3.8	0.3 (0.4)	1.4	1.5	0.2 (0.2)
6.0 – 7.0	3.0 (1.8)	3.6 (3.1)	2.6	5.2	3.5 (3.5)	1.3	0.4	0.2 (0.2)
7.0 – 8.0	2.7 (1.8)	3.3 (2.9)	4.2	1.6	0.4 (0.3)	1.4	0.9	0.0 (0.2)
8.0 – 9.0	2.7 (1.8)	2.9 (2.6)	2.1	3.8	0.3 (0.4)	1.4	1.0	0.1 (0.1)
9.0 – 10.0	2.7 (1.9)	2.8 (2.5)	5.3	0.6	0.4 (0.3)	1.4	0.4	0.1 (0.0)
10.0 – 11.0	2.6 (1.8)	2.6 (2.3)	5.6	0.8	0.4 (0.3)	1.2	3.2	0.3 (0.0)
11.0 – 12.0	2.6 (1.8)	2.3 (2.1)	2.2	0.2	0.4 (0.4)	0.7	2.5	0.2 (0.2)
12.0 – 13.0	2.7 (2.0)	2.4 (2.1)	3.1	0.0	0.3 (0.4)	1.1	1.0	0.6 (0.0)
13.0 – 14.0	2.7 (2.0)	2.2 (2.0)	5.3	0.2	0.3 (0.3)	1.4	0.2	0.2 (0.5)
14.0 – 15.0	2.7 (2.0)	2.2 (2.0)	6.8	0.2	0.4 (0.3)	1.3	0.1	0.6 (0.4)
15.0 – 16.0	2.7 (2.0)	2.0 (1.8)	6.4	0.7	0.3 (0.3)	1.4	0.2	0.6 (0.2)
16.0 – 18.0	2.7 (2.1)	1.9 (1.7)	6.5	1.0	0.3 (0.3)	1.2	0.9	0.0 (0.5)
18.0 – 20.0	2.7 (2.0)	1.8 (1.6)	5.5	0.9	0.4 (0.3)	1.4	0.0	0.1 (0.1)
20.0 – 22.0	2.8 (2.2)	1.7 (1.6)	3.5	1.8	0.3 (0.3)	1.1	0.5	0.0 (0.0)
22.0 – 25.0	2.8 (2.2)	1.6 (1.4)	3.3	1.6	0.3 (0.3)	1.5	1.1	0.5 (0.2)
25.0 – 30.0	2.8 (2.4)	1.6 (1.5)	2.0	1.6	0.3 (0.3)	1.3	0.5	0.4 (0.2)
30.0 – 50.0	2.6 (2.2)	1.8 (1.6)	4.6	2.0	0.3 (0.3)	1.3	3.7	0.0 (1.0)

Table 4.14: Relative values of the systematic uncertainties on the $\Upsilon(2S)$ integrated and differential fiducial cross section times the dimuon branching fraction, for $|y| < 2.4$, in units of percent. The p_T intervals are in units of GeV/c. The following abbreviations are used: ϵ_{muid}, ϵ_{trig}, ϵ_ρ, ϵ_{func}, ϵ_{trk}, PDF_{CB}, PDF_{bkgd} and M_{scale}, for the systematic uncertainties arising from the statistical uncertainties from tag and probe efficiencies, fixinging the tail parameters in fitting, the background PDF, the mismeasurement of the track momentum shifts that broadens the reconstructed dimuon resonances, fixing the tail parameters in fitting, the statistical uncertainties in tracking efficiencies, the choice of bin size for the efficiencies and from ρ factors. The luminosity uncertainty of 4% is not shown in the table. The numbers in parentheses are negative variations.

$|\mathbf{y}^{\Upsilon}| < \mathbf{2.4}$

$\Upsilon(2S)$

p_T	$\varepsilon_{\text{muid}}$	$\varepsilon_{\text{trig}}$	ε_ρ	$\varepsilon_{\text{func}}$	ε_{trk}	PDF_{CB}	PDF_{bkgd}	M_{scale}
0.0 – 42.0	2.9 (1.9)	3.2 (2.8)	6.7	1.3	0.4 (0.3)	2.2	0.5	0.0 (0.0)
0.0 – 1.0	2.9 (2.9)	3.6 (4.9)	7.4	0.4	0.3 (0.4)	3.3	1.0	1.0 (1.0)
1.0 – 2.5	3.7 (3.7)	4.1 (3.7)	7.6	2.3	0.3 (0.4)	2.2	2.2	3.5 (3.5)
2.5 – 4.0	2.9 (8.7)	3.7 (3.3)	7.1	3.8	0.3 (0.4)	2.5	1.0	0.0 (0.0)
4.0 – 5.5	3.2 (1.0)	3.8 (2.6)	7.6	3.1	0.6 (0.4)	2.4	3.2	0.1 (0.1)
5.5 – 7.0	2.9 (1.6)	3.5 (2.4)	7.0	1.6	0.4 (0.3)	1.8	1.3	0.1 (0.0)
7.0 – 8.5	2.4 (2.1)	3.2 (3.2)	5.6	1.4	0.2 (0.5)	2.6	4.1	0.3 (0.1)
8.5 – 10.0	2.2 (2.2)	2.6 (2.7)	4.7	0.8	0.4 (0.4)	2.6	0.6	0.4 (0.4)
10.0 – 11.5	2.4 (2.0)	2.4 (2.3)	5.8	0.4	0.3 (0.3)	1.1	3.0	0.4 (0.1)
11.5 – 13.0	0.1 (2.5)	2.2 (2.1)	5.1	1.0	0.3 (0.4)	0.3	1.2	0.1 (0.1)
13.0 – 14.5	2.4 (3.5)	1.7 (2.0)	5.7	0.8	0.4 (0.3)	1.7	0.0	0.5 (0.1)
14.5 – 16.0	1.0 (3.7)	0.2 (3.3)	4.8	0.8	0.4 (0.3)	1.5	2.6	0.1 (0.6)
16.0 – 18.0	2.7 (2.0)	1.9 (1.5)	7.2	1.2	0.4 (0.3)	1.7	1.6	0.0 (0.0)
18.0 – 19.5	1.9 (2.5)	1.0 (2.0)	5.0	1.0	0.3 (0.3)	1.7	0.4	0.9 (0.0)
19.5 – 22.0	2.8 (2.3)	1.7 (1.6)	4.5	1.3	0.4 (0.3)	1.7	1.1	1.2 (1.2)
22.0 – 26.0	1.7 (3.2)	0.7 (2.6)	3.7	1.4	0.3 (0.3)	1.7	1.4	1.3 (0.4)
26.0 – 42.0	2.5 (2.4)	1.1 (1.4)	4.4	1.9	0.3 (0.3)	1.7	3.1	0.2 (0.2)

Table 4.15: Relative values of the systematic uncertainties on the $\Upsilon(3S)$ integrated and differential fiducial cross section times the dimuon branching fraction, for $|y| < 2.4$, in units of percent. The p_T intervals are in units of GeV/c. The following abbreviations are used: ϵ_{muid}, ϵ_{trig}, ϵ_{ρ}, ϵ_{func}, ϵ_{trk}, PDF_{CB}, PDF_{bkgd} and M_{scale}, for the systematic uncertainties arising from the statistical uncertainties from tag and probe identification efficiencies, trigger efficiencies, the ρ factors, the choice of bin size of the efficiencies, the statistical uncertainties in tracking efficiencies, fixinging the tail parameters in fitting, the background PDF and the mismeasurement of the track momentum shifts that broadens the reconstructed dimuon resonances. The luminosity uncertainty of 4% is not shown in the table. The numbers in parentheses are negative variations.

$|\mathbf{y}^{\Upsilon}| < \mathbf{2.4}$

$\Upsilon(3S)$

p_T	$\varepsilon_{\text{muid}}$	$\varepsilon_{\text{trig}}$	ε_{ρ}	$\varepsilon_{\text{func}}$	ε_{trk}	PDF_{CB}	PDF_{bkgd}	M_{scale}
0.0 – 38.0	2.9 (1.9)	3.0 (2.6)	6.7	1.5	0.4 (0.3)	3.0	0.6	0.2 (0.2)
0.0 – 2.5	3.2 (2.4)	4.0 (3.5)	8.0	1.6	0.3 (0.3)	3.1	0.0	0.2 (0.1)
2.5 – 5.0	3.7 (3.7)	4.1 (3.0)	7.1	3.7	0.3 (0.4)	3.6	0.0	0.1 (0.5)
5.0 – 7.5	2.7 (1.6)	3.3 (2.7)	3.1	1.4	0.3 (0.5)	3.4	2.5	0.7 (0.2)
7.5 – 10.0	2.8 (1.9)	3.1 (2.8)	4.8	5.2	0.3 (0.4)	2.3	4.2	0.2 (0.2)
10.0 – 13.0	1.2 (2.7)	1.7 (4.2)	4.6	4.0	0.4 (0.4)	1.2	2.5	0.2 (0.2)
13.0 – 16.0	1.4 (4.2)	3.3 (3.3)	3.3	0.5	0.3 (0.4)	1.7	1.3	0.2 (0.5)
16.0 – 18.0	3.1 (2.0)	2.5 (1.8)	6.0	1.3	0.4 (0.3)	2.6	0.5	0.0 (0.0)
18.0 – 22.0	2.5 (2.3)	1.7 (1.9)	4.2	1.3	0.4 (0.3)	2.7	5.1	0.3 (0.3)
22.0 – 38.0	2.5 (2.5)	1.3 (1.8)	1.5	1.4	0.4 (0.3)	2.8	7.9	0.1 (0.1)

Table 4.16: Relative values of the systematic uncertainties on the Υ(nS) integrated and differential fiducial cross section times the dimuon branching fraction, for $|y| < 0.4$, in units of percent. The p_{T} intervals are in units of GeV/c. The following abbreviations are used: ϵ_{muid}, ϵ_{trig}, ϵ_{ρ}, ϵ_{func}, ϵ_{trk}, PDF_{CB}, PDF_{bkgd} and M_{scale}, for the systematic uncertainties arising from the statistical uncertainties from tag and probe identification efficiencies, trigger efficiencies, the ρ factors, the choice of bin size of the efficiencies, the statistical uncertainties in tracking efficiencies, fixinging the tail parameters in fitting, the background PDF and the mismeasurement of the track momentum shifts that broadens the reconstructed dimuon resonances. The luminosity uncertainty of 4% is not shown in the table. The numbers in parentheses are negative variations.

$|\mathbf{y}^{\boldsymbol{\Upsilon}}| < \mathbf{0.4}$

Υ(1S)

p_{T}	$\varepsilon_{\mathrm{muid}}$	$\varepsilon_{\mathrm{trig}}$	ε_{ρ}	$\varepsilon_{\mathrm{func}}$	$\varepsilon_{\mathrm{trk}}$	PDF_{CB}	PDF_{bkgd}	M_{scale}
0.0 – 50.0	3.0 (2.1)	3.8 (3.3)	6.9	1.8	0.4 (0.3)	1.7	0.2	0.0 (0.0)
0.0 – 2.0	3.6 (3.3)	8.6 (7.4)	11.4	6.8	0.4 (0.4)	1.8	3.9	0.1 (0.1)
2.0 – 4.0	3.2 (2.8)	7.0 (6.1)	9.8	5.7	0.4 (0.4)	2.1	1.9	0.1 (0.1)
4.0 – 6.0	2.8 (2.3)	5.6 (5.0)	11.1	4.8	0.4 (0.4)	2.1	0.6	0.3 (0.0)
6.0 – 8.0	7.3 (7.3)	9.4 (9.4)	10.1	4.6	0.4 (0.4)	1.4	3.7	0.4 (0.4)
8.0 – 11.0	2.0 (2.0)	3.2 (3.3)	8.5	2.6	0.4 (0.4)	1.8	2.0	0.1 (0.1)
11.0 – 15.0	2.0 (1.7)	2.3 (2.5)	6.8	0.6	0.3 (0.4)	1.6	0.0	0.2 (0.2)
15.0 – 50.0	1.4 (2.1)	1.1 (2.4)	4.5	0.4	0.3 (0.4)	1.4	2.0	0.0 (0.1)

Υ(2S)

p_{T}	$\varepsilon_{\mathrm{muid}}$	$\varepsilon_{\mathrm{trig}}$	ε_{ρ}	$\varepsilon_{\mathrm{func}}$	$\varepsilon_{\mathrm{trk}}$	PDF_{CB}	PDF_{bkgd}	M_{scale}
0.0 – 42.0	2.9 (1.9)	3.2 (2.8)	6.7	1.3	0.4 (0.3)	2.2	0.5	0.0 (0.0)
0.0 – 3.0	3.4 (3.1)	7.8 (6.7)	10.4	6.6	0.4 (0.4)	1.7	1.6	0.1 (0.1)
3.0 – 7.0	3.7 (3.7)	4.1 (4.0)	13.1	5.6	0.4 (0.3)	3.2	0.5	0.0 (0.0)
7.0 – 11.0	2.9 (1.2)	3.8 (2.5)	8.9	3.3	0.4 (0.4)	1.8	2.1	0.3 (0.3)
11.0 – 15.0	1.9 (1.9)	2.2 (2.6)	6.8	0.2	0.3 (0.4)	1.9	2.0	0.4 (0.4)
15.0 – 42.0	0.7 (2.7)	0.3 (2.9)	4.2	0.6	0.3 (0.4)	1.6	2.3	0.1 (0.1)

Υ(3S)

p_{T}	$\varepsilon_{\mathrm{muid}}$	$\varepsilon_{\mathrm{trig}}$	ε_{ρ}	$\varepsilon_{\mathrm{func}}$	$\varepsilon_{\mathrm{trk}}$	PDF_{CB}	PDF_{bkgd}	M_{scale}
0.0 – 38.0	2.9 (1.9)	3.0 (2.6)	6.7	1.5	0.4 (0.3)	3.0	0.6	0.2 (0.2)
0.0 – 7.0	5.1 (5.1)	7.2 (1.9)	13.1	7.2	0.4 (0.4)	3.5	3.9	0.0 (0.1)
7.0 – 12.0	3.7 (3.7)	4.1 (3.5)	8.8	3.1	0.3 (0.4)	2.8	4.9	0.2 (0.0)
12.0 – 38.0	1.9 (1.9)	1.8 (2.2)	5.4	0.8	0.4 (0.4)	2.5	1.0	0.0 (0.3)

Table 4.17: Relative values of the systematic uncertainties on the Υ(nS) integrated and differential fiducial cross section times the dimuon branching fraction, for $0.4 < |y| < 0.8$, in units of percent. The p_{T} intervals are in units of GeV/c. The following abbreviations are used: ϵ_{muid}, ϵ_{trig}, ϵ_{ρ}, ϵ_{func}, ϵ_{trk}, PDF_{CB}, PDF_{bkgd} and M_{scale}, for the systematic uncertainties arising from the statistical uncertainties from tag and probe identification efficiencies, trigger efficiencies, the ρ factors, the choice of bin size of the efficiencies, the statistical uncertainties in tracking efficiencies, fixinging the tail parameters in fitting, the background PDF and the mismeasurement of the track momentum shifts that broadens the reconstructed dimuon resonances. The luminosity uncertainty of 4% is not shown in the table. The numbers in parentheses are negative variations.

$\mathbf{0.4 < |y^{\Upsilon}| < 0.8}$

Υ(1S)

p_{T}	$\varepsilon_{\mathrm{muid}}$	$\varepsilon_{\mathrm{trig}}$	ε_{ρ}	$\varepsilon_{\mathrm{func}}$	$\varepsilon_{\mathrm{trk}}$	PDF_{CB}	PDF_{bkgd}	M_{scale}
0.0 – 50.0	3.0 (2.1)	3.8 (3.3)	6.9	1.8	0.4 (0.3)	1.7	0.2	0.0 (0.0)
0.0 – 2.0	3.6 (3.3)	8.0 (7.1)	9.8	6.5	0.4 (0.4)	1.7	1.6	0.1 (0.1)
2.0 – 4.0	3.2 (2.7)	6.0 (5.3)	10.5	3.5	0.4 (0.4)	2.1	0.6	0.0 (0.1)
4.0 – 6.0	2.9 (2.4)	4.7 (4.1)	9.0	3.3	0.4 (0.4)	1.8	0.2	0.0 (0.1)
6.0 – 8.0	6.6 (6.6)	8.2 (8.2)	8.2	2.6	0.4 (0.3)	1.4	0.4	0.1 (0.1)
8.0 – 11.0	2.8 (1.4)	3.3 (2.2)	7.0	0.8	0.4 (0.4)	1.6	0.6	0.0 (0.0)
11.0 – 15.0	1.9 (2.0)	1.9 (2.3)	6.6	0.9	0.4 (0.3)	1.5	3.1	0.2 (0.2)
15.0 – 50.0	2.2 (2.0)	1.4 (2.0)	5.1	0.1	0.4 (0.4)	1.4	1.3	0.0 (0.0)

Υ(2S)

p_{T}	$\varepsilon_{\mathrm{muid}}$	$\varepsilon_{\mathrm{trig}}$	ε_{ρ}	$\varepsilon_{\mathrm{func}}$	$\varepsilon_{\mathrm{trk}}$	PDF_{CB}	PDF_{bkgd}	M_{scale}
0.0 – 42.0	2.9 (1.9)	3.2 (2.8)	6.7	1.3	0.4 (0.3)	2.2	0.5	0.0 (0.0)
0.0 – 3.0	3.4 (3.1)	8.1 (6.8)	10.4	5.3	0.3 (0.3)	1.4	1.2	0.2 (0.2)
3.0 – 7.0	1.9 (1.8)	3.1 (3.2)	8.8	2.7	0.4 (0.3)	2.3	0.4	0.1 (0.1)
7.0 – 11.0	4.0 (0.2)	4.3 (1.1)	7.5	1.4	0.4 (0.4)	1.6	0.6	0.3 (0.1)
11.0 – 15.0	1.4 (2.5)	1.3 (2.8)	6.6	1.6	0.3 (0.4)	1.8	0.8	0.5 (0.5)
15.0 – 42.0	1.7 (2.1)	1.1 (2.0)	5.2	0.3	0.3 (0.4)	1.7	1.6	0.2 (0.2)

Υ(3S)

p_{T}	$\varepsilon_{\mathrm{muid}}$	$\varepsilon_{\mathrm{trig}}$	ε_{ρ}	$\varepsilon_{\mathrm{func}}$	$\varepsilon_{\mathrm{trk}}$	PDF_{CB}	PDF_{bkgd}	M_{scale}
0.0 – 38.0	2.9 (1.9)	3.0 (2.6)	6.7	1.5	0.4 (0.3)	3.0	0.6	0.2 (0.2)
0.0 – 7.0	4.5 (0.7)	6.3 (2.3)	11.9	4.7	0.4 (0.3)	3.4	6.4	0.0 (0.1)
7.0 – 12.0	3.7 (3.7)	4.1 (2.3)	6.9	1.8	0.3 (0.4)	2.5	1.8	0.2 (0.2)
12.0 – 38.0	1.6 (2.5)	1.4 (2.7)	6.0	0.1	0.3 (0.3)	2.7	0.8	0.0 (0.2)

Table 4.18: Relative values of the systematic uncertainties on the Υ(nS) integrated and differential fiducial cross section times the dimuon branching fraction, for $0.8 < |y| < 1.2$, in units of percent. The p_{T} intervals are in units of GeV/c. The following abbreviations are used: ϵ_{muid}, ϵ_{trig}, ϵ_{ρ}, ϵ_{func}, ϵ_{trk}, PDF_{CB}, PDF_{bkgd} and M_{scale}, for the systematic uncertainties arising from the statistical uncertainties from tag and probe identification efficiencies, trigger efficiencies, the ρ factors, the choice of bin size of the efficiencies, the statistical uncertainties in tracking efficiencies, fixinging the tail parameters in fitting, the background PDF and the mismeasurement of the track momentum shifts that broadens the reconstructed dimuon resonances. The luminosity uncertainty of 4% is not shown in the table. The numbers in parentheses are negative variations.

$\mathbf{0.8 < |y^{\Upsilon}| < 1.2}$

Υ(1S)

p_{T}	$\varepsilon_{\mathrm{muid}}$	$\varepsilon_{\mathrm{trig}}$	ε_{ρ}	$\varepsilon_{\mathrm{func}}$	$\varepsilon_{\mathrm{trk}}$	PDF_{CB}	PDF_{bkgd}	M_{scale}
0.0 – 50.0	3.0 (2.1)	3.8 (3.3)	6.9	1.8	0.4 (0.3)	1.7	0.2	0.0 (0.0)
0.0 – 2.0	3.7 (3.2)	4.5 (4.0)	8.7	5.1	0.3 (0.3)	1.9	0.4	0.0 (0.0)
2.0 – 4.0	3.0 (2.4)	4.6 (4.1)	8.9	2.7	0.3 (0.3)	2.0	4.8	0.1 (0.1)
4.0 – 6.0	2.8 (2.2)	3.8 (3.4)	7.4	2.1	0.3 (0.4)	1.6	1.6	0.0 (0.2)
6.0 – 8.0	5.9 (5.9)	7.0 (7.0)	7.4	1.1	0.4 (0.3)	1.7	5.9	0.1 (0.2)
8.0 – 11.0	0.0 (4.0)	0.3 (4.6)	6.1	1.3	0.3 (0.3)	1.6	3.3	0.1 (0.1)
11.0 – 15.0	2.0 (2.3)	1.9 (2.5)	6.2	0.8	0.3 (0.4)	1.6	3.0	0.2 (0.2)
15.0 – 50.0	1.5 (2.9)	0.7 (2.3)	6.5	0.1	0.3 (0.3)	1.3	2.6	0.1 (0.1)

Υ(2S)

p_{T}	$\varepsilon_{\mathrm{muid}}$	$\varepsilon_{\mathrm{trig}}$	ε_{ρ}	$\varepsilon_{\mathrm{func}}$	$\varepsilon_{\mathrm{trk}}$	PDF_{CB}	PDF_{bkgd}	M_{scale}
0.0 – 42.0	2.9 (1.9)	3.2 (2.8)	6.7	1.3	0.4 (0.3)	2.2	0.5	0.0 (0.0)
0.0 – 3.0	3.9 (2.9)	4.4 (3.4)	9.5	6.8	0.6 (0.1)	1.8	2.5	0.4 (0.4)
3.0 – 7.0	3.8 (1.1)	5.0 (2.5)	8.5	2.6	0.3 (0.4)	1.7	3.1	0.3 (0.3)
7.0 – 11.0	7.5 (7.5)	8.2 (8.2)	6.6	0.7	0.3 (0.3)	1.9	7.4	0.2 (0.1)
11.0 – 15.0	1.4 (2.7)	1.0 (2.7)	6.1	0.6	0.4 (0.3)	1.8	3.9	0.0 (0.0)
15.0 – 42.0	0.5 (2.5)	3.3 (3.3)	6.2	0.3	0.2 (0.5)	1.7	3.8	0.3 (0.3)

Υ(3S)

p_{T}	$\varepsilon_{\mathrm{muid}}$	$\varepsilon_{\mathrm{trig}}$	ε_{ρ}	$\varepsilon_{\mathrm{func}}$	$\varepsilon_{\mathrm{trk}}$	PDF_{CB}	PDF_{bkgd}	M_{scale}
0.0 – 38.0	2.9 (1.9)	3.0 (2.6)	6.7	1.5	0.4 (0.3)	3.0	0.6	0.2 (0.2)
0.0 – 7.0	2.9 (2.4)	3.7 (3.3)	9.0	1.3	0.4 (0.3)	3.3	15.0	0.3 (0.3)
7.0 – 12.0	3.7 (4.5)	4.1 (9.4)	6.2	0.8	0.3 (0.3)	2.8	9.1	0.4 (0.0)
12.0 – 38.0	4.6 (4.6)	4.6 (4.6)	6.6	0.2	0.3 (0.4)	2.6	5.8	0.5 (0.5)

Table 4.19: Relative values of the systematic uncertainties on the Υ(nS) integrated and differential fiducial cross section times the dimuon branching fraction, for $1.2 < |y| < 1.6$, in units of percent. The p_{T} intervals are in units of GeV/c. The following abbreviations are used: ϵ_{muid}, ϵ_{trig}, ϵ_{ρ}, ϵ_{func}, ϵ_{trk}, PDF_{CB}, PDF_{bkgd} and M_{scale}, for the systematic uncertainties arising from the statistical uncertainties from tag and probe identification efficiencies, trigger efficiencies, the ρ factors, the choice of bin size of the efficiencies, the statistical uncertainties in tracking efficiencies, fixinging the tail parameters in fitting, the background PDF and the mismeasurement of the track momentum shifts that broadens the reconstructed dimuon resonances. The luminosity uncertainty of 4% is not shown in the table. The numbers in parentheses are negative variations.

$\mathbf{1.2 < |y^{\Upsilon}| < 1.6}$

Υ(1S)

p_{T}	$\varepsilon_{\mathrm{muid}}$	$\varepsilon_{\mathrm{trig}}$	ε_{ρ}	$\varepsilon_{\mathrm{func}}$	$\varepsilon_{\mathrm{trk}}$	PDF_{CB}	PDF_{bkgd}	M_{scale}
0.0 – 50.0	3.0 (2.1)	3.8 (3.3)	6.9	1.8	0.4 (0.3)	1.7	0.2	0.0 (0.0)
0.0 – 2.0	3.0 (9.5)	1.2 (3.4)	4.1	1.3	0.3 (0.3)	3.9	2.6	0.2 (2.0)
2.0 – 4.0	2.9 (1.8)	3.6 (3.1)	5.5	1.7	0.3 (0.3)	1.9	1.5	0.1 (0.1)
4.0 – 6.0	2.8 (1.6)	3.1 (2.7)	6.6	1.9	0.4 (0.3)	1.4	0.4	0.2 (0.0)
6.0 – 8.0	2.1 (2.2)	2.1 (2.9)	5.4	1.8	0.3 (0.3)	1.5	2.2	0.1 (0.1)
8.0 – 11.0	2.4 (2.3)	2.1 (2.7)	6.1	0.6	0.4 (0.3)	1.4	1.5	0.1 (0.0)
11.0 – 15.0	2.5 (2.3)	1.7 (2.1)	5.9	0.1	0.3 (0.3)	1.3	2.2	0.2 (0.3)
15.0 – 50.0	0.5 (4.4)	3.6 (3.6)	4.7	1.0	0.3 (0.3)	1.3	4.9	0.0 (0.1)

Υ(2S)

p_{T}	$\varepsilon_{\mathrm{muid}}$	$\varepsilon_{\mathrm{trig}}$	ε_{ρ}	$\varepsilon_{\mathrm{func}}$	$\varepsilon_{\mathrm{trk}}$	PDF_{CB}	PDF_{bkgd}	M_{scale}
0.0 – 42.0	2.9 (1.9)	3.2 (2.8)	6.7	1.3	0.4 (0.3)	2.2	0.5	0.0 (0.0)
0.0 – 3.0	2.8 (1.7)	3.5 (3.1)	6.2	0.1	0.3 (0.3)	2.2	2.3	0.4 (0.4)
3.0 – 7.0	3.0 (1.1)	3.2 (2.1)	6.7	1.4	0.3 (0.3)	2.1	0.3	0.2 (0.2)
7.0 – 11.0	2.3 (2.5)	2.0 (2.8)	5.8	1.4	0.3 (0.3)	1.8	2.5	0.1 (0.1)
11.0 – 15.0	2.4 (2.3)	1.5 (1.9)	5.9	0.7	0.3 (0.3)	1.7	1.7	0.1 (0.3)
15.0 – 42.0	0.0 (4.8)	3.9 (3.9)	4.5	1.0	0.3 (0.3)	1.7	6.2	0.2 (0.2)

Υ(3S)

p_{T}	$\varepsilon_{\mathrm{muid}}$	$\varepsilon_{\mathrm{trig}}$	ε_{ρ}	$\varepsilon_{\mathrm{func}}$	$\varepsilon_{\mathrm{trk}}$	PDF_{CB}	PDF_{bkgd}	M_{scale}
0.0 – 38.0	2.9 (1.9)	3.0 (2.6)	6.7	1.5	0.4 (0.3)	3.0	0.6	0.2 (0.2)
0.0 – 7.0	2.5 (1.5)	2.7 (2.4)	5.9	2.0	0.4 (0.3)	2.9	0.9	0.1 (0.1)
7.0 – 12.0	3.7 (3.7)	4.1 (3.0)	6.1	0.4	0.3 (0.3)	2.7	6.2	0.8 (0.8)
12.0 – 38.0	2.5 (2.6)	1.5 (2.1)	5.2	0.6	0.4 (0.3)	2.7	5.9	0.0 (0.0)

Table 4.20: Relative values of the systematic uncertainties on the Υ(nS) integrated and differential fiducial cross section times the dimuon branching fraction, for $1.6 < |y| < 2.0$, in units of percent. The p_{T} intervals are in units of GeV/c. The following abbreviations are used: ϵ_{muid}, ϵ_{trig}, ϵ_{ρ}, ϵ_{func}, ϵ_{trk}, PDF_{CB}, PDF_{bkgd} and M_{scale}, for the systematic uncertainties arising from the statistical uncertainties from tag and probe identification efficiencies, trigger efficiencies, the ρ factors, the choice of bin size of the efficiencies, the statistical uncertainties in tracking efficiencies, fixinging the tail parameters in fitting, the background PDF and the mismeasurement of the track momentum shifts that broadens the reconstructed dimuon resonances. The luminosity uncertainty of 4% is not shown in the table. The numbers in parentheses are negative variations.

$\mathbf{1.6 < |y^{\Upsilon}| < 2.0}$

Υ(1S)

p_{T}	$\varepsilon_{\mathrm{muid}}$	$\varepsilon_{\mathrm{trig}}$	ε_{ρ}	$\varepsilon_{\mathrm{func}}$	$\varepsilon_{\mathrm{trk}}$	PDF_{CB}	PDF_{bkgd}	M_{scale}
0.0 – 50.0	3.0 (2.1)	3.8 (3.3)	6.9	1.8	0.4 (0.3)	1.7	0.2	0.0 (0.0)
0.0 – 2.0	4.0 (2.7)	3.3 (2.9)	4.4	1.7	0.3 (0.3)	2.0	5.9	0.2 (0.2)
2.0 – 4.0	3.4 (1.6)	3.6 (2.6)	4.4	0.6	0.4 (0.4)	1.3	1.7	0.7 (0.1)
4.0 – 6.0	3.0 (1.3)	2.7 (2.5)	3.5	0.4	0.3 (0.4)	1.5	1.9	0.0 (0.1)
6.0 – 8.0	2.5 (1.6)	1.9 (2.5)	3.2	0.3	0.3 (0.3)	1.3	0.8	0.0 (0.0)
8.0 – 11.0	2.7 (2.0)	1.8 (2.3)	2.3	0.0	0.4 (0.3)	1.3	4.5	0.1 (0.1)
11.0 – 15.0	3.2 (2.8)	1.9 (2.2)	3.8	1.3	0.4 (0.3)	1.1	0.1	0.1 (0.1)
15.0 – 50.0	3.4 (3.2)	1.8 (2.0)	1.9	3.7	0.3 (0.3)	1.0	0.2	0.0 (0.1)

Υ(2S)

p_{T}	$\varepsilon_{\mathrm{muid}}$	$\varepsilon_{\mathrm{trig}}$	ε_{ρ}	$\varepsilon_{\mathrm{func}}$	$\varepsilon_{\mathrm{trk}}$	PDF_{CB}	PDF_{bkgd}	M_{scale}
0.0 – 42.0	2.9 (1.9)	3.2 (2.8)	6.7	1.3	0.4 (0.3)	2.2	0.5	0.0 (0.0)
0.0 – 3.0	3.8 (2.9)	2.7 (2.3)	4.2	1.3	0.3 (0.4)	2.7	5.7	0.2 (0.2)
3.0 – 7.0	2.9 (0.9)	2.8 (2.4)	3.7	0.4	0.5 (0.3)	2.2	3.9	0.0 (0.2)
7.0 – 11.0	2.7 (2.3)	1.8 (2.0)	2.1	0.1	0.3 (0.3)	1.9	9.4	0.3 (0.3)
11.0 – 15.0	3.3 (3.0)	2.0 (2.3)	3.9	1.1	0.4 (0.4)	1.6	1.8	0.2 (0.1)
15.0 – 42.0	3.6 (3.2)	1.9 (1.9)	1.6	3.4	0.3 (0.3)	1.8	0.5	0.1 (0.2)

Υ(3S)

p_{T}	$\varepsilon_{\mathrm{muid}}$	$\varepsilon_{\mathrm{trig}}$	ε_{ρ}	$\varepsilon_{\mathrm{func}}$	$\varepsilon_{\mathrm{trk}}$	PDF_{CB}	PDF_{bkgd}	M_{scale}
0.0 – 38.0	2.9 (1.9)	3.0 (2.6)	6.7	1.5	0.4 (0.3)	3.0	0.6	0.2 (0.2)
0.0 – 7.0	3.3 (1.6)	2.7 (2.4)	3.9	0.7	0.4 (0.3)	3.7	6.8	0.2 (0.2)
7.0 – 12.0	3.7 (3.7)	4.1 (2.1)	1.9	0.2	0.3 (0.3)	2.9	13.7	1.3 (1.3)
12.0 – 38.0	3.2 (3.2)	1.6 (2.2)	2.9	2.6	0.3 (0.3)	2.5	2.8	0.1 (1.7)

Table 4.21: Relative values of the systematic uncertainties on the Υ(nS) integrated and differential fiducial cross section times the dimuon branching fraction, for $2.0 < |y| < 2.4$, in units of percent. The p_{T} intervals are in units of GeV/c. The following abbreviations are used: ϵ_{muid}, ϵ_{trig}, ϵ_{ρ}, ϵ_{func}, ϵ_{trk}, PDF_{CB}, PDF_{bkgd} and M_{scale}, for the systematic uncertainties arising from the statistical uncertainties from tag and probe identification efficiencies, trigger efficiencies, the ρ factors, the choice of bin size of the efficiencies, the statistical uncertainties in tracking efficiencies, fixinging the tail parameters in fitting, the background PDF and the mismeasurement of the track momentum shifts that broadens the reconstructed dimuon resonances. The luminosity uncertainty of 4% is not shown in the table. The numbers in parentheses are negative variations.

$\mathbf{2.0 < |y^{\Upsilon}| < 2.4}$

Υ(1S)

p_{T}	$\varepsilon_{\mathrm{muid}}$	$\varepsilon_{\mathrm{trig}}$	ε_{ρ}	$\varepsilon_{\mathrm{func}}$	$\varepsilon_{\mathrm{trk}}$	PDF_{CB}	PDF_{bkgd}	M_{scale}
0.0 – 50.0	3.0 (2.1)	3.8 (3.3)	6.9	1.8	0.4 (0.3)	1.7	0.2	0.0 (0.0)
0.0 – 2.0	5.2 (5.3)	2.7 (2.3)	3.6	2.1	0.4 (0.4)	1.6	6.2	0.2 (0.2)
2.0 – 4.0	4.5 (1.2)	3.6 (2.1)	3.2	0.5	1.0 (0.0)	1.7	0.2	0.2 (0.2)
4.0 – 6.0	5.6 (5.6)	7.4 (7.4)	3.6	1.8	0.4 (0.4)	1.2	6.7	0.0 (0.2)
6.0 – 8.0	0.8 (4.6)	5.3 (5.3)	2.4	0.1	0.4 (0.4)	1.0	2.0	0.0 (0.0)
8.0 – 11.0	4.2 (2.9)	2.3 (2.7)	1.3	2.7	0.4 (0.4)	1.2	2.3	0.4 (0.4)
11.0 – 15.0	4.5 (3.6)	2.8 (2.7)	1.5	4.9	0.4 (0.4)	0.9	4.7	0.4 (0.4)
15.0 – 50.0	5.0 (4.5)	2.2 (2.8)	0.1	6.3	0.4 (0.4)	0.7	9.3	0.6 (0.6)

Υ(2S)

p_{T}	$\varepsilon_{\mathrm{muid}}$	$\varepsilon_{\mathrm{trig}}$	ε_{ρ}	$\varepsilon_{\mathrm{func}}$	$\varepsilon_{\mathrm{trk}}$	PDF_{CB}	PDF_{bkgd}	M_{scale}
0.0 – 42.0	2.9 (1.9)	3.2 (2.8)	6.7	1.3	0.4 (0.3)	2.2	0.5	0.0 (0.0)
0.0 – 3.0	4.6 (3.4)	2.1 (1.9)	3.6	0.8	0.3 (0.4)	2.5	9.1	0.0 (0.0)
3.0 – 7.0	3.9 (0.8)	3.0 (2.5)	3.1	0.4	0.4 (0.4)	2.2	6.2	0.0 (0.2)
7.0 – 11.0	4.4 (3.2)	2.4 (2.6)	1.6	3.5	0.4 (0.3)	1.8	5.7	0.5 (0.5)
11.0 – 15.0	4.5 (3.4)	2.3 (2.4)	1.6	4.6	0.3 (0.3)	1.6	3.3	0.5 (0.5)
15.0 – 42.0	4.9 (3.8)	2.5 (2.2)	0.3	6.2	0.4 (0.2)	2.3	4.4	1.4 (1.4)

Υ(3S)

p_{T}	$\varepsilon_{\mathrm{muid}}$	$\varepsilon_{\mathrm{trig}}$	ε_{ρ}	$\varepsilon_{\mathrm{func}}$	$\varepsilon_{\mathrm{trk}}$	PDF_{CB}	PDF_{bkgd}	M_{scale}
0.0 – 38.0	2.9 (1.9)	3.0 (2.6)	6.7	1.5	0.4 (0.3)	3.0	0.6	0.2 (0.2)
0.0 – 7.0	4.3 (1.9)	2.4 (2.2)	3.3	0.0	0.4 (0.4)	3.5	7.8	0.6 (0.1)
7.0 – 12.0	3.7 (3.7)	4.1 (3.1)	1.2	4.3	0.4 (0.4)	2.5	0.3	0.3 (0.3)
12.0 – 38.0	4.5 (4.2)	2.1 (2.6)	0.8	6.3	0.4 (0.4)	2.0	1.0	0.6 (0.6)

Table 4.22: Relative values of the systematic uncertainties on the Υ(nS) integrated and rapidity differential fiducial cross section times the dimuon branching fraction, for $p_{\mathrm{T}} < 50$ GeV/c, in units of percent. The following abbreviations are used: ϵ_{muid}, ϵ_{trig}, ϵ_{ρ}, ϵ_{func}, ϵ_{trk}, PDF_{CB}, PDF_{bkgd} and M_{scale}, for the systematic uncertainties arising from the statistical uncertainties from tag and probe identification efficiencies, trigger efficiencies, the ρ factors, the choice of bin size of the efficiencies, the statistical uncertainties in tracking efficiencies, fixinging the tail parameters in fitting, the background PDF and the mismeasurement of the track momentum shifts that broadens the reconstructed dimuon resonances. The luminosity uncertainty of 4% is not shown in the table. The numbers in parentheses are negative variations.

$p_{\mathrm{T}}^{\Upsilon} < 50\,\mathrm{GeV}/c$

Υ(1S)

$\lvert y\rvert$	$\varepsilon_{\mathrm{muid}}$	$\varepsilon_{\mathrm{trig}}$	ε_{ρ}	$\varepsilon_{\mathrm{func}}$	$\varepsilon_{\mathrm{trk}}$	PDF_{CB}	PDF_{bkgd}	M_{scale}
0.0 – 2.4	3.0 (2.1)	3.8 (3.4)	6.9	1.8	0.4 (0.3)	1.7	0.2	0.0 (0.0)
0.0 – 0.2	2.8 (2.3)	5.5 (4.8)	10.5	3.6	0.4 (0.4)	2.2	2.1	0.0 (0.0)
0.2 – 0.4	4.0 (4.0)	4.1 (4.5)	8.8	4.1	0.4 (0.4)	2.3	1.3	0.0 (0.0)
0.4 – 0.6	2.8 (2.3)	4.8 (4.3)	12.2	2.8	0.4 (0.4)	2.2	1.1	0.0 (0.0)
0.6 – 0.8	2.9 (2.4)	4.3 (3.8)	5.6	2.6	0.4 (0.4)	2.2	1.5	0.0 (0.0)
0.8 – 1.0	2.9 (2.3)	3.9 (3.4)	12.0	2.4	0.3 (0.3)	2.1	0.6	0.1 (0.1)
1.0 – 1.2	2.8 (2.1)	3.2 (3.2)	3.7	1.9	0.3 (0.3)	1.9	2.2	0.0 (0.0)
1.2 – 1.4	2.7 (1.9)	3.2 (2.8)	9.1	1.9	0.3 (0.3)	1.8	2.2	0.0 (0.0)
1.4 – 1.6	2.9 (1.7)	3.1 (2.7)	2.9	0.9	0.3 (0.3)	1.8	0.5	0.0 (0.0)
1.6 – 1.8	3.2 (1.8)	2.9 (2.5)	5.9	0.1	0.3 (0.3)	2.0	2.1	0.0 (0.1)
1.8 – 2.0	3.6 (1.8)	2.7 (2.3)	0.8	0.8	0.3 (0.3)	1.7	3.3	0.0 (0.0)
2.0 – 2.2	4.7 (1.1)	3.3 (1.9)	2.5	0.1	1.0 (1.0)	1.7	3.4	0.7 (0.7)
2.2 – 2.4	4.4 (1.1)	2.8 (2.4)	3.2	1.4	0.7 (0.7)	1.8	2.3	0.6 (0.6)

Υ(2S)

$\lvert y\rvert$	$\varepsilon_{\mathrm{muid}}$	$\varepsilon_{\mathrm{trig}}$	ε_{ρ}	$\varepsilon_{\mathrm{func}}$	$\varepsilon_{\mathrm{trk}}$	PDF_{CB}	PDF_{bkgd}	M_{scale}
0.0 – 2.4	2.9 (1.9)	3.2 (2.8)	6.7	1.3	0.4 (0.3)	2.2	0.5	0.0 (0.0)
0.0 – 0.4	2.5 (1.9)	4.0 (3.6)	9.1	2.7	0.4 (0.4)	2.7	1.7	0.0 (0.0)
0.4 – 0.8	3.7 (3.7)	4.1 (3.0)	8.4	1.9	0.4 (0.3)	2.6	0.4	0.0 (0.0)
0.8 – 1.2	2.6 (2.0)	3.2 (2.8)	7.6	1.6	0.3 (0.3)	2.6	3.8	0.0 (0.0)
1.2 – 1.6	2.7 (1.7)	2.7 (2.4)	6.0	1.1	0.3 (0.3)	2.2	2.4	0.1 (0.1)
1.6 – 2.0	3.3 (2.0)	2.5 (2.2)	3.5	0.6	0.4 (0.3)	2.5	3.5	0.1 (0.1)
2.0 – 2.4	3.7 (2.2)	3.2 (3.2)	2.6	1.0	0.2 (0.6)	2.7	3.9	0.5 (0.5)

Υ(3S)

$\lvert y\rvert$	$\varepsilon_{\mathrm{muid}}$	$\varepsilon_{\mathrm{trig}}$	ε_{ρ}	$\varepsilon_{\mathrm{func}}$	$\varepsilon_{\mathrm{trk}}$	PDF_{CB}	PDF_{bkgd}	M_{scale}
0.0 – 2.4	2.9 (1.9)	3.0 (2.6)	6.7	1.5	0.4 (0.3)	3.0	0.6	0.2 (0.2)
0.0 – 0.4	2.4 (1.8)	3.6 (3.2)	9.0	3.0	0.4 (0.3)	3.5	2.5	0.0 (0.0)
0.4 – 0.8	3.7 (3.7)	4.1 (2.9)	8.4	2.1	0.4 (0.3)	3.4	0.6	0.1 (0.1)
0.8 – 1.4	2.5 (1.9)	2.9 (2.6)	8.1	0.7	0.3 (0.4)	3.3	2.9	0.1 (0.1)
1.4 – 2.0	3.1 (1.8)	2.4 (2.1)	3.4	0.7	0.3 (0.3)	3.5	4.7	0.0 (0.1)
2.0 – 2.4	4.6 (1.3)	2.6 (2.5)	2.6	0.6	0.2 (0.2)	2.3	3.3	0.5 (1.1)

Table 4.23: The product of the Υ(nS) production cross sections and the dimuon branching fraction, in nb, integrated over the rapidity range $|y^{\Upsilon}| < 1.2$ and the p_{T} range from 10 to 50 GeV/c. The cross sections assume the Υ(nS) are unpolarized. The statistical uncertainty (stat.), the sum in quadrature of the systematic uncertainties apart from the ones from the polarization ($\sum_{\mathrm{syst.}}$), the systematic uncertainties from the polarization (syst.(pol)), and the total uncertainty ($\Delta\sigma$; including stat., $\sum_{\mathrm{syst.}}$, syst.(pol), luminosity terms) are in percent. The numbers in parentheses are negative variations.

	σ	$\frac{stat.}{\sigma}$	$\frac{\sum_{\mathrm{syst.}}}{\sigma}$	$\frac{syst.(pol.)}{\sigma}$	$\frac{\Delta\sigma}{\sigma}$
Υ(1S)	0.56	1.2	7.6 (5.5)	3.5 (1.5)	8.5 (5.8)
Υ(2S)	0.21	2.3	7.7 (5.5)	7.5 (3.5)	11.0 (6.9)
Υ(3S)	0.13	3.2	8.3 (5.9)	6.5 (3.4)	11.0 (7.5)

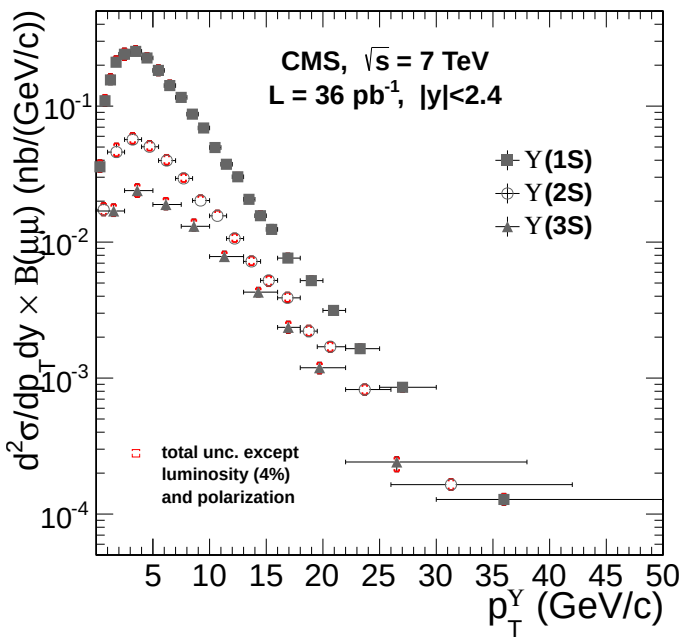

Figure 4.7.: Differential cross section of the Υ(nS) as a function of p_{T} in the rapidity range $|y| < 2.4$.

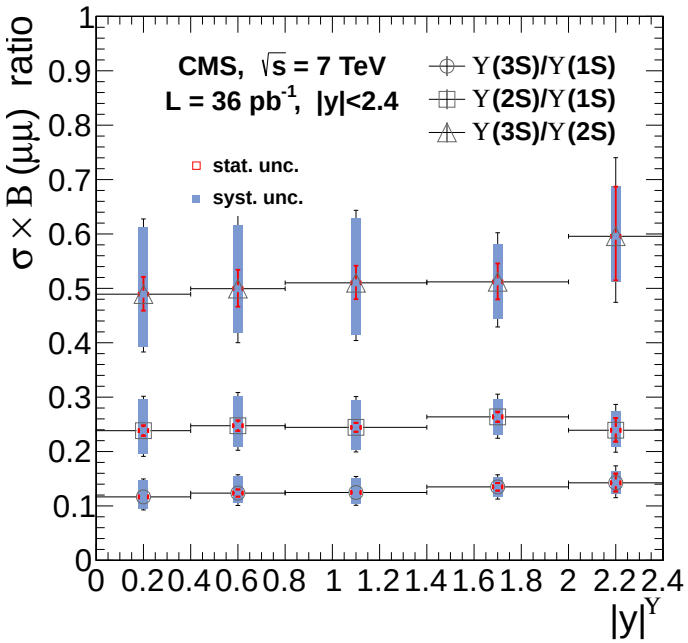

Figure 4.8.: Ratio of differential cross section of the Υ(nS) as a function of rapidity in the p_{T} range $p_T < 50\,\mathrm{GeV}/c$.

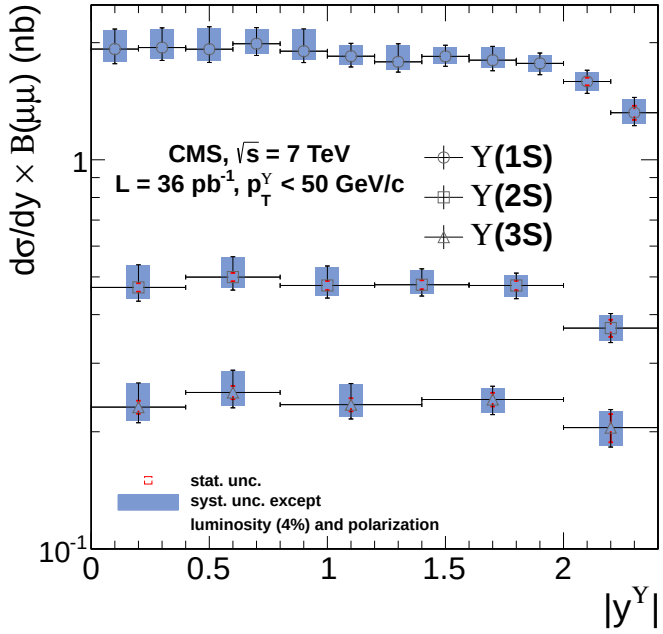

Figure 4.9.: Differential production cross section of the Υ(nS) as a function of rapidity.

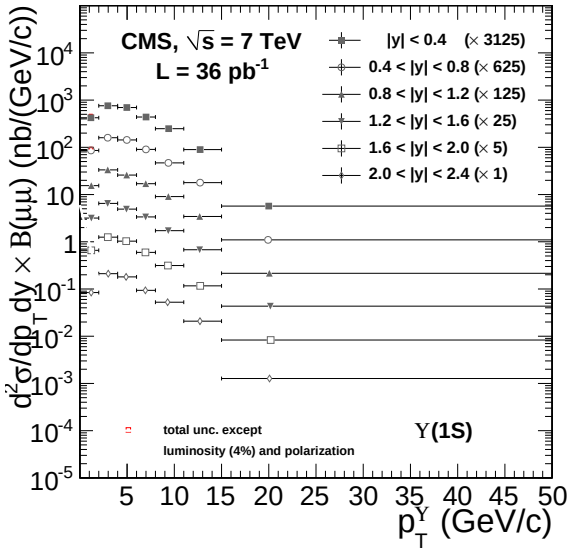

(a) Υ(1S)

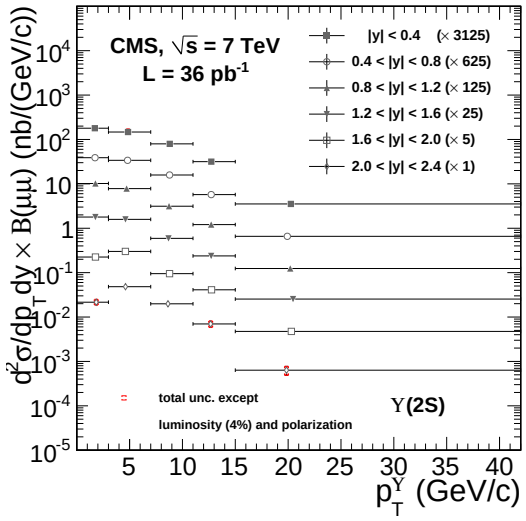

(b) Υ(2S)

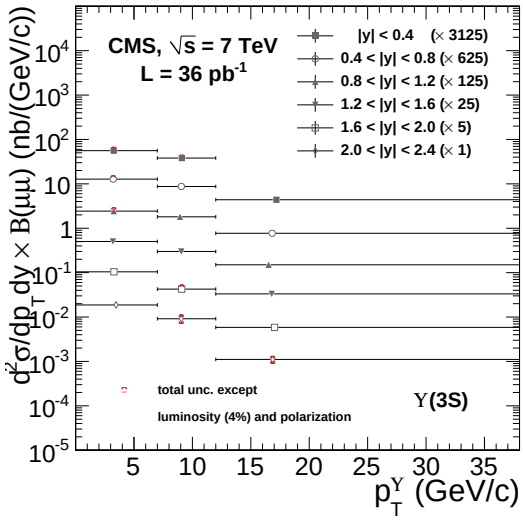

(c) Υ(3S)

Figure 4.10.: Differential production cross section results of the Υ(nS) as a function of p_{T} in six rapidity regions.

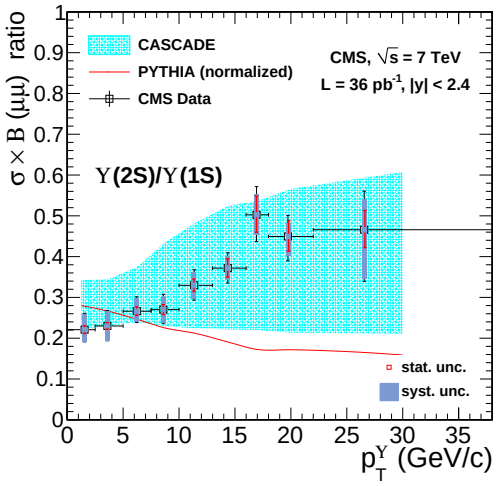

(a) $\Upsilon(2S)/\Upsilon(1S)$

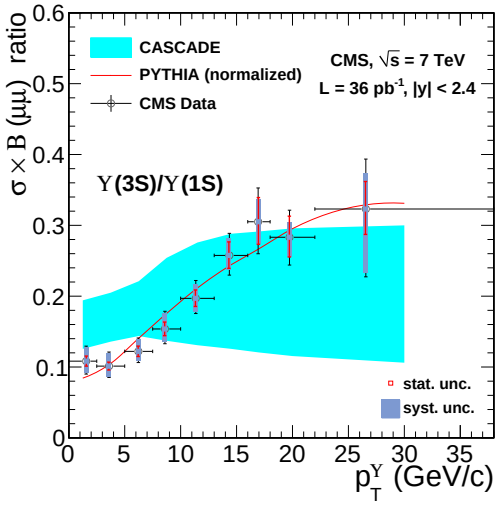

(b) $\Upsilon(3S)/\Upsilon(1S)$

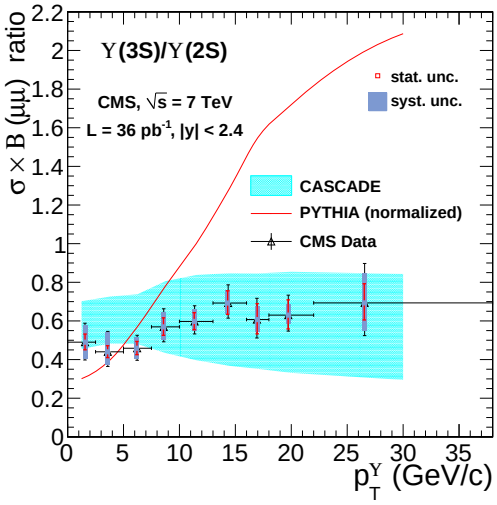

(c) $\Upsilon(3S)/\Upsilon(2S)$

Figure 4.11.: Ratios of differential cross sections for $\Upsilon(\mathrm{nS})$ as a function of $p_{\mathrm{T}}^{\Upsilon}$ in the rapidity range $|y|^{\Upsilon} < 2.4$ and comparison to CASCADE and PYTHIA. The width of a band indicates an estimate of the uncertainty in the prediction by the author of the prediction.

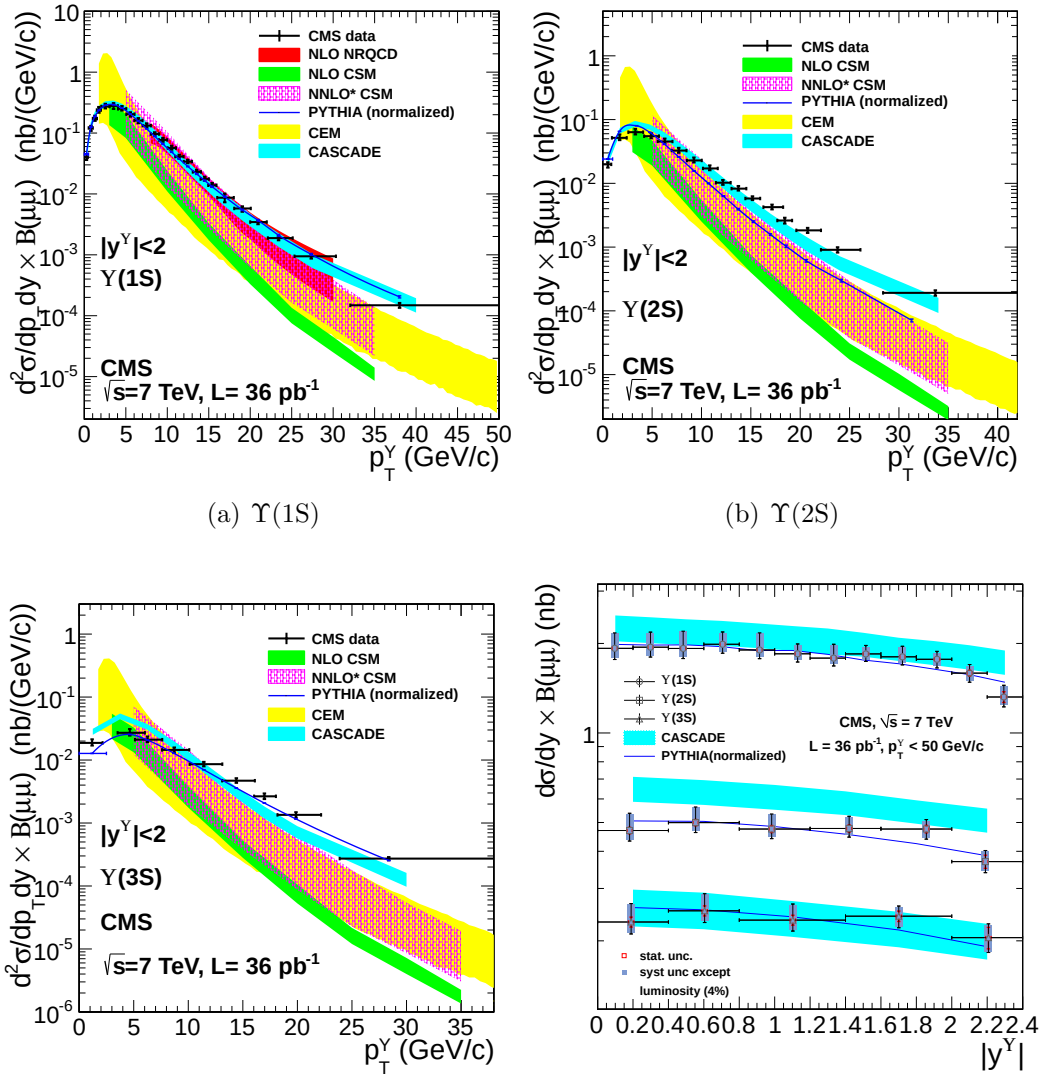

(a) $\Upsilon(1S)$ (b) $\Upsilon(2S)$

(c) $\Upsilon(3S)$ (d)

Figure 4.12.: Differential cross section of the (a) $\Upsilon(1S)$, (b) $\Upsilon(2S)$ and (c) $\Upsilon(3S)$ as a function of p_T^{Υ} in the rapidity range $|y|^{\Upsilon} < 2$, and comparison to various theoretical predictions. (d) Differential cross section of the $\Upsilon(nS)$ as a function of rapidity and comparison to CASCADE and PYTHIA. The width of a band indicates an estimate of the uncertainty in the prediction by the author of the prediction.

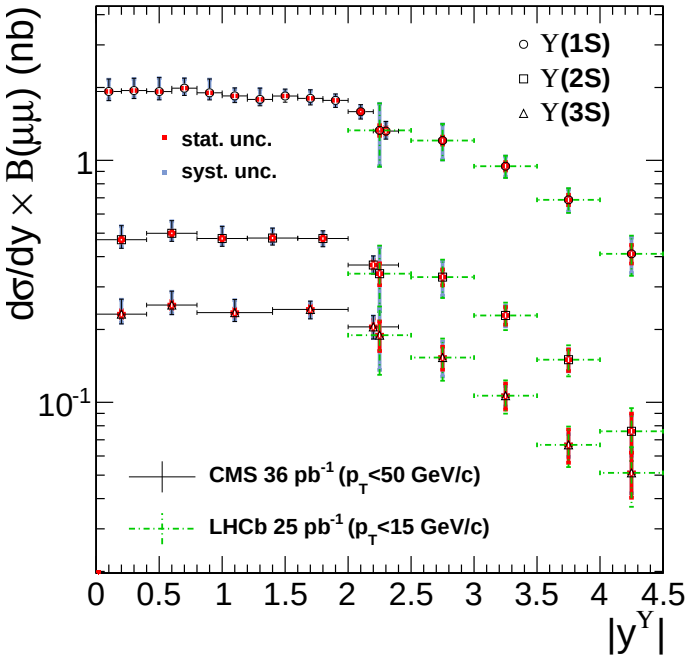

Figure 4.13.: Differential cross section of the $\Upsilon(1S)$ as a function of rapidity and comparison to LHCb results.

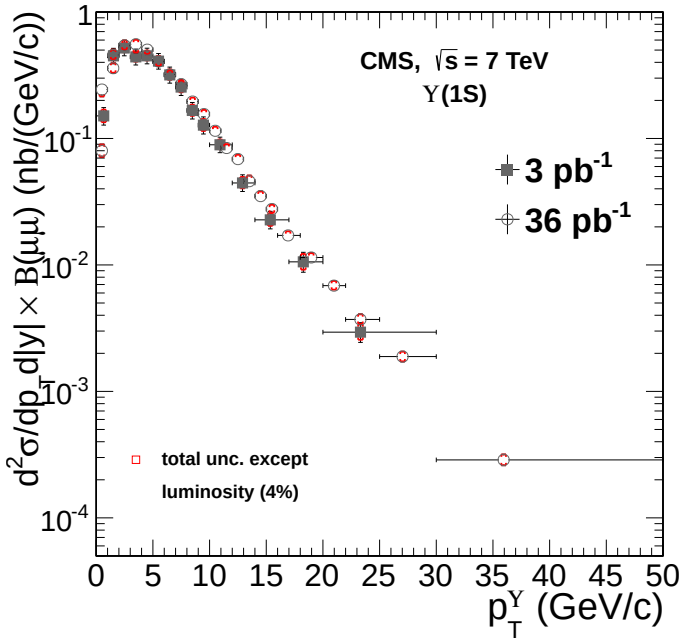

Figure 4.14.: Differential cross section of the $\Upsilon(1S)$ as a function of p_T in the rapidity range $|y| < 2.0$, and comparison to the previous results using 3 pb^{-1} of data.

Table 4.24: The product of the $\Upsilon(1S)$ integrated and differential production cross sections and the dimuon branching fraction, in nb, measured for four polarization scenarios, in helicity frame (HX) and Collins-Soper (CS) frame, each for L= 100% longitudinal, and T= 100% transverse, integrated over the rapidity range $|y^{\Upsilon}| < 2.4$. The statistical uncertainty (stat.), the sum of the systematic uncertainties in quadrature ($\Sigma_{\text{syst.}}$), and the total uncertainty ($\Delta\sigma$; including stat., $\sum_{\text{syst.}}$, luminosity terms) are in percent. For the four polarization scenarios the fractional change in percent to the central value of the cross section relative to the unpolarized value is given. The numbers in parentheses are negative variations.

$|y^{\Upsilon}| < 2.4$

$\Upsilon(1S)$

p_T (GeV/c)	σ	stat./σ	$\sum_{\text{syst.}}/\sigma$	$\Delta\sigma/\sigma$	HX T	HX L	CS T	CS L
0.0 – 50.0	8.55	0.6	9 (8)	10 (9)	+19	−24	+16	−19
0.0 – 0.5	0.09	5.4	11 (10)	13 (12)	+19	−24	+21	−26
0.5 – 1.0	0.26	3.3	11 (10)	12 (12)	+22	−24	+23	−25
1.0 – 1.5	0.37	2.6	10 (10)	11 (11)	+23	−22	+26	−24
1.5 – 2.0	0.50	2.4	11 (10)	12 (11)	+16	−27	+19	−29
2.0 – 3.0	1.16	1.6	10 (12)	11 (13)	+20	−25	+26	−27
3.0 – 4.0	1.21	2.1	10 (9)	11 (10)	+20	−26	+21	−26
4.0 – 5.0	1.08	2.1	9 (9)	10 (10)	+21	−25	+21	−24
5.0 – 6.0	0.88	1.9	9 (11)	10 (11)	+19	−25	+16	−23
6.0 – 7.0	0.68	2.6	9 (8)	10 (9)	+18	−24	+13	−23
7.0 – 8.0	0.56	2.0	7 (7)	9 (8)	+20	−22	+12	−13
8.0 – 9.0	0.42	2.2	7 (6)	8 (8)	+19	−22	+9	−9
9.0 – 10.0	0.33	2.3	6 (5)	8 (7)	+19	−21	+7	−4
10.0 – 11.0	0.24	2.5	7 (6)	8 (8)	+17	−20	+4	−1
11.0 – 12.0	0.18	2.9	5 (4)	7 (7)	+18	−19	+6	+0
12.0 – 13.0	0.15	2.9	7 (6)	8 (8)	+16	−20	+2	+2
13.0 – 14.0	0.10	3.2	6 (7)	8 (8)	+14	−21	−0	+3
14.0 – 15.0	0.08	3.6	8 (7)	9 (9)	+15	−20	−1	+5
15.0 – 16.0	0.06	3.8	7 (7)	9 (9)	+13	−19	−1	+5
16.0 – 18.0	0.07	3.4	7 (7)	9 (9)	+12	−20	−3	+6
18.0 – 20.0	0.05	3.8	7 (7)	9 (9)	+13	−18	−2	+7
20.0 – 22.0	0.03	5.1	5 (5)	8 (8)	+11	−18	−3	+6
22.0 – 25.0	0.02	5.6	5 (5)	9 (8)	+9	−18	−3	+4
25.0 – 30.0	0.02	6.0	5 (4)	9 (8)	+10	−16	−1	+4
30.0 – 50.0	0.01	7.4	7 (7)	11 (11)	+5	−17	−7	+3

Table 4.25: The product of the Υ(2S) integrated and differential production cross sections and the dimuon branching fraction, in nb, measured for four polarization scenarios, in helicity frame (HX) and Collins-Soper (CS) frame, each for L= 100% longitudinal, and T= 100% transverse, integrated over the rapidity range $|y^{\Upsilon}| < 2.4$. The statistical uncertainty (stat.), the sum of the systematic uncertainties in quadrature ($\Sigma_{\text{syst.}}$), and the total uncertainty ($\Delta\sigma$; including stat., $\sum_{\text{syst.}}$, luminosity terms) are in percent. For the four polarization scenarios the fractional change in percent to the central value of the cross section relative to the unpolarized value is given. The numbers in parentheses are negative variations.

$|y^{\Upsilon}| < 2.4$

Υ(2S)

p_{T} (GeV/c)	σ	stat./σ	$\sum_{\text{syst.}}/\sigma$	$\Delta\sigma/\sigma$	HX T	HX L	CS T	CS L
0.0 – 42.0	2.21	1.2	10 (9)	10 (10)	+14	−24	+13	−20
0.0 – 1.0	0.08	5.9	11 (11)	13 (13)	+18	−23	+19	−24
1.0 – 2.5	0.33	3.3	15 (15)	16 (16)	+14	−23	+18	−25
2.5 – 4.0	0.41	3.1	12 (11)	13 (12)	+22	−24	+21	−26
4.0 – 5.5	0.36	3.3	10 (9)	11 (11)	+18	−22	+16	−24
5.5 – 7.0	0.29	3.6	10 (10)	12 (11)	+17	−23	+15	−20
7.0 – 8.5	0.21	3.9	8 (7)	9 (9)	+21	−20	+15	−12
8.5 – 10.0	0.15	4.0	8 (7)	10 (9)	+20	−18	+11	−5
10.0 – 11.5	0.11	4.1	8 (8)	10 (10)	+19	−18	+8	−0
11.5 – 13.0	0.08	4.6	7 (7)	9 (9)	+17	−18	+6	+1
13.0 – 14.5	0.05	5.1	7 (7)	10 (9)	+14	−20	+0	+3
14.5 – 16.0	0.04	5.7	6 (8)	9 (11)	+14	−19	+1	+3
16.0 – 18.0	0.04	5.3	8 (8)	10 (10)	+13	−18	+1	+3
18.0 – 19.5	0.02	7.4	7 (6)	11 (10)	+13	−18	−3	+9
19.5 – 22.0	0.02	6.6	6 (6)	10 (10)	+11	−16	−1	+5
22.0 – 26.0	0.02	7.2	6 (5)	10 (10)	+11	−16	−3	+7
26.0 – 42.0	0.01	7.7	7 (7)	11 (11)	+10	−15	−4	+9

Table 4.26: The product of the Υ(3S) integrated and differential production cross sections and the dimuon branching fraction, in nb, measured for four polarization scenarios, in helicity frame (HX) and Collins-Soper (CS) frame, each for L= 100% longitudinal, and T= 100% transverse, integrated over the rapidity range $|y^{\Upsilon}| < 2.4$. The statistical uncertainty (stat.), the sum of the systematic uncertainties in quadrature ($\Sigma_{\text{syst.}}$), and the total uncertainty ($\Delta\sigma$; including stat., $\sum_{\text{syst.}}$, luminosity terms) are in percent. For the four polarization scenarios the fractional change in percent to the central value of the cross section relative to the unpolarized value is given. The numbers in parentheses are negative variations.

$|y^{\Upsilon}| < 2.4$

Υ(3S)

p_{T} (GeV/c)	σ	stat./σ	$\sum_{\text{syst.}}/\sigma$	$\Delta\sigma/\sigma$	HX T	HX L	CS T	CS L
0.0 – 38.0	1.11	2.0	11 (10)	11 (11)	+16	-21	+14	-17
0.0 – 2.5	0.20	5.3	12 (11)	13 (13)	+17	-21	+20	-25
2.5 – 5.0	0.29	4.5	13 (13)	14 (14)	+17	-22	+20	-25
5.0 – 7.5	0.23	4.6	12 (11)	13 (13)	+16	-22	+20	-22
7.5 – 10.0	0.16	4.8	12 (11)	13 (13)	+23	-16	+16	-5
10.0 – 13.0	0.11	4.3	8 (7)	10 (9)	+20	-15	+12	-1
13.0 – 16.0	0.06	5.0	7 (6)	9 (9)	+14	-17	+4	+1
16.0 – 18.0	0.02	7.4	8 (7)	11 (11)	+12	-18	-1	+4
18.0 – 22.0	0.02	7.0	7 (7)	11 (11)	+12	-17	-1	+6
22.0 – 38.0	0.02	7.6	13 (13)	15 (15)	+10	-15	-0	+6

Table 4.27: The product of the Υ(nS) integrated and differential production cross sections and the dimuon branching fraction, in nb, measured for four polarization scenarios, in helicity frame (HX) and Collins-Soper (CS) frame, each for L= 100% longitudinal, and T= 100% transverse, integrated over the rapidity range $|y^{\Upsilon}| < 0.4$. The statistical uncertainty (stat.), the sum of the systematic uncertainties in quadrature ($\Sigma_{\text{syst.}}$), and the total uncertainty ($\Delta\sigma$; including stat., $\sum_{\text{syst.}}$, luminosity terms) are in percent. For the four polarization scenarios the fractional change in percent to the central value of the cross section relative to the unpolarized value is given. The numbers in parentheses are negative variations.

$|y^{\Upsilon}| < 0.4$

Υ(1S)

p_{T} (GeV/c)	σ	stat./σ	$\sum_{\text{syst.}}/\sigma$	$\Delta\sigma/\sigma$	HX T	HX L	CS T	CS L
0.0 – 50.0	1.51	0.2	9 (9)	10 (10)	+19	-24	+16	-19
0.0 – 2.0	0.22	3.4	17 (16)	18 (17)	+10	-16	+21	-27
2.0 – 4.0	0.39	3.2	14 (13)	15 (14)	+15	-22	+20	-26
4.0 – 6.0	0.36	3.0	14 (14)	15 (15)	+21	-27	+16	-22
6.0 – 8.0	0.22	3.2	12 (12)	13 (13)	+17	-30	+3	-17
8.0 – 11.0	0.19	2.9	10 (10)	11 (11)	+22	-27	-0	+1
11.0 – 15.0	0.09	3.3	8 (8)	9 (9)	+20	-25	-4	+10
15.0 – 50.0	0.05	3.7	6 (6)	8 (8)	+17	-22	-5	+13

Υ(2S)

p_{T} (GeV/c)	σ	stat./σ	$\sum_{\text{syst.}}/\sigma$	$\Delta\sigma/\sigma$	HX T	HX L	CS T	CS L
0.0 – 42.0	0.43	0.4	9 (8)	10 (9)	+5	-30	+3	-26
0.0 – 3.0	0.14	4.5	12 (12)	14 (13)	-33	-4	-26	-17
3.0 – 7.0	0.15	4.9	16 (19)	18 (20)	+12	-26	+10	-24
7.0 – 11.0	0.08	5.3	12 (12)	14 (13)	+21	-26	+2	-3
11.0 – 15.0	0.03	6.1	8 (8)	11 (11)	+20	-25	-4	+9
15.0 – 42.0	0.02	5.7	6 (6)	9 (9)	+16	-21	-5	+12

Υ(3S)

p_{T} (GeV/c)	σ	stat./σ	$\sum_{\text{syst.}}/\sigma$	$\Delta\sigma/\sigma$	HX T	HX L	CS T	CS L
0.0 – 38.0	0.18	0.7	11 (10)	11 (11)	+16	-21	+14	-17
0.0 – 7.0	0.10	6.5	19 (19)	20 (20)	+12	-16	+16	-22
7.0 – 12.0	0.05	7.5	14 (14)	16 (16)	+20	-25	+2	-3
12.0 – 38.0	0.03	5.9	7 (7)	10 (10)	+17	-23	-5	+11

Table 4.28: The product of the Υ(nS) integrated and differential production cross sections and the dimuon branching fraction, in nb, measured for four polarization scenarios, in helicity frame (HX) and Collins-Soper (CS) frame, each for L= 100% longitudinal, and T= 100% transverse, integrated over the rapidity range $0.4 < |y^{\Upsilon}| < 0.8$. The statistical uncertainty (stat.), the sum of the systematic uncertainties in quadrature ($\Sigma_{\text{syst.}}$), and the total uncertainty ($\Delta\sigma$; including stat., $\sum_{\text{syst.}}$, luminosity terms) are in percent. For the four polarization scenarios the fractional change in percent to the central value of the cross section relative to the unpolarized value is given. The numbers in parentheses are negative variations.

$0.4 < |y^{\Upsilon}| < 0.8$

Υ(1S)

p_{T} (GeV/c)	σ	stat./σ	$\sum_{\text{syst.}}/\sigma$	$\Delta\sigma/\sigma$	HX T	HX L	CS T	CS L
0.0 – 50.0	1.55	0.2	9 (9)	10 (10)	+19	-24	+16	-19
0.0 – 2.0	0.22	4.5	15 (15)	16 (16)	+20	-25	+21	-26
2.0 – 4.0	0.41	3.0	13 (13)	14 (14)	+21	-25	+22	-25
4.0 – 6.0	0.37	2.9	11 (11)	12 (12)	+20	-25	+16	-21
6.0 – 8.0	0.23	3.3	10 (9)	11 (11)	+13	-27	+2	-15
8.0 – 11.0	0.18	2.9	8 (8)	10 (9)	+19	-23	-0	+2
11.0 – 15.0	0.09	3.3	8 (8)	10 (9)	+18	-23	-4	+10
15.0 – 50.0	0.05	3.8	6 (6)	8 (8)	+15	-20	-5	+13

Υ(2S)

p_{T} (GeV/c)	σ	stat./σ	$\sum_{\text{syst.}}/\sigma$	$\Delta\sigma/\sigma$	HX T	HX L	CS T	CS L
0.0 – 42.0	0.46	0.5	9 (8)	10 (9)	+5	-30	+3	-26
0.0 – 3.0	0.15	4.2	11 (10)	12 (12)	+17	-23	+19	-24
3.0 – 7.0	0.17	4.6	13 (13)	15 (15)	+16	-24	+14	-21
7.0 – 11.0	0.08	5.2	9 (9)	11 (11)	+17	-23	+1	-2
11.0 – 15.0	0.03	6.6	8 (8)	11 (11)	+17	-22	-4	+9
15.0 – 42.0	0.02	5.9	6 (6)	10 (9)	+15	-20	-5	+12

Υ(3S)

p_{T} (GeV/c)	σ	stat./σ	$\sum_{\text{syst.}}/\sigma$	$\Delta\sigma/\sigma$	HX T	HX L	CS T	CS L
0.0 – 38.0	0.20	0.8	11 (10)	11 (11)	+16	-21	+14	-17
0.0 – 7.0	0.11	6.7	18 (18)	20 (20)	+16	-22	+16	-21
7.0 – 12.0	0.06	6.8	10 (9)	13 (12)	+16	-22	+1	-2
12.0 – 38.0	0.03	6.5	8 (7)	11 (11)	+15	-21	-4	+10

Table 4.29: The product of the Υ(nS) integrated and differential production cross sections and the dimuon branching fraction, in nb, measured for four polarization scenarios, in helicity frame (HX) and Collins-Soper (CS) frame, each for L= 100% longitudinal, and T= 100% transverse, integrated over the rapidity range $0.8 < |y^{\Upsilon}| < 1.2$ The statistical uncertainty (stat.), the sum of the systematic uncertainties in quadrature ($\Sigma_{\text{syst.}}$), and the total uncertainty ($\Delta\sigma$; including stat., $\sum_{\text{syst.}}$, luminosity terms) are in percent. For the four polarization scenarios the fractional change in percent to the central value of the cross section relative to the unpolarized value is given. The numbers in parentheses are negative variations.

$0.8 < |y^{\Upsilon}| < 1.2$

Υ(1S)

p_{T} (GeV/c)	σ	stat./σ	$\sum_{\text{syst.}}/\sigma$	$\Delta\sigma/\sigma$	HX T	HX L	CS T	CS L
0.0 – 50.0	1.48	0.2	9 (9)	10 (10)	+19	-24	+16	-19
0.0 – 2.0	0.20	3.7	13 (12)	14 (13)	+20	-25	+20	-24
2.0 – 4.0	0.43	2.7	12 (12)	13 (13)	+20	-26	+19	-25
4.0 – 6.0	0.33	2.9	9 (9)	11 (10)	+17	-25	+13	-21
6.0 – 8.0	0.22	3.4	10 (9)	11 (11)	+22	-18	+12	-7
8.0 – 11.0	0.17	2.9	8 (7)	9 (9)	+15	-21	-1	+2
11.0 – 15.0	0.09	3.4	8 (8)	9 (9)	+15	-21	-4	+9
15.0 – 50.0	0.05	3.8	8 (8)	10 (9)	+13	-19	-5	+12

Υ(2S)

p_{T} (GeV/c)	σ	stat./σ	$\sum_{\text{syst.}}/\sigma$	$\Delta\sigma/\sigma$	HX T	HX L	CS T	CS L
0.0 – 42.0	0.53	0.4	9 (8)	10 (9)	+5	-30	+3	-26
0.0 – 3.0	0.20	3.1	8 (8)	10 (10)	+18	-23	+17	-23
3.0 – 7.0	0.20	3.9	11 (9)	12 (11)	+18	-23	+15	-20
7.0 – 11.0	0.08	5.3	10 (10)	12 (12)	+14	-20	+2	-2
11.0 – 15.0	0.03	6.2	8 (8)	11 (11)	+14	-20	-4	+9
15.0 – 42.0	0.02	6.2	8 (8)	11 (11)	+13	-18	-5	+11

Υ(3S)

p_{T} (GeV/c)	σ	stat./σ	$\sum_{\text{syst.}}/\sigma$	$\Delta\sigma/\sigma$	HX T	HX L	CS T	CS L
0.0 – 38.0	0.19	0.8	11 (10)	11 (11)	+16	-21	+14	-17
0.0 – 7.0	0.11	7.7	18 (18)	20 (20)	+16	-22	+14	-20
7.0 – 12.0	0.06	6.9	11 (11)	14 (13)	+13	-19	+2	-3
12.0 – 38.0	0.03	6.8	9 (8)	12 (11)	+13	-19	-4	+10

Table 4.30: The product of the Υ(nS) integrated and differential production cross sections and the dimuon branching fraction, in nb, measured for four polarization scenarios, in helicity frame (HX) and Collins-Soper (CS) frame, each for L= 100% longitudinal, and T= 100% transverse, integrated over the rapidity range $1.2 < |y^{\Upsilon}| < 1.6$ The statistical uncertainty (stat.), the sum of the systematic uncertainties in quadrature ($\Sigma_{\text{syst.}}$), and the total uncertainty ($\Delta\sigma$; including stat., $\sum_{\text{syst.}}$, luminosity terms) are in percent. For the four polarization scenarios the fractional change in percent to the central value of the cross section relative to the unpolarized value is given. The numbers in parentheses are negative variations.

$1.2 < |y^{\Upsilon}| < 1.6$

Υ(1S)

p_{T} (GeV/c)	σ	stat./σ	$\sum_{\text{syst.}}/\sigma$	$\Delta\sigma/\sigma$	HX T	HX L	CS T	CS L
0.0 – 50.0	1.45	0.2	9 (9)	10 (10)	+19	-24	+16	-19
0.0 – 2.0	0.20	3.5	13 (11)	14 (12)	+19	-23	+21	-22
2.0 – 4.0	0.42	2.4	8 (7)	10 (9)	+20	-26	+18	-25
4.0 – 6.0	0.31	2.8	8 (8)	10 (9)	+20	-24	+17	-21
6.0 – 8.0	0.21	3.0	7 (7)	9 (9)	+17	-22	+11	-15
8.0 – 11.0	0.17	3.0	7 (7)	9 (9)	+13	-19	+2	-4
11.0 – 15.0	0.09	3.3	7 (7)	9 (9)	+13	-19	-3	+6
15.0 – 50.0	0.05	3.8	6 (6)	8 (8)	+12	-18	-5	+11

Υ(2S)

p_{T} (GeV/c)	σ	stat./σ	$\sum_{\text{syst.}}/\sigma$	$\Delta\sigma/\sigma$	HX T	HX L	CS T	CS L
0.0 – 42.0	0.50	0.4	9 (8)	10 (9)	+5	-30	+3	-26
0.0 – 3.0	0.17	3.7	7 (7)	9 (9)	+18	-24	+18	-23
3.0 – 7.0	0.20	3.5	8 (7)	9 (9)	+18	-23	+17	-22
7.0 – 11.0	0.08	5.5	8 (8)	11 (11)	+14	-19	+6	-9
11.0 – 15.0	0.03	6.5	7 (7)	11 (10)	+12	-18	-2	+5
15.0 – 42.0	0.02	6.4	6 (6)	10 (10)	+11	-17	-4	+10

Υ(3S)

p_{T} (GeV/c)	σ	stat./σ	$\sum_{\text{syst.}}/\sigma$	$\Delta\sigma/\sigma$	HX T	HX L	CS T	CS L
0.0 – 38.0	0.19	0.8	11 (10)	11 (11)	+16	-21	+14	-17
0.0 – 7.0	0.11	6.8	10 (9)	13 (12)	+17	-23	+16	-22
7.0 – 12.0	0.05	7.7	12 (11)	14 (14)	+13	-18	+5	-8
12.0 – 38.0	0.03	6.7	9 (9)	12 (12)	+11	-17	-3	+7

Table 4.31: The product of the Υ(nS) integrated and differential production cross sections and the dimuon branching fraction, in nb, measured for four polarization scenarios, in helicity frame (HX) and Collins-Soper (CS) frame, each for L= 100% longitudinal, and T= 100% transverse, integrated over the rapidity range $1.6 < |y^{\Upsilon}| < 2.0$. The statistical uncertainty (stat.), the sum of the systematic uncertainties in quadrature ($\Sigma_{\text{syst.}}$), and the total uncertainty ($\Delta\sigma$; including stat., $\sum_{\text{syst.}}$, luminosity terms) are in percent. For the four polarization scenarios the fractional change in percent to the central value of the cross section relative to the unpolarized value is given. The numbers in parentheses are negative variations.

$1.6 < |y^{\Upsilon}| < 2.0$

Υ(1S)

p_{T} (GeV/c)	σ	stat./σ	$\sum_{\text{syst.}}/\sigma$	$\Delta\sigma/\sigma$	HX T	HX L	CS T	CS L
0.0 – 50.0	1.40	0.2	9 (9)	10 (10)	+19	-24	+16	-19
0.0 – 2.0	0.21	3.1	8 (7)	9 (9)	+22	-26	+23	-27
2.0 – 4.0	0.40	2.5	6 (5)	8 (7)	+22	-26	+24	-27
4.0 – 6.0	0.33	2.6	6 (5)	7 (7)	+20	-25	+23	-27
6.0 – 8.0	0.19	3.2	5 (5)	7 (7)	+18	-22	+20	-24
8.0 – 11.0	0.15	3.4	5 (5)	8 (7)	+15	-20	+15	-19
11.0 – 15.0	0.07	4.1	6 (6)	8 (8)	+10	-16	+5	-9
15.0 – 50.0	0.05	4.4	6 (6)	9 (8)	+9	-14	-1	+3

Υ(2S)

p_{T} (GeV/c)	σ	stat./σ	$\sum_{\text{syst.}}/\sigma$	$\Delta\sigma/\sigma$	HX T	HX L	CS T	CS L
0.0 – 42.0	0.41	0.4	9 (8)	10 (9)	+5	-30	+3	-26
0.0 – 3.0	0.11	5.3	7 (7)	10 (10)	+20	-25	+22	-27
3.0 – 7.0	0.19	3.9	7 (6)	9 (9)	+19	-24	+23	-27
7.0 – 11.0	0.06	7.0	7 (6)	11 (10)	+14	-20	+17	-22
11.0 – 15.0	0.03	8.3	6 (6)	11 (11)	+10	-15	+7	-11
15.0 – 42.0	0.02	8.1	6 (6)	11 (11)	+8	-13	-0	+1

Υ(3S)

p_{T} (GeV/c)	σ	stat./σ	$\sum_{\text{syst.}}/\sigma$	$\Delta\sigma/\sigma$	HX T	HX L	CS T	CS L
0.0 – 38.0	0.18	0.8	11 (10)	11 (11)	+16	-21	+14	-17
0.0 – 7.0	0.12	7.2	10 (9)	13 (13)	+19	-23	+23	-26
7.0 – 12.0	0.03	10.6	12 (12)	16 (16)	+13	-19	+16	-21
12.0 – 38.0	0.02	8.8	7 (7)	12 (12)	+8	-13	+4	-6

Table 4.32: The product of the Υ(nS) integrated and differential production cross sections and the dimuon branching fraction, in nb, measured for four polarization scenarios, in helicity frame (HX) and Collins-Soper (CS) frame, each for L= 100% longitudinal, and T= 100% transverse, integrated over the rapidity range $2.0 < |y^{\Upsilon}| < 2.4$. The statistical uncertainty (stat.), the sum of the systematic uncertainties in quadrature ($\Sigma_{\text{syst.}}$), and the total uncertainty ($\Delta\sigma$; including stat., $\sum_{\text{syst.}}$, luminosity terms) are in percent. For the four polarization scenarios the fractional change in percent to the central value of the cross section relative to the unpolarized value is given.

$2.0 < |y^{\Upsilon}| < 2.4$

Υ(1S)								
p_{T} (GeV/c)	σ	stat./σ	$\sum_{\text{syst.}}/\sigma$	$\Delta\sigma/\sigma$	HX T	HX L	CS T	CS L
0.0 – 50.0	1.14	0.2	9 (9)	10 (10)	+19	-24	+16	-19
0.0 – 2.0	0.13	5.3	9 (7)	11 (10)	+30	-31	+32	-31
2.0 – 4.0	0.34	2.8	8 (7)	9 (8)	+23	-28	+30	-32
4.0 – 6.0	0.29	4.1	8 (7)	10 (9)	+27	-21	+38	-28
6.0 – 8.0	0.15	5.8	8 (6)	10 (9)	+23	-21	+34	-29
8.0 – 11.0	0.13	5.8	7 (5)	10 (9)	+18	-20	+31	-29
11.0 – 15.0	0.07	7.2	8 (7)	12 (11)	+14	-18	+28	-29
15.0 – 50.0	0.04	9.1	9 (9)	14 (13)	+6	-13	+18	-24
Υ(2S)								
p_{T} (GeV/c)	σ	stat./σ	$\sum_{\text{syst.}}/\sigma$	$\Delta\sigma/\sigma$	HX T	HX L	CS T	CS L
0.0 – 42.0	0.31	0.6	9 (8)	10 (9)	+5	-30	+3	-26
0.0 – 3.0	0.05	12.6	9 (8)	16 (15)	+16	-35	+19	-37
3.0 – 7.0	0.15	7.7	8 (6)	12 (11)	+15	-28	+25	-35
7.0 – 11.0	0.06	10.9	8 (7)	14 (13)	+16	-22	+29	-31
11.0 – 15.0	0.02	14.7	8 (7)	17 (16)	+12	-18	+26	-29
15.0 – 42.0	0.01	20.4	9 (9)	22 (22)	+9	-14	+20	-24
Υ(3S)								
p_{T} (GeV/c)	σ	stat./σ	$\sum_{\text{syst.}}/\sigma$	$\Delta\sigma/\sigma$	HX T	HX L	CS T	CS L
0.0 – 38.0	0.16	1.3	11 (10)	11 (11)	+16	-21	+14	-17
0.0 – 7.0	0.10	11.2	9 (7)	15 (14)	+22	-28	+30	-32
7.0 – 12.0	0.04	19.3	11 (9)	22 (22)	+14	-20	+29	-31
12.0 – 38.0	0.02	15.8	9 (8)	19 (18)	+9	-14	+24	-27

Table 4.33: The product of the $\Upsilon(1S)$ integrated and rapidity differential production cross sections and the dimuon branching fraction, in nb, measured for four polarization scenarios, in helicity frame (HX) and Collins-Soper (CS) frame, each for L= 100% longitudinal, and T= 100% transverse, integrated over the p_T range $p_T^{\Upsilon} < 50\,\mathrm{GeV}/c$. The statistical uncertainty (stat.), the sum of the systematic uncertainties in quadrature ($\Sigma_{\mathrm{syst.}}$), and the total uncertainty ($\Delta\sigma$; including stat., $\sum_{\mathrm{syst.}}$, luminosity terms) are in percent. For the four polarization scenarios the fractional change in percent to the central value of the cross section relative to the unpolarized value is given. The numbers in parentheses are negative variations.

$\mathbf{p_T^{\Upsilon} < 50\,GeV/c}$

$\Upsilon(1S)$

$\lvert y\rvert$	σ	stat./σ	$\sum_{\mathrm{syst.}}/\sigma$	$\Delta\sigma/\sigma$	HX T	HX L	CS T	CS L
0.0 – 2.4	8.66	0.6	9 (8)	10 (9)	+19	-24	+16	-19
0.0 – 0.2	0.77	1.7	13 (12)	13 (13)	+27	-16	+22	-9
0.2 – 0.4	0.78	1.7	12 (12)	13 (12)	+19	-25	+12	-16
0.4 – 0.6	0.77	1.7	14 (14)	15 (14)	+20	-18	+13	-15
0.6 – 0.8	0.79	1.7	10 (10)	11 (11)	+20	-24	+13	-15
0.8 – 1.0	0.76	1.7	14 (13)	14 (14)	+18	-24	+12	-15
1.0 – 1.2	0.74	1.8	7 (6)	8 (8)	+18	-24	+11	-16
1.2 – 1.4	0.71	1.7	11 (10)	11 (11)	+18	-23	+12	-16
1.4 – 1.6	0.74	1.7	6 (5)	7 (6)	+18	-23	+14	-18
1.6 – 1.8	0.72	1.7	8 (7)	9 (8)	+19	-23	+18	-21
1.8 – 2.0	0.71	1.9	6 (5)	7 (7)	+20	-24	+23	-26
2.0 – 2.2	0.64	2.3	7 (6)	8 (7)	+20	-24	+28	-30
2.2 – 2.4	0.53	4.2	8 (7)	10 (9)	+22	-26	+32	-32

$\Upsilon(2S)$

$\lvert y\rvert$	σ	stat./σ	$\sum_{\mathrm{syst.}}/\sigma$	$\Delta\sigma/\sigma$	HX T	HX L	CS T	CS L
0.0 – 2.4	2.21	1.3	10 (10)	11 (11)	+26	-16	+23	-12
0.0 – 0.4	0.38	2.5	14 (14)	15 (14)	+16	-21	+10	-13
0.4 – 0.8	0.40	2.5	12 (12)	13 (13)	+17	-23	+10	-13
0.8 – 1.2	0.38	2.8	12 (11)	13 (12)	+16	-22	+10	-13
1.2 – 1.6	0.38	2.7	9 (9)	10 (10)	+16	-22	+12	-16
1.6 – 2.0	0.38	2.9	7 (7)	9 (8)	+17	-22	+19	-23
2.0 – 2.4	0.30	5.1	7 (6)	10 (9)	+19	-24	+29	-31

$\Upsilon(3S)$

$\lvert y\rvert$	σ	stat./σ	$\sum_{\mathrm{syst.}}/\sigma$	$\Delta\sigma/\sigma$	HX T	HX L	CS T	CS L
0.0 – 2.4	1.12	2.1	10 (10)	11 (11)	+16	-21	+14	-17
0.0 – 0.4	0.19	3.9	15 (15)	16 (16)	+15	-20	+9	-11
0.4 – 0.8	0.20	3.9	14 (13)	15 (15)	+16	-22	+9	-11
0.8 – 1.4	0.28	3.8	13 (12)	14 (14)	+15	-21	+8	-11
1.4 – 2.0	0.29	4.0	8 (7)	10 (9)	+16	-21	+16	-20
2.0 – 2.4	0.16	8.3	8 (7)	12 (11)	+18	-23	+29	-31

Table 4.34: The ratio of Υ(nS) cross sections, and its p_{T} dependence, for the unpolarized scenario, with statistical and systematic uncertainties combined in quadrature. The numbers in parentheses are negative variations.

p_{T} (GeV/c)	Υ(3S) / Υ(1S)	Υ(2S) / Υ(1S)	Υ(3S) / Υ(2S)
$0-38$	$0.13 \pm 0.02\,(0.02)$	$0.26 \pm 0.02\,(0.04)$	$0.49 \pm 0.08\,(0.05)$
$0-2$	$0.11 \pm 0.02\,(0.02)$	$0.22 \pm 0.04\,(0.03)$	$0.49 \pm 0.10\,(0.09)$
$2-5$	$0.10 \pm 0.02\,(0.02)$	$0.23 \pm 0.04\,(0.04)$	$0.44 \pm 0.11\,(0.08)$
$5-8$	$0.12 \pm 0.02\,(0.02)$	$0.27 \pm 0.04\,(0.03)$	$0.46 \pm 0.07\,(0.06)$
$8-10$	$0.15 \pm 0.02\,(0.02)$	$0.27 \pm 0.04\,(0.03)$	$0.57 \pm 0.09\,(0.08)$
$10-13$	$0.20 \pm 0.03\,(0.02)$	$0.33 \pm 0.04\,(0.04)$	$0.60 \pm 0.08\,(0.06)$
$13-16$	$0.26 \pm 0.03\,(0.03)$	$0.37 \pm 0.04\,(0.04)$	$0.69 \pm 0.09\,(0.08)$
$16-18$	$0.31 \pm 0.05\,(0.05)$	$0.50 \pm 0.07\,(0.07)$	$0.61 \pm 0.11\,(0.10)$
$18-22$	$0.28 \pm 0.04\,(0.04)$	$0.45 \pm 0.05\,(0.06)$	$0.63 \pm 0.10\,(0.08)$
$22-38$	$0.32 \pm 0.07\,(0.10)$	$0.47 \pm 0.09\,(0.13)$	$0.69 \pm 0.20\,(0.17)$

Table 4.35: The ratio of Υ(nS) cross sections, and its rapidity dependence, with statistical and systematic uncertainties combined in quadrature. The numbers in parentheses are negative variations.

$\lvert y \rvert$	Υ(3S) / Υ(1S)	Υ(2S) / Υ(1S)	Υ(3S) / Υ(2S)
$0.0-2.4$	$0.13 \pm 0.02\,(0.02)$	$0.26 \pm 0.03\,(0.03)$	$0.49 \pm 0.07\,(0.06)$
$0.0-0.4$	$0.12 \pm 0.03\,(0.02)$	$0.24 \pm 0.06\,(0.04)$	$0.49 \pm 0.12\,(0.09)$
$0.4-0.8$	$0.12 \pm 0.04\,(0.02)$	$0.25 \pm 0.08\,(0.04)$	$0.50 \pm 0.14\,(0.10)$
$0.8-1.4$	$0.12 \pm 0.03\,(0.02)$	$0.24 \pm 0.05\,(0.04)$	$0.51 \pm 0.12\,(0.10)$
$1.4-2.0$	$0.14 \pm 0.02\,(0.02)$	$0.26 \pm 0.04\,(0.03)$	$0.51 \pm 0.08\,(0.08)$
$2.0-2.4$	$0.14 \pm 0.03\,(0.02)$	$0.24 \pm 0.04\,(0.04)$	$0.60 \pm 0.14\,(0.12)$

Table 4.36: Relative values of the systematic uncertainties on the $\Upsilon(1S)$ integrated and differential production cross section times the dimuon branching fraction, for $|y| < 2.4$, assuming null production polarization, in units of percent. The p_{T} intervals are in units of GeV/c. The following abbreviations are used: A, S_p, $A_{p_{\mathrm{T}}}$, A_{fsr}, ϵ_{muid}, ϵ_{trig}, ϵ_{ρ}, ϵ_{func}, ϵ_{trk}, PDF_{CB}, PDF_{bkgd} and M_{scale} for the systematic uncertainties arising from the statistical uncertainties in acceptance, imperfect knowledge of the production p_{T} spectrum, imperfect knowledge of the momentum scale, the modeling of FSR, the statistical uncertainties in tag and probe muon identification, trigger efficiencies and the ρ factor, the choice of bin size for the efficiencies, the statistical uncertainties in tracking efficiencies, fixing the tail parameters in fitting, the background PDF and imperfect knowledge of the momentum scale. The luminosity uncertainty of 4% is not shown in the table. The numbers in parentheses are negative variations.

$\Upsilon(1S)$ $|\mathbf{y}^{\Upsilon}| < \mathbf{2.4}$

p_{T}	A	S_p	A_{p_T}	A_{fsr}	$\varepsilon_{\mathrm{muid}}$	$\varepsilon_{\mathrm{trig}}$	ε_{ρ}	$\varepsilon_{\mathrm{func}}$	$\varepsilon_{\mathrm{trk}}$	PDF_{CB}	PDF_{bkgd}	M_{scale}
0.0 – 50.0	0.8 (0.8)	0.3 (0.3)	0.1	0.5	3.1 (2.0)	3.4 (3.4)	6.8	1.8	0.4 (0.3)	1.7	0.6	0.0 (0.0)
0.0 – 0.5	0.7 (0.8)	0.0 (0.1)	0.2	0.8	4.2 (3.2)	5.6 (4.9)	7.4	0.4	0.4 (0.3)	2.0	0.7	0.1 (0.1)
0.5 – 1.0	0.8 (0.8)	0.1 (0.1)	0.2	0.8	3.2 (3.2)	5.3 (4.6)	8.3	0.7	0.3 (0.4)	1.8	1.3	0.0 (0.4)
1.0 – 1.5	0.8 (0.8)	0.3 (0.2)	0.2	0.5	2.8 (3.5)	4.9 (4.7)	7.3	3.7	0.4 (0.4)	2.1	0.5	0.0 (0.0)
1.5 – 2.0	0.9 (0.8)	0.3 (0.3)	0.2	0.4	5.2 (2.7)	4.5 (4.5)	7.8	3.3	0.3 (0.3)	1.2	2.7	0.1 (0.0)
2.0 – 3.0	0.7 (0.7)	0.7 (0.7)	0.2	0.7	3.4 (2.4)	5.0 (8.5)	7.2	2.6	0.4 (0.3)	1.7	2.5	0.0 (0.0)
3.0 – 4.0	0.8 (0.8)	0.5 (0.6)	0.1	0.6	3.2 (1.9)	4.4 (3.8)	7.1	1.9	0.3 (0.4)	2.0	1.2	0.1 (0.1)
4.0 – 5.0	0.9 (0.7)	0.1 (1.1)	0.0	0.8	3.0 (1.8)	3.6 (3.6)	7.5	2.6	0.4 (0.6)	1.5	0.4	0.0 (0.2)
5.0 – 6.0	1.0 (0.8)	0.3 (0.2)	0.0	0.3	3.0 (1.7)	3.8 (7.3)	6.7	2.2	0.3 (0.4)	1.3	1.8	0.2 (0.2)
6.0 – 7.0	0.9 (0.9)	0.2 (0.2)	0.2	0.4	2.9 (1.8)	3.6 (3.1)	6.8	1.9	0.4 (0.2)	1.3	0.6	0.3 (0.3)
7.0 – 8.0	0.8 (0.8)	0.1 (0.1)	0.2	0.3	2.9 (1.8)	3.2 (2.8)	5.3	1.4	0.4 (0.4)	1.5	0.9	0.2 (0.2)
8.0 – 9.0	1.7 (1.7)	0.0 (0.0)	0.2	0.3	2.9 (1.8)	2.9 (2.6)	4.4	1.2	0.4 (0.4)	1.4	1.0	0.0 (0.0)
9.0 – 10.0	0.7 (1.0)	0.0 (0.1)	0.1	0.2	2.9 (2.0)	2.8 (2.5)	3.9	0.1	0.4 (0.4)	1.3	1.3	0.2 (0.1)
10.0 – 11.0	0.7 (0.6)	0.1 (0.1)	0.2	0.2	2.8 (1.9)	2.6 (2.3)	5.0	0.5	0.4 (0.4)	1.2	1.2	0.2 (0.0)
11.0 – 12.0	0.7 (0.7)	0.1 (0.1)	0.1	0.1	2.9 (2.0)	2.4 (2.1)	1.8	0.5	0.4 (0.4)	0.7	2.4	0.2 (0.2)
12.0 – 13.0	0.6 (0.6)	0.1 (0.1)	0.1	0.0	2.9 (2.1)	2.4 (2.1)	5.1	0.4	0.4 (0.4)	1.2	1.1	0.6 (0.6)
13.0 – 14.0	0.6 (0.6)	0.7 (0.7)	0.1	0.0	2.4 (2.6)	1.7 (2.5)	5.2	0.2	0.3 (0.3)	1.2	0.1	0.1 (1.0)
14.0 – 15.0	0.6 (0.6)	0.2 (0.1)	0.1	0.1	2.9 (2.2)	2.3 (2.1)	6.4	0.7	0.4 (0.3)	1.3	0.1	1.2 (0.4)
15.0 – 16.0	0.5 (0.5)	0.2 (0.3)	0.1	0.0	3.0 (2.3)	2.1 (1.9)	5.8	1.3	0.4 (0.3)	1.2	0.1	0.8 (0.1)
16.0 – 18.0	0.5 (0.4)	0.2 (0.1)	0.1	0.1	2.9 (2.2)	1.9 (1.7)	6.1	1.5	0.3 (0.3)	1.1	0.7	0.1 (0.4)
18.0 – 20.0	0.5 (0.5)	0.2 (0.2)	0.1	0.1	2.9 (2.2)	1.8 (1.6)	5.6	1.4	0.4 (0.3)	1.4	0.2	0.2 (0.2)
20.0 – 22.0	0.4 (0.4)	0.2 (0.2)	0.1	0.0	3.0 (2.4)	1.8 (1.6)	3.0	2.2	0.3 (0.3)	0.9	0.6	0.0 (0.0)
22.0 – 25.0	0.4 (0.5)	0.2 (0.2)	0.0	0.0	3.1 (2.5)	1.6 (1.5)	2.7	2.1	0.4 (0.3)	1.5	1.3	0.4 (0.4)
25.0 – 30.0	0.5 (0.5)	0.2 (0.2)	0.0	0.7	3.1 (2.7)	1.7 (1.5)	1.1	2.3	0.4 (0.4)	1.3	0.5	0.3 (0.2)
30.0 – 50.0	0.3 (0.3)	0.2 (0.2)	0.0	0.3	2.7 (2.2)	1.8 (1.6)	4.5	2.1	0.3 (0.3)	1.2	3.8	0.1 (1.0)

Table 4.37: Relative values of the systematic uncertainties on the $\Upsilon(2S)$ integrated and differential production cross section times the dimuon branching fraction, for $|y| < 2.4$, assuming null production polarization, in units of percent. The p_T intervals are in units of GeV/c. The following abbreviations are used: A, S_p, A_{p_T}, $A_{\rm fsr}$, ϵ_{muid}, $\epsilon_{\rm trig}$, ϵ_ρ, $\epsilon_{\rm func}$, $\epsilon_{\rm trk}$, $PDF_{\rm CB}$, $PDF_{\rm bkgd}$ and $M_{\rm scale}$ for the systematic uncertainties arising from the statistical uncertainties in acceptance, imperfect knowledge of the production p_T spectrum, imperfect knowledge of the momentum scale, the modeling of FSR, the statistical uncertainties in tag and probe muon identification, trigger efficiencies and the ρ factor, the choice of bin size for the efficiencies, the statistical uncertainties in tracking efficiencies, fixinging the tail parameters in fitting, the background PDF and imperfect knowledge of the momentum scale. The luminosity uncertainty of 4% is not shown in the table. The numbers in parentheses are negative variations.

$\Upsilon(2S)$ $|\mathbf{y}^{\Upsilon}| < \mathbf{2.4}$

p_T	A	S_p	A_{p_T}	$A_{\rm fsr}$	$\varepsilon_{\rm muid}$	$\varepsilon_{\rm trig}$	ε_ρ	$\varepsilon_{\rm func}$	$\varepsilon_{\rm trk}$	$PDF_{\rm CB}$	$PDF_{\rm bkgd}$	$M_{\rm scale}$
0.0 – 42.0	0.9 (0.9)	0.3 (0.3)	0.1	0.5	3.3 (2.1)	3.8 (3.8)	7.4	1.5	0.4 (0.4)	2.6	0.3	0.1 (0.1)
0.0 – 1.0	0.8 (0.8)	0.1 (0.1)	0.2	0.8	4.1 (2.9)	4.6 (4.0)	8.6	0.2	3.2 (3.2)	2.6	0.2	0.2 (0.2)
1.0 – 2.5	0.9 (0.8)	0.5 (0.6)	0.2	0.7	3.9 (3.0)	5.0 (4.4)	12.8	2.7	0.4 (0.4)	2.2	4.7	0.0 (0.0)
2.5 – 4.0	1.0 (0.9)	0.7 (0.8)	0.2	0.8	3.7 (2.2)	4.7 (4.1)	9.0	3.1	0.4 (0.5)	3.0	0.9	0.0 (0.2)
4.0 – 5.5	1.1 (1.1)	0.6 (0.5)	0.2	0.8	3.4 (1.7)	4.1 (3.5)	7.2	1.8	1.1 (1.1)	3.1	2.2	0.7 (0.7)
5.5 – 7.0	1.1 (0.8)	0.6 (0.1)	0.2	0.5	3.6 (1.7)	3.3 (3.3)	8.4	1.6	0.4 (0.4)	2.1	1.1	0.2 (0.2)
7.0 – 8.5	0.9 (0.9)	0.0 (0.1)	0.2	0.4	3.2 (2.2)	3.3 (3.0)	3.0	1.3	0.4 (0.4)	2.1	4.5	0.6 (0.6)
8.5 – 10.0	0.8 (0.7)	0.0 (0.0)	0.2	0.3	3.1 (2.0)	2.8 (2.4)	5.6	3.1	0.4 (0.4)	0.7	2.1	0.5 (0.5)
10.0 – 11.5	0.7 (0.7)	0.1 (0.1)	0.2	0.4	3.0 (2.1)	2.6 (2.3)	5.9	2.6	0.4 (0.4)	0.9	3.0	0.6 (0.1)
11.5 – 13.0	0.7 (0.7)	0.1 (0.1)	0.1	0.3	3.1 (2.2)	2.3 (2.1)	5.5	2.1	0.4 (0.4)	0.2	1.3	0.2 (0.0)
13.0 – 14.5	0.6 (0.6)	0.2 (0.2)	0.1	0.0	2.8 (2.0)	2.0 (1.8)	5.9	1.0	0.3 (0.4)	1.7	0.4	0.2 (0.1)
14.5 – 16.0	0.6 (0.6)	0.2 (0.2)	0.1	0.0	3.0 (4.7)	2.0 (4.2)	4.3	1.6	0.4 (0.4)	1.6	1.6	0.5 (0.5)
16.0 – 18.0	0.6 (0.5)	0.2 (0.1)	0.1	0.2	3.0 (2.3)	1.9 (1.7)	6.4	1.8	0.3 (0.3)	1.7	1.1	0.0 (0.1)
18.0 – 19.5	0.4 (0.4)	0.2 (0.3)	0.1	0.0	2.6 (2.1)	1.5 (1.5)	5.4	1.1	0.4 (0.3)	1.7	0.0	1.0 (0.0)
19.5 – 22.0	0.5 (0.4)	0.2 (0.2)	0.0	0.0	3.1 (2.5)	1.8 (1.6)	3.9	1.8	0.4 (0.3)	1.5	1.1	1.2 (1.2)
22.0 – 26.0	0.4 (0.4)	0.2 (0.2)	0.1	0.0	2.9 (2.3)	1.8 (1.6)	3.3	1.7	0.3 (0.4)	1.8	1.4	1.3 (0.4)
26.0 – 42.0	0.3 (0.3)	0.2 (0.2)	0.0	0.3	2.7 (2.2)	1.3 (1.2)	4.5	1.9	0.3 (0.3)	1.6	3.4	0.2 (0.1)

Table 4.38: Relative values of the systematic uncertainties on the $\Upsilon(3S)$ integrated and differential production cross section times the dimuon branching fraction, for $|y| < 2.4$, assuming null production polarization, in units of percent. The p_T intervals are in units of GeV/c. The following abbreviations are used: A, S_p, A_{p_T}, $A_{\rm fsr}$, ϵ_{muid}, $\epsilon_{\rm trig}$, ϵ_ρ, $\epsilon_{\rm func}$, $\epsilon_{\rm trk}$, $PDF_{\rm CB}$, $PDF_{\rm bkgd}$ and $M_{\rm scale}$ for the systematic uncertainties arising from the statistical uncertainties in acceptance, imperfect knowledge of the production p_T spectrum, imperfect knowledge of the momentum scale, the modeling of FSR, the statistical uncertainties in tag and probe muon identification, trigger efficiencies and the ρ factor, the choice of bin size for the efficiencies, the statistical uncertainties in tracking efficiencies, fixinging the tail parameters in fitting, the background PDF and imperfect knowledge of the momentum scale. The luminosity uncertainty of 4% is not shown in the table. The numbers in parentheses are negative variations.

$\Upsilon(3S)$ $|\mathbf{y}^{\Upsilon}| < \mathbf{2.4}$

p_T	A	S_p	A_{p_T}	$A_{\rm fsr}$	$\varepsilon_{\rm muid}$	$\varepsilon_{\rm trig}$	ε_ρ	$\varepsilon_{\rm func}$	$\varepsilon_{\rm trk}$	$PDF_{\rm CB}$	$PDF_{\rm bkgd}$	$M_{\rm scale}$
0.0 – 38.0	1.0 (0.9)	0.3 (0.3)	0.2	0.6	3.5 (2.2)	3.2 (3.2)	8.0	3.1	0.4 (0.4)	3.8	0.0	0.2 (0.3)
0.0 – 2.5	1.0 (0.8)	0.5 (0.5)	0.2	0.2	4.2 (3.1)	4.2 (4.2)	9.5	1.9	0.4 (0.4)	2.0	0.0	0.4 (0.3)
2.5 – 5.0	0.8 (0.8)	2.3 (2.3)	0.2	1.4	2.3 (3.5)	5.6 (5.6)	8.6	5.6	1.9 (1.9)	0.7	1.4	2.2 (2.2)
5.0 – 7.5	0.7 (1.0)	0.5 (0.5)	0.2	0.5	3.2 (2.8)	4.4 (3.9)	8.8	1.3	0.3 (0.5)	3.8	3.3	0.4 (0.4)
7.5 – 10.0	0.9 (0.9)	0.0 (0.0)	0.2	0.5	3.4 (2.3)	3.5 (3.1)	5.4	0.2	1.6 (1.6)	1.1	8.6	1.5 (1.5)
10.0 – 13.0	1.2 (0.4)	0.5 (0.4)	0.2	0.7	3.7 (1.9)	3.1 (2.0)	4.7	1.7	1.0 (1.0)	1.3	2.7	0.5 (0.5)
13.0 – 16.0	0.6 (0.6)	0.2 (0.6)	0.1	0.1	3.1 (2.3)	2.2 (2.0)	4.0	1.0	0.4 (0.4)	2.5	1.9	0.1 (0.4)
16.0 – 18.0	0.5 (0.5)	0.1 (0.2)	0.1	0.0	3.1 (2.4)	2.3 (2.1)	5.9	1.7	0.3 (0.4)	2.6	0.1	0.0 (0.0)
18.0 – 22.0	0.4 (0.4)	0.1 (0.2)	0.0	0.1	2.9 (2.3)	1.9 (1.7)	4.3	1.7	0.4 (0.3)	2.6	4.0	0.3 (0.3)
22.0 – 38.0	0.4 (0.4)	0.2 (0.2)	0.0	0.2	3.1 (2.5)	1.9 (1.7)	1.0	1.9	0.3 (0.4)	2.8	11.8	0.2 (0.0)

Table 4.39: Relative values of the systematic uncertainties on the Υ(nS) integrated and differential production cross section times the dimuon branching fraction, for $|y| < 0.4$, assuming null production polarization, in units of percent. The p_{T} intervals are in units of GeV/c. The following abbreviations are used: A, S_p, $A_{p_{\mathrm{T}}}$, A_{fsr}, ϵ_{muid}, ϵ_{trig}, ϵ_ρ, ϵ_{func}, ϵ_{trk}, PDF_{CB}, PDF_{bkgd} and M_{scale} for the systematic uncertainties arising from the statistical uncertainties in acceptance, imperfect knowledge of the production p_{T} spectrum, imperfect knowledge of the momentum scale, the modeling of FSR, the statistical uncertainties in tag and probe muon identification, trigger efficiencies and the ρ factor, the choice of bin size for the efficiencies, the statistical uncertainties in tracking efficiencies, fixinging the tail parameters in fitting, the background PDF and imperfect knowledge of the momentum scale. The luminosity uncertainty of 4% is not shown in the table. The numbers in parentheses are negative variations.

$|\mathbf{y}^{\boldsymbol{\Upsilon}}| < \mathbf{0.4}$

Υ(1S)

p_{T}	A	S_p	A_{p_T}	A_{fsr}	$\varepsilon_{\mathrm{muid}}$	$\varepsilon_{\mathrm{trig}}$	ε_ρ	$\varepsilon_{\mathrm{func}}$	$\varepsilon_{\mathrm{trk}}$	PDF_{CB}	PDF_{bkgd}	M_{scale}
0.0 – 50.0	0.8 (0.8)	0.3 (0.3)	0.1	0.5	3.1 (2.0)	3.4 (3.4)	6.8	3.1	0.3 (0.4)	1.8	0.7	0.0 (0.0)
0.0 – 2.0	0.8 (0.8)	0.5 (0.6)	0.2	0.9	3.6 (3.3)	8.6 (7.3)	11.4	6.7	0.4 (0.4)	1.8	4.3	0.1 (0.1)
2.0 – 4.0	0.8 (0.8)	1.1 (1.2)	0.2	0.7	3.2 (2.8)	7.0 (6.1)	9.8	5.5	0.4 (0.4)	2.1	1.6	0.1 (0.1)
4.0 – 6.0	0.6 (1.2)	0.5 (0.5)	0.1	0.9	2.4 (2.7)	5.6 (5.0)	11.1	4.8	0.4 (0.4)	2.0	0.6	0.2 (0.2)
6.0 – 8.0	0.8 (0.8)	0.2 (0.2)	0.2	0.3	2.4 (1.9)	4.3 (3.9)	9.7	4.4	0.4 (0.4)	1.3	3.6	0.5 (0.5)
8.0 – 11.0	0.6 (0.6)	0.0 (0.0)	0.0	0.3	2.3 (1.7)	3.4 (3.0)	8.4	2.8	0.4 (0.4)	1.8	1.0	0.1 (0.1)
11.0 – 15.0	0.5 (0.5)	0.1 (0.1)	0.0	0.0	2.2 (1.5)	2.5 (2.3)	6.7	0.6	0.4 (0.4)	1.6	0.0	0.3 (0.3)
15.0 – 50.0	0.4 (0.4)	0.2 (0.2)	0.2	0.2	2.1 (1.4)	1.8 (1.7)	4.7	0.4	0.4 (0.4)	1.4	1.9	0.0 (0.2)

Υ(2S)

p_{T}	A	S_p	A_{p_T}	A_{fsr}	$\varepsilon_{\mathrm{muid}}$	$\varepsilon_{\mathrm{trig}}$	ε_ρ	$\varepsilon_{\mathrm{func}}$	$\varepsilon_{\mathrm{trk}}$	PDF_{CB}	PDF_{bkgd}	M_{scale}
0.0 – 42.0	0.8 (0.8)	0.3 (0.3)	0.1	0.5	3.0 (1.9)	3.5 (3.5)	6.8	1.4	1.4 (0.4)	2.4	0.3	0.1 (0.1)
0.0 – 3.0	0.6 (0.8)	0.7 (0.8)	0.2	0.7	2.7 (2.4)	6.1 (5.2)	8.3	5.6	0.3 (0.3)	1.3	0.2	0.1 (0.1)
3.0 – 7.0	1.3 (0.8)	3.6 (3.6)	0.2	0.8	0.0 (5.3)	2.4 (7.8)	12.4	8.6	0.5 (0.4)	3.9	0.8	2.8 (2.8)
7.0 – 11.0	0.8 (0.7)	0.1 (0.1)	0.2	0.3	2.6 (1.9)	3.9 (3.5)	9.7	3.7	0.4 (0.4)	2.0	3.0	0.3 (0.3)
11.0 – 15.0	0.5 (0.5)	0.1 (0.1)	0.2	0.1	2.3 (1.7)	2.6 (2.3)	7.0	0.2	0.4 (0.4)	1.9	2.3	0.5 (0.5)
15.0 – 42.0	0.4 (0.4)	0.1 (0.1)	0.2	0.2	2.1 (1.4)	1.7 (1.6)	4.5	0.6	0.4 (0.4)	1.6	2.2	0.0 (0.0)

Υ(3S)

p_{T}	A	S_p	A_{p_T}	A_{fsr}	$\varepsilon_{\mathrm{muid}}$	$\varepsilon_{\mathrm{trig}}$	ε_ρ	$\varepsilon_{\mathrm{func}}$	$\varepsilon_{\mathrm{trk}}$	PDF_{CB}	PDF_{bkgd}	M_{scale}
0.0 – 38.0	1.0 (0.9)	0.3 (0.3)	0.2	0.6	3.5 (2.2)	3.2 (3.2)	8.0	3.2	0.4 (0.4)	3.8	0.0	0.2 (0.3)
0.0 – 7.0	1.1 (0.8)	0.9 (1.0)	0.2	1.3	3.6 (2.8)	6.2 (5.6)	13.8	8.1	1.6 (1.6)	6.1	2.0	1.2 (1.2)
7.0 – 12.0	0.8 (0.8)	0.1 (0.0)	0.0	0.2	2.6 (1.9)	4.2 (3.7)	10.4	3.9	0.7 (0.1)	2.7	6.5	0.6 (0.6)
12.0 – 38.0	0.4 (0.4)	0.1 (0.2)	0.2	0.1	2.3 (1.6)	2.3 (2.1)	5.7	1.0	0.2 (0.5)	2.7	0.8	0.5 (0.5)

Table 4.40: Relative values of the systematic uncertainties on the Υ(nS) integrated and differential production cross section times the dimuon branching fraction, for $0.4 < |y| < 0.8$, assuming null production polarization, in units of percent. The p_{T} intervals are in units of GeV/c. The following abbreviations are used: A, S_p, $A_{p_{\mathrm{T}}}$, A_{fsr}, ϵ_{muid}, ϵ_{trig}, ϵ_{ρ}, ϵ_{func}, ϵ_{trk}, PDF_{CB}, PDF_{bkgd} and M_{scale} for the systematic uncertainties arising from the statistical uncertainties in acceptance, imperfect knowledge of the production p_{T} spectrum, imperfect knowledge of the momentum scale, the modeling of FSR, the statistical uncertainties in tag and probe muon identification, trigger efficiencies and the ρ factor, the choice of bin size for the efficiencies, the statistical uncertainties in tracking efficiencies, fixinging the tail parameters in fitting, the background PDF and imperfect knowledge of the momentum scale. The luminosity uncertainty of 4% is not shown in the table. The numbers in parentheses are negative variations.

$\mathbf{0.4 < |y^{\Upsilon}| < 0.8}$

Υ(1S)

p_{T}	A	S_p	A_{p_T}	A_{fsr}	$\varepsilon_{\mathrm{muid}}$	$\varepsilon_{\mathrm{trig}}$	ε_{ρ}	$\varepsilon_{\mathrm{func}}$	$\varepsilon_{\mathrm{trk}}$	PDF_{CB}	PDF_{bkgd}	M_{scale}
0.0 – 50.0	0.8 (0.8)	0.3 (0.3)	0.1	0.5	3.1 (2.0)	3.4 (3.4)	6.8	3.1	0.3 (0.4)	1.8	0.7	0.0 (0.0)
0.0 – 2.0	0.7 (0.8)	0.4 (0.4)	0.0	0.8	3.6 (3.3)	8.1 (7.1)	10.0	6.7	0.3 (0.4)	1.7	2.5	0.1 (0.1)
2.0 – 4.0	0.8 (0.8)	1.0 (1.0)	0.2	1.1	3.1 (2.7)	6.0 (5.2)	10.6	3.5	0.4 (0.4)	2.1	0.5	0.1 (0.1)
4.0 – 6.0	0.9 (0.8)	0.3 (0.7)	0.0	0.6	2.9 (2.4)	4.5 (4.1)	9.1	3.4	0.3 (0.3)	1.8	0.2	0.1 (0.1)
6.0 – 8.0	0.8 (0.8)	0.2 (0.2)	0.2	0.4	2.7 (2.2)	4.0 (3.6)	8.0	2.5	0.3 (0.3)	1.3	0.2	0.2 (0.2)
8.0 – 11.0	0.6 (0.6)	0.0 (0.0)	0.2	0.4	2.5 (1.9)	3.0 (2.7)	7.0	0.8	0.4 (0.4)	1.6	1.1	0.1 (0.0)
11.0 – 15.0	0.5 (0.5)	0.1 (0.1)	0.2	0.2	2.3 (1.7)	2.2 (2.0)	6.6	0.9	0.3 (0.4)	1.5	3.0	0.2 (0.2)
15.0 – 50.0	0.4 (0.4)	0.2 (0.1)	0.2	0.2	2.2 (1.6)	1.8 (1.6)	5.3	0.1	0.4 (0.3)	1.4	1.1	0.0 (0.0)

Υ(2S)

p_{T}	A	S_p	A_{p_T}	A_{fsr}	$\varepsilon_{\mathrm{muid}}$	$\varepsilon_{\mathrm{trig}}$	ε_{ρ}	$\varepsilon_{\mathrm{func}}$	$\varepsilon_{\mathrm{trk}}$	PDF_{CB}	PDF_{bkgd}	M_{scale}
0.0 – 42.0	0.8 (0.8)	0.3 (0.3)	0.1	0.5	3.0 (1.9)	3.5 (3.5)	6.8	1.4	1.4 (0.4)	2.4	0.3	0.1 (0.1)
0.0 – 3.0	0.5 (0.8)	0.6 (0.6)	0.2	0.7	2.4 (2.2)	5.6 (4.7)	8.0	3.4	0.3 (0.2)	1.0	1.2	0.1 (0.0)
3.0 – 7.0	1.1 (0.8)	2.0 (2.0)	0.1	0.7	3.3 (3.8)	4.7 (4.4)	11.0	3.5	0.4 (0.3)	2.7	0.1	0.1 (0.0)
7.0 – 11.0	0.7 (0.7)	0.0 (0.0)	0.2	0.5	2.7 (2.0)	3.0 (2.7)	8.1	1.6	0.4 (0.4)	1.7	0.3	0.2 (0.1)
11.0 – 15.0	0.5 (0.5)	0.1 (0.1)	0.2	0.2	2.3 (1.7)	2.2 (2.0)	6.8	1.8	0.4 (0.4)	1.9	1.0	0.6 (0.6)
15.0 – 42.0	0.4 (0.4)	0.2 (0.1)	0.2	0.2	2.2 (1.7)	1.7 (1.5)	5.4	0.3	0.4 (0.4)	1.7	1.1	0.2 (0.2)

Υ(3S)

p_{T}	A	S_p	A_{p_T}	A_{fsr}	$\varepsilon_{\mathrm{muid}}$	$\varepsilon_{\mathrm{trig}}$	ε_{ρ}	$\varepsilon_{\mathrm{func}}$	$\varepsilon_{\mathrm{trk}}$	PDF_{CB}	PDF_{bkgd}	M_{scale}
0.0 – 38.0	1.0 (0.9)	0.3 (0.3)	0.2	0.6	3.5 (2.2)	3.2 (3.2)	8.0	3.2	0.4 (0.4)	3.8	0.0	0.2 (0.3)
0.0 – 7.0	1.1 (0.8)	0.9 (0.9)	0.2	1.0	3.7 (3.2)	5.7 (5.0)	14.4	5.5	0.8 (0.2)	4.6	5.7	0.4 (0.4)
7.0 – 12.0	0.7 (0.8)	0.0 (0.0)	0.2	0.4	2.8 (2.0)	3.2 (2.9)	7.9	2.1	0.6 (0.2)	2.6	1.4	0.1 (0.1)
12.0 – 38.0	0.4 (0.4)	0.1 (0.2)	0.2	0.2	2.4 (1.8)	2.2 (2.0)	6.2	0.1	0.2 (0.5)	2.9	1.0	0.4 (0.4)

Table 4.41: Relative values of the systematic uncertainties on the Υ(nS) integrated and differential production cross section times the dimuon branching fraction, for $0.8 < |y| < 1.2$, assuming null production polarization, in units of percent. The p_{T} intervals are in units of GeV/c. The following abbreviations are used: A, S_p, $A_{p_{\mathrm{T}}}$, A_{fsr}, ϵ_{muid}, ϵ_{trig}, ϵ_{ρ}, ϵ_{func}, ϵ_{trk}, PDF_{CB}, PDF_{bkgd} and M_{scale} for the systematic uncertainties arising from the statistical uncertainties in acceptance, imperfect knowledge of the production p_{T} spectrum, imperfect knowledge of the momentum scale, the modeling of FSR, the statistical uncertainties in tag and probe muon identification, trigger efficiencies and the ρ factor, the choice of bin size for the efficiencies, the statistical uncertainties in tracking efficiencies, fixinging the tail parameters in fitting, the background PDF and imperfect knowledge of the momentum scale. The luminosity uncertainty of 4% is not shown in the table. The numbers in parentheses are negative variations.

$\mathbf{0.8 < |y^{\Upsilon}| < 1.2}$

Υ(1S)

p_{T}	A	S_p	A_{p_T}	A_{fsr}	$\varepsilon_{\mathrm{muid}}$	$\varepsilon_{\mathrm{trig}}$	ε_{ρ}	$\varepsilon_{\mathrm{func}}$	$\varepsilon_{\mathrm{trk}}$	PDF_{CB}	PDF_{bkgd}	M_{scale}
0.0 – 50.0	0.8 (0.8)	0.3 (0.3)	0.1	0.5	3.1 (2.0)	3.4 (3.4)	6.8	3.1	0.3 (0.4)	1.8	0.7	0.0 (0.0)
0.0 – 2.0	0.7 (0.8)	0.3 (0.3)	0.1	0.6	3.7 (3.2)	7.4 (4.0)	8.8	5.3	0.3 (0.3)	2.0	0.2	0.0 (0.0)
2.0 – 4.0	0.7 (0.8)	0.7 (0.9)	0.2	0.8	3.0 (2.4)	4.6 (4.1)	9.4	2.8	0.3 (0.3)	2.0	4.1	0.1 (0.1)
4.0 – 6.0	0.8 (0.8)	0.6 (0.3)	0.0	0.4	2.8 (2.1)	3.9 (3.4)	7.6	2.1	0.3 (0.3)	1.7	0.5	0.1 (0.2)
6.0 – 8.0	0.7 (0.7)	0.1 (0.2)	0.2	0.6	2.6 (1.9)	3.5 (3.1)	7.8	1.1	0.4 (0.4)	1.7	3.1	0.0 (0.2)
8.0 – 11.0	0.6 (0.6)	0.0 (0.0)	0.2	0.1	2.4 (1.7)	2.7 (2.5)	6.1	1.2	0.3 (0.3)	1.6	1.6	0.2 (0.2)
11.0 – 15.0	0.5 (0.5)	0.1 (0.1)	0.2	0.1	2.4 (1.8)	2.4 (2.1)	6.1	0.8	0.3 (0.3)	1.6	2.9	0.0 (0.2)
15.0 – 50.0	0.4 (0.4)	0.1 (0.2)	0.2	0.1	2.4 (2.0)	1.6 (1.4)	6.5	0.0	0.3 (0.3)	1.3	2.7	0.1 (0.1)

Υ(2S)

p_{T}	A	S_p	A_{p_T}	A_{fsr}	$\varepsilon_{\mathrm{muid}}$	$\varepsilon_{\mathrm{trig}}$	ε_{ρ}	$\varepsilon_{\mathrm{func}}$	$\varepsilon_{\mathrm{trk}}$	PDF_{CB}	PDF_{bkgd}	M_{scale}
0.0 – 42.0	0.8 (0.8)	0.3 (0.3)	0.1	0.5	3.0 (1.9)	3.5 (3.5)	6.8	1.4	1.4 (0.4)	2.4	0.3	0.1 (0.1)
0.0 – 3.0	0.4 (0.8)	0.3 (0.3)	0.1	0.4	2.1 (1.8)	2.5 (2.2)	5.7	3.7	0.2 (0.2)	1.2	3.3	0.1 (0.1)
3.0 – 7.0	0.9 (0.8)	1.7 (1.7)	0.2	0.5	3.8 (0.8)	5.1 (2.2)	7.5	1.5	0.3 (0.3)	2.1	2.8	0.2 (0.2)
7.0 – 11.0	0.7 (0.7)	0.0 (0.0)	0.2	0.3	2.5 (1.6)	3.2 (2.8)	7.2	0.7	0.4 (0.4)	2.0	5.0	0.3 (0.1)
11.0 – 15.0	0.5 (0.5)	0.1 (0.1)	0.2	0.1	2.4 (1.8)	2.0 (1.9)	6.1	0.6	0.3 (0.4)	1.9	3.9	0.0 (0.0)
15.0 – 42.0	0.4 (0.4)	0.2 (0.2)	0.2	0.1	2.4 (2.0)	1.6 (1.5)	6.5	0.2	0.3 (0.3)	1.6	3.8	0.1 (0.2)

Υ(3S)

p_{T}	A	S_p	A_{p_T}	A_{fsr}	$\varepsilon_{\mathrm{muid}}$	$\varepsilon_{\mathrm{trig}}$	ε_{ρ}	$\varepsilon_{\mathrm{func}}$	$\varepsilon_{\mathrm{trk}}$	PDF_{CB}	PDF_{bkgd}	M_{scale}
0.0 – 38.0	1.0 (0.9)	0.3 (0.3)	0.2	0.6	3.5 (2.2)	3.2 (3.2)	8.0	3.2	0.4 (0.4)	3.8	0.0	0.2 (0.3)
0.0 – 7.0	1.0 (0.8)	0.8 (0.8)	0.2	0.9	3.7 (3.0)	5.3 (4.7)	12.0	0.7	0.1 (0.9)	5.2	10.2	0.7 (0.7)
7.0 – 12.0	0.7 (0.8)	0.1 (0.1)	0.2	0.3	2.7 (1.8)	3.8 (3.3)	7.0	0.7	0.3 (0.5)	3.1	6.5	0.3 (0.1)
12.0 – 38.0	0.4 (0.4)	0.2 (0.1)	0.2	0.1	2.4 (1.8)	2.1 (1.9)	6.6	0.0	0.2 (0.5)	2.9	3.1	0.7 (0.7)

Table 4.42: Relative values of the systematic uncertainties on the Υ(nS) integrated and differential production cross section times the dimuon branching fraction, for $1.2 < |y| < 1.6$, assuming null production polarization, in units of percent. The p_{T} intervals are in units of GeV/c. The following abbreviations are used: A, S_p, $A_{p_{\mathrm{T}}}$, A_{fsr}, ϵ_{muid}, ϵ_{trig}, ϵ_{ρ}, ϵ_{func}, ϵ_{trk}, PDF_{CB}, PDF_{bkgd} and M_{scale} for the systematic uncertainties arising from the statistical uncertainties in acceptance, imperfect knowledge of the production p_{T} spectrum, imperfect knowledge of the momentum scale, the modeling of FSR, the statistical uncertainties in tag and probe muon identification, trigger efficiencies and the ρ factor, the choice of bin size for the efficiencies, the statistical uncertainties in tracking efficiencies, fixinging the tail parameters in fitting, the background PDF and imperfect knowledge of the momentum scale. The luminosity uncertainty of 4% is not shown in the table. The numbers in parentheses are negative variations.

$\mathbf{1.2 < |y^{\Upsilon}| < 1.6}$

Υ(1S)

p_{T}	A	S_p	A_{p_T}	A_{fsr}	$\varepsilon_{\mathrm{muid}}$	$\varepsilon_{\mathrm{trig}}$	ε_{ρ}	$\varepsilon_{\mathrm{func}}$	$\varepsilon_{\mathrm{trk}}$	PDF_{CB}	PDF_{bkgd}	M_{scale}
0.0 – 50.0	0.8 (0.8)	0.3 (0.3)	0.1	0.5	3.1 (2.0)	3.4 (3.4)	6.8	3.1	0.3 (0.4)	1.8	0.7	0.0 (0.0)
0.0 – 2.0	2.9 (0.8)	2.3 (2.3)	0.2	0.1	5.3 (2.3)	4.1 (3.3)	9.0	2.8	2.1 (0.6)	2.1	1.3	0.1 (0.4)
2.0 – 4.0	0.6 (0.8)	0.5 (0.5)	0.2	0.5	2.9 (1.8)	4.4 (3.1)	5.7	1.7	0.3 (0.3)	1.9	1.3	0.1 (0.1)
4.0 – 6.0	0.7 (0.7)	0.4 (0.4)	0.0	0.6	2.7 (1.6)	3.1 (2.7)	6.7	1.9	0.3 (0.3)	1.4	0.4	0.2 (0.1)
6.0 – 8.0	0.7 (0.7)	0.5 (0.5)	0.2	0.3	2.3 (2.0)	2.4 (2.7)	5.4	1.9	0.3 (0.3)	1.5	2.3	0.1 (0.1)
8.0 – 11.0	0.6 (0.6)	0.1 (0.1)	0.1	0.1	2.8 (1.9)	2.6 (2.3)	6.0	0.6	0.3 (0.3)	1.4	0.1	0.0 (0.0)
11.0 – 15.0	0.5 (0.5)	0.2 (0.1)	0.2	0.1	2.7 (2.0)	2.0 (1.8)	5.9	0.2	0.3 (0.3)	1.3	2.0	0.2 (0.3)
15.0 – 50.0	0.4 (0.4)	0.2 (0.2)	0.2	0.2	2.7 (2.2)	1.6 (1.5)	4.8	1.0	0.3 (0.3)	1.3	1.0	0.0 (0.1)

Υ(2S)

p_{T}	A	S_p	A_{p_T}	A_{fsr}	$\varepsilon_{\mathrm{muid}}$	$\varepsilon_{\mathrm{trig}}$	ε_{ρ}	$\varepsilon_{\mathrm{func}}$	$\varepsilon_{\mathrm{trk}}$	PDF_{CB}	PDF_{bkgd}	M_{scale}
0.0 – 42.0	0.8 (0.8)	0.3 (0.3)	0.1	0.5	3.0 (1.9)	3.5 (3.5)	6.8	1.4	1.4 (0.4)	2.4	0.3	0.1 (0.1)
0.0 – 3.0	0.3 (0.8)	0.2 (0.2)	0.0	0.3	1.7 (1.1)	2.2 (2.0)	3.9	0.0	0.2 (0.2)	1.4	5.2	0.3 (0.3)
3.0 – 7.0	0.7 (0.8)	0.4 (0.6)	0.0	0.5	2.5 (1.3)	2.7 (2.2)	6.4	1.3	0.3 (0.3)	2.0	0.0	0.2 (0.0)
7.0 – 11.0	0.7 (0.7)	0.0 (0.0)	0.2	0.1	3.0 (2.0)	2.7 (2.4)	5.9	1.5	0.4 (0.4)	1.9	3.5	0.1 (0.1)
11.0 – 15.0	0.5 (0.5)	0.2 (0.1)	0.2	0.1	2.8 (2.0)	1.8 (1.6)	5.9	0.7	0.3 (0.4)	1.7	1.4	0.1 (0.4)
15.0 – 42.0	0.4 (0.4)	0.2 (0.2)	0.2	0.1	2.7 (2.3)	1.4 (1.3)	4.6	1.0	0.3 (0.3)	1.7	1.5	0.2 (0.2)

Υ(3S)

p_{T}	A	S_p	A_{p_T}	A_{fsr}	$\varepsilon_{\mathrm{muid}}$	$\varepsilon_{\mathrm{trig}}$	ε_{ρ}	$\varepsilon_{\mathrm{func}}$	$\varepsilon_{\mathrm{trk}}$	PDF_{CB}	PDF_{bkgd}	M_{scale}
0.0 – 38.0	1.0 (0.9)	0.3 (0.3)	0.2	0.6	3.5 (2.2)	3.2 (3.2)	8.0	3.2	0.4 (0.4)	3.8	0.0	0.2 (0.3)
0.0 – 7.0	0.8 (0.8)	0.5 (0.4)	0.1	0.6	3.1 (1.7)	3.2 (2.8)	7.5	2.5	0.7 (0.2)	3.6	1.2	0.5 (0.5)
7.0 – 12.0	0.6 (0.8)	0.0 (0.1)	0.2	0.2	3.1 (2.2)	2.4 (2.2)	6.4	0.5	0.2 (0.5)	3.0	8.1	1.1 (1.1)
12.0 – 38.0	0.4 (0.4)	0.1 (0.2)	0.2	0.2	2.9 (2.3)	1.9 (1.7)	5.3	0.6	0.3 (0.3)	2.7	5.7	0.0 (0.0)

Table 4.43: Relative values of the systematic uncertainties on the Υ(nS) integrated and differential production cross section times the dimuon branching fraction, for $1.6 < |y| < 2.4$, assuming null production polarization, in units of percent. The p_{T} intervals are in units of GeV/c. The following abbreviations are used: A, S_p, $A_{p_{\mathrm{T}}}$, A_{fsr}, ϵ_{muid}, ϵ_{trig}, ϵ_{ρ}, ϵ_{func}, ϵ_{trk}, PDF_{CB}, PDF_{bkgd} and M_{scale} for the systematic uncertainties arising from the statistical uncertainties in acceptance, imperfect knowledge of the production p_{T} spectrum, imperfect knowledge of the momentum scale, the modeling of FSR, the statistical uncertainties in tag and probe muon identification, trigger efficiencies and the ρ factor, the choice of bin size for the efficiencies, the statistical uncertainties in tracking efficiencies, fixinging the tail parameters in fitting, the background PDF and imperfect knowledge of the momentum scale. The luminosity uncertainty of 4% is not shown in the table. The numbers in parentheses are negative variations.

$1.6 < |y^{\Upsilon}| < 2.0$

Υ(1S)

p_{T}	A	S_p	A_{p_T}	A_{fsr}	$\varepsilon_{\mathrm{muid}}$	$\varepsilon_{\mathrm{trig}}$	ε_{ρ}	$\varepsilon_{\mathrm{func}}$	$\varepsilon_{\mathrm{trk}}$	PDF_{CB}	PDF_{bkgd}	M_{scale}
0.0 – 50.0	0.8 (0.8)	0.3 (0.3)	0.1	0.5	3.1 (2.0)	3.4 (3.4)	6.8	3.1	0.3 (0.4)	1.8	0.7	0.0 (0.0)
0.0 – 2.0	0.7 (0.8)	0.1 (0.0)	0.2	0.4	4.0 (2.7)	3.3 (2.8)	4.0	1.3	0.3 (0.3)	2.0	3.9	0.2 (0.2)
2.0 – 4.0	0.5 (0.8)	0.0 (0.3)	0.0	0.5	3.6 (1.5)	2.9 (2.7)	3.6	0.1	0.5 (0.2)	1.6	1.5	0.3 (0.0)
4.0 – 6.0	0.8 (0.7)	0.4 (0.3)	0.1	0.4	3.1 (1.2)	2.8 (2.4)	3.4	0.4	0.4 (0.3)	1.4	0.8	0.0 (0.0)
6.0 – 8.0	0.8 (0.8)	0.5 (0.5)	0.2	0.3	2.7 (1.5)	2.1 (2.4)	3.0	0.3	0.3 (0.3)	1.3	1.1	0.1 (0.1)
8.0 – 11.0	0.7 (0.7)	0.1 (0.1)	0.1	0.1	3.2 (1.7)	2.2 (1.9)	2.0	0.1	0.4 (0.3)	1.3	2.9	0.1 (0.1)
11.0 – 15.0	0.6 (0.6)	0.2 (0.2)	0.0	0.1	3.5 (2.5)	2.2 (2.0)	3.5	1.4	0.3 (0.3)	1.1	2.2	0.2 (0.2)
15.0 – 50.0	0.4 (0.4)	0.2 (0.2)	0.1	0.1	3.7 (3.0)	2.1 (1.9)	2.1	3.9	0.3 (0.4)	1.0	1.3	0.0 (0.2)

Υ(2S)

p_{T}	A	S_p	A_{p_T}	A_{fsr}	$\varepsilon_{\mathrm{muid}}$	$\varepsilon_{\mathrm{trig}}$	ε_{ρ}	$\varepsilon_{\mathrm{func}}$	$\varepsilon_{\mathrm{trk}}$	PDF_{CB}	PDF_{bkgd}	M_{scale}
0.0 – 42.0	0.8 (0.8)	0.3 (0.3)	0.1	0.5	3.0 (1.9)	3.5 (3.5)	6.8	1.4	1.4 (0.4)	2.4	0.3	0.1 (0.1)
0.0 – 3.0	0.6 (0.8)	0.1 (0.1)	0.0	0.4	3.4 (2.5)	2.4 (2.1)	3.5	1.1	0.3 (0.3)	2.4	4.4	0.2 (0.2)
3.0 – 7.0	0.8 (0.8)	0.4 (0.2)	0.0	0.4	3.1 (1.0)	2.8 (2.3)	3.6	0.4	0.4 (0.4)	2.3	4.1	0.1 (0.2)
7.0 – 11.0	0.8 (0.8)	0.0 (0.1)	0.2	0.1	3.4 (1.9)	2.4 (2.1)	1.9	0.1	0.4 (0.3)	2.0	4.6	0.3 (0.3)
11.0 – 15.0	0.6 (0.6)	0.2 (0.3)	0.2	0.2	3.6 (2.7)	2.3 (2.1)	3.5	1.1	0.3 (0.3)	1.6	1.8	0.2 (0.3)
15.0 – 42.0	0.4 (0.4)	0.2 (0.3)	0.1	0.0	3.7 (3.1)	2.0 (1.8)	1.7	3.4	0.3 (0.3)	1.8	0.3	0.1 (0.2)

Υ(3S)

p_{T}	A	S_p	A_{p_T}	A_{fsr}	$\varepsilon_{\mathrm{muid}}$	$\varepsilon_{\mathrm{trig}}$	ε_{ρ}	$\varepsilon_{\mathrm{func}}$	$\varepsilon_{\mathrm{trk}}$	PDF_{CB}	PDF_{bkgd}	M_{scale}
0.0 – 38.0	1.0 (0.9)	0.3 (0.3)	0.2	0.6	3.5 (2.2)	3.2 (3.2)	8.0	3.2	0.4 (0.4)	3.8	0.0	0.2 (0.3)
0.0 – 7.0	0.8 (0.8)	0.2 (0.2)	0.1	0.5	3.9 (1.9)	3.3 (2.9)	4.3	1.1	0.5 (0.4)	4.0	6.4	0.3 (0.0)
7.0 – 12.0	0.8 (0.8)	0.1 (0.1)	0.2	0.1	3.4 (1.8)	1.4 (1.3)	2.1	5.6	0.3 (0.3)	2.2	14.2	0.3 (0.3)
12.0 – 38.0	0.5 (0.5)	0.2 (0.2)	0.2	0.0	3.6 (2.8)	2.0 (1.8)	3.1	2.5	0.4 (0.3)	2.5	2.3	0.2 (2.3)

Table 4.44: Relative values of the systematic uncertainties on the Υ(nS) integrated and differential production cross section times the dimuon branching fraction, for $2.0 < |y| < 2.4$, assuming null production polarization, in units of percent. The p_{T} intervals are in units of GeV/c. The following abbreviations are used: A, S_p, $A_{p_{\mathrm{T}}}$, A_{fsr}, ϵ_{muid}, ϵ_{trig}, ϵ_{ρ}, ϵ_{func}, ϵ_{trk}, PDF_{CB}, PDF_{bkgd} and M_{scale} for the systematic uncertainties arising from the statistical uncertainties in acceptance, imperfect knowledge of the production p_{T} spectrum, imperfect knowledge of the momentum scale, the modeling of FSR, the statistical uncertainties in tag and probe muon identification, trigger efficiencies and the ρ factor, the choice of bin size for the efficiencies, the statistical uncertainties in tracking efficiencies, fixinging the tail parameters in fitting, the background PDF and imperfect knowledge of the momentum scale. The luminosity uncertainty of 4% is not shown in the table. The numbers in parentheses are negative variations.

$\mathbf{2.0 < |y^{\Upsilon}| < 2.4}$

Υ(1S)

p_{T}	A	S_p	A_{p_T}	A_{fsr}	$\varepsilon_{\mathrm{muid}}$	$\varepsilon_{\mathrm{trig}}$	ε_{ρ}	$\varepsilon_{\mathrm{func}}$	$\varepsilon_{\mathrm{trk}}$	PDF_{CB}	PDF_{bkgd}	M_{scale}
0.0 – 50.0	0.8 (0.8)	0.3 (0.3)	0.1	0.5	3.1 (2.0)	3.4 (3.4)	6.8	3.1	0.3 (0.4)	1.8	0.7	0.0 (0.0)
0.0 – 2.0	3.1 (0.8)	0.2 (0.2)	0.2	0.2	5.7 (4.0)	2.7 (2.3)	3.8	0.5	3.4 (3.4)	0.2	1.4	2.3 (2.3)
2.0 – 4.0	1.2 (0.8)	1.0 (1.0)	0.1	0.4	4.3 (1.4)	3.4 (2.9)	3.3	1.3	0.4 (2.2)	3.2	1.5	1.5 (1.5)
4.0 – 6.0	1.3 (1.3)	0.4 (0.4)	0.0	0.6	3.8 (0.8)	3.1 (2.7)	4.0	1.9	0.4 (0.4)	1.2	4.7	0.2 (0.2)
6.0 – 8.0	1.5 (1.5)	0.1 (0.2)	0.0	0.1	4.3 (1.7)	2.7 (2.3)	2.7	0.2	0.4 (0.4)	1.0	4.5	0.4 (0.1)
8.0 – 11.0	1.4 (1.4)	0.0 (0.0)	0.2	0.4	4.8 (2.7)	2.7 (2.3)	1.6	2.7	0.4 (0.4)	1.2	1.5	0.3 (0.3)
11.0 – 15.0	1.4 (1.3)	0.1 (0.1)	0.1	0.3	4.9 (3.3)	2.7 (2.4)	1.6	4.7	0.4 (0.4)	1.1	2.4	0.3 (0.3)
15.0 – 50.0	1.1 (1.0)	0.3 (0.3)	0.1	0.1	5.2 (4.2)	2.6 (2.3)	0.2	6.5	0.4 (0.4)	0.4	2.9	0.6 (0.3)

Υ(2S)

p_{T}	A	S_p	A_{p_T}	A_{fsr}	$\varepsilon_{\mathrm{muid}}$	$\varepsilon_{\mathrm{trig}}$	ε_{ρ}	$\varepsilon_{\mathrm{func}}$	$\varepsilon_{\mathrm{trk}}$	PDF_{CB}	PDF_{bkgd}	M_{scale}
0.0 – 42.0	0.8 (0.8)	0.3 (0.3)	0.1	0.5	3.0 (1.9)	3.5 (3.5)	6.8	1.4	1.4 (0.4)	2.4	0.3	0.1 (0.1)
0.0 – 3.0	1.1 (0.8)	0.2 (0.1)	0.2	0.1	4.5 (3.3)	2.1 (1.7)	3.5	0.3	0.3 (0.3)	2.3	5.8	0.1 (0.1)
3.0 – 7.0	1.5 (0.8)	0.2 (0.2)	0.0	0.5	4.3 (1.2)	3.3 (2.8)	3.6	0.1	0.4 (0.4)	2.2	2.7	0.4 (0.4)
7.0 – 11.0	1.5 (1.5)	0.0 (0.0)	0.2	0.4	5.2 (3.3)	3.0 (2.6)	1.8	4.1	0.4 (0.4)	1.9	1.4	0.5 (0.5)
11.0 – 15.0	1.2 (1.2)	0.2 (0.1)	0.1	0.1	4.9 (3.3)	2.4 (2.1)	1.7	4.7	0.4 (0.4)	1.8	2.3	0.4 (0.4)
15.0 – 42.0	1.1 (1.1)	0.3 (0.3)	0.1	0.0	5.3 (4.2)	2.5 (2.2)	1.1	6.5	0.4 (0.4)	2.9	0.4	0.6 (0.6)

Υ(3S)

p_{T}	A	S_p	A_{p_T}	A_{fsr}	$\varepsilon_{\mathrm{muid}}$	$\varepsilon_{\mathrm{trig}}$	ε_{ρ}	$\varepsilon_{\mathrm{func}}$	$\varepsilon_{\mathrm{trk}}$	PDF_{CB}	PDF_{bkgd}	M_{scale}
0.0 – 38.0	1.0 (0.9)	0.3 (0.3)	0.2	0.6	3.5 (2.2)	3.2 (3.2)	8.0	3.2	0.4 (0.4)	3.8	0.0	0.2 (0.3)
0.0 – 7.0	1.5 (0.8)	0.1 (0.1)	0.1	0.3	5.4 (2.8)	3.2 (2.6)	4.5	0.3	1.2 (1.2)	2.5	2.1	2.2 (2.2)
7.0 – 12.0	1.8 (0.8)	0.1 (0.2)	0.2	0.5	5.5 (3.7)	3.2 (2.8)	1.0	5.4	1.0 (1.0)	3.3	4.6	1.9 (1.9)
12.0 – 38.0	1.1 (1.1)	0.2 (0.3)	0.2	0.0	4.8 (3.6)	2.6 (2.3)	0.9	6.1	0.2 (0.5)	2.1	1.6	1.2 (1.2)

Table 4.45: Relative values of the systematic uncertainties on the $\Upsilon(1S)$ integrated and rapidity differential production cross section times the dimuon branching fraction, for $p_T < 50$ GeV/c, assuming null production polarization, in units of percent. The following abbreviations are used: A, S_p, A_{p_T}, $A_{\rm fsr}$, $\epsilon_{\rm muid}$, $\epsilon_{\rm trig}$, ϵ_ρ, $\epsilon_{\rm func}$, $\epsilon_{\rm trk}$, $PDF_{\rm CB}$, $PDF_{\rm bkgd}$ and $M_{\rm scale}$ for the systematic uncertainties arising from the statistical uncertainties in acceptance, imperfect knowledge of the production p_T spectrum, imperfect knowledge of the momentum scale, the modeling of FSR, the statistical uncertainties in tag and probe muon identification, trigger efficiencies and the ρ factor, the choice of bin size for the efficiencies, the statistical uncertainties in tracking efficiencies, fixinging the tail parameters in fitting, the background PDF and imperfect knowledge of the momentum scale. The luminosity uncertainty of 4% is not shown in the table. The numbers in parentheses are negative variations.

	$\|y\|$	A	S_p	A_{p_T}	$A_{\rm fsr}$	$\varepsilon_{\rm muid}$	$\varepsilon_{\rm trig}$	ε_ρ	$\varepsilon_{\rm func}$	$\varepsilon_{\rm trk}$	$PDF_{\rm CB}$	$PDF_{\rm bkgd}$	$M_{\rm scale}$
$\Upsilon(1S)$	$0.0-2.4$	0.8 (0.8)	0.3 (0.3)	0.1	0.5	3.1 (2.0)	3.4 (3.4)	6.8	1.7	0.3 (0.3)	1.7	0.7	0.0 (0.0)
	$0.0-0.2$	0.8 (0.8)	0.5 (0.5)	0.2	0.7	2.8 (2.4)	5.7 (5.0)	9.0	4.0	0.4 (0.4)	2.2	3.6	0.0 (0.0)
	$0.2-0.4$	0.8 (0.8)	0.5 (0.4)	0.2	0.5	2.8 (2.3)	5.3 (4.6)	8.9	4.3	0.4 (0.4)	2.3	1.4	0.0 (0.0)
	$0.4-0.6$	0.8 (0.7)	0.5 (0.5)	0.2	1.4	2.9 (2.4)	5.0 (4.4)	11.9	2.5	0.8 (0.8)	2.6	1.7	0.5 (0.5)
	$0.6-0.8$	0.7 (0.7)	0.4 (0.5)	0.2	0.6	2.9 (2.4)	4.4 (4.4)	6.5	2.6	0.3 (0.4)	2.2	1.8	3.3 (3.3)
	$0.8-1.0$	0.7 (0.7)	0.4 (0.4)	0.2	0.6	2.9 (2.3)	4.0 (3.5)	12.2	2.3	0.3 (0.3)	2.0	1.0	0.1 (0.1)
	$1.0-1.2$	0.7 (0.6)	0.4 (0.4)	0.1	0.4	2.8 (2.1)	3.5 (3.1)	4.0	2.1	0.3 (0.3)	2.0	1.5	0.0 (0.0)
	$1.2-1.4$	0.6 (0.6)	0.3 (0.3)	0.1	0.5	2.7 (1.9)	3.2 (2.8)	9.2	1.9	0.3 (0.3)	1.9	1.3	0.0 (0.0)
	$1.4-1.6$	0.6 (0.6)	0.2 (0.2)	0.1	0.3	2.9 (1.7)	3.0 (2.6)	2.8	1.1	0.3 (0.3)	1.8	0.3	0.0 (0.0)
	$1.6-1.8$	0.7 (0.6)	0.1 (0.2)	0.0	0.4	3.2 (1.7)	2.9 (2.5)	5.9	0.1	0.3 (0.3)	2.0	1.9	0.1 (0.1)
	$1.8-2.0$	0.8 (0.7)	0.8 (0.8)	0.0	0.3	3.5 (1.6)	2.6 (2.3)	0.7	0.6	0.4 (0.3)	1.7	3.1	0.0 (0.0)
	$2.0-2.2$	1.1 (0.7)	0.2 (0.2)	0.2	0.3	3.1 (1.5)	2.9 (2.3)	2.6	0.5	0.4 (0.4)	1.4	3.8	0.0 (0.1)
	$2.2-2.4$	1.7 (2.2)	0.3 (0.5)	0.2	0.5	4.5 (2.4)	3.1 (2.0)	4.9	1.7	0.5 (0.3)	1.7	0.2	0.2 (0.2)
	$\|y\|$	A	S_p	A_{p_T}	$A_{\rm fsr}$	$\varepsilon_{\rm muid}$	$\varepsilon_{\rm trig}$	ε_ρ	$\varepsilon_{\rm func}$	$\varepsilon_{\rm trk}$	$PDF_{\rm CB}$	$PDF_{\rm bkgd}$	$M_{\rm scale}$
$\Upsilon(2S)$	$0.0-2.4$	1.0 (0.9)	0.4 (0.4)	0.2	0.6	3.6 (2.3)	4.2 (4.2)	8.1	1.6	0.4 (0.4)	2.8	0.3	0.1 (0.1)
	$0.0-0.4$	0.9 (0.8)	0.5 (0.5)	0.2	0.7	3.0 (2.3)	5.0 (4.4)	11.3	4.2	0.4 (0.5)	3.3	1.2	0.1 (0.1)
	$0.4-0.8$	0.9 (0.8)	0.5 (0.6)	0.2	0.7	3.1 (2.5)	4.2 (3.8)	10.3	2.4	0.4 (0.4)	3.2	0.6	0.1 (0.1)
	$0.8-1.2$	0.8 (0.8)	0.5 (0.4)	0.2	0.5	3.0 (2.3)	3.9 (3.4)	9.1	1.8	0.4 (0.4)	3.1	3.7	0.0 (0.0)
	$1.2-1.6$	0.7 (0.7)	0.2 (0.3)	0.1	0.4	3.0 (1.9)	3.1 (2.7)	6.8	1.3	0.4 (0.4)	2.5	2.5	0.1 (0.1)
	$1.6-2.0$	0.8 (0.7)	0.1 (0.1)	0.0	0.3	3.6 (1.9)	2.7 (2.4)	3.5	0.4	0.4 (0.4)	2.8	3.7	0.1 (0.1)
	$2.0-2.4$	1.4 (1.4)	0.1 (0.1)	0.2	0.4	4.7 (2.1)	2.8 (2.6)	2.7	1.2	0.4 (0.6)	2.6	1.8	0.1 (0.3)
	$\|y\|$	A	S_p	A_{p_T}	$A_{\rm fsr}$	$\varepsilon_{\rm muid}$	$\varepsilon_{\rm trig}$	ε_ρ	$\varepsilon_{\rm func}$	$\varepsilon_{\rm trk}$	$PDF_{\rm CB}$	$PDF_{\rm bkgd}$	$M_{\rm scale}$
$\Upsilon(3S)$	$0.0-2.4$	1.0 (0.9)	0.3 (0.3)	0.2	0.6	3.5 (2.2)	3.2 (3.2)	8.0	1.9	0.4 (0.5)	3.8	0.0	0.2 (0.3)
	$0.0-0.4$	0.9 (0.8)	0.5 (0.6)	0.2	0.7	3.0 (2.3)	4.7 (4.2)	12.0	5.2	0.5 (0.1)	4.6	1.4	0.1 (0.1)
	$0.4-0.8$	0.9 (0.8)	0.5 (0.5)	0.2	0.8	3.2 (2.6)	4.3 (3.8)	11.2	3.3	0.5 (0.4)	4.6	0.0	0.1 (0.1)
	$0.8-1.4$	0.8 (0.8)	0.4 (0.4)	0.2	0.6	3.1 (2.2)	3.8 (3.4)	10.3	0.6	0.4 (0.4)	4.2	3.7	0.1 (0.1)
	$1.4-2.0$	0.7 (0.7)	0.2 (0.1)	0.0	0.4	3.5 (1.9)	2.8 (2.4)	3.6	0.8	0.4 (0.4)	3.7	4.1	0.1 (0.1)
	$2.0-2.4$	1.5 (1.5)	0.1 (0.6)	0.1	1.0	4.7 (2.3)	2.5 (3.0)	3.0	1.6	0.5 (0.4)	3.6	0.9	0.4 (0.0)

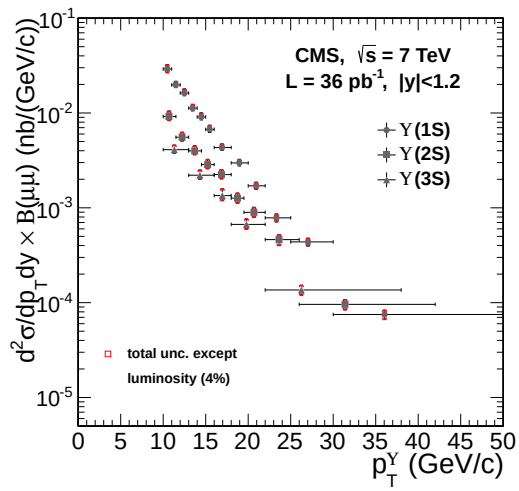

Figure 4.15.: Differential cross sections of the Υ(nS) as a function of $p_{\mathrm{T}}^{\Upsilon}$ for $10 < p_{\mathrm{T}}^{\Upsilon} < 50\,\mathrm{GeV}/c$, $|y^{\Upsilon}| < 1.2$. The total uncertainties include the systematic uncertainty from the polarization measurement in Ref. [49].

Table 4.46: The product of the Υ(nS) production cross sections and the dimuon branching fraction, in nb, integrated over the rapidity range $|y^{\Upsilon}| < 1.2$ and the p_{T} range from 10 to 50 GeV/c. The cross sections assume the Υ(nS) are unpolarized. The statistical uncertainty (stat.), the sum in quadrature of the systematic uncertainties apart from the ones from the polarization ($\sum_{\mathrm{syst.}}$), the systematic uncertainties from the polarization (syst.(pol)), and the total uncertainty ($\Delta\sigma$; including stat., $\sum_{\mathrm{syst.}}$, syst.(pol), luminosity terms) are in percent. The numbers in parentheses are negative variations.

	σ	$\frac{stat.}{\sigma}$	$\frac{\sum_{\mathrm{syst.}}}{\sigma}$	$\frac{syst.(pol.)}{\sigma}$	$\frac{\Delta\sigma}{\sigma}$
Υ(1S)	0.56	1.2	7.6 (5.5)	3.5 (1.5)	8.5 (5.8)
Υ(2S)	0.21	2.3	7.7 (5.5)	7.5 (3.5)	11.0 (6.9)
Υ(3S)	0.13	3.2	8.3 (5.9)	6.5 (3.4)	11.0 (7.5)

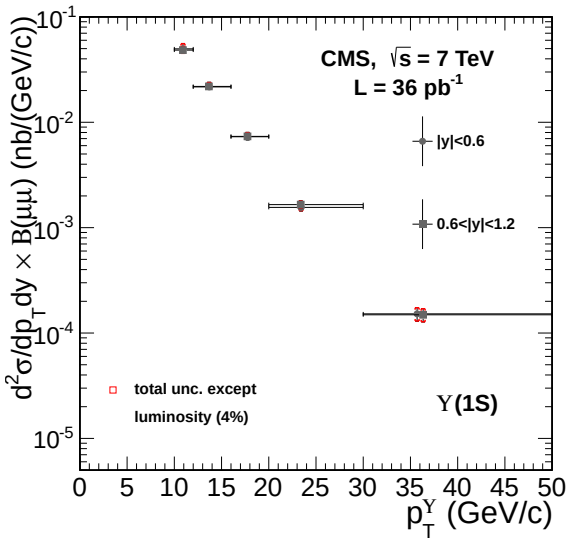

(a) Υ(1S)

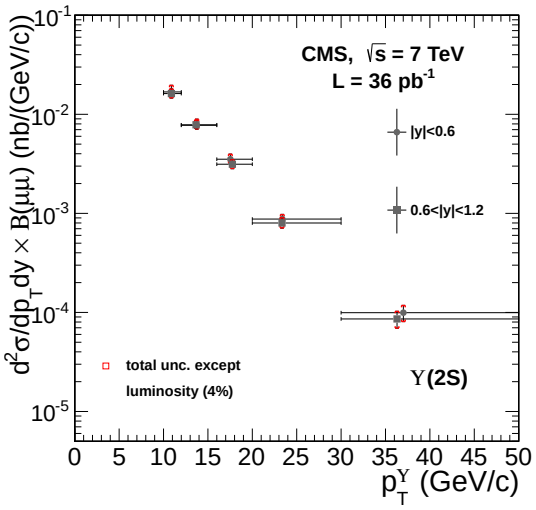

(b) Υ(2S)

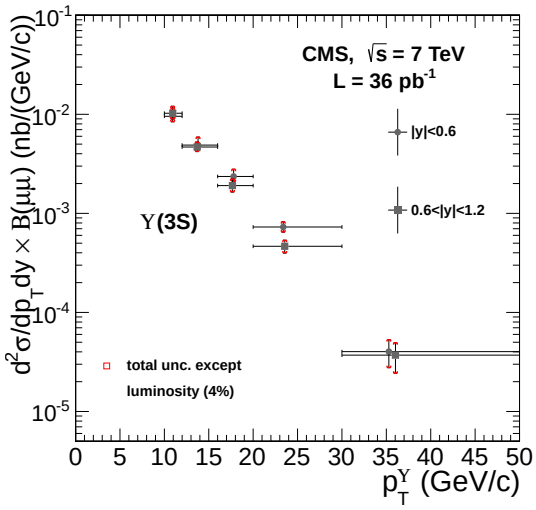

(c) Υ(3S)

Figure 4.16.: Differential production cross section results of the Υ(nS) as a function of p_{T} in two rapidity regions for $10 < p_{\mathrm{T}}^{\Upsilon} < 50\,\mathrm{GeV}/c$. The total uncertainties include the systematic uncertainty from the polarization measurement in Ref. [49].

Table 4.47: The product of the Υ(nS) integrated and differential production cross sections and the dimuon branching fraction, in nb, integrated over the rapidity range $|y^{\Upsilon}| < 1.2$ and the $p_{\mathrm{T}}^{\Upsilon}$ range from 10 to 50 GeV/c. The cross sections assume the Υ(nS) are unpolarized. The statistical uncertainty (stat.), the sum in quadrature of the systematic uncertainties excluding the contribution from the polarization uncertainty ($\sum_{\mathrm{syst.}}$), the systematic uncertainties from the polarization (syst.(pol)), and the total uncertainty ($\Delta\sigma$; including stat., $\sum_{\mathrm{syst.}}$, syst.(pol), and the uncertainty in the integrated luminosity) are in percent. The numbers in parentheses are negative variations.

$|y^{\Upsilon}| < 1.2$

Υ(1S)

p_{T} (GeV/c)	σ	stat./σ	$\sum_{\mathrm{syst.}}/\sigma$	$\frac{\mathrm{syst.(pol.)}}{\sigma}$	$\Delta\sigma/\sigma$
10.0 – 50.0	0.56	1.3	9 (8)	4 (2)	11 (9)
10.0 – 11.0	0.14	2.8	11 (10)	5 (1)	13 (11)
11.0 – 12.0	0.09	3.4	6 (6)	4 (1)	9 (8)
12.0 – 13.0	0.08	3.6	9 (8)	3 (1)	10 (10)
13.0 – 14.0	0.05	4.1	7 (7)	3 (1)	9 (9)
14.0 – 15.0	0.04	4.4	8 (8)	3 (1)	10 (10)
15.0 – 16.0	0.03	5.0	8 (8)	3 (1)	10 (10)
16.0 – 18.0	0.04	4.2	7 (7)	2 (2)	9 (9)
18.0 – 20.0	0.03	4.9	7 (6)	2 (2)	9 (9)
20.0 – 22.0	0.02	6.4	6 (6)	2 (2)	10 (9)
22.0 – 25.0	0.01	7.6	6 (5)	2 (2)	10 (10)
25.0 – 30.0	0.01	7.8	5 (5)	1 (2)	10 (10)
30.0 – 50.0	0.01	9.4	6 (5)	3 (2)	12 (12)

Υ(2S)

p_{T} (GeV/c)	σ	stat./σ	$\sum_{\mathrm{syst.}}/\sigma$	$\frac{\mathrm{syst.(pol.)}}{\sigma}$	$\Delta\sigma/\sigma$
10.0 – 42.0	0.21	2.4	7 (8)	7 (3)	11 (9)
10.0 – 11.5	0.07	4.9	10 (10)	9 (3)	15 (12)
11.5 – 13.0	0.04	5.7	9 (8)	8 (4)	14 (12)
13.0 – 14.5	0.03	6.3	8 (8)	8 (4)	14 (12)
14.5 – 16.0	0.02	6.9	9 (9)	7 (4)	14 (13)
16.0 – 18.0	0.02	6.4	11 (10)	6 (3)	14 (13)
18.0 – 19.5	0.01	9.5	8 (7)	5 (3)	14 (13)
19.5 – 22.0	0.01	8.5	8 (8)	6 (4)	13 (13)
22.0 – 26.0	0.01	9.3	9 (9)	7 (4)	16 (15)
26.0 – 42.0	0.01	9.7	7 (6)	6 (4)	13 (13)

Υ(3S)

p_{T} (GeV/c)	σ	stat./σ	$\sum_{\mathrm{syst.}}/\sigma$	$\frac{\mathrm{syst.(pol.)}}{\sigma}$	$\Delta\sigma/\sigma$
10.0 – 38.0	0.13	3.2	9 (8)	7 (3)	12 (9)
10.0 – 13.0	0.06	5.2	9 (9)	5 (3)	12 (11)
13.0 – 16.0	0.03	6.3	8 (8)	8 (4)	14 (12)
16.0 – 18.0	0.01	9.1	12 (12)	9 (5)	17 (16)
18.0 – 22.0	0.01	8.4	8 (8)	8 (4)	14 (13)
22.0 – 38.0	0.01	8.9	7 (6)	6 (4)	13 (13)

Table 4.48: The product of the Υ(nS) integrated and differential production cross sections and the dimuon branching fraction, in nb, measured for four polarization scenarios, in helicity frame (HX) and Collins-Soper (CS) frame, each for L= 100% longitudinal, and T= 100% transverse, integrated over the rapidity range $|y^{\Upsilon}| < 0.6$. The statistical uncertainty (stat.), the sum of the systematic uncertainties in quadrature ($\Sigma_{\text{syst.}}$), and the total uncertainty ($\Delta\sigma$; including stat., $\sum_{\text{syst.}}$, luminosity terms) are in percent. For the four polarization scenarios the fractional change in percent to the central value of the cross section relative to the unpolarized value is given. The numbers in parentheses are negative variations.

$|y^{\Upsilon}| < 0.6$

Υ(1S)

p_{T} (GeV/c)	σ	stat./σ	$\sum_{\text{syst.}}/\sigma$	syst.(pol.)/σ	$\Delta\sigma/\sigma$
10.0 – 50.0	0.28	0.9	8 (8)	3 (2)	9 (9)
10.0 – 12.0	0.12	3.1	10 (9)	7 (3)	13 (11)
12.0 – 16.0	0.10	3.0	8 (8)	4 (1)	11 (10)
16.0 – 20.0	0.03	4.5	7 (6)	3 (2)	9 (9)
20.0 – 30.0	0.02	5.9	4 (4)	1 (1)	9 (8)
30.0 – 50.0	0.00	13.5	5 (5)	3 (2)	15 (15)

Υ(2S)

p_{T} (GeV/c)	σ	stat./σ	$\sum_{\text{syst.}}/\sigma$	syst.(pol.)/σ	$\Delta\sigma/\sigma$
10.0 – 50.0	0.11	1.7	8 (8)	7 (3)	11 (9)
10.0 – 12.0	0.04	6.1	10 (10)	11 (4)	17 (13)
12.0 – 16.0	0.04	5.4	9 (9)	11 (5)	16 (12)
16.0 – 20.0	0.02	6.9	7 (7)	8 (3)	13 (11)
20.0 – 30.0	0.01	8.4	5 (4)	6 (3)	12 (11)
30.0 – 50.0	0.00	16.8	7 (6)	6 (4)	20 (19)

Υ(3S)

p_{T} (GeV/c)	σ	stat./σ	$\sum_{\text{syst.}}/\sigma$	syst.(pol.)/σ	$\Delta\sigma/\sigma$
10.0 – 50.0	0.06	2.3	8 (8)	7 (3)	11 (10)
10.0 – 12.0	0.02	9.3	12 (11)	8 (3)	17 (16)
12.0 – 16.0	0.02	7.5	9 (9)	10 (5)	16 (13)
16.0 – 20.0	0.01	9.3	7 (7)	8 (4)	15 (13)
20.0 – 30.0	0.01	9.3	5 (4)	7 (4)	13 (12)
30.0 – 50.0	0.00	28.7	11 (11)	6 (4)	31 (31)

Table 4.49: The product of the Υ(nS) integrated and differential production cross sections and the dimuon branching fraction, in nb, measured for four polarization scenarios, in helicity frame (HX) and Collins-Soper (CS) frame, each for L= 100% longitudinal, and T= 100% transverse, integrated over the rapidity range $0.6 < |y^{\Upsilon}| < 1.2$. The statistical uncertainty (stat.), the sum of the systematic uncertainties in quadrature ($\Sigma_{\text{syst.}}$), and the total uncertainty ($\Delta\sigma$; including stat., $\sum_{\text{syst.}}$, luminosity terms) are in percent. For the four polarization scenarios the fractional change in percent to the central value of the cross section relative to the unpolarized value is given. The numbers in parentheses are negative variations.

$0.6 < |y^{\Upsilon}| < 1.2$

Υ(1S)

p_{T} (GeV/c)	σ	stat./σ	$\sum_{\text{syst.}}/\sigma$	syst.(pol.)/σ	$\Delta\sigma/\sigma$
10.0 – 50.0	0.28	0.9	8 (8)	3 (2)	9 (9)
10.0 – 12.0	0.12	3.2	8 (8)	2 (1)	10 (9)
12.0 – 16.0	0.11	2.9	8 (8)	2 (2)	10 (9)
16.0 – 20.0	0.04	4.5	7 (7)	2 (2)	10 (10)
20.0 – 30.0	0.02	5.7	6 (6)	2 (2)	9 (10)
30.0 – 50.0	0.00	12.9	6 (6)	3 (2)	15 (15)

Υ(2S)

p_{T} (GeV/c)	σ	stat./σ	$\sum_{\text{syst.}}/\sigma$	syst.(pol.)/σ	$\Delta\sigma/\sigma$
10.0 – 50.0	0.10	1.7	8 (8)	7 (3)	11 (9)
10.0 – 12.0	0.04	6.3	8 (8)	6 (2)	13 (11)
12.0 – 16.0	0.04	5.4	8 (8)	3 (3)	11 (11)
16.0 – 20.0	0.02	7.6	8 (8)	3 (3)	12 (12)
20.0 – 30.0	0.01	8.8	6 (6)	8 (5)	14 (12)
30.0 – 50.0	0.00	18.0	7 (7)	5 (3)	20 (20)

Υ(3S)

p_{T} (GeV/c)	σ	stat./σ	$\sum_{\text{syst.}}/\sigma$	syst.(pol.)/σ	$\Delta\sigma/\sigma$
10.0 – 50.0	0.06	2.4	8 (8)	7 (3)	11 (10)
10.0 – 12.0	0.02	8.9	9 (9)	1 (4)	13 (14)
12.0 – 16.0	0.02	7.6	8 (8)	6 (3)	13 (12)
16.0 – 20.0	0.01	10.6	9 (9)	10 (6)	18 (16)
20.0 – 30.0	0.01	12.7	7 (7)	5 (4)	16 (15)
30.0 – 50.0	0.00	32.4	11 (11)	6 (3)	35 (34)

LIST OF REFERENCES

LIST OF REFERENCES

[1] Robert Oerter. The Theory Of Almost Everything: The Standard Model, The Unsung Triumph Of Modern Physics. Plume, 2006.

[2] Anthony D. Frawley, T. Ullrich, and R. Vogt. Heavy flavor in heavy-ion collisions at RHIC and RHIC II. Phys. Rept., 462:125, 2008. And private communication.

[3] N. Brambilla et al. Heavy quarkonium physics. arXiv:0412158.

[4] Braaten, Eric and Lee, Jungil. Polarization of Υ(nS) at the Fermilab Tevatron. Phys. Rev. D, 63:071501, Mar 2001.

[5] Acosta, D. and others. Υ Production and Polarization in $p\overline{p}$ Collisions at $\sqrt{s} =$ 1.8 TeV. Phys. Rev. Lett., 88:161802, Apr 2002.

[6] Artoisenet, P. and Campbell, J. and Lansberg, J. P. and Maltoni, F. and Tramontano, F. Υ Production at Fermilab Tevatron and LHC Energies. Phys. Rev. Lett., 101:152001, Oct 2008.

[7] V. M. Abazov et al. Measurement of inclusive differential cross sections for Υ(1S) production in $p\overline{p}$ collisions at $\sqrt{s} = 1.96$ TeV. Phys. Rev. Lett., 94:232001, Jun 2005.

[8] T. Aaltonen et al. Measurements of the angular distributions of muons from Υ decays in $p\overline{p}$ collisions at $\sqrt{s} = 1.96$ TeV. Phys. Rev. Lett., 108:151802, Apr 2012.

[9] V. M. Abazov et al. Measurement of the polarization of the Υ(1S) and Υ(2S) states in $p\overline{p}$ collisions at $\sqrt{s} = 1.96$ TeV. Phys. Rev. Lett., 101:182004, Oct 2008.

[10] Lyndon Evans and Philip Bryant. LHC Machine. Journal of Instrumentation, 3(08):S08001, 2008.

[11] H. Schopper and R.D. Heuer. LEP - The Lord of the Collider Rings at CERN 1980-2000: The Making, Operation and Legacy of the World's Largest Scientific Instrument. Springer, 2009.

[12] The ATLAS Collaboration. The ATLAS Experiment at the CERN Large Hadron Collider. Journal of Instrumentation, 3(08):S08003, 2008.

[13] The CMS experiment at the CERN LHC. JINST, page 0803:S08004, 2008.

[14] The LHCb Collaboration. The LHCb Detector at the LHC. Journal of Instrumentation, 3(08):S08005, 2008.

[15] The ALICE Collaboration. The ALICE experiment at the CERN LHC. Journal of Instrumentation, 3(08):S08002, 2008.

[16] The accelerator complex. `http://public.web.cern.ch/public/en/research/AccelComplex-en.html`.

[17] CMS Luminosity Collision Data. `https://twiki.cern.ch/twiki/bin/view/CMSPublic/LumiPublicResults2010`.

[18] CMS Luminosity Collision Data. `https://twiki.cern.ch/twiki/bin/view/CMSPublic/LumiPublicResults2011`.

[19] The accelerator complex. `https://twiki.cern.ch/twiki/bin/view/CMSPublic/LumiPublicResults`.

[20] J. Bensinger and T. Rodrigo. Alignment systems in LHC general purpose detectors. Nuclear Instruments and Methods in Physics Research, 666(0):173 – 196, 2012.

[21] The CMS magnet project: Technical Design Report. Technical Design Report CMS. CERN, Geneva, 1997.

[22] Bayatyan, G L and Della Negra, Michel and Fo, and Herv, A and Petrilli, Achille. CMS computing: Technical Design Report. Technical Design Report CMS. CERN, Geneva, 2005. Submitted on 31 May 2005.

[23] The CMS Collabration. CMS TriDAS project: Technical Design Report; 1, the trigger systems. Technical Design Report CMS.

[24] Sergio Cittolin, Attila Rcz, and Paris Sphicas. CMS trigger and data-acquisition project: Technical Design Report. Technical Design Report CMS. CERN, Geneva, 2002.

[25] Vardan Khachatryan et al. Upsilon production cross section in pp collisions at $\sqrt{s} = 7$ TeV. Phys. Rev. D, 83:112004, 2011.

[26] Darin E. Acosta et al. Upsilon production and polarization in $p\bar{p}$ collisions at $\sqrt{s} = 1.8$-TeV. Phys. Rev. Lett., 88:161802, 2002.

[27] V. M. Abazov et al. Measurement of inclusive differential cross sections for υ_{1S} production in $p\bar{p}$ collisions at $\sqrt{s} = 1.96$-TeV. Phys. Rev. Lett., 94:232001, 2005.

[28] N. Brambilla et al. CERN Yellow Report, CERN-2005-005, 2005.

[29] Sung-Sheng Chang. Hamiltonian operator of gauge invariant gluons. Nucl. Phys., B172:335, 1980.

[30] R. Baier and R. Ruckl. Hadronic Production of J/Ψ and Upsilon: Transverse Momentum Distributions. Phys. Lett., B102:364, 1981.

[31] Edmond L. Berger and Daniel L. Jones. Heavy quark contributions to inelastic photoproduction of the J/Ψ, upsilon, and other states. Phys. Lett., B121:61, 1983.

[32] Eric Braaten, Sean Fleming, and Adam K. Leibovich. NRQCD analysis of bottomonium production at the Tevatron. Phys. Rev., D63:094006, 2001.

[33] CMS. Vertex studies. PAS, TRK-10-005, 2010.

[34] CMS. Alignment of the CMS Silicon Tracker during Commissioning with Cosmic Rays. JINST, 5:T03009, 2010.

[35] S. Van der Meer. Calibration of the effective beam height in the ISR. CERN-ISR-PO/68-31:250, 1968.

[36] CMS. Measurement of luminosity. CMS PAS EWK-10-004.

[37] T. Sjöstrand, S. Mrenna, and P. Z. Skands. Pythia 6.4 physics and manual. JHEP, 0605:026, 2006.

[38] M. Krämer. Prog. Part. Nucl. Phys., 47:141, 2001.

[39] S. Agostinelli et al. G4 - a simulation toolkit. Nucl. Instrum. Meth., A506:250–303, 2003.

[40] Barberio, E. and van Eijk, B. and Was, Z. Photos - a universal Monte Carlo for QED radiative corrections in decays. Comput. Phys. Commun., 66:115–128, 1991.

[41] Barberio, E. and Was, Z. PHOTOS - a universal Monte Carlo for QED radiative corrections: version 2.0. Comput. Phys. Commun., 79:291–308, 1994.

[42] CMS. Muon reconstruction. PAS, MUO-10-002, 2010.

[43] CMS. Precise Mapping of the Magnetic Field in the CMS Barrel Yoke using Cosmic Rays. JINST, 5:T03021, 2010.

[44] CMS. Tracker Material. PAS, TRK-10-003, 2010.

[45] CMS. Momentum scale. PAS, TRK-10-004, 2010.

[46] CMS. Upsilon production in PbPb collisions. CMS AN-2011/455.

[47] Lange, D.J. The `EvtGen` particle decay simulation package. Nucl. Instrum. Meth., A462:152–155, 2001.

[48] John C. Collins and Davison E. Soper. Angular Distribution of Dileptons in High-Energy Hadron Collisions. Phys. Rev., D16:2219, 1977.

[49] CMS Collaboration. Measurement of the $\Upsilon(1S)$, $\Upsilon(2S)$ and $\Upsilon(3S)$ polarizations in pp collisions at $\sqrt{s} = 7$ TeV. submitted to PRL. arXiv:1209.2922.

[50] CMS. Tracking Efficiency. PAS, TRK-10-002, 2010.

[51] CMS. Inclusive and Total Differential Production Cross Section of the J/ψ and b-hadron in pp Collisions at $\sqrt{s} = 7$ TeV with the CMS Experiment. PAS, BPH-10-002, 2010.

[52] Serguei Chatrchyan et al. Performance of CMS Muon Reconstruction in Cosmic-Ray Events. JINST, 5:T03022, 2010.

[53] H. Jung et al. The CCFM Monte Carlo generator CASCADE 2.2.0. The European Physical Journal C - Particles and Fields, 70:1237, 2010. And private communication.

[54] S. P. Baranov. Prompt Υ(nS) production at the LHC in view of the k_t-factorization approach. Phys. Rev. D, 86:054015, Sep 2012.

[55] Kai Wang, Yan-Qing Ma, and Kuang-Ta Chao. Υ(1S) prompt production at the Tevatron and LHC in nonrelativistic QCD. Phys. Rev. D, 85:114003, 2012. And private communication.

[56] Jean-Philippe Lansberg. J/Ψ production at $\sqrt{s} = 1.96$ and 7 TeV: Color-Singlet Model, NNLO* and polarisation. 2011. arXiv:1107.0292. And private communication.

APPENDICES

A. Track embedding

Efficiency measurements using the track embedding method are based on embedding simulated tracks which lie inside the detector acceptance into pp collision events and reconstructing the embedded track. Tracks are classified as being within the detector acceptance if a reconstructed track is found that has at least 75% of its hits originating from the generated muon if the track is reconstructed in an empty event. Tables A.5 and A.6 list the probability of muon tracks lying inside the detector acceptance as functions of p_T and pseudo-rapidity η.

Tables A.7 and A.8 list the muon track reconstruction efficiency as functions of p_T and η using the track embedding method for tracks which lie inside the detector acceptance.

Table A.1: Muon track acceptance as a function of p_T (GeV/c) and η for muons embedded into 7 TeV data.

η	-2.4 to -2.1	-2.1 to -1.2	-1.2 to -0.8	-0.8 to 0.8
p_T				
500	.9959±.0021	.9959±.0012	.9977±.0013	.9963±.0008
200	.9940±.0024	.9939±.0020	.9964±.0016	.9962±.0008
100	.9912±.0029	.9957±.0012	.9929±.0023	.9958±.0009
50	.9940±.0025	.9958±.0012	.9985±.0011	.9957±.0009
20	.9916±.0029	.9966±.0011	.9979±.0012	.9954±.0009
10	.9880±.0035	.9963±.0011	.9993±.0007	.9958±.0009
5	.9915±.0028	.9970±.0010	.9910±.0026	.9962±.0008
2	.9877±.0041	.9968±.0012	.9912±.0029	.9929±.0013
1	.9950±.0022	.9947±.0013	.9874±.0030	.9826±.0018
0.50	.9373±.0089	.9817±.0028	.8997±.0094	.9183±.0043

Table A.2: Muon track acceptance as a function of p_T (GeV/c) and η for muons embedded into 7 TeV data.

η	0.8 to 1.2	1.2 to 2.1	2.1 to 2.4
p_T			
500	.9914±.0025	.9947±.0013	.9959±.0021
200	.9917±.0025	.9949±.0013	.9918±.0029
100	.9897±.0027	.9949±.0013	.9915±.0028
50	.9906±.0027	.9944±.0013	.9970±.0017
20	.9962±.0017	.9931±.0015	.9961±.0019
10	.9918±.0025	.9934±.0015	.9950±.0022
5	.9962±.0017	.9939±.0014	.9969±.0018
2	.9881±.0034	.9947±.0023	.9962±.0022
1	.9862±.0031	.9924±.0016	.9917±.0029
0.50	.8841±.0103	.9749±.0033	.9712±.0061

Table A.3: Muon track reconstruction efficiencies as a function of p_T (GeV/c) and η for muons embedded into 7 TeV data.

η	-2.4 to -2.1	-2.1 to -1.2	-1.2 to -0.8	-0.8 to 0.8
p_T				
500	.9969±.0018	.9990±.0006	.9992±.0008	.9981±.0006
200	.9990±.0010	.9986±.0007	1.0±.00	.9985±.0005
100	.9971±.0017	.9983±.0007	.9976±.0014	.9966±.0008
50	.9990±.0010	.9994±.0005	1.0±.00	.9989±.0005
20	.9989±.0011	.9987±.0007	.9993±.0007	.9977±.0007
10	.9990±.0010	.9980±.0008	.9978±.0013	.9971±.0007
5	.9981±.0013	.9987±.0007	1.0±.00	.9981±.0006
2	1.0±.00	.9982±.0009	.9970±.0017	.9967±.0009
1	1.0±.00	.9983±.0007	.9985±.0011	.9934±.0011
0.50	.9993±.0032	.9978±.0010	.9880±.0036	.9923±.0014

Table A.4: Muon track reconstruction efficiencies as a function of p_T (GeV/c) and η for muons embedded into 7 TeV data.

η	0.8 to 1.2	1.2 to 2.1	2.1 to 2.4
p_T			
500	.9993±.0007	.9983±.0007	1.0±.00
200	.9939±.0021	.9990±.0006	1.0±.00
100	.9970±.0015	.9990±.0006	1.0±.00
50	1.0±.00	.9993±.0005	1.0±.00
20	.9985±.0011	.9984±.0007	.9990±.0010
10	.9992±.0008	.9993±.0005	1.0±.00
5	.9992±.0008	.9970±.0010	1.0±.00
2	.9960±.0020	.9978±.0010	1.0±.00
1	.9934±.0022	.9977±.0009	.9990±.0010
0.50	.9883±.0037	.9991±.0007	.9973±.0019

The change in efficiency is the result of an improved treatment of the primary vertex position which is used in the seeding of non-pixel triplet tracks. It is not expected to have any affect on pixel triplet seeded tracks.

Table A.5: Muon track acceptance as a function of p_T (GeV/c) and η for muons embedded into 7 TeV data.

η	-2.4 to -2.1	-2.1 to -1.2	-1.2 to -0.8	-0.8 to 0.8
p_T				
500	0.9977 ± 0.0010	0.9991 ± 0.0004	0.9997 ± 0.0003	0.9997 ± 0.0001
200	0.9954 ± 0.0015	0.9991 ± 0.0004	$1.0 \pm {}^{0.0}_{.0004}$	0.9997 ± 0.0001
100	$1.0 \pm {}^{0.0}_{.0005}$	0.9991 ± 0.0004	0.9983 ± 0.0008	0.9997 ± 0.0002
50	0.9973 ± 0.0011	0.9987 ± 0.0004	$1.0 \pm {}^{0.0}_{.0004}$	0.9997 ± 0.0002
20	0.9982 ± 0.0009	0.9987 ± 0.0004	0.9993 ± 0.0005	0.9998 ± 0.0001
10	0.9946 ± 0.0016	0.9988 ± 0.0004	0.9993 ± 0.0005	0.9995 ± 0.0002
5	0.9975 ± 0.0011	0.9988 ± 0.0005	0.9988 ± 0.0007	0.9994 ± 0.0002
2	0.9968 ± 0.0012	0.9967 ± 0.0007	0.9990 ± 0.0006	0.9996 ± 0.0002
1	0.9951 ± 0.0015	0.9970 ± 0.0007	0.9973 ± 0.0010	0.9993 ± 0.0002
0.5	0.9943 ± 0.0017	0.9962 ± 0.0008	0.9411 ± 0.0046	0.9821 ± 0.0013

Table A.6: Muon track acceptance as a function of p_T (GeV/c) and η for muons embedded into 7 TeV data.

η	0.8 to 1.2	1.2 to 2.1	2.1 to 2.4
p_T			
500	0.9990 ± 0.0006	0.9982 ± 0.0005	0.9977 ± 0.0010
200	0.9984 ± 0.0007	0.9982 ± 0.0005	0.9982 ± 0.0009
100	0.9997 ± 0.0003	0.9974 ± 0.0006	0.9986 ± 0.0008
50	0.9997 ± 0.0003	0.9979 ± 0.0006	0.9963 ± 0.0013
20	0.9993 ± 0.0005	0.9986 ± 0.0005	0.9991 ± 0.0006
10	0.9997 ± 0.0003	0.9984 ± 0.0005	0.9986 ± 0.0008
5	0.9992 ± 0.0006	0.9976 ± 0.0006	0.9964 ± 0.0014
2	0.9993 ± 0.0005	0.9980 ± 0.0005	0.9951 ± 0.0015
1	0.9984 ± 0.0007	0.9967 ± 0.0007	0.9924 ± 0.0018
0.5	0.9344 ± 0.0048	0.9943 ± 0.0010	0.9885 ± 0.0024

Table A.7: Muon track reconstruction efficiencies as a function of p_T (GeV/c) and η for muons embedded into 7 TeV data.

η	-2.4 to -2.1	-2.1 to -1.2	-1.2 to -0.8	-0.8 to 0.8
p_T				
500	$1.0 \pm {}^{0}_{0.0005}$	$1.0 \pm {}^{0.0}_{0.0002}$	0.9997 ± 0.0003	0.9998 ± 0.0001
200	0.9995 ± 0.0005	0.9992 ± 0.0003	$1.0 \pm {}^{0.0}_{0.0004}$	0.9998 ± 0.0001
100	0.9996 ± 0.0004	0.9997 ± 0.0002	$1.0 \pm {}^{0.0}_{0.0004}$	$0.9999 \pm {}^{0.0}_{.0001}$
50	$1.0 \pm {}^{0.0}_{0.0005}$	0.9998 ± 0.0002	0.9997 ± 0.0003	0.9997 ± 0.0001
20	$1.0 \pm {}^{0.0}_{0.0005}$	0.9995 ± 0.0003	$1.0 \pm {}^{0.0}_{0.0004}$	0.9998 ± 0.0001
10	0.9991 ± 0.0006	0.9998 ± 0.0002	$1.0 \pm {}^{0.0}_{0.0004}$	0.9997 ± 0.0001
5	$1.0 \pm {}^{0.0}_{0.0006}$	$1.0 \pm {}^{0.0}_{0.0002}$	0.9996 ± 0.0004	$0.9999 \pm {}^{0.0}_{.0001}$
2	$1.0 \pm {}^{0.0}_{0.0005}$	0.9997 ± 0.0002	$1.0 \pm {}^{0.0}_{0.0004}$	0.9997 ± 0.0002
1	0.9996 ± 0.0004	0.9998 ± 0.0002	$1.0 \pm {}^{0.0}_{0.0004}$	0.9998 ± 0.0001
0.5	0.9995 ± 0.0005	0.9985 ± 0.0005	0.9887 ± 0.0021	0.9962 ± 0.0006

Table A.8: Muon track reconstruction efficiencies as a function of p_T (GeV/c) and η for muons embedded into 7 TeV data.

η	0.8 to 1.2	1.2 to 2.1	2.1 to 2.4
p_T			
500	$1.0 \pm {}^{0}_{0.0004}$	0.9998 ± 0.0002	0.9995 ± 0.0005
200	0.9997 ± 0.0003	0.9995 ± 0.0003	0.9991 ± 0.0007
100	$1.0 \pm {}^{0}_{0.0004}$	0.9997 ± 0.0002	$1.0 \pm {}^{0}_{0.0005}$
50	$1.0 \pm {}^{0}_{0.0004}$	0.9992 ± 0.0003	$1.0 \pm {}^{0}_{0.0005}$
20	0.9997 ± 0.0003	0.9995 ± 0.0003	$1.0 \pm {}^{0}_{0.0005}$
10	0.9997 ± 0.0003	0.9994 ± 0.0003	$1.0 \pm {}^{0}_{0.0005}$
5	0.9996 ± 0.0004	0.9995 ± 0.0003	$1.0 \pm {}^{0}_{0.0006}$
2	0.9993 ± 0.0005	0.9998 ± 0.0002	$1.0 \pm {}^{0}_{0.0005}$
1	0.9993 ± 0.0005	0.9995 ± 0.0003	$1.0 \pm {}^{0.0}_{0.0005}$
0.5	0.9906 ± 0.0019	0.9984 ± 0.0005	0.999 ± 0.0007

B. Monte Carlo Closure Test

We perform a Monte Carlo closure test to validate our analysis procedures. We treat simulated events from a detailed Pythia/Geant simulations as collider data and perform a full analysis. At each analysis step, we check if the predictions from parameterized MC match MC truth. We use Fall 2010 Monte Carlo samples to perform this test. Mind the total size of $\Upsilon(1S)$ sample is $160pb^{-1}$, we divide the sample into 160 small samples each corresponding to $1pb^{-1}$. We measure the cross section of each sample, compare to the Monte Carlo generated value and make pull distributions at each stage of the analysis.

Before doing this test, we notice several things that need to be corrected at the beginning. As mentioned in the section of Event Selection, the longitudinal separation between the two muons along the beam axis is required to be less than 2 cm. In Monte Carlo and Data, the distribution can be found in Figs. B.1. The cut removes a lot more Monte Carlo signal events than in Data. In the closure test, this cuts is removed in order to avoid losing too much signal events. But in data, the cut optimizes the signal over background significance, which can be found in Figs. B.2(a) and Figs. B.2(b). The significance is increased from 0.224 to 0.256. Therefore, we keep this cut for the analysis.

The Fall 2010 Monte Carlo samples were generated with a pre-filter which requires $|\eta|$ of muon less than 2.5, which means the generated number of upsilons is not the truth number that we should compare with. We have two options to fix this problem. One is to generate another Monte Carlo sample without any pre-filters but this is

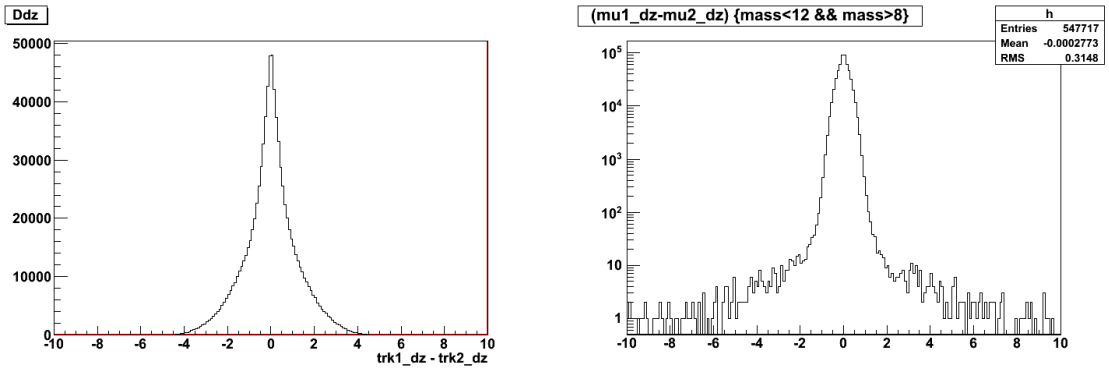

(a) Monte Carlo (b) Data

Figure B.1.: The distribution of the longitudinal separation between the two muons along the beam axis

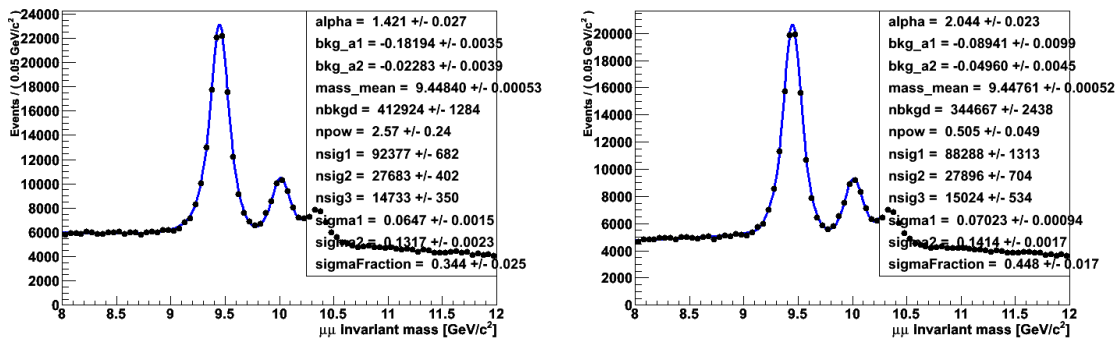

(a) Without the Ddz Cut (b) With the Ddz Cut

Figure B.2.: The mass fits before and after adding the Ddz cuts

time consuming. The other one is to modify the acceptance calculation to take the pre-filter into account, which means to define the acceptance by the following ratio:

$$\mathcal{A}\left(p_T^{\Upsilon}, y^{\Upsilon}\right) = \frac{N^{\text{reco}}\left(p_T^{\Upsilon}, y^{\Upsilon} \middle| \text{SiTRK track pair satisfies Eq. (3.1)}\right)}{N^{\text{gen}}\left(p'^{\Upsilon}_T, y'^{\Upsilon} \middle| \text{generated muons satisfy pre-filter}\right)}, \tag{B.1}$$

We only use this definition in the closure test. The difference between the acceptance with this definition and the default definition can be found in Figs. B.3.

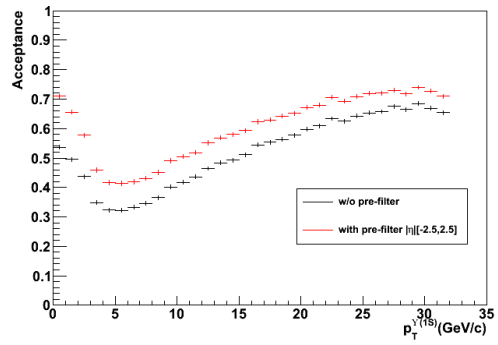

Figure B.3.: 1D acceptance used in closure test comparing with the default acceptance

After making the above changes, we start from Monte Carlo sample after skimming which was explained in Section. 3.2. We apply offline selection cuts step by step and apply corresponding correction factors to check if each step performs reasonably. We decide not to fit any mass spectrum in each step in order to avoid involving more than one factors at a time. Instead, we count the number of events during each step and check the fits at the end. We first select events by applying the acceptance cuts only. And we do event weighting by using the acceptance weight only. The pull is defined as the difference between the weighted yield and the generated yield divided by the error on the weighted yield [1].

The pull can be found in Figs. B.4. The pull is centered close to 0 and with a sigma at 1. This means the acceptance is validated.

After acceptance is validated, we select events further with the track quality cuts and apply the corresponding weight. The pull can be found in Figs. B.5. The pull is centered close to 0 and with a sigma at 1. This means the track quality efficiency is validated.

[1]The statistics of the pull is binomial because we are selecting events by applying a cut. The binomial error can be estimated with the simple formula $\sqrt{p \cdot (1-p)/Ngen}$, where $Ngen$ is the number of generated events and $p = Nraw/Ngen$, with $Nraw$ the number of reconstructed events corrected with event-by-event weights, is the efficiency of the selection ($p = 1/weight$). While this is not the best estimator of the binomial error it is a good estimator as far as p is not too close to 0 or 1 as in the case being considered. It is also a good estimate of the error given the statistics we have. Note that this is a relative error, to get the error on the number of events it must be multiplied by $Ngen$, so the full error is $\sqrt{Ngen \cdot p \cdot (1-p)}$.

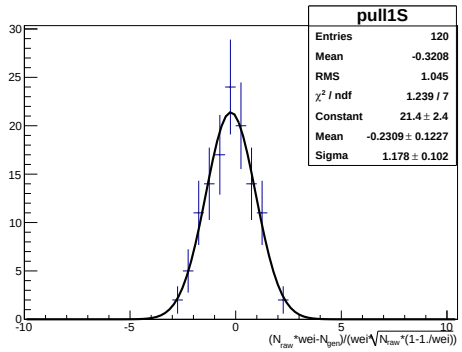

Figure B.4.: The pull distribution for checking acceptance

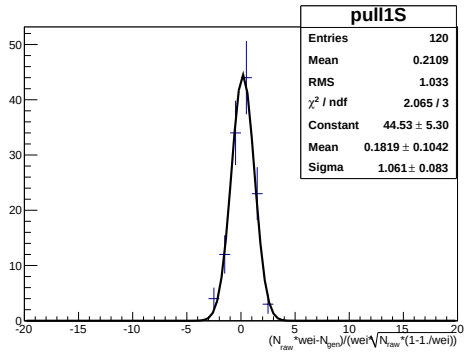

Figure B.5.: The pull distribution for checking track quality efficiency

After the track quality efficiency is validated, we select events further with the muon identification cuts. When applying the corresponding weight, we test the MC truth Υ identification efficiency first. The pull can be found in Figs. B.6. The pull is centered close to 0 and with a sigma at 1. This means the MC truth Υ identification efficiency is validated. We then use the MC truth single muon identification efficiency product. The pull can be found in Figs. B.7. The mean of the pull is shifted to 3.42 which indicates there is a bias in the MC truth single muon efficiency product. We treat this bias as a correction factor called ρ'. After correcting with the corresponding correction factor map, the pull can be found in Figs. B.8 which looks reasonable.

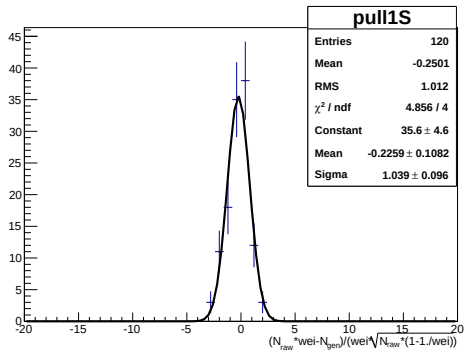

Figure B.6.: The pull distribution for checking MC truth dimuon(Υ) identification efficiency

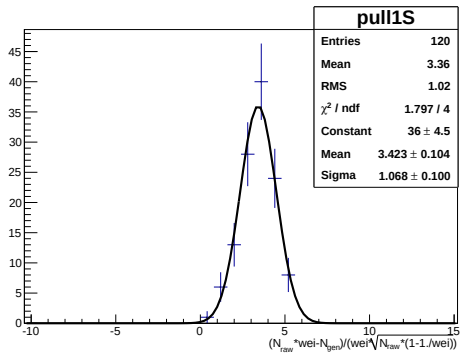

Figure B.7.: The pull distribution for checking MC truth single muon identification efficiency product

After validating the muon identification efficiencies, we select events further with the HLT_DoubleMu0 trigger requirements. The pull is shown in Figs. B.9. Both mean and sigma of the pull look reasonable. We then use the MC truth single muon trigger efficiency product. The pull can be found in Figs. B.10. It shows a small bias in the mean. After correcting with the corresponding ρ' factor map, the pull can be found in Figs. B.11 which looks reasonable.

As in the analysis, we used muon efficiencies measured with J/ψ samples, we now switch to the MC truth single muon identification efficiency measured with MC J/ψ sample while the trigger efficiency remains to be the one measured with Υ sample.

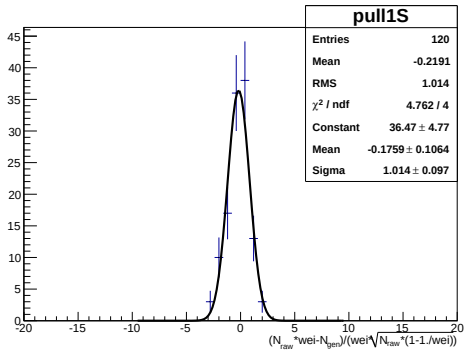

Figure B.8.: The pull distribution for checking MC truth single muon identification efficiency product corrected with ρ' factor

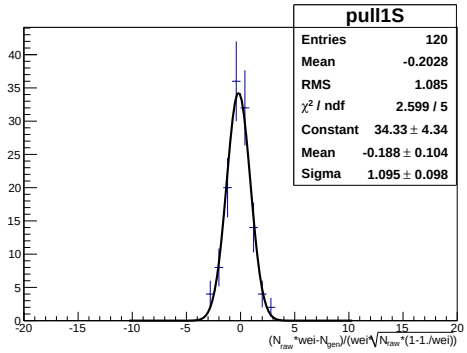

Figure B.9.: The pull distribution for checking MC truth Υ trigger efficiency

The ρ' factor that measured with Υ sample is also applied. The resulting pull can be found in Figs. B.12. Only a small shift in mean is observed which means the muon identification efficiency measured with Υ or J/ψ is very similar. We now replace the trigger efficiency with the one measured with J/ψ sample. The pull is shown in Figs. B.13. A big bias is found in this pull which means the muon trigger efficiency for HLT_DoubleMu0 measured with Υ or J/ψ shows difference. This is due to the difference in J/ψ and Υ kinematics. In the $3pb^{-1}$ analysis, we used an open trigger therefore the difference between J/ψ and Υ efficiencies is very small. For the HLT_DoubleMu0 used in this analysis, a further correction is needed. As in the analysis, we use tag and probe efficiencies instead of MC truth matching efficiencies. We'd

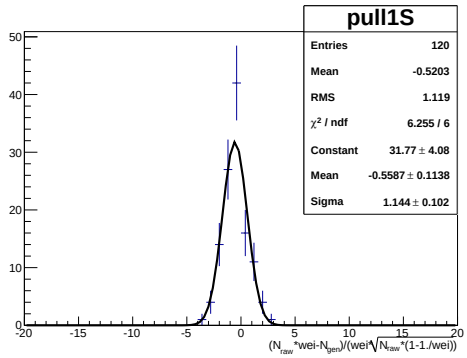

Figure B.10.: The pull distribution for checking MC truth single muon trigger efficiency measured with Υ sample

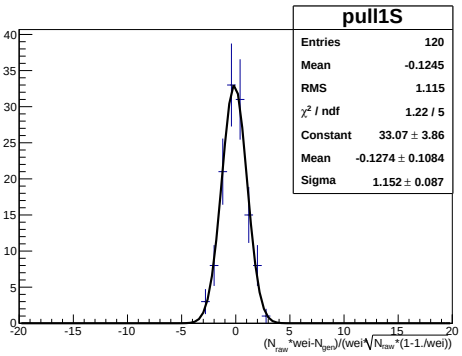

Figure B.11.: The pull distribution for checking MC truth single muon trigger efficiency measured with Υ sample and corrected with ρ'

like to see how the pull changes after using the tag and probe efficiencies which should also introduce a small bias due to measuring efficiencies with a subselection of muons. After replacing the MC truth efficiencies with the tag and probe efficiencies measured with J/ψ, the pull can be found in Figs. B.14. It is observed that the total effect gives a smaller bias in mean. We combine this bias with the ρ' together and define a combined correction factor called ρ. The pull for HLT_DoubleMu0 after correcting with the combined ρ factor can be found in Figs. B.15. The pull shows a reasonable distribution. Finally, we replace the counting method with the fitting technique used in the analysis to measure the yield. The final pull is shown in Fig. B.16.

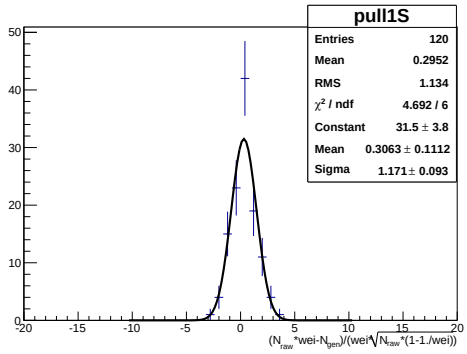

Figure B.12.: The pull distribution for checking MC truth single muon ID efficiencies measured with J/ψ sample and trigger efficiencies measured with Υ sample, corrected with ρ' factor

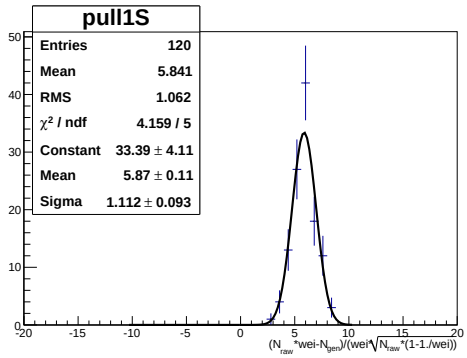

Figure B.13.: The pull distribution for checking MC truth single muon efficiencies product measured with J/ψ sample and corrected with ρ' factor

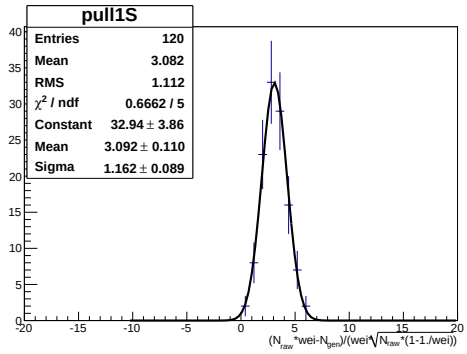

Figure B.14.: The pull distribution for checking MC tag and probe muon efficiencies product measured with J/ψ sample and corrected with ρ' factor

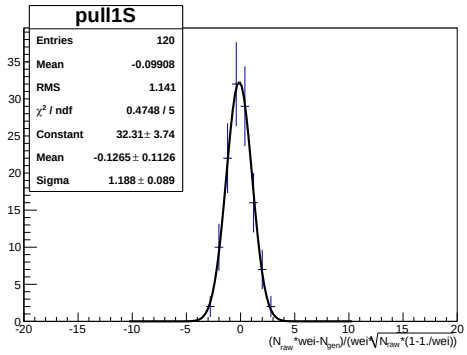

Figure B.15.: The pull distribution for checking MC tag and probe muon efficiencies product measured with J/ψ sample and corrected with the combined ρ factor

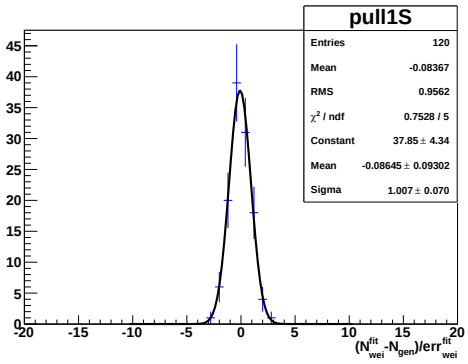

Figure B.16.: The pull distribution for checking the tag and probe efficiencies corrected with ρ factor and the measured yield is extracted via an unbinned maximum likelihood fit.

C. Like Sign Background

We validate the background model, exponential with err function, using like sign dimuons from data. The nominal fit layed with the like sign dimuon invariant mass is shown in Figs. C.1. The integral of the like sign dimuon mass is scaled to be the same with the fitted number of the background events. The like sign shape agrees well with the nominal fit to the background.

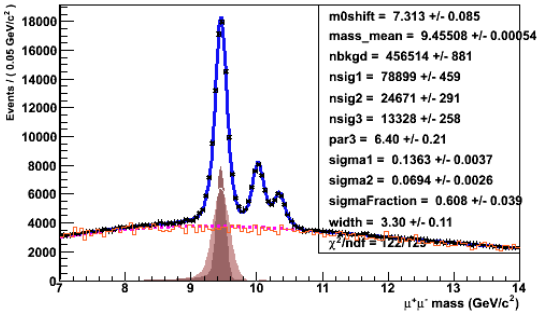

Figure C.1.: The nominal fit to the dimuon invariant mass using total statistics and is layed together with the likesign background(red line).

VITA

VITA

Yu Zheng was born in a small city near the Yangtze River in China. Yu's first interest in science was inspired by her father, who was very much into science. Yu kept excellent grades, especially in science, during the middle school and high school. As the top one student in her class, she was chosen to attend the preliminary screening exam offered by the University of Science and Technology of China in early 2003 and got admitted to the gifted program in advance of the national college entrance exam. As a bonus, she was given the freedom to choose her major in the second year in college. Her first choice was not Physics but Biology at that moment. However, after talking with many senior students, she realized that studying Biology in college requires the students to do experiments on little rats and rabbits. She gave up Biology but decided to study Physics because she dared not to cut the body of little animals. At the beginning of the third year in college, the students were required to choose their own specialties in Physics. Yu chose the nuclear physics for two reasons: she likes small things in general; she wants to be different and at that time seventy percent of her classmates in physics chose to study condensed matter physics. Fortunately, she never regretted with any of her decisions so far. She enjoyed a lot what she was learning and she graduated with a B.S. degree in Physics in 2007. Her bachelor thesis was "Transition Radiation in the Quark-Gluon-Plasma matter". Yu was then accepted by the Purdue University for the Ph.D. program. She was a teaching assistant for one semester before starting her research assistant position. She joined the CMS in 2008 and spent five years working on the particle data analysis. She was an active member in the B physics group. She focused on the quarkonia studies and had been the contact person for the trigger validation. She received her Ph.D. in winter 2012.